Multiple Interacting Rotational, Focal, and Wavelet Activities at Heterogeneous Tissue in Atrial Fibrillation

Zur Erlangung des akademischen Grades eines

DOKTOR-INGENIEURS

von der Fakultät für

Elektrotechnik und Informationstechnik

des Karlsruher Instituts für Technologie (KIT)

genehmigte

DISSERTATION

von

M.Sc. Markus Rottmann

geb. in Hermannstadt

Tag der mündlichen Prüfung:	19. 10. 2017
Referent:	Prof. Dr. rer. nat. Olaf Dössel
Korreferent:	Prof. Dr. Thomas Arentz

Abstract

Despite extensive research, the mechanisms of atrial fibrillation are still not clear. The central scientific question is what are the necessary conditions for the induction and maintenance of atrial fibrillation. This thesis presents simulation-, clinical- and experimental- studies of atrial fibrillation beginning from simplified to complex models. Main topics are the understanding of influence parameters of signal recordings, understanding the impact of fibrosis on the development of AF sources, and the development of new methods and catheter designs for the detection of AF sources.

Acknowledgments

I would like to acknowledge and thank all persons who contributed to the success of this PhD research.
I would like to thank to my PhD advisor, Professor Dössel, for supporting me during these past three years, for proofreading this PhD thesis, and for providing insightful discussions about the research.
I am also very grateful to Meir and Yaniv and Dr. Jadidi, Prof. Arentz, Prof. Klingel, Prof. Wellens and Richard for the scientific advice and knowledge and many insightful discussions and suggestions.
I also have to thank the members of my PhD committee for their helpful career advice and suggestions in general.
I am thankful for students who contributed to the work: Laura Unger, Max Barchet, Constantin Kohl, Christian Reich, Wenzel Kaltenbacher, Ufuk Arslan, Farhan Rafdionza, Linus Kienle and Pala Ahmed.
I thank my parents, for their support and faith in me and allowing me to be as ambitious as I wanted.
Finally, and most importantly, I would like to thank my wife Franziska-Rebekka. Her support, encouragement, quiet patience and unwavering love were undeniably the bedrock upon which the past years of my life have been built.

Contents

Abbrevation

ACh	acetylcholine
AF	atrial fibrillation
AP	action potential
AFCL	atrial fibrillation cycle length
APD	action potential duration
ApEn	approximate entropy
C	stiffness matrix
Ca^{2+}	calcium ions
CRN	Courtemanche Ramirez Nattel
CFAE	complex fractionated atrial electrogram
CLC	cycle length coverage
CLF	cycle length fluctuation
CV	conduction velocity
DOF	direction of propagation
DP	double potential
E	modulus of elasticity
EGM	electrogram
ERP	effective refractory period
F	force
FFT	fast Fourier transform
g	distance between the gap and the wall
g_{Na}	maximal Na conductance
g_K	maximal K conductance
HM	heterogeneous myocardium
I_K	potassium current
I_{KACh}	inward potassium current through ACh-activated K^+ channel
I_{Ks}	slowly activating outward rectifying potassium current
I_{Kur}	ultrarapidly activating outward rectifying potassium current
I_m	transmembrane current density per unit area
I_{ion}	total sarcolemmal ionic current

I_{Na}	fast Na^+ current
I_{K1}	inward rectifier K^+ current
I_{to}	transient outward K^+ current
I_{Kurd}	dog ultrarapid delayed rectifier K^+ current
I_{Kr}	rapid delayed rectifier K^+ current component
I_{Ks}	slow delayed rectifier K^+ current component
I_{Ca}	L-type Ca^{2+} current
I_{ClCa}	Ca^{2+}-activated Cl^- current
I_{NaCa}	Na^{2+}/Ca^{2+} exchanger current
I_{NaK}	Na^+-K^+ pump current
I_{bNa}	background Na^+ current
I_{bCa}	background Ca^{2+} current
I_{se}	externally current source in the extracellular domain
I_{si}	externally current source in the intracellular domain
J_i	impressed current density in the intracellular space
J_e	impressed current density in the extracellular space
k	constant
LAT	local activation time
m	gating variable
n	gating variable
NM	normal myocardium
h	gating variable
MRI	magnetic resonance imaging
NLEO	non-linear energy operator
NCX	sodium-calcium exchanger
PS	phase singularity
RotA	rotational activity
RIPV	right inferior pulmonary vein
PV	pulmonary vein
PVI	pulmonary vein isolation
SNR	signal-to-noise ratio
TAP	turnaround point
u	deformation
Ve	extracellular potential
Vm	transmembrane voltage
W	energy
3D	three-dimensional
β	cell surface- to-volume ratio
ε	strain tensor
ϕ_i	intracellular potential
ϕ_e	extracellular potential
λ	Lamé constant
μ	Lamé constant
ν	Poisson's ratio
σ_i	intracellular conductivity tensor
σ_e	extracellular conductivity tensor
κ	scalar value
σ	stress tensor

CHAPTER 1

Introduction and Fundamentals

"What we know is a drop, what we don't know is an ocean."

— Sir Isaac Newton

1.1 Motivation

Atrial fibrillation (AF) is the most common irregular heart beat and a main risk of stroke and sudden cardiac death [1]. 8% to 10% of the western population older than 80 years suffer from AF [2] [3] [4] [5] [6]. Because of the demographic change, the number of suffering people will increase significantly [2] [3] [4] [5] [6]. AF is commonly treated by the catheter ablation procedure [7]. The catheter ablation procedure lasts 4 to 6 hours [8]. Success rate studies of the catheter ablation procedures were about 59% (follow-up period of 18 months) [9]. The costs of AF are approximately 13.5 billion euros in the european union [10].

There is a need of research to understand the mechanisms of AF, because until today the mechanisms are still not clear. This thesis presents numerical field simulation models for better understanding the mechanisms of atrial fibrillation and for better detection of proarrhythmogenic sources and substrates to optimize the catheter ablation procedure.

Various catheter designs and signal processing methods were investigated regarding their ability to detect AF sources. The developed models were compared with clinical data with the aim to optimize the catheter ablation procedure to reducing patient burdens.

1.2 Aims of the Thesis

1.2.1 Impact of 3D atrial fibrosis on development and stability of AF sources

One central topic is the understanding of AF mechanisms and the development of methods to analyze signal characteristics of AF sources in simulation models with different catheter designs. These realistic AF simulation models including 3D fibrosis regions were compared with clinical data and showed high similarities. Furthermore, the effects of fibrosis on extracellular potentials were investigated in this thesis. In order to evaluate fibrosis simulations, the effects of fibrosis reconstructed from histological tissue sections on the extracellular potential were investigated.

1.2.2 Development of methods for the detection of AF sources

One central topic is the development of methods for analyzing signal characteristics of stable and unstable AF sources in realistic models and the comparison of different methods and catheter designs to estimate the AF source positions. Phase singularities and rotor center trajectories were calculated based on the Hilbert transform in atrial voxel models. Also, methods for calculating the conduction velocity were developed. Furthermore, signal characteristics at AF sources and analysis of signal morphologies at different excitations were analyzed. The simulation results of AF sources were compared with clinical studies of signal characteristics at rotational and focal sources. Table 1.1 provides an overview of this study's developed methods, AF models, and modeled catheter designs.

1.2.3 Impact of catheter design for identification of AF sources

Another central topic in this thesis is the impact of catheter design for identification of rotational activity (RotA) in atrial fibrillation. Commonly used but also new catheter designs were modeled, and recordings from simulation results were analyzed based on these catheter models. In order to get realistic scenarios a mechanical deformation model of catheter splines was modeled and evaluated with experimental data.

atrial tissue geometry	depolarization pattern	substrate properties	type of catheter	electrode to tissue geometry	methods and features	
planar patch model	plane wave	physiological	Lasso	distance to tissue	local activation time (LAT)	distance to rotor tip
sphere model	ectopic focus	fibrotic with various degrees	AFocusII	depth in tissue	conduction velocity (CV)	distance to block
realistic atrial model	endo-epicardial break through	including lines of block	PentaRay	point versus volume electrodes	peak-to-peak voltage	distance to ectopic focus
	rotor		array (n x m)		Hilbert phase	distance to collision
	collision				approximate entropy (ApEn)	degree of fibrosis (DOF)
	u-turn				R-S-difference	

Table 1.1: Overview of developed methods, AF models and modeled catheter designs Lasso, PentaRay (Biosense Webster, Inc., Diamond Bar, CA), AFocusII (St. Jude Medical, Inc., St. Paul, MN), and novel array (n x m grid) catheter.

1.2.4 Impact of Ablation Strategies

Furthermore, in this thesis, different ablation strategies in clinical use are evaluated with realistic AF simulation models, and new ablation strategies are investigated and tested in simulation studies. The simulation results of ablations were compared with the clinical studies of pulmonary vein isolation and low voltage guided ablation strategies.

1.3 Structure of the Thesis

Chapter 1 presents an overview of the medical fundamentals underlying the work in this thesis.
Chapter 2 provides quantitative parameter determination of atrial fibrillation depolarization patterns.
Chapter 3 describes electrogram characteristics at rotational and focal sources and correlations to low-voltage and slow-conduction areas.
Chapter 4 explains signal processing methods for the detection of atrial fibrillation sources as part of this thesis.
Chapter 5 shows the impact of catheter design on the detection of atrial fibrillation sources.
Chapter 6 presents the effects of ablation strategies on the termination of atrial fibrillation.

Chapter 7 describes the effects of fibrosis on extracellular potentials based on histological tissue sections.
Chapter 8 concludes the thesis.

1.3.1 Publications and supervised Student Theses

I published 1 peer review journal publication as first author, 3 as second author and 1 as coauthor. As first author, i published 16 conference publications in forms of publications and abstracts. I wrote 4 invention disclosures. I supervised 9 student theses that partly form the basis of this work. The list of publications and supervised theses are at the end of the thesis.

1.4 Fundamentals

> *"At one and the same time, in one and the same subject, two opposite motions cannot take place, that is, repentance and desire. Therefore, if the right upper [auricle] and lower ventricles are one and the same, it is necessary that the whole should cause at the same time one and the same effect and not two effects arising from diametrically opposite purposes as one sees in the case of the right ventricle with the lower, for whenever the lower contracts, the upper dilates to accommodate the blood which has been driven out of the lower ventricle."*
>
> — Leonardo da Vinci (1452-1519)

1.4.1 Anatomy and Physiology of the Heart

Ancient physicians have described the heart, such like Galen (200 A.D.), Avicenna, (980-1037), Zerbi (1502), Harvey (1653). Leonardo da Vinci (1452-1519) investigated the anatomy of the heart (cf. Figure 1.1) and illustrated his findings [11] [12] [13].

The size of a human adult heart is 12 cm x 8.5 cm x 6 cm [15]. The female adult heart comprises 0.4% (275 ± 75g) and the male adult heart 0.45% (325 ± 75g) of the body weight [16]. The human heart consists of 4 chambers, which are the left and right atria and the left and right ventricles (cf. Figure 1.2).

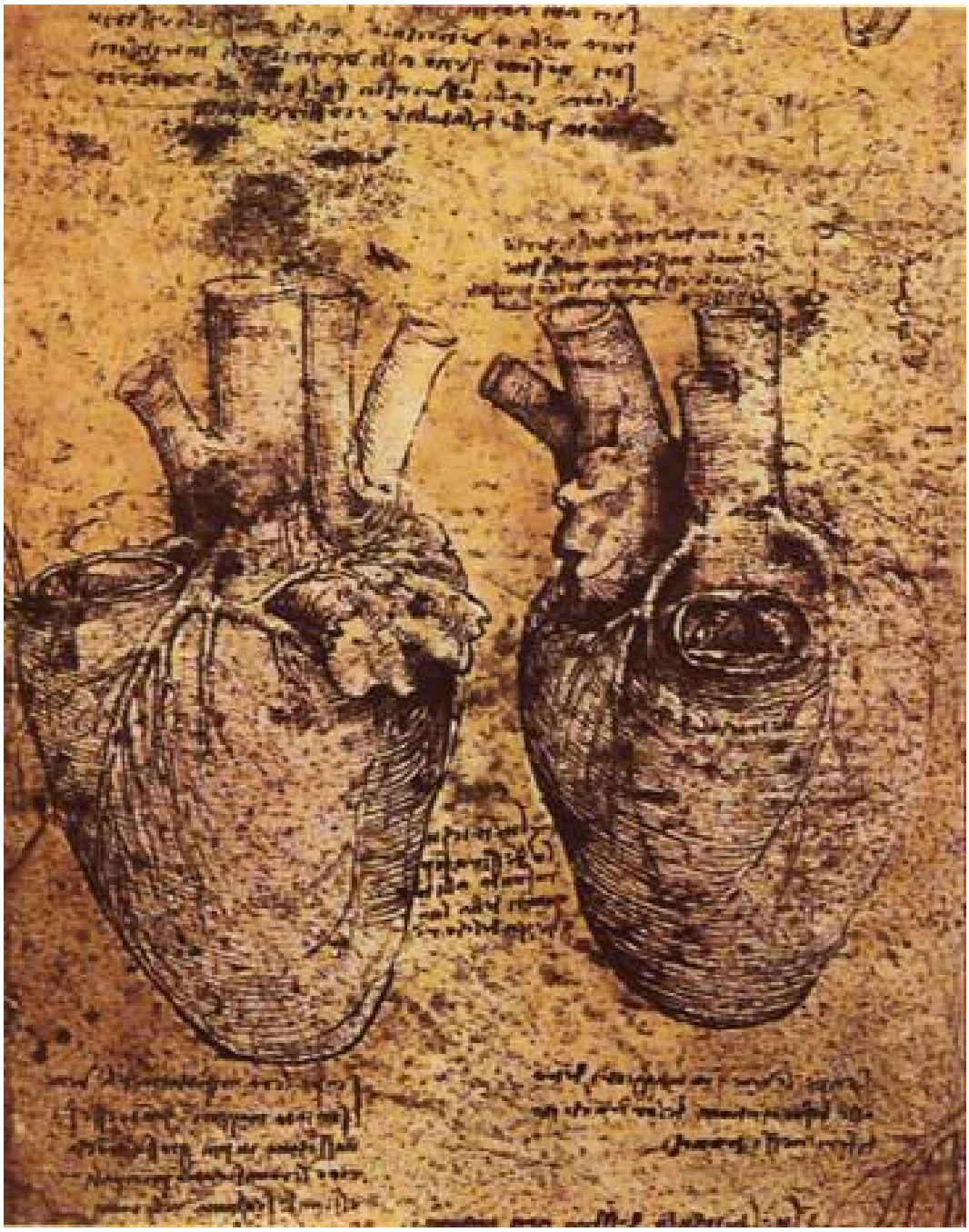

Figure 1.1: Illustrations of the heart by Leonardo da Vinci (1452-1519). The figure from [14] with permission.

1.4.2 Atrial Anatomy and Physiology

The heart as a muscular organ pumps blood into the body by rhythmical contraction. The human heart pumps more than 14,000 liters of blood per day, or 10 million liters per year [18]. The human heart consists on the four chambers left and right ventri-

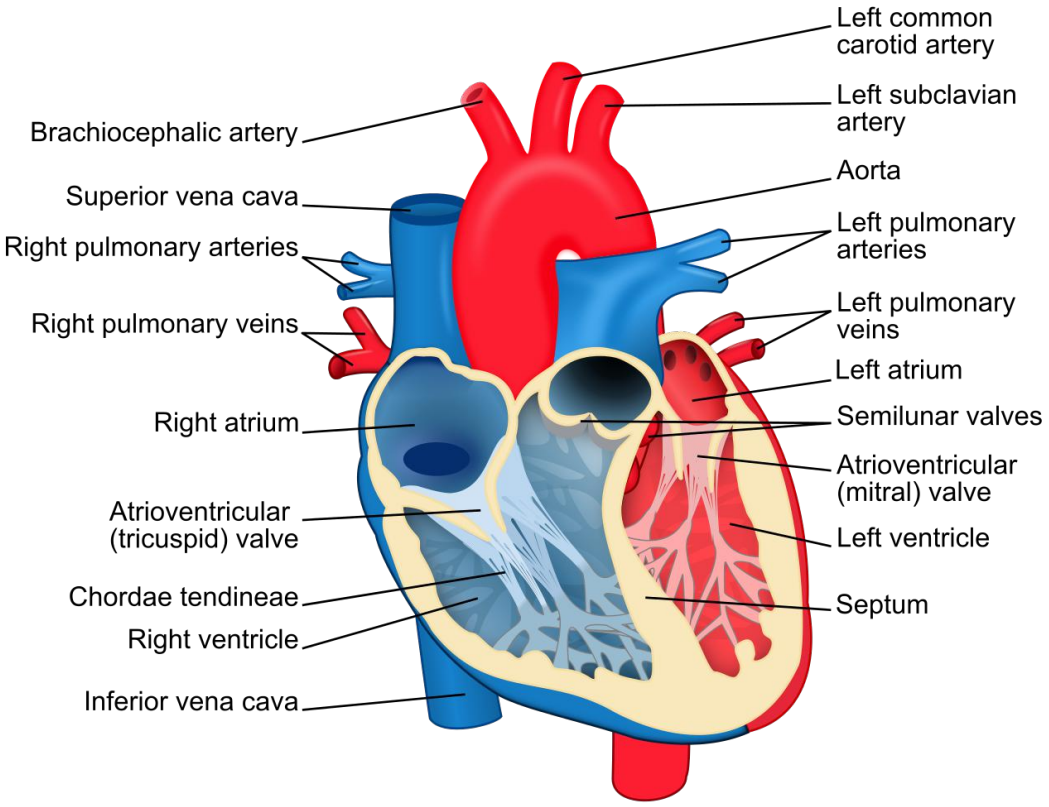

Figure 1.2: Human atria and ventricles (left and right). The figure is from [17] with permission.

cles and atria. The right and left atria are separated by the septum [19]. Atria are receiving chambers and, therefore, have thin walls, whereas ventricles are pumping chambers with thick walls [19]. Deoxygenated blood flows from the head, neck, and upper extremities through the inferior vena cava into the right atrium [19]. Further, deoxygenated blood flows in through the inferior vena cava from the thorax and lower extremities [19]. The blood then flows to the right ventricle, which pumps the deoxygenated blood to the lungs [19]. After briefly circulating in the lungs, oxygenated blood flows back through pulmonary veins to left atrium [19]. The left ventricle transports oxygenated blood through the systemic cardiovascular circulatory system to the blood capillaries [19]. The Figure 1.3 shows the blood flow of the oxygenated and deoxygenated blood [20].

1.4.3 Electrophysiology

The electrical currents in cardiac cells are responsible for the activation of ionic channels [21]. If the transmembrane voltage of a cell is above a certain threshold (-40 mV), the cell is activated, and the action potential is generated in its different phases [21].

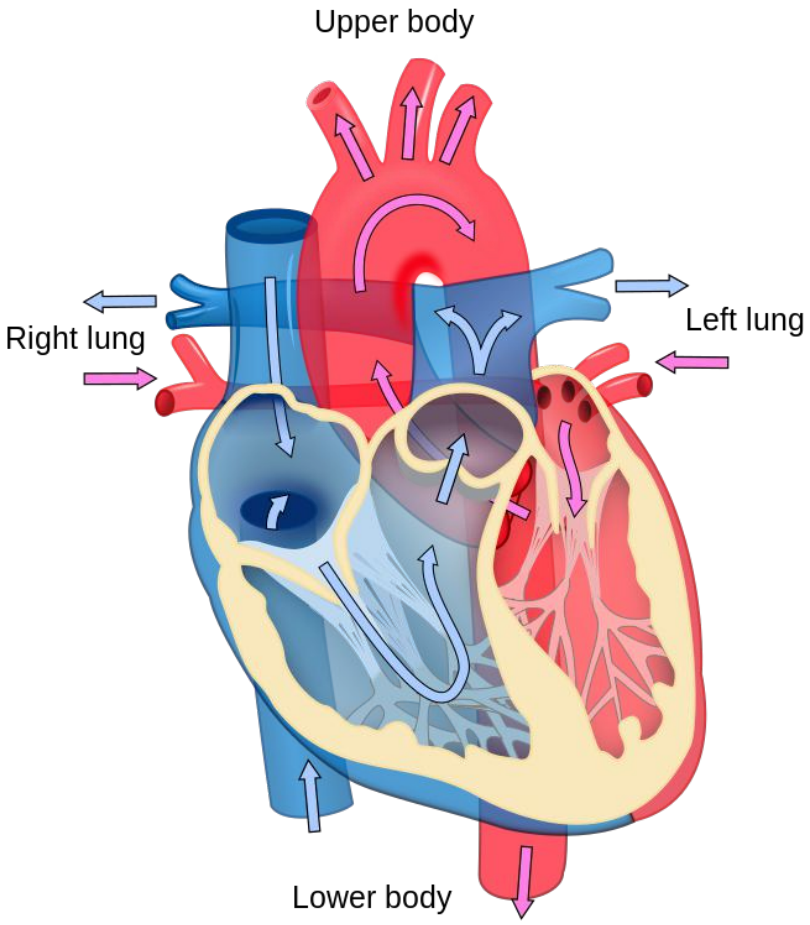

Figure 1.3: Blood flow of the oxygenated and deoxygenated blood in human body [20]. Also described are the capillary beds of lungs and of body tissues where gas exchange occurs [20]. The figure is adapted from [20] with permission.

The action potential (cf. Figure 1.4) in heart tissue consists on 4 phases (resting (4), upstroke (0), early repolarization (1), plateau (2), and final repolarization (3)) and has a voltage range between -80 mV and +30 mV. The corresponding ion currents of sodium, calcium, potassium currents and action potential duration (APD) are shown in Figure 1.4 [22] [23].

1.4.4 Hodgkin-Huxley Model

In the Physiological Laboratory in Cambridge and at the Laboratory of the Marine Biological Association in Plymouth, Hodgkin and Huxley developed a model for calculating action potentials [24]. Alan Lloyd Hodgkin and Andrew Fielding Huxley, jointly with Sir John Carew Eccles, won the 1963 Nobel Prize in Physiology or Medicine for their discoveries concerning the ionic mechanisms involved in excitation and inhibition

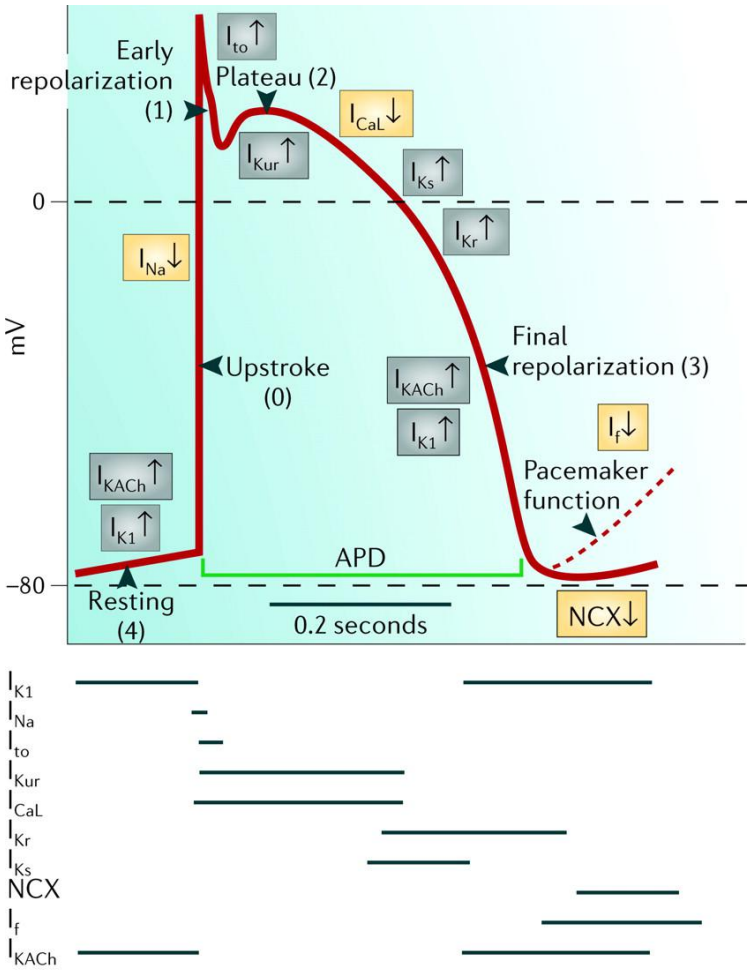

Figure 1.4: Transmembrane voltage with the phases resting (4), upstroke (0), early repolarization (1), plateau (2), and final repolarization (3) dependent on membrane currents, (B) sodium I_{Na}, calcium I_{Ca} and potassium currents I_K [22]. NCX is the sodium-calcium exchanger (yellow), I_{KACh} is the inward potassium current through ACh-activated K^+ channel, I_{K1} potassium current in inward rectifier ion channel, I_{to} is the transient outward potassium current, I_{Kur} is the ultra-rapidly activating outward rectifying potassium current, I_{Kr} is the rapidly activating outward rectifying potassium current, and I_{Ks} is the slowly activating outward rectifying potassium current [22]. This figure is from [22] with permission, from [23] reproduced with permission.

in the peripheral and central portions of the nerve cell membrane [25]. The electrical circuit model of a nerve is represented in Figure 1.5. Inner and outer cellular spaces are separated by the cellular membrane [25]. The potential in the membrane is caused by differences in ion concentrations and is in the range of -80 mV to +20 mV [26].

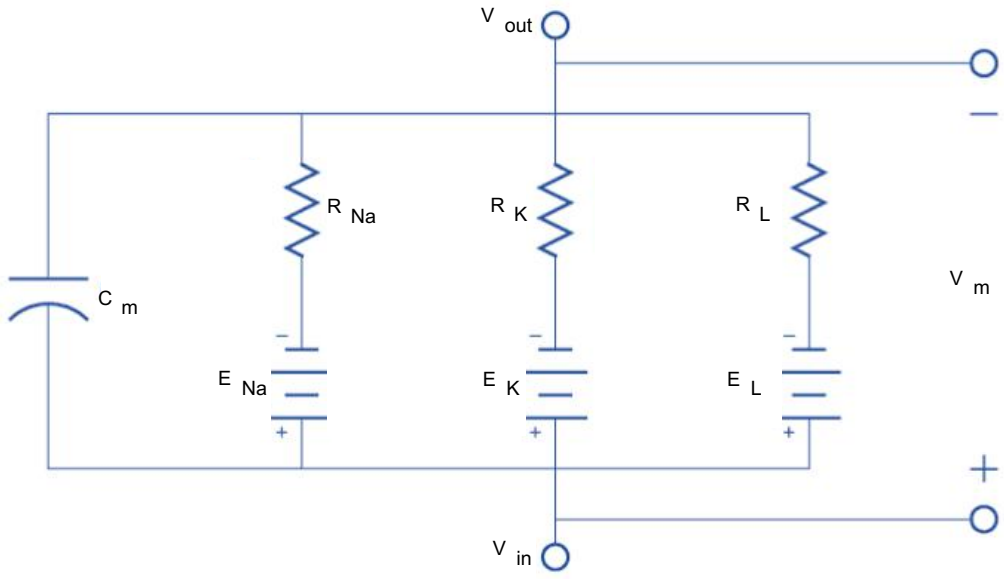

Figure 1.5: Equivalent electrical circuit model of a nerve with passive elements [25]. The capacitance C_m represents the lipid bilayer [25]. The resistances R_{Na} (sodium), R_K (potassium) and R_L (leak ion channels) represent ion channels [25]. The potentials E_{Na}, E_K, and E_L represent the electrochemical gradients [25]. V_m is the transmembrane voltage [25]. The figure is adapted from [25] [27] adapted with permission.

1.4.5 Atrial Fibrillation

1.4.5.1 History of Atrial Fibrillation Research

The first description (‘rebellious palpitation‘) of an irregular heart beat was published in the year 1749 by Jean-Baptiste de Sénac [28], a physician of King Louis XV. Physicians described the irregularities of the heart beat as ‘ataxia of the pulse‘ [29], ‘delirium cordis‘ [30], or ‘pulsus irregularis perpetuus‘ [31]. In 1906, Willem Einthoven (1860−1927) published an electrocardiogram of atrial fibrillation [32]. Willem Einthoven awarded the Nobel Prize in 1924 in physiology and medicine for his discoveries [33].

1.4.5.2 Types of Atrial Fibrillation

There are different types of atrial fibrillation, paroxysmal, persistent, and permanent, depending on irregularities that occurred in the atria over time (cf. Figure 1.6) [34].

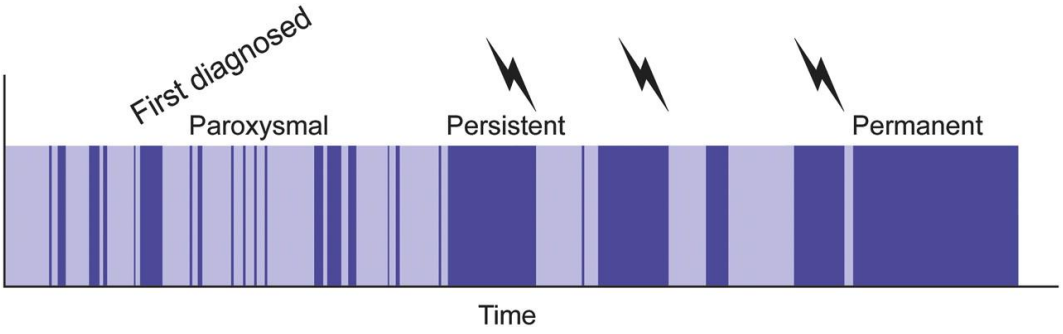

Figure 1.6: Example of a pattern of time in sinus rhythm (light purple) and in an AF pattern (dark purple) [34]. The figure is from [35] with permission, reproduced from [34] with permission.

1.4.5.3 Hypotheses of AF Mechanisms

Despite extensive research, the AF mechanisms are not well understood. In the early 1900s, hypotheses and explanations for the induction and maintenance of atrial fibrillation were the 'circus movement reentry', the 'ectopic focus hypothesis', and the 'multiple wavelet hypothesis' [36] [37] (cf. Figure 1.7). Various controversial hypotheses are described in the literature. Major AF hypotheses were the reentrant hypothesis, the leading circle concept, the rotor theory reentry, and multiple wavelets [38]. An overview of the atrial process mechanisms with four AF driving processes is described in Figure 1.8 [38]. In this thesis, the focus is on the structural loops that especially affect fibrosis in AF.

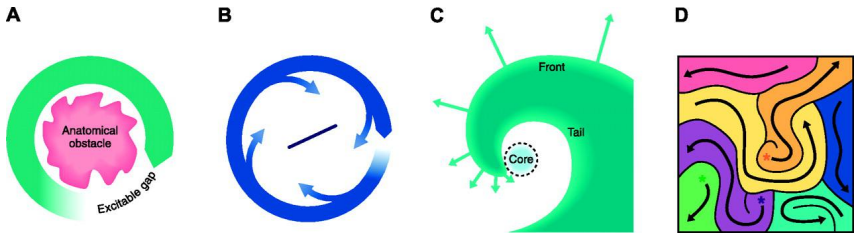

Figure 1.7: Hypotheses of AF mechanisms [38]. A: Circus movement reentry. The parameters influencing reentries around obstacles are, one the one hand, size of the anatomical obstacle, and on the other hand, refractory period and conduction velocity. B: Leading circle concept. Without any obstacle, reentry is along a minimally possible reentry path length, which is dependent on the refractory period and conduction velocity [38]. C: Rotor theory reentry signifies a rotating rotor around an unexcited core [38]. Conduction velocity vectors are dependent on the distance to core [38]. D: Multiple wavelets result in a chaotic excitation pattern [38]. Multiple waves interact and are separated by multiple conduction block lines [38]. The red asterisks symbolize the waves that appear in the mapping data. The appearing waves might originate from transmural conduction breakthroughs [38]. The figure is adapted from [38] with permission.

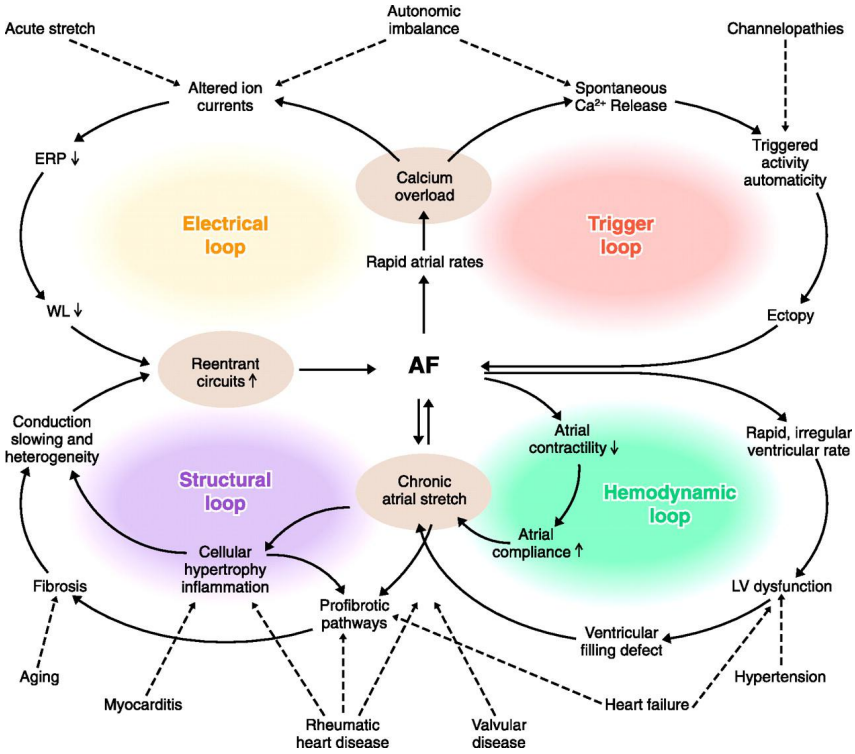

Figure 1.8: Overview of atrial process mechanisms with four main AF driving processes [38]. Processes are shown of electrical-, trigger-, structural-, and hemodynamic positive feedback loops [38]. An electrical loop remodeling of cells in AF by altered ion currents results in decreasing effective refractory period (ERP) and wavelengths, therefore promoting reentrant circuits [38]. This results in regions of fibrosis in slow conduction areas, which may lead to reentries in the structural loop [38]. Increased Ca^{2+} loading supports trigger activities [38]. AF is enhanced by changes of the contractile properties and by increased stretch in atrial tissue due to an irregular ventricular rate [38]. The four positive feedback loops described interact and enhance proarrhythmogenic mechanisms over time [38]. This might explain the AF behavior, which begins with paroxysmal AF to more regular, persistent AF [38]. The figure is from [38] with permission.

1.4.6 Fibrosis

Fibrosis is defined as formation of excess fibrous connective tissue [39]. Cardiac arrhythmias correlate with fibrosis areas [40] [41]. Furthermore, fibrosis strongly reduces the cardiac velocity [42] [43] and increases AF progress. There are different types of fibrosis described in the literature: interstitial, compact, diffuse, and patchy (cf. Figure 1.9) [40]. In this work, mainly patchy fibrosis was used in the developed computer models.

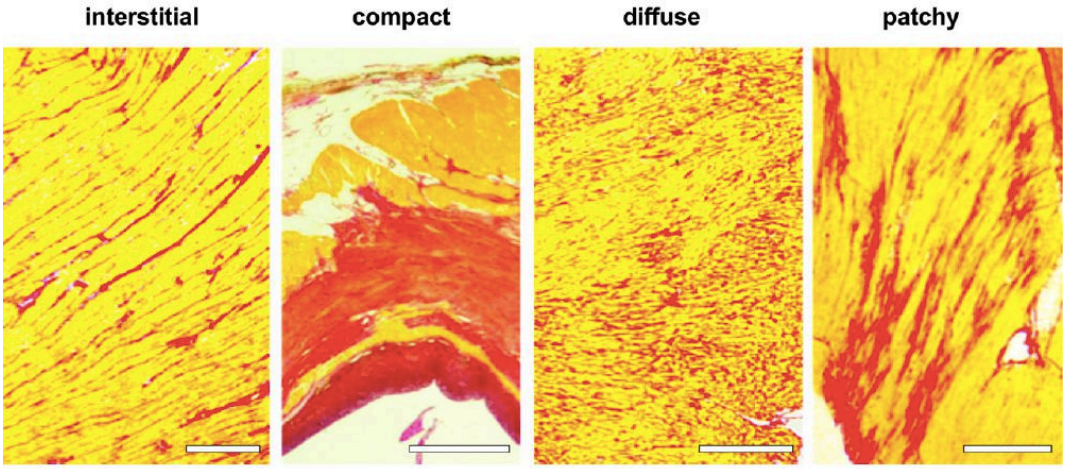

Figure 1.9: Different fibrosis textures: interstitial, compact, diffuse, and patchy. Red symbolizes fibrosis. The white bar symbolizes 1mm. The figure is from [44], with permission from [40].

1.4.7 Electrophysiological Study

Electrophysiological studies analyze the electrical excitations of the heart in order to detect arrhythmias and their sources in electrophysiology laboratories. In these labs, physicians work with clinical navigation systems, such as Carto (Biosense Webster, Inc., Diamond Bar, CA) or NavX (St. Jude Medical, Inc., St. Paul, MN), in order to navigate the mapping catheter and ablation catheters for signal recordings, generating 3D maps (cf. Figure 1.10) and ablating tissue regions responsible for the arrhythmia. The aim of the catheter ablation procedure is destroying tissue that is causing the arrhythmia with radiofrequency energy [45]. Common used mapping catheters are the catheters Lasso (Biosense Webster, Inc., Diamond Bar, CA), AFocusII (St. Jude Medical, Inc., St. Paul, MN) and PentaRay (Biosense Webster, Inc., Diamond Bar, CA).

Figure 1.10: Example of a cardiac operation room. The figure is from [46] with permission.

1.4.8 Cardiac Modeling

The first model to describe the action potential (AP) was published by Hodgkin and Huxley [25]. They analyzed the electrophysiological behavior of giant squid axons and developed mathematical models to calculate the ionic currents [25]. Moe et al. published the publication 'A computer model of atrial fibrillation' [47] already in the year 1964.

1.4.9 Cell models of atrial electrophysiology

The ionic mechanisms in cells and of action potentials can be described in terms of mathematical cell models [25]. Commonly used cell models for numerical field simulations are based on the model developed by Hodgkin and Huxley, which uses three ionic currents, a current carried by sodium ions I_{Na}, a current carried by potassium ions I_K, and a leakage current I_L (cf. Figure 1.5) [25] [48]. The formula for I_{ion} is described in Equation 1.1 [25].

$$I_{ion} = I_{Na} + I_K + I_L \tag{1.1}$$

The ionic currents are dependent on transmembrane voltage V_m, reversal potential E for that ion, and the conductance g (cf. Equations 1.2 to 1.4) [25].

$$I_{Na} = g_{Na}(V_m - E_{Na}) \tag{1.2}$$

$$I_K = g_K(V_m - E_K) \tag{1.3}$$

$$I_L = g_{Na}(V_m - E_L) \tag{1.4}$$

Noble et al. developed a cardiac cell model already in 1962 [49]. The complexity of the cell models increased over time, from the Hodgkin-Huxley model with three currents ($_{Na}$, I_K, I_L) and gating variables (m, n, and h) [25] to the cell model by Courtemanche, Ramirez, Nattel [26] (CRN) with 15 implemented gating variables and five concentration variables. The CRN cell model is more detailed and accurate and results in similar currents and action potential behavior than those in the observations of human atrial myocytes [26]. The cell models are mainly based on calculations of K^+, Na^+, and Ca^+ currents [26]. Furthermore, this model is dependent on the frequency and reduces the action potential duration under the AF condition [26]. Different cell models of atrial electrophysiology were developed and described in the literature (cf. the Table 1.2).

In this work, mainly the cell model by Courtemanche, Ramirez, Nattel (cf. Figure 1.11) under AF conditions was used [85]. The total transmembrane ionic current [86] is defined as :

$$I_{Ion} = I_{Na} + I_{K1} + I_{to} + I_{Kur,d} + I_{Kr} + I_{Ks} + I_{Ca} + I_{Cl,Ca} + I_{p,Ca} + I_{Na,Ca} + I_{NaK} + I_{b,Na} + I_{b,Ca} \tag{1.5}$$

1.4.10 Atrial arrhythmogenic remodeling

Remodeling is defined as a change in structure or function in atria that develop arrhythmias [87]. In 1995, Wijffels et al. developed chronic AF in goat models by using external fibrillator in Allessie's laboratory [88][89]. With a programmed electronic device that delivers a 1 s burst of electrical stimuli directly when detecting a sinus rhythm, they could maintain AF 24 hours per day over a period of several weeks [88][89]. At the beginning of the week, the AF was temporary, but the rate and stability of fibrillation continued developing to an ever more progressive level [88][89]. Notably, they demonstrated that 'AF begets AF', and with increased stability of AF, the ERP shortened because of the electrical remodeling induced [88][89]. It was also demonstrated that the remodeling process was reversible and that the ERP values returned to normal values after a period of one week [88][89]. Electrical remodeling shortens the refractory period and therefore facilitates persistent AF [88][89].

Different action potentials of the human cell models Courtemanche et al. [26], 1998, Nygren et al. [90], 1998, Maleckar et al. [91], 2008, Koivumäki et al. [92], 2011,

Year	*Author*	*Specimen*	*Species*
1962	Noble [49]	Purkinje fiber	-
1975	McAllister, Noble, Tsien [50]	Purkinje fiber	-
1977	Beeler, Reuter [51]	Ventricular myocardium	Mammalian
1980	Yanagihara, Noma, Irisawa [52]	Sinoatrial node	Rabbit
1982	Bristow, Clark [53]	Sinoatrial node	Rabbit
1983	Bristow, Clark [54]	Sinoatrial node	Rabbit
1984	Noble, Noble [55]	Sinoatrial node	Rabbit
1985	DiFrancesco, Noble [56]	Purkinje fiber	Mammalian
1987	Hilgemann, Noble [57]	Atrial working myocardium	Rabbit
1990	Earm, Noble [58]	Atrial working myocardium	Rabbit
1991	Luo, Rudy [59]	Ventricular myocardium	Mammalian
1994	Luo, Rudy [60] [61]	Ventricular myocardium	Guinea-pig
1994	Demir, Clark, Murphey, Giles [62]	Sinoatrial node	Rabbit
1996	Dokos, Celler, Lovell [63]	Sinoatrial node	Mammalian
1996	Lindblad, Murphey, Clark, Giles [64]	Atrial working myocardium	Rabbit
1996	Demir, Rourke, Tomaselli, Marban, Winslow [65]	Ventricular myocardium	Rabbit
1998	Courtemanche, Ramirez, Nattel [26]	Atrial working myocardium	Human
1998	Jafri, Rice, Winslow [66]	Ventricular myocardium	Guinea-pig
1998	Noble, Varghese, Kohl, Noble [67]	Ventricular myocardium	Guinea-pig
1998	Priebe, Beuckelmann [68]	Ventricular myocardium	Human
1999	Demir, Clark, Giles [69]	Sinoatrial node	Rabbit
1999	Winslow, Rice, Jafri, Marbán, O'Rourke [70]	Ventricular myocardium	Canine
2000	Ramirez, Nattel, Courtemanche [71]	Atrial working myocardium	Canine
2000	Zhang, Holden, Kodoma, Honjo, Lei, Varghese, Boyett [72]	Sinoatrial node	Rabbit
2001	Boyett, Zhang, Garny, Holden [73]	Sinoatrial node	Rabbit
2001	Pandit, Clark, Giles, Demir [74]	Ventricular myocardium	Rat
2001	Puglisi, Bers [75]	Ventricular myocardium	Rabbit
2002	Kneller, Ramirez, Chartier, Courtemanche, Nattel [76]	Atrial working myocardium	Canine
2002	Kurata, Hisatome, Imanishi, Shibamoto [77]	Sinoatrial node	Rabbit
2002	Bernus, Wilders, Zemlin, Verschelde, Panfilov [78]	Ventricular myocardium	Human
2004	Lovell, Cloherty, Celler, Dokos [79]	Sinoatrial node	Rabbit
2004	ten Tusscher, Noble, Panfilov [80]	Ventricular myocardium	Human
2004	Iyer, Mazhari, Winslow [81]	Ventricular myocardium	Human
2006	ten Tusscher, Paniflov [82]	Ventricular myocardium	Human

Table 1.2: Overview of cardiac cell models described in the literature [83] [84].

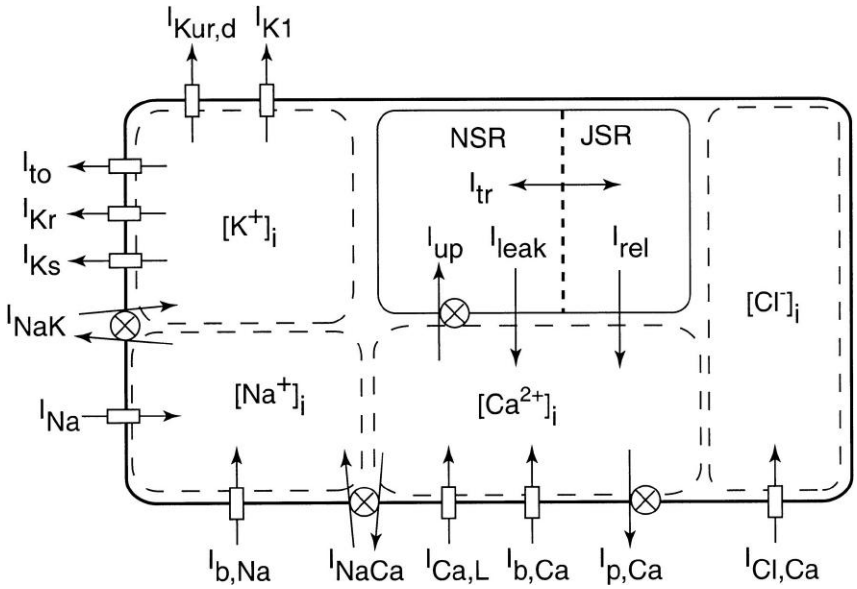

Figure 1.11: Schematic of the Courtemanche-Ramirez-Nattel model [86] with I_{Na} the fast Na^+ current, I_{K1} the inward rectifier K^+ current, I_{to} the transient outward K^+ current, $I_{Kur,d}$ the dog ultra-rapid delayed rectifier K^+ current, I_{Kr}, and I_{Ks} the rapid and slow delayed rectifier K^+ current components, I_{Ca} the L-type Ca^{2+} current, $I_{Cl,Ca}$ the Ca^{2+}-activated Cl^- current, $I_{Na,Ca}$ the Na^{2+}/Ca^{2+} exchanger current, I_{NaK} the Na^+-K^+ pump current and $I_{b,Na}$ and $I_{b,Ca}$ are the background Na^+ and Ca^{2+} currents [86]. The figure is from [86] with permission.

and Grandi et al. [93], 2011 during sinus rhythm and under AF condition (ERP shortened) are depicted in Figure 1.12.

1.4.11 Modeling of excitation propagation

1.4.11.1 Bidomain simulation

The bidomain model defines a model that includes two interpenetrating domains, the intracellular domain, and the extracellular domain. Schmitt et al. [94] proposed the bidomain model as a continuum approach in 1969, and Tung et al. [95] developed the mathematical model in 1978. With the bidomain equations, the currents in the intra- and extracellular domain are independently calculated. The schematic figure of the bidomain model is depicted in Figure 1.13.

The transmembrane potential V_m is defined as the potential difference across the cell membrane. Φ_i and Φ_e are the intra- and extracellular potentials [97] [98] [99].

$$V_m = \Phi_i - \Phi_e \tag{1.6}$$

J_i^i and J_e^i are the impressed current densities. σ_i and σ_e are the conductivity tensors (cf. Equation 1.7 and Equation 1.8) [97] [98] [99].

$$J_i = -\sigma_i \nabla \Phi_i + J_i^i \tag{1.7}$$

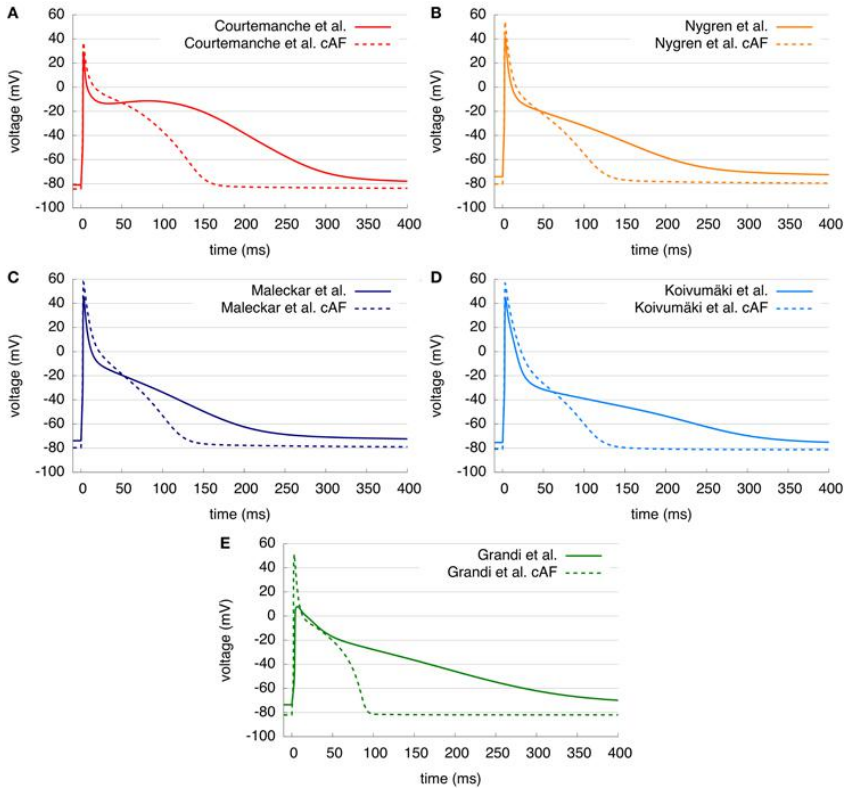

Figure 1.12: Action potentials of different human cell models during sinus rhythm and during chronic atrial fibrillation (cAF) (dashed line). A.) Courtemanche et al. (1998) [26], B.) Nygren et al. (1998) [90], C.) Maleckar et al. (2008) [91], D.) Koivumäki et al. (2011) [92], and E.) Grandi et al. (2011) [93]. The figure is from [85] with permission.

$$J_e = -\sigma_e \nabla \Phi_e + J_e^{\mathrm{i}} \tag{1.8}$$

C_m is the membrane capacitance, I_m the transmembrane current density per unit area (cf. Equation 1.9) [97] [98] [99].

$$I_m = C_m \frac{dV_m}{dt} + I_{ion} \tag{1.9}$$

The bidomain equations are described in Equations 1.10 to 1.11. β is the cell surface-to-volume ratio. I_{se} is the externally current source in the extracellular and I_{si} the externally current source in the intracellular domain [97] [98] [99].

$$\nabla(\sigma_e \nabla \phi_e) = -\beta I_m - I_{se} \tag{1.10}$$

$$\nabla(\sigma_i \nabla \phi_i) = \beta I_m - I_{si} \tag{1.11}$$

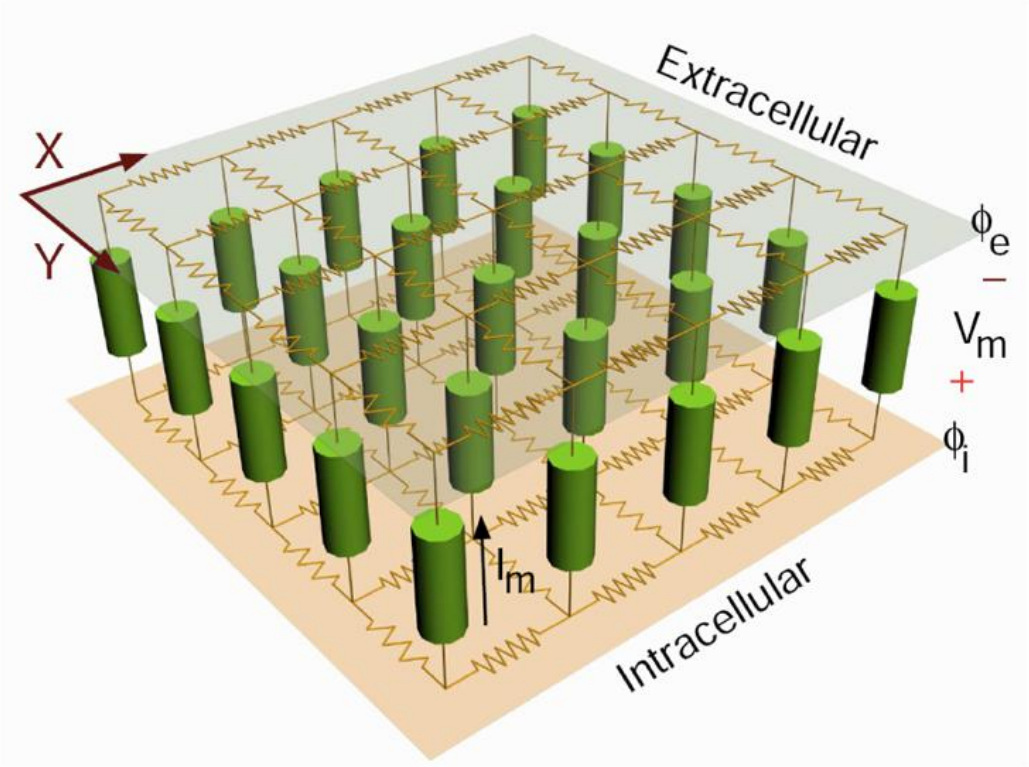

Figure 1.13: Bidomain model with two interpenetrating domains, the intracellular domain Φ_i and the extracellular domain Φ_e. V_m is the transmembrane voltage, and I_m is the cell membrane current. The cylinders (green) represent membrane which is described by a nonlinear current-voltage relationship. The figure is from [96] with permission.

1.4.11.2 Monodomain simulation

In complex simulation models, the computational effort to solve the bidomain equations is high. Instead of the bidomain equations, the monodomain equations can be used to improve the computational performance. The parameter extracellular potential can be calculated from the resultant intracellular current by using the Poisson equation (cf. Equations 1.12) [100] [99] with the scalar value κ.

$$\nabla(\sigma_i \nabla V_m) = (\kappa + 1) \cdot \beta \cdot C_m \frac{dV_m}{dt} + I_{ion} \tag{1.12}$$

CHAPTER 2

Quantitative Parameter Determination of Atrial Fibrillation Depolarization Patterns

"The important thing is not to stop questioning."

— Albert Einstein

2.1 Introduction

In electrophysiological studies, intracardiac recordings were measured to map wave excitations in commonly used clinical navigation systems [101]. But until today, there is only little information available on quantitative parameters displayed during the catheter ablation procedure [102]. Quantitative parameters can provide physicians with more information for better understanding and treating arrhythmias [101] [102]. During normal sinus rhythm, planar waves were observed. During persistent AF, complex patterns and signal characteristics of focal waves, blocks and near-field effects, rotational activity, colliding wavefronts, and endo-epicardial breakthroughs were observed and described in the literature [103] [104]. However, the typical signal morphologies dependent on the distance to the specific excitation source are not clearly understood. Therefore, this study presents detailed quantitative analyses of excitation patterns dependent on different parameters such as excitation patterns and distances. The simulations quantified parameters influencing, for example, distance to tissue, excitation pattern, electrode size, and nearfield effects [105]. This simulation study also compares the underlying transmembrane voltages and describes typical activation patterns and typical signal morphologies of the specific excitation patterns for better identifying proarrhythmogenic excitations and forming better ablation strategies.

2.2 Methods

2.2.1 Sensitivity analysis of unipolar signals

In order to quantify the parameters influencing unipolar and bipolar recordings, this chapter analyzed the dependency of the distance to tissue, the contribution from different tissue depth layers, different electrode sizes, and micro-electrodes at different distances to the tissue. Sensitivity analyses were made on different influence parameters, of which the overview is shown in Figure 2.1. In this simulation study the CRN cell model was used.

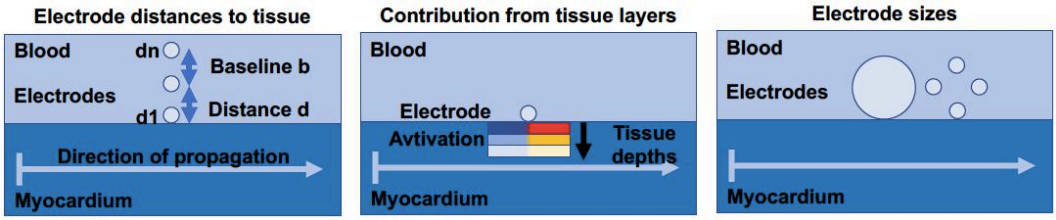

Figure 2.1: Overview of sensitivity analysis. Analysis of (Left) distance to tissue and (Center) contribution from tissue depth layers. (Right) Analysis of different electrode sizes. Figure (Left, Center) adapted from [S3] [106].

2.2.1.1 Distance to tissue

In clinical measurements, electrodes have a certain distance to the tissue. In order to model and analyze realistic simulation results, different distances to tissue were used to determine signal characteristics. Signal morphologies, amplitude, and width of unipolar and bipolar recordings were measured at different distances to tissue (cf. schematic Figure 2.1 (Left)).

2.2.1.2 Contribution from tissue layers

In order to analyze the influence of signal contributions from different tissue depths (cf. Figure 2.1), the excitations were modeled for different tissue depth layers separately (cf. Figure 2.2 (Center)). The material file of the myocardium consisted of seven tissue depth layers, separated by thin layers of 50 μm. Each layer was stimulated with a time delay (cf. Figure 2.2).

A.)

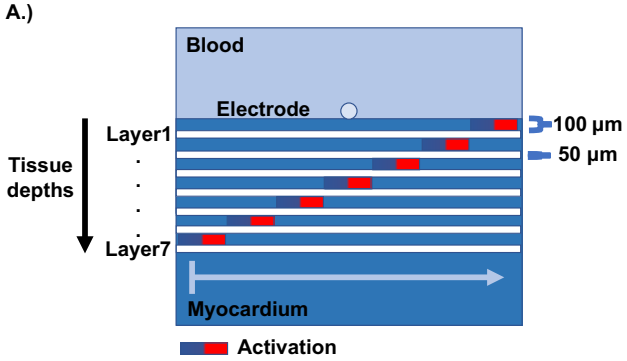

B.)

Tissue layer	Depth of layer (mm)
1	0.0 – 0.10
2	0.15 – 0.20
3	0.30 – 0.40
4	0.45 – 0.55
5	0.60 – 0.70
6	0.75 – 0.85
7	0.90 – 1.00

Figure 2.2: Sensitivity analysis of activations in different tissue layers. Schematic view in A). (B) Tissue layers at different depths in mm. The figure adapted from [S3] [106].

2.2.1.3 Electrode size

In clinical measurements, different electrode sizes have been used to collect signal recordings. Furthermore, different metal electrode sizes have been modeled, and the resulting simulated signal morphologies have been analyzed (cf. schematic Figure 2.1 (Right)).

2.2.2 Modeling of different AF excitation patterns

During AF, there were different complex excitation patterns observed. This simulation study presents the relationships between different patterns and corresponding signal morphologies. The excitation patterns (transmembrane voltages) observed of the planar wave, focal wave, excitation around line of block, collision, rotational activity, and break-through during AF are shown in simplified models in Figure 2.3.

In this simulation study planar waves, focal waves, excitations around blocks, collisions, and break-throughs were simulated using the Courtemanche cell model. Reentries within healthy tissue were simulated using the cell model Nygren. Rotational activities around non-conducting areas were simulated using the remodeled CRN cell model. Cardiac depolarization waves were simulated using the simulation framework acCELLerate [110] in this work.

2.2.2.1 Modeling of planar waves, ectopic foci, and endo-epicardial breakthroughs

Planar waves were stimulated at a region in the left side in the 3D tissue patch (cf. Figure 2.3 (A)). Focal waves (cf. Figure 2.3 (B)) were induced by stimulating a 3D region within the center of the 3D patch. The activation patterns were measured with different catheter designs and the resulting signal morphologies of planar waves

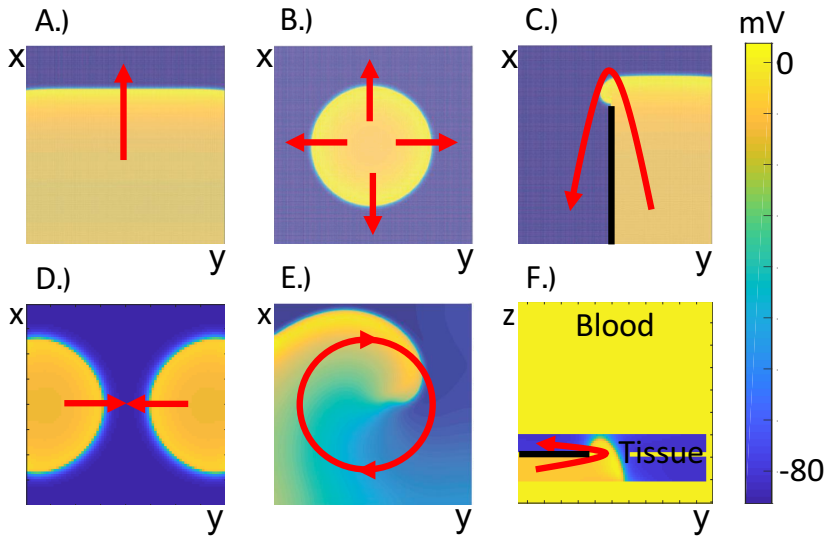

Figure 2.3: Overview of simplified models of excitation patterns during AF: (A) Planar wave, (B) ectopic focus (centrifugal excitation), (C) excitation around a block line, (D) colliding wavefronts, (E) rotational activity, and (F) break-through. Figure parts are adapted from Rottmann et al. (2014) [107], [85], [108], [109].

.

and ectopic foci were analyzed. Ectopic beats resulted in curved wavefronts and the resulting signals had S-wave predominance morphologies [104]. Especially, the RS-ratio [111] [112] parameter was used for statistical analysis in order to characterize the signal morphology of curved wavefronts in the case of an ectopic focus excitation [104]. Endo-epicardial breakthroughs were observed by high-resolution electrode measurements [113]. In simplified simulation models, breakthroughs were modeled using a two-layer model [104] (cf. Figure 2.3 (F)).

Typical signal characteristics of the modeled breakthroughs and clinical measurements were analyzed at different distances to the breakthrough point and were then compared.

2.2.2.2 Modeling of excitations around block lines

Cardiac excitations around block lines were modeled with a stimulation at a region in the 3D tissue patch under a non-conducting block line (cf. Figure 2.3 (C)). Unipolar signals near the u-turns around the non-conducting block line resulted in double potentials with various time differences between the first and the second activations. Signal characteristics were analyzed in different distances to the line of block.

2.2.2.3 Modeling of collision

Collisions were modeled with different stimulations from different sides (cf. Figure 2.3 (D)). Typical signal characteristics and morphologies of collisions were analyzed. The

focus of the analyses was the predominance of R-waves [104] in unipolar recordings at collision points. After the collision, excitations propagated in a vertical direction or resulted in the termination of the wavefronts.

2.2.2.4 Inducing rotational activities around non-conducting areas

Rotational activities were induced with cross-field stimulations [85] (cf. Figure 2.4 (A) and (C)). Signal characteristics of rotational activities were analyzed at different distances to the center of the rotational activity. Furthermore, stable and unstable rotational activities and anchored rotational activities at heterogeneous regions were analyzed.

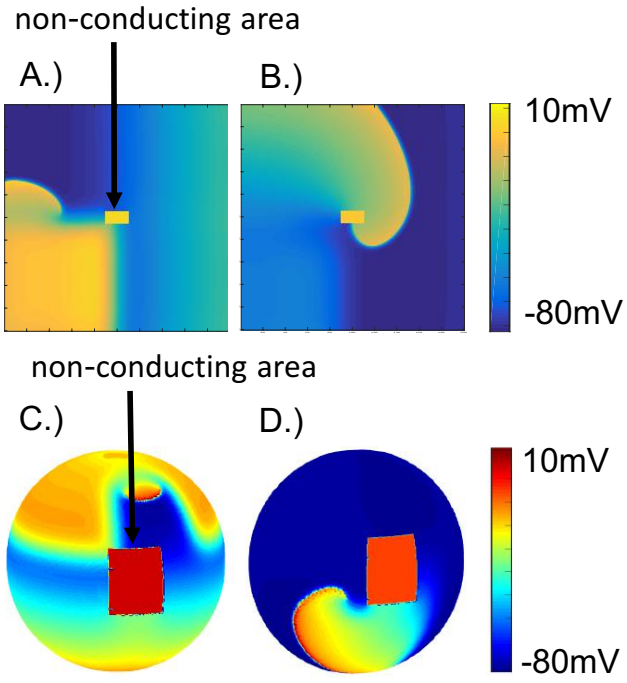

Figure 2.4: (A) Rotational activity induced by a cross-field stimulation. (B) Anchoring of the rotational activity around small non-conducting regions. Inducing rotational activity around the non-conducting area in a 3D sphere model. (C-D) Model of implemented non-conducting area within the atrial sphere model. (C) First stimulation from the upper side and second cross-field stimulation in the upper sphere region. (D) Resulting rotational activity. The figure is adapted from [S6] [114].

Rotational activity around a non-conducting area (cf. Figure 2.4 (A)) in a sphere model was induced by first stimulating the upper sphere area (cf. Figure 2.4 (B)) and then a cross-field stimulation in the upper sphere region (cf. Figure 2.4 (C)). The resulting rotational activity was anchored stably around this non-conductive area (cf. Figure 2.4 (D)).

2.3 Results

2.3.1 Activation patterns of different excitation waves

The Figure 2.5 shows different AF activation patterns measured with commonly used catheters in the case of a centered catheter and a distant catheter. With circular catheters, planar waves resulted in activation patterns in the form of cosines [113]. The direction of propagation and conduction velocity can be determined from these typical cosine patterns by the phase shift and amplitude of the fitted cosine pattern between the bipolar local activation times detected [113].

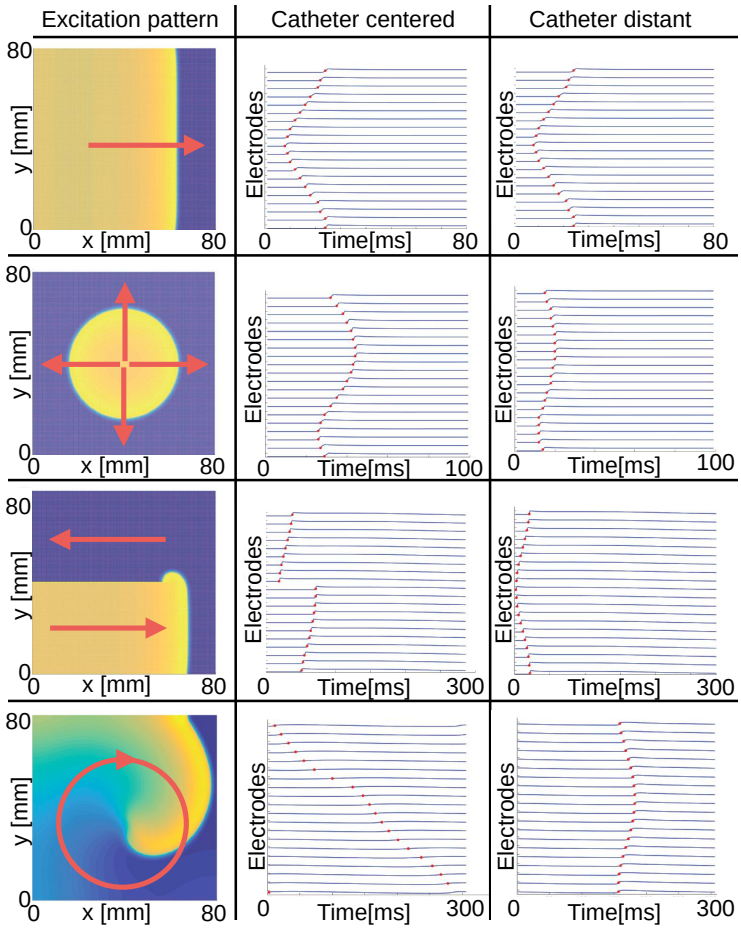

Figure 2.5: Activation patterns of the excitation waves, planar wave, focus, excitation around the block line, and rotational activity, measured with a circular catheter. Figure parts are adapted from Rottmann et al. (2014) [107], [115], [85], [108], [109], [116], [S4], [117], [118], [S5].

2.3.2 Sensitivity analysis of unipolar signals in a 3-dimensional patch

2.3.2.1 Signal morphologies at different distances to tissue

The quality of intracardiac recordings strongly depended on the distances between the measuring electrodes and the myocardial tissue [99]. In clinical measurements during a catheter ablation procedure, electrodes measure intracardiac recordings at a certain distance to tissue (cf. Figure 2.6). On the one hand, peak-to-peak amplitudes and the absolute of the steepest negative slope decreased with increasing distances to the tissue. On the other hand, the signal width and the time between the maximum and minimum of the unipolar recordings increased with increasing distance to the tissue.

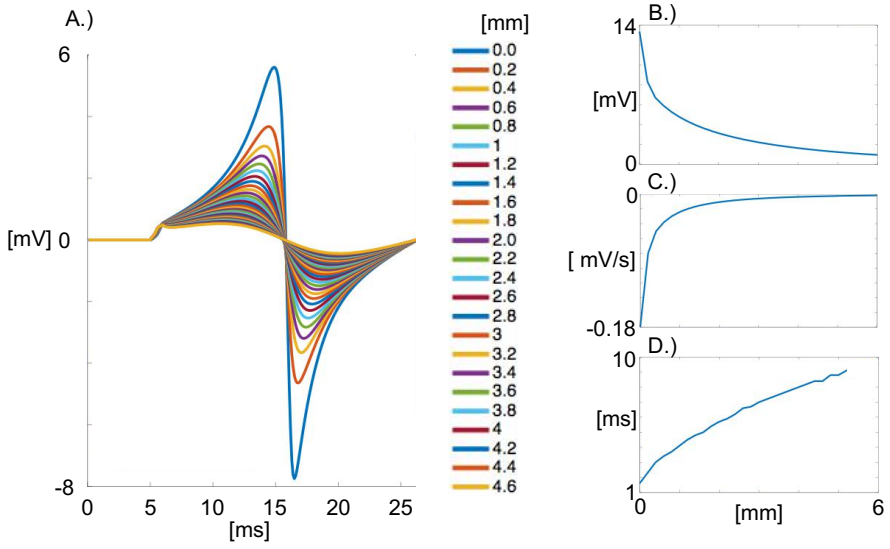

Figure 2.6: Sensitivity analysis of unipolar recording dependent on the distance to the tissue. (A) Signal morphology. (B) Peak-to-peak amplitude. (C) Steepest negative slope and (D) time between the maximum and the minimum in unipolar recordings.

2.3.2.2 Contribution from tissue layers

The measured intracardiac recordings resulted from different tissue layers in different depths. In fibrotic tissue, cardiac excitations in different tissue depths contributed to the resulting signals measured and could result in fractionated signals. In Figure 2.7(A), the contributions from different tissue depth layers and the schematic simulation setups of stimulations in different tissue depth layers are shown. The resulting signals from deeper tissue layers resulted in smaller amplitudes and greater signal widths (cf. Figure 2.7 (B)). These results show that the excitations in the upper tissue layers contribute more strongly to the signals measured in the blood layers.

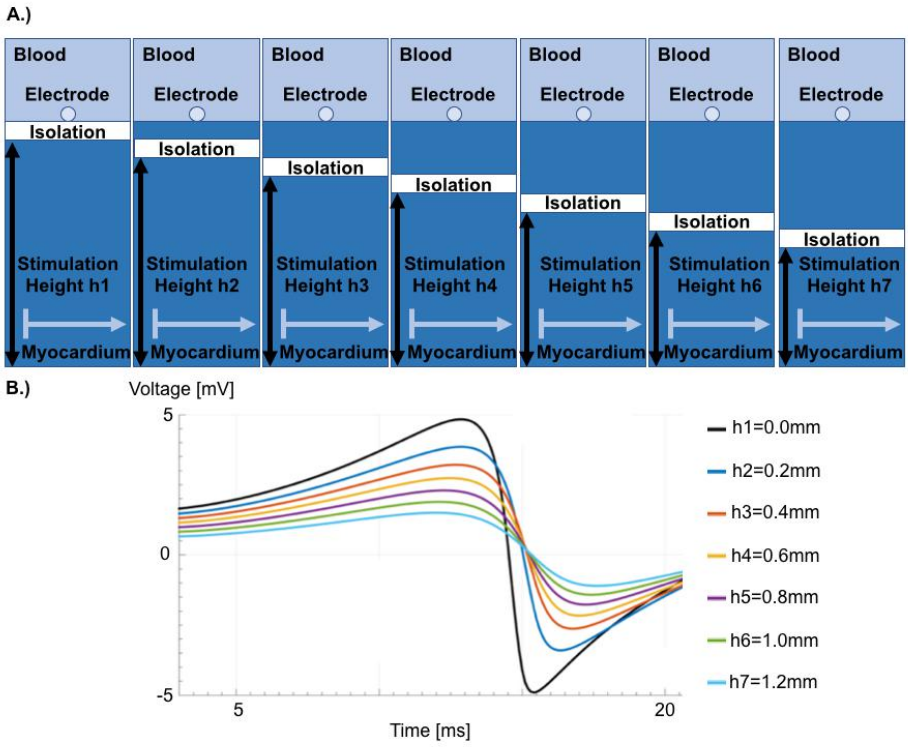

Figure 2.7: (A) Stimulations in different tissue depths (Height h1- Height h7). (B) Various signal contributions resulting from different tissue depths (h1- h7). The figure is adapted from [S3] [106].

Figure 2.8 (A) shows the different signal contributions from the submyocardial layers 1 to 7. The normalized contributions in Figure 2.8 (B) show that the upper contributions resulted in clearer signals of smaller signal widths. The resulting contributions from stimulations with a time delay in each sublayer and measured at the same point in time are depicted in the voltage map in Figure 2.8 (C). The contributions were then stacked according to tissue depth in Figure 2.8 (D). The contour plot of the stacked contributions in Figure 2.8 (E) shows that excitations measured at 0.5 mm

depth from the epicardium only contribute amplitudes that are less than a quarter of those in the top layer.

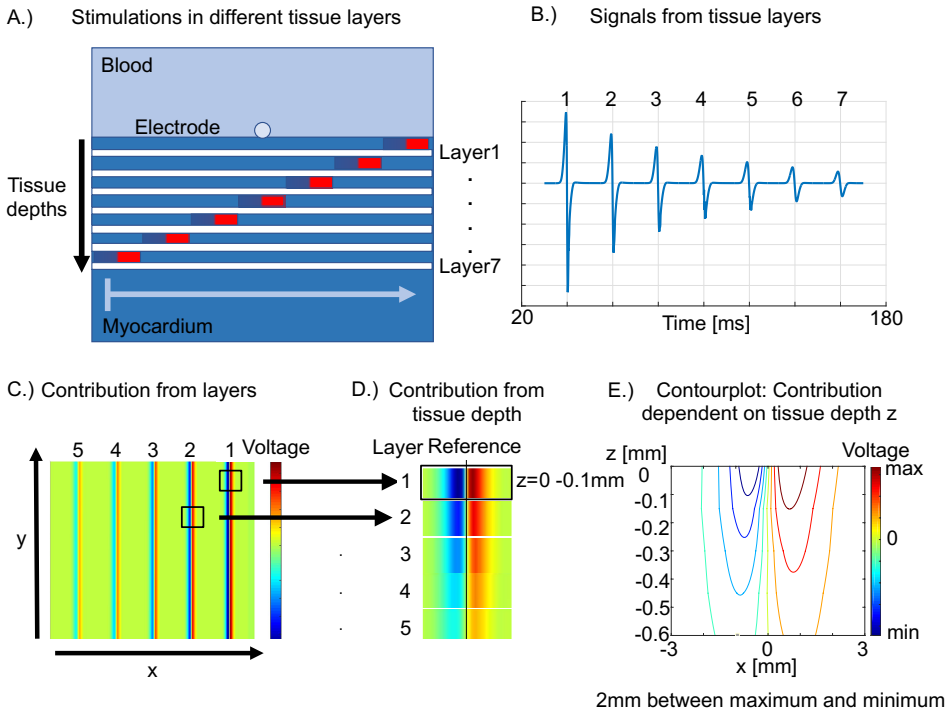

Figure 2.8: (A) Contributions from the submyocardial layer. (B) Signal contributions from the submyocardial layers. (C) Voltage map of contributions from tissue depth layers. (D) Contribution dependent on tissue depth. (E) Contour plot of contributions dependent on tissue depth z. The figure parts (A,B) are adapted from [S3] [106].

2.3.3 Signal morphologies resulting from different atrial fibrillation excitation patterns

2.3.3.1 Morphologies of ectopic focus

Ectopic foci had curved wavefronts and resulted in morphologies with S-waves predominating [104](cf. Figure 2.9) at different distances to tissue and at different conduction velocities.

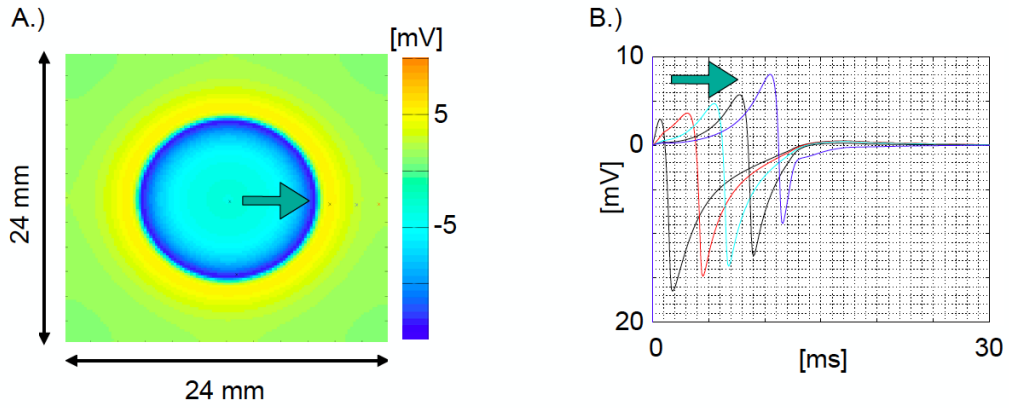

Figure 2.9: A.) Extracellular potential map of an ectopic focus. B.) Signal morphologies near the focal source point measured in a line at different distances to the focal source point. The distance between two measuring points was 2mm.

2.3.3.2 Morphologies of endo-epicardial breakthrough

Endo-epicardial breakthrough signals resulted in the described simplified simulation model (two-layer model) in similarities to the ectopic focus morphologies (cf. Figure 2.10). The voltage maps, excitation directions, and the resulting morphologies are shown in Figure 2.10. In this model, the resulting signals near the breakthrough point were predominantly S-wave signals [104]. But the morphologies differed depending on the direction of propagation in the lower myocardial layer (cf. Figure 2.10 (C) and (F)).

2.3.3.3 Morphologies of the rotor

Resulting signal morphologies of simulated rotors depended on the distance to the rotor core and the trajectory of the simulated rotational activity (cf. Figure 2.11) [107]. The amplitudes decreased significantly at the rotor tip position [107]. Furthermore, the signal morphologies were stable over time because of the the stable rotational activity [107]. Because of the curved wavefronts, the resulting morphologies were predominantly S-waves [107].

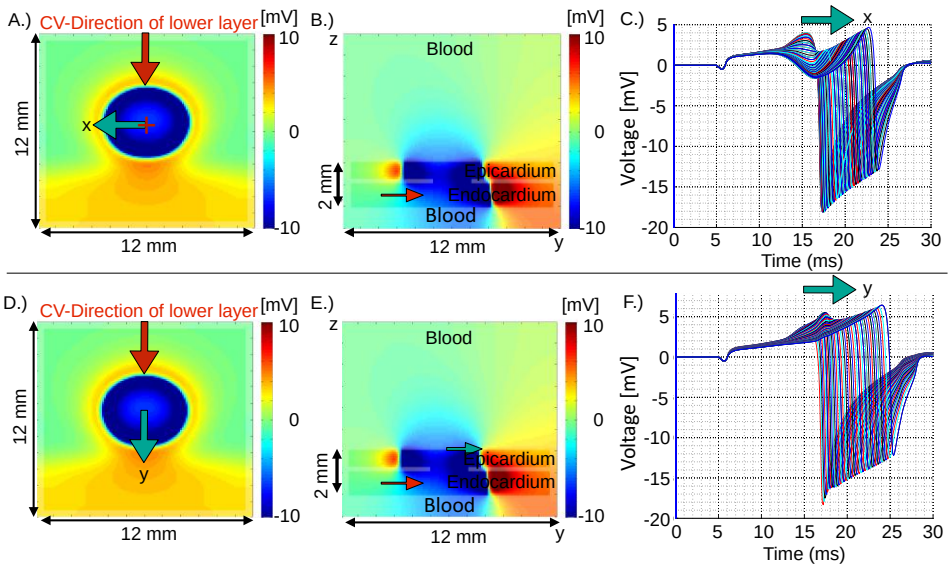

Figure 2.10: Endo-epicardial breakthrough. (A)-(C): Breakthrough signal analysis in the x-direction. (A) Extracellular potential map (xy-view) of the epicardium. (B) (Yz-view) of the epicardium, endocardium, and blood. (C) Unipolar signals measured in a line from the center in the x-direction. Endo-epicardial breakthrough. (D)-(F): Breakthrough signal analysis in the x-direction. (D) Extracellular potential map (xy-view) of the epicardium. (E) (yz-view) of the epicardium, endocardium, and blood. (F) Unipolar signals measured in a line from the center in the y-direction.

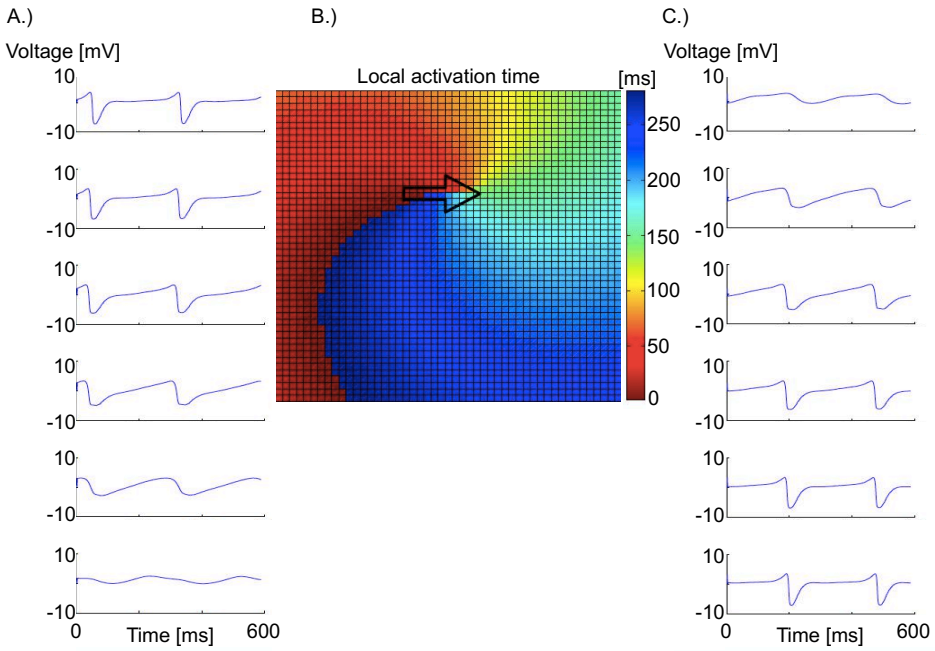

Figure 2.11: Electrograms measured in a line through the rotor tip A.) left side to center, C.) center to right side. The distance between two measuring points was 4mm. (B) Local activation time map in an area of 50 mm x 50 mm. The figure is adapted from Rottmann et al. 2014 [107] © IEEE [2014] with permission.

2.3.3.4 Morphologies of collision

Collisions between two or more excitation patterns resulted in R-wave signals (positive peak) predominating, in excitations terminated after collisions, or in excitations with the vertical direction of propagation (cf. Figure 2.12). The amplitude of the positive signal part was reduced with increasing distance to the collision point. In a distance of 4 mm to the collision point the positive signal part was reduced with a factor of 3 from 6mV to 2mV.

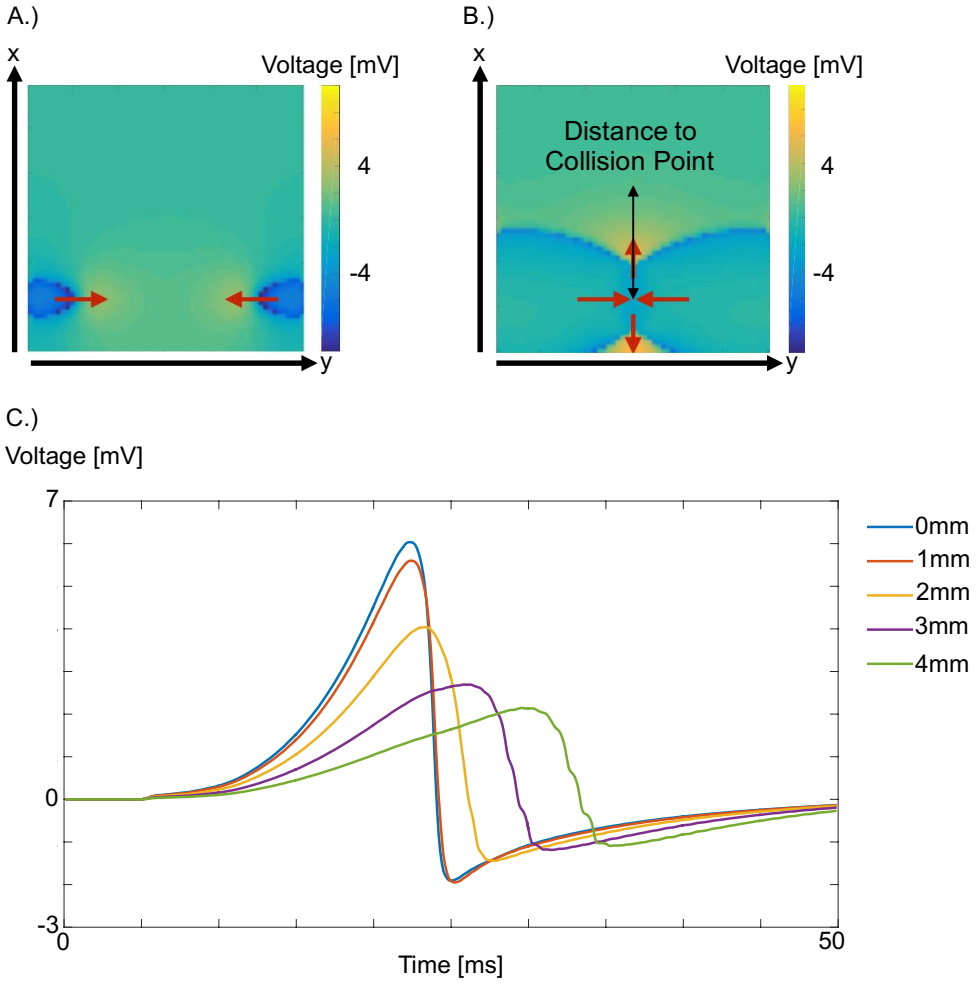

Figure 2.12: Wavefront collision of two curved excitations. The red arrow symbolizes the direction of propagation. (A) Stimulations at two edges. (B) Distance to collision point (black) for the signal analysis in (C). (C) R-signals dominated at different distances to the collision point, namely at 0 mm, 1 mm, 2 mm, 3 mm, and 4 mm. The figure is adapted from [S7] [119].

2.3.3.5 Influence of scar or block lines on resulting signal morphology

Functional and non-functional blocks and lines of blocks were observed during AF. Figure 2.13 depicts the typical signal characteristics at excitations around block lines. Unipolar signals near non-conducting block line (black line) with the turnaround point (TAP) resulted in double potentials with various time differences between the first and the second activation part. Amplitudes of second double potential activation part decreased near block lines from maximal amplitude with the factor ≈ 6 in a distance of > 4mm to the block line (at the other side of the block line).

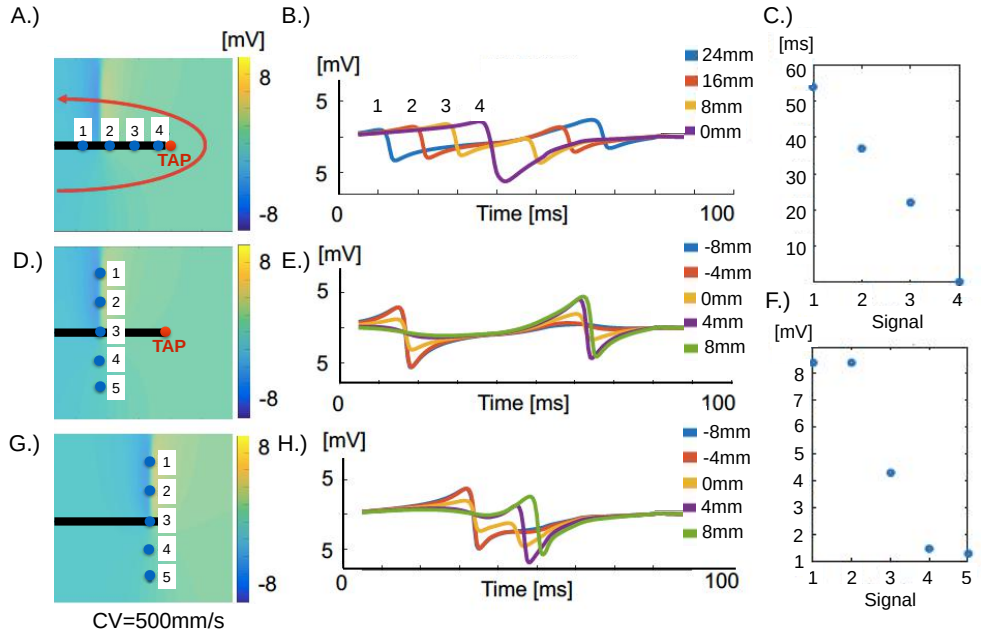

Figure 2.13: A.) Extracellular voltage map of excitation around block line (black) with turnaround point (TAP) and signal measurement points at the block line1 to 4. B.) Unipolar signal morphologies depended on distances 0mm to 24mm (compare figure part A.)) to the turnaround point (TAP). C.) The time between the first and the second activation of the double potential signal 1 to 4 dependent on distance 24mm, 16mm, 8mm, 0mm to TAP. D.) Extracellular voltage map with signal measurement points 1 to 5 vertical to the block line distant to the TAP. E.) Unipolar signal morphologies depended on vertical distances 8mm to -8mm (compare figure part D.)) to the block line. F.) Peak-to-peak voltage of second double potential activation part of signal1 to signal5 (vertical distances 8mm to -8mm). G.) Extracellular voltage map with signal measurement points (1 to 5) vertical to the block line near the TAP. H.) Unipolar signal morphologies depended on vertical distances 8mm to -8mm (compare figure part G.)) to the block line. The conduction velocity was 500mm/s.

2.3.4 Understanding the effect of different metal electrode sizes

2.3.4.1 Influence of electrode size

Metal electrodes collect electrical potentials in the blood layers. Larger electrodes resulted in smaller signals with greater signal widths. Figure 2.14 A.) shows a schematic of point-like electrodes (blue) signals measured at the volume of a Lasso electrode (orange) in Figure 2.14 B.). The signals of the point-like electrodes measured at the volume of the Lasso electrode in the simulation without integrated metal electrode are shown in Figure 2.14 C.). Figure 2.14 D.) shows that the average signal of the point-like electrode signals and the signal of the metal electrode in the full bidomain simulation are similar. Different electrode sizes commonly used were investigated. Flat microelectrodes were analyzed and resulted in larger amplitudes and smaller amplitudes widths compared to signals of large electrodes (i.e., ablation electrodes).

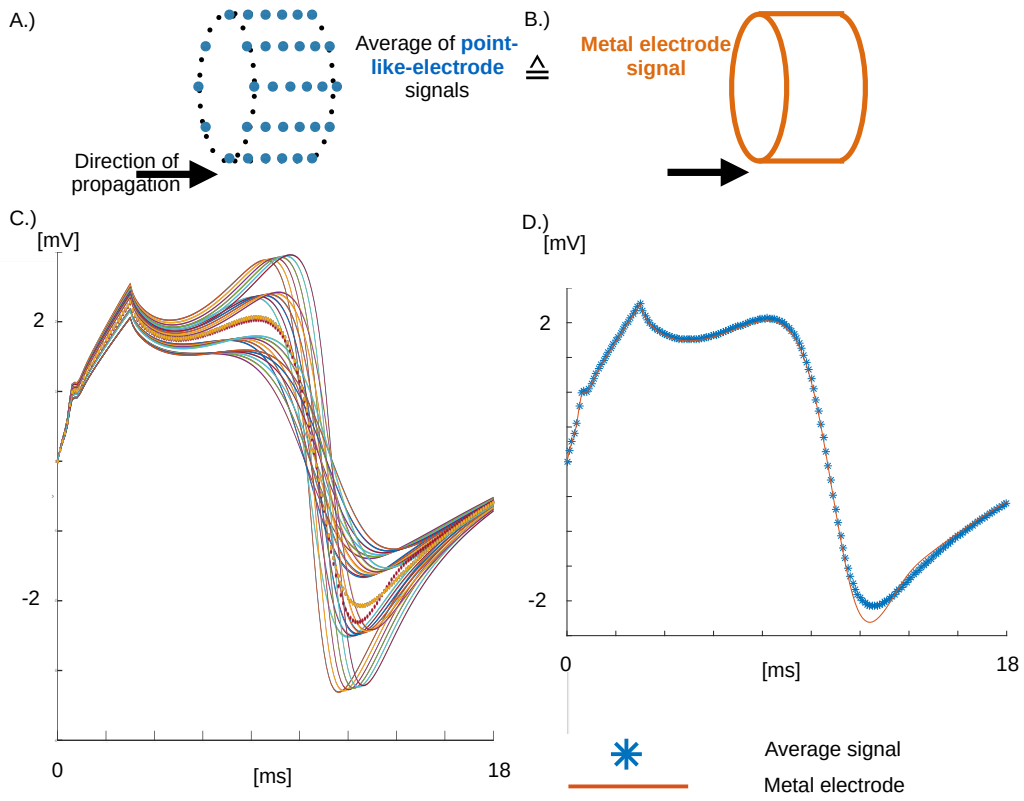

Figure 2.14: (A) Point-like electrodes (blue dots) located at the volume of a Lasso electrode (B). (C) Point-like electrodes signals measured at the volume of a Lasso electrode in the simulation without the integrated metal electrode. (D) Resulting signal of a Lasso metal electrode from a full bidomain simulation (orange). The average signal (blue dots) of point-like electrodes signals measured at the volume of a Lasso electrode.

2.3.4.2 Impact of electrode size on the amplitude and width of signal recordings

Figure 2.15 (A) depicts different metal electrode heights and the resulting unipolar signal recordings of a planar wave. The amplitudes of the signal recordings were reduced in measurements with larger electrode heights (cf. Figure 2.15 (B)). The electrodes had the form of rectangular electrodes. Figure 2.15 (C) shows the schematic locations of 6 point-like-electrodes located in a line within blood layers under the Lasso metal electrode with 1mm electrode width. Figure 2.15 (D) presents the impact of electrode width on the width of the intracardiac recordings. The signal widths increased with increasing widths of the metal electrodes.

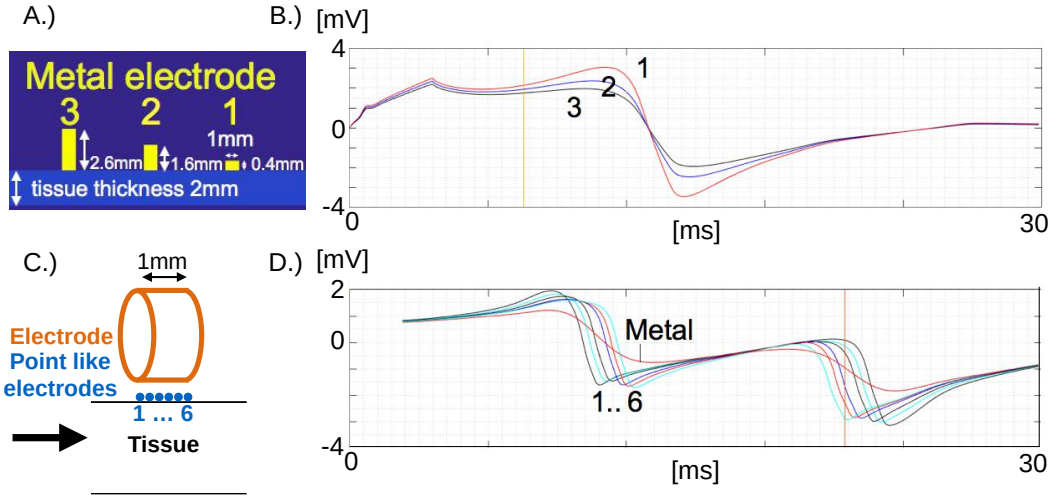

Figure 2.15: A.) 3 Different rectangular metal electrode sizes. B.) Unipolar signal recordings measured with the electrode 1-3. Influence of different electrode sizes. The smallest, Electrode 1, resulted in the largest amplitude. C.) Locations of 6 point like electrodes located in a line under the Lasso electrode. D.) Resulting signals of 6 point like electrodes in comparison to the metal electrode (Lasso). The metal electrode increased the signal width dependent on the electrode width.

2.4 Discussion

High-quality measurements of recordings are important for the electrophysiological study. However, the influence parameters of unipolar and bipolar recordings are still not well understood. In this simulation study, the main parameters that influence intracardiac electrograms were analyzed. The parameter distance to the tissue significantly influenced the amplitude and width of the signals. The upper (closer to blood) myocardial layers contributed most significantly to the resultant signals measured. The signal morphologies were strongly dependent on the specific excitation pattern. Focal waves, endo- epicardial breakthroughs and rotational activities resulted in S-

wave predominance signal [104] recordings. Signal recordings near collision points were R-wave predominance signals. At block lines, the double potential interval and amplitudes of the first and the second activation of measured double potentials were dependent on the horizontal and vertical distances to the turn around point. The metal electrode signal was similar to that of the average signal for point-like electrodes in the 3D volume of the metal electrode. This is the reason why flat electrodes resulted in higher signal quality with larger amplitudes and clearer signals with smaller signal widths. These simulation results show the limitations of current mapping and ablation catheters and electrode designs but also show optimization potentials for future catheter concepts for better signal quality.

2.5 Resulting Publications

Results of this chapter were published in :

M. Rottmann, T. Oesterlein, C. Reich, A. Luik, C. Schmitt, O. Dössel. Characteristic features of electrograms of depolarization waves during atrial fibrillation. In 38th Annual International Conference of the IEEE Engineering in Medicine and Biology Society, 2016.

C. Reich, T. Oesterlein, M. Rottmann, G. Seemann, O. Dössel. Classification of cardiac excitation patterns during atrial fibrillation. In Current Directions in Biomedical Engineering, Vol. 2(1), 2016.

M. Rottmann, L. A. Unger, W. Kaltenbacher, Seemann G., A. Loewe, M. W. Krueger, A. S. Jadidi, T. Arentz, and O. Dössel. Methods for analyzing signal characteristics of stable and unstable rotors in a realistic heart model. In Computing in Cardiology, Vol. 42, 2015.

M. Rottmann, G. Seemann, and O. Dössel. Analysis of characteristic signal morphologies of double potentials near block lines in an atrial simulation model. In Biomedizinische Technik / Biomedical Engineering, 2015.

M. Rottmann, M. W. Keller, T. Oesterlein, G. Seemann and O. Dössel, Comparison of different methods and catheter designs to estimate the rotor tip position- A simulation study, Computing in Cardiology, Cambridge, 2014.

CHAPTER 3

Electrogram Characteristics at Rotational and Focal Sources and Correlations to Low-Voltage and Slow-Conduction Areas

"Truth is ever to be found in the simplicity, and not in the multiplicity and confusion of things."

— Isaac Newton

3.1 Introduction

Despite extensive research, the underlying mechanisms of drivers maintaining AF are not well understood. Pulmonary vein isolation has become the standard catheter ablation procedure [120], but its efficacy for persistent atrial fibrillation is limited [121] [122]. There is a need of research for optimized ablation strategies in addition to pulmonary vein isolation [123]. Atrial fibrillation was associated with fibrosis and low-voltage regions, which became additional ablation target points after pulmonary vein isolation [123].

3.2 Simulation Methods

3.2.1 Modeling of fibrosis

In the literature, fibrosis models are based on data from histological tissue sections using a node split algorithm Costa (2014) et al. [124]. Jacquemet (2009) et al. [43] described randomly distributed fibrosis models based on small patch models in 2D by

with the model size 8.64 mm x 2.88 mm; and Keller (2013) et al. [125] used 3D models with passive elements with dimensions 11 mm x 6.5 mm x 2.5 mm. Alonso (2016) et al. [126] presented randomly distributed fibrosis models with 2D models including non-conducting bonds and non-conducting elements. Furthermore, Kazbanov (2016) et al. [127] published 2D models with a non-conducting character of fibroblasts with dimensions 16mm x 16mm. Fibrosis models based on delayed enhancement magnetic resonance imaging (MRI) data have also been published. For instance, Vigmond (2016) et al. [128] described fibrosis models using pixel intensity to determine the fibrosis probability. Haïssaguerre (2016) et al. [129] published two-dimensional models of atrial tissue with areas that were randomly replaced by collagen-dependent on a probability. The used model size was 20mm x 20mm. Finally, Mcdowell (2015) et al. [130] published fibrosis models based on late gadolinium enhancement (LGE) MRI images. They modeled patchy collagen was modeled using passive insulators which interrupted transverse and longitudinal cell connections. MRI-LGE images were created with the resolution of 0.667mm x 0.667mm x 1.500mm.

3.2.2 Modeling of substrate modifications

In this work high-resolution 3D collagenous septa were implanted in tissue using passive elements of different sizes and by degrees of fibrosis. Different fibrosis types (patchy and diffuse) with different degrees of fibrosis (0%, 10%, 20%, 30%, 40%, 50%, >50% non-conductive area) were modeled with spatial, high-voxel resolution of 0.1mm x 0.1mm x 0.1mm. Also, homogeneous and inhomogeneous degrees of fibrosis and different sizes of fibrosis, from 5mm x 5mm to 50mm x 50mm, were modeled and analyzed. Specific anatomical structures, i.e. fibrosis regions near pulmonary veins, were investigated. Additional multiple fibrosis areas with various locations, sizes, forms, and degrees of fibrosis and additional reconstructions of fibrosis regions from clinical data, were analyzed, and furthermore, the influence of tissue dilatation was investigated. Three-dimensional AF simulation models were developed with voxel resolution of 0.1mm x 0.1mm x 0.1mm

$$Degree\,of\ fibrosis = \frac{non-conductive\ elements}{non-conductive\ elements + conductive\ elements} \tag{3.1}$$

3.2.3 3D Simulation of atrial fibrillation in atrial patches and sphere models with fibrotic areas

Fibrotic elements in a small area of 10 mm x 10 mm x 2 mm were incorporated into a patch of 30 mm x30 mm x 2mm (cf. Figure 3.1(A)). Fibrotic elements in a large area with a degree of fibrosis of 30% (cf. Figure 3.1(B)) and 40% (cf. Figure 3.1(C)) were incorporated into a large atrial path of 60 mm x 60 mm x 2 mm. A 3D sphere model

of the left atrium incorporated a fibrotic region of 40 mm x 40 mm x 2 mm (cf. Figure 3.1(D)).

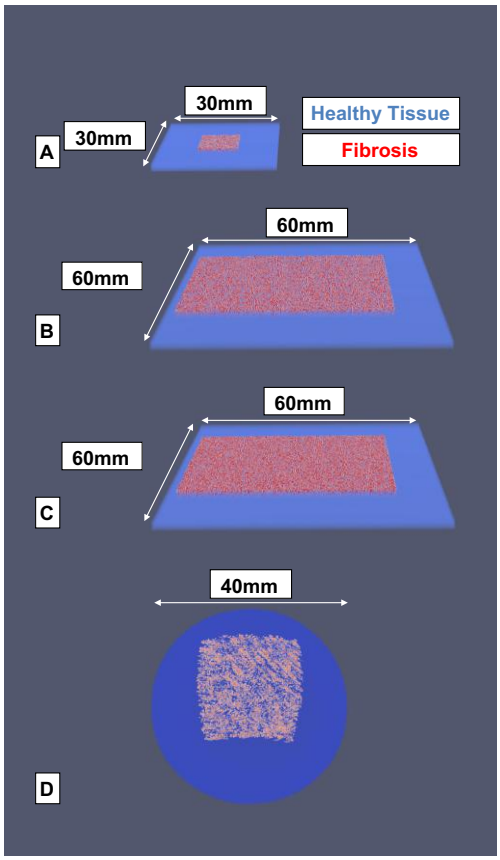

Figure 3.1: 3D fibrosis models surrounded by healthy tissue. (A) A patch incorporating 3D fibrotic elements with the size of 30 mm x 30 mm, (B) 60 mm x 60 mm with the degree of fibrosis at 30%, (C) 60 mm x 60 mm with the degree of fibrosis at 40%. (D) Sphere model mimicking the left atrium (40 mm) with implanted 3D fibrosis region.

3.3 Results

3.3.1 Effects of small fibrosis regions

3.3.1.1 Effects of small fibrosis regions on planar waves

During sinus rhythm, planar waves resulted in zig-zag excitation movements within the fibrotic region. Wavefronts around the fibrosis regions (area of 10 mm x 10 mm) are shown in Figure 3.2. Because of reduced conduction velocity in the fibrosis region, wavefronts were split (cf. Figure 3.2). The fibrotic regions displayed low unipolar (<1.0 mV) and bipolar voltages. The effects of fibrosis on extracellular potentials were dependent on the size and degree of the fibrosis. With increasing degrees of fibrosis, conduction velocity and peak-to-peak amplitude decreased at the fibrotic tissue.

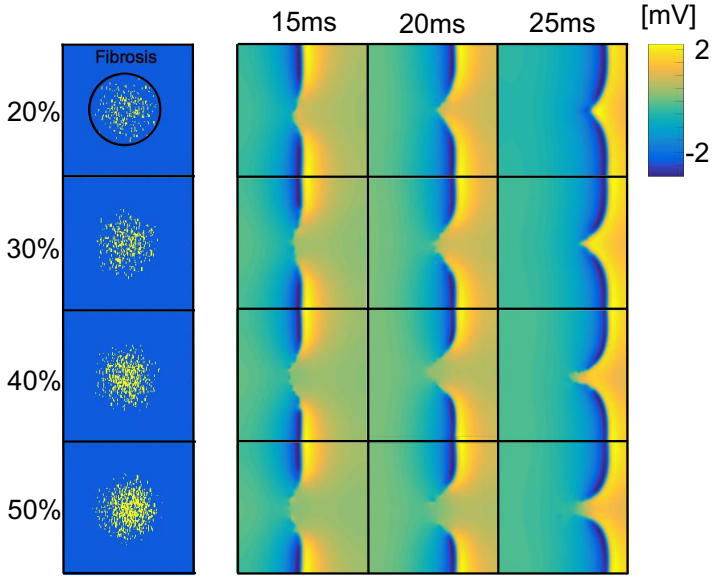

Figure 3.2: Effects of planar waves on high-resolution fibrosis with different degrees of fibrosis at 20%, 30%, 40%, and 50% (vertical direction). (In horizontal direction) (Left) Model of the fibrosis region. (Right) Maps of the extracellular potentials at 15 ms, at 20 ms, and at 25 ms. Extracellular potentials resulted in low-voltage signals above the fibrotic tissue. Because of slow conduction in the fibrotic tissue, planar waves resulted in split wavefronts with curvature dependent on the degree of fibrosis. With an increased degree of fibrosis, the curvature of the split waves increased, and the amplitude above fibrosis decreased. The figure is adapted from [S6] [114].

Figure 3.3(E) presents the resulting peak-to-peak amplitude map and unipolar recordings (cf. Figure 3.3(F)) from the split planar wave Figure in 3.3(B-D), mimicking the sinus rhythm around the fibrotic region (cf. Figure 3.3(A)). The curvature of split excitation fronts increased with a rising degree of fibrosis. The fibrosis region displayed low peak-to-peak amplitudes similar to clinical data (<1 mV) and at strong curvatures, compare region near the center electrode where late potentials were observed.

3.3.1.2 Effects of small fibrosis region on rotational activities

By inducing rotational activities around a small fibrosis region (10 mm x 10 mm) with the cross-field stimulation, the rotational activity became anchored in the case of a fibrosis degree of 40%, (cf. Figure 3.4)(A-D). Figure 3.4(F) shows the resulting unipolar recordings of rotational activity around the fibrosis regions. Functional low-voltage resulted in the peak-to-peak map at the center of the rotational activity (cf. Figure 3.4(F)). The amplitudes in the center were 10 times smaller than those measured at a 4mm distance from the rotor tip.

3.3.2 Induced stimulations by two planar waves

3.3.2.1 Effects of no implanted fibrotic patterns on the persistence of rotational activity

A curved wavefront with rapid excitation velocity resulted and excited the observation area in the case of two stimulation wavefronts (from the left side and from the lower side) within the healthy tissue, (cf. Figure 3.5 (A-D)). Rotational activity induced by two planar wave stimulations from the left and the lower side was anchored, if minimal fibrosis size was 10 mm x 10 mm and degree of fibrosis was 40%. In the same stimulation scenario with a regional heterogeneity of 40 % degree of fibrosis, the rotational activity was anchored on the low-voltage area over multiple (>20) cycles (cf. Figure 3.5 (E)). Focal excitations with circular wavefronts were located at exit points of the fibrosis border zone.

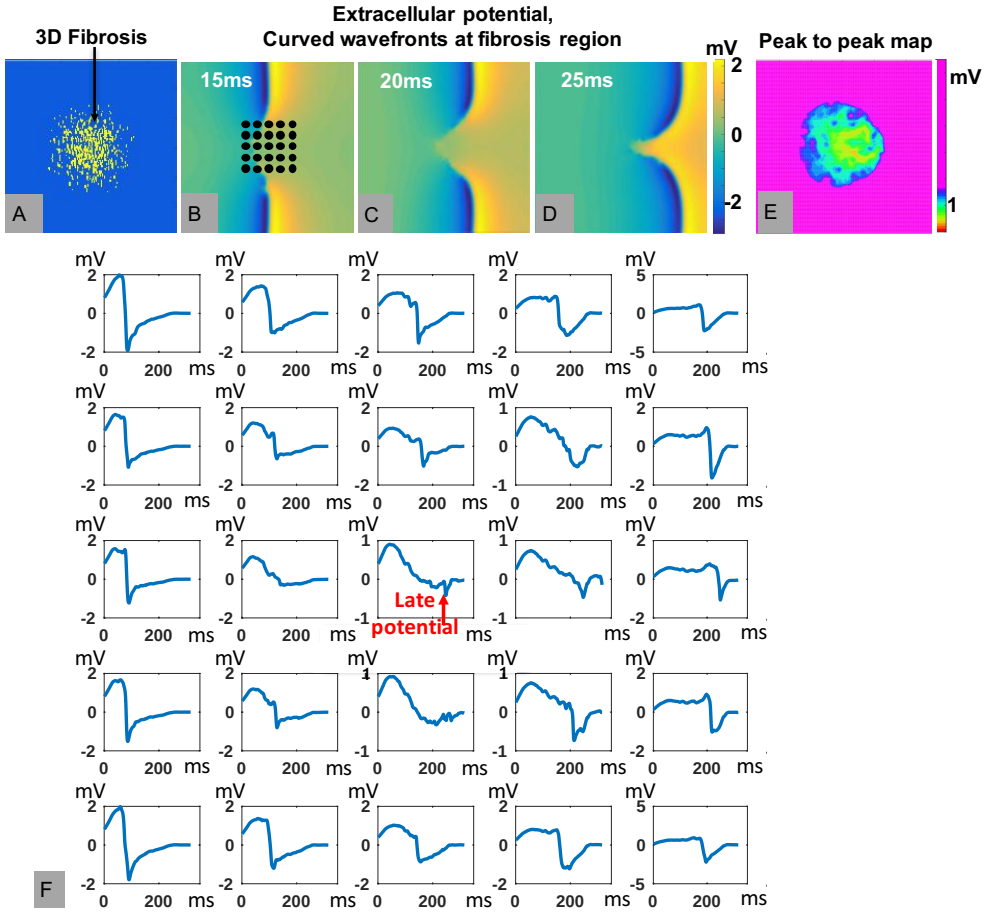

Figure 3.3: The effects of planar waves on high-resolution fibrosis with differing degrees of fibrosis 20%, 30%, 40%, 50% (vertical direction). In horizontal direction: (A) Model of fibrosis region. (B) Extracellular potentials (positions of 5 x 5 electrode mapping are marked in black) at 15 ms, (C) 20 ms, and (D) 25 ms. Extracellular potentials resulted in low-voltage signals above the fibrotic tissue. Because of slow conduction in fibrotic tissue, the planar wave resulted in two split wavefronts with the curvature dependent on the degree of fibrosis. With an increased degree of fibrosis, the curvature of the split waves increased, and the amplitude above the fibrosis decreased. (E) The fibrotic area displayed low-voltage in the corresponding amplitude map. (F) Unipolar recordings with late potentials near the center of the electrode arrangement. The figure is adapted from [S6] [114].

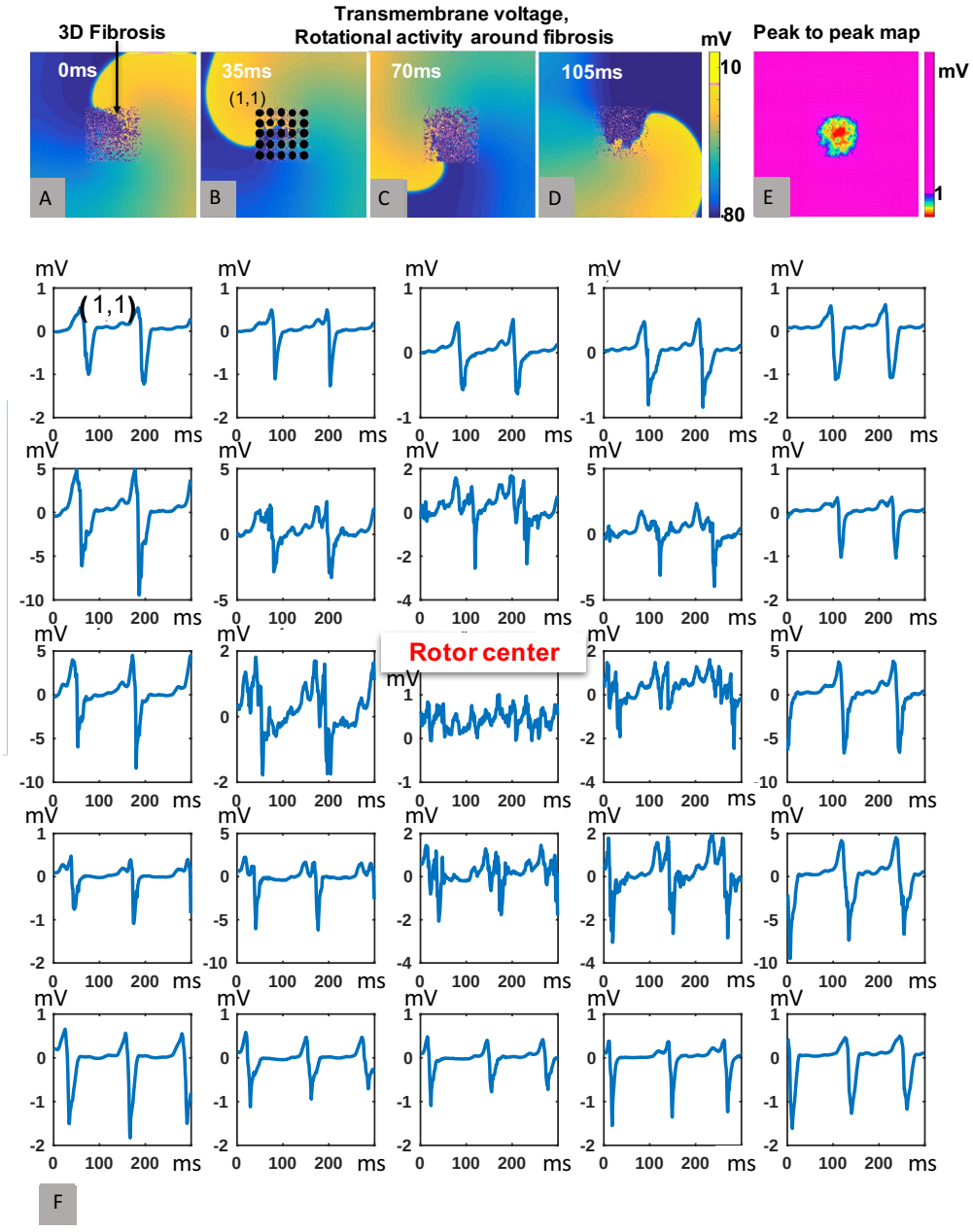

Figure 3.4: (A-D) Transmembrane voltage maps of rotational activity around fibrosis region (10mm x 10mm), (B) with electrode positions. (E) The corresponding peak-to-peak voltage map displays low-voltage at the fibrotic area. (F) Unipolar recordings resulted in small and fractionated signals near the rotor center. The figure is adapted from [S6] [114] and Rottmann et al. 2016 [131] © IEEE [2016] with permission.

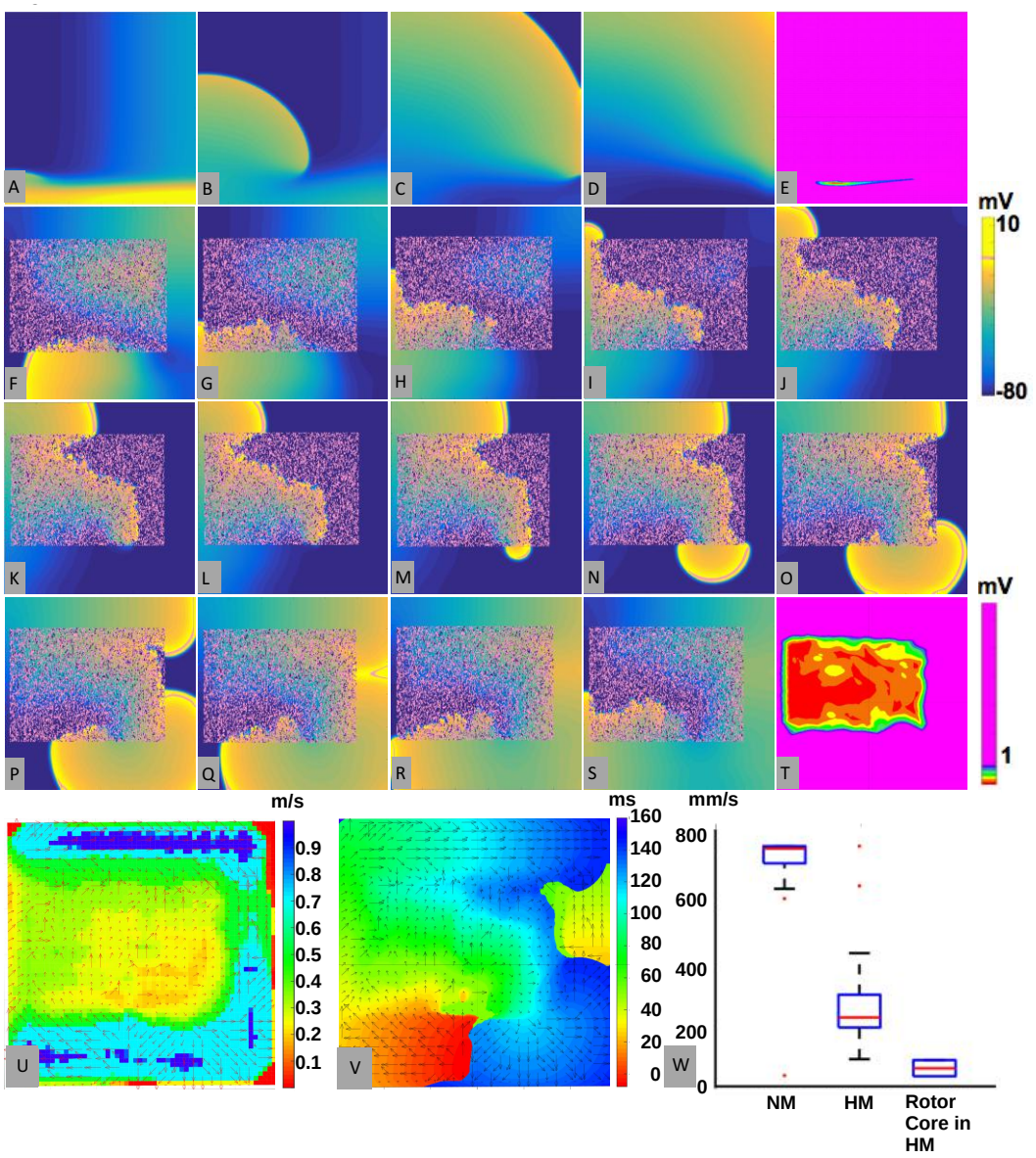

Figure 3.5: (A)-(D) Rotational activity was induced by two planar waves from the left and from the lower side and resulted in a curved wavefront, which exited the observation area without anchoring. (E) Peak-to-peak map shows the functional low-voltage region at the center of the meandering rotational activity. (F)-(S) Transmembrane voltage of rotational activation partially between fibrotic tissue and partially between healthy tissue, compare [131]. (M)-(S) Focal waves were located at exit points of the fibrosis border zone. Rotational activity around the fibrosis area resulted in (L) colliding wavefronts near the border zone. (T) The peak-to-peak map with a threshold < 1 mV. Healthy tissue is displayed in purple color. The low-voltage area displays the colors red to blue. (U) Conduction-velocity map and overlapping CV vectors. (V) Local activation time map and overlapping CV vectors. (W) Boxplots of characteristic conduction velocities in the normal myocardium (NM), in the heterogeneous tissue (HM) and at the rotor core. The figure is partially adapted from [S6] [114] and Rottmann et al. 2016 [131] © IEEE [2016] with permission.

3.3.3 Effects of a large fibrosis region on the persistence of rotational activity

The same stimulation protocol at a large fibrosis region resulted in persistent AF with one rotational activity around the fibrosis region and another part in between fibrosis and healthy tissue. Furthermore, the peak-to-peak map (cf. Figure 3.5 (T)) is presented and correlates with the fibrosis region (cf. Figure 3.5 (F-S)).

3.3.4 Effects of rotational activity on conduction velocity vectors

Significant differences of conduction velocity vectors between healthy tissue (conduction velocity of 0.8 m/s), fibrotic tissue (conduction of velocity 0.22 m/s, $p<0.001$), and rotor center within the fibrotic tissue (conduction velocity of 0.05 m/s, $p<0.001$) are shown in Figure 3.5 (U-W).

3.3.5 Signal characteristics at simulated persistent AF with rotational and focal sources

Signals at rotational and focal activities were measured using virtual square catheters at the focal exit in the lower part (cf. Figure 3.6). The signal morphologies and amplitudes changed cycle by cycle in the case of 30% degree of fibrosis during rotational and focal activities, compare measurements at focal exit location in the lower part of the tissue patch in Figure 3.7). The unipolar signals were, in most cases, S-wave predominance signals.

The resulting signal morphologies of one AF cycle at rotational and focal activities are depicted in Figure 3.6 (B), 3.7 (B). These results show double potentials at focal exit locations, similar to observations in high-density measurements [132] [133] [111] [112].

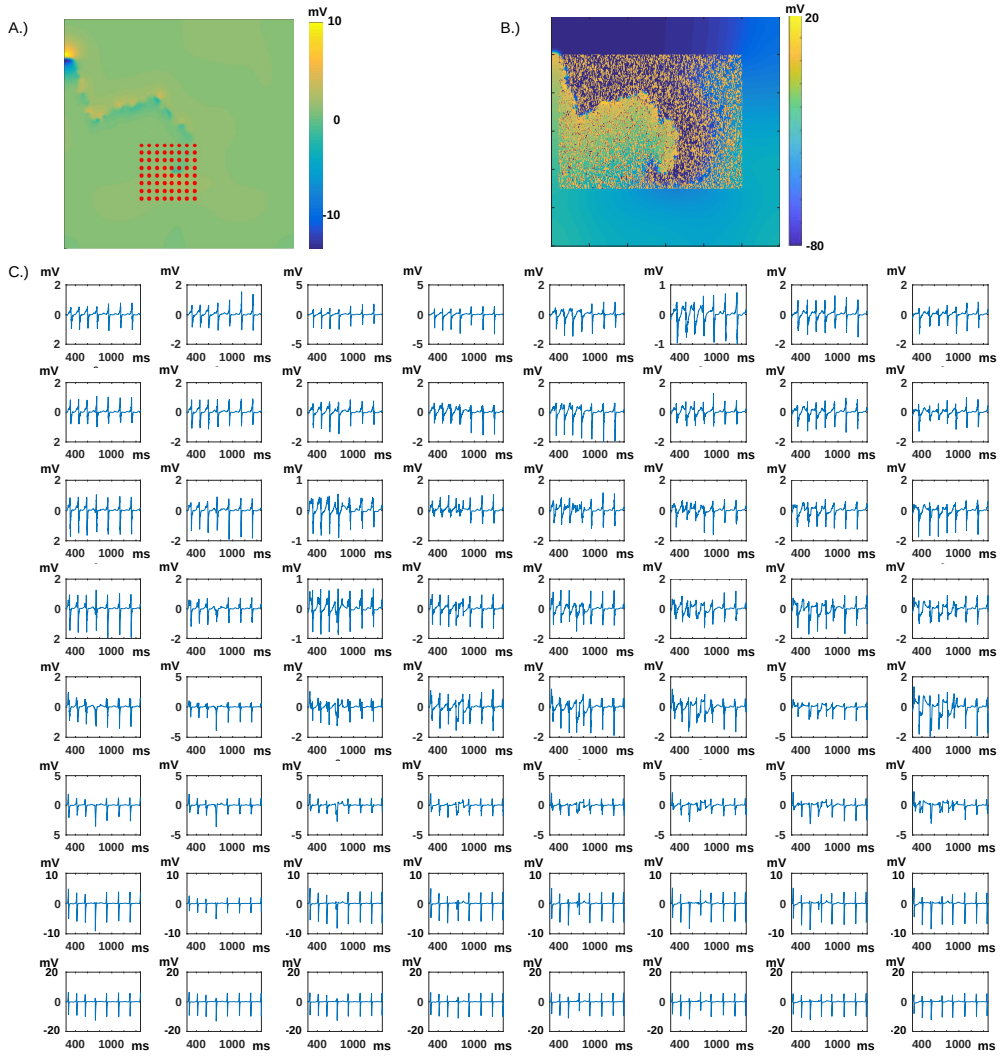

Figure 3.6: (A) Extracellular potential map and square catheter (8 x 8) placed in the lower part. (B) Transmembrane voltage map. (C) Resulting unipolar recordings from the square catheter (8 x 8). Signal analysis of multiple AF cycles.

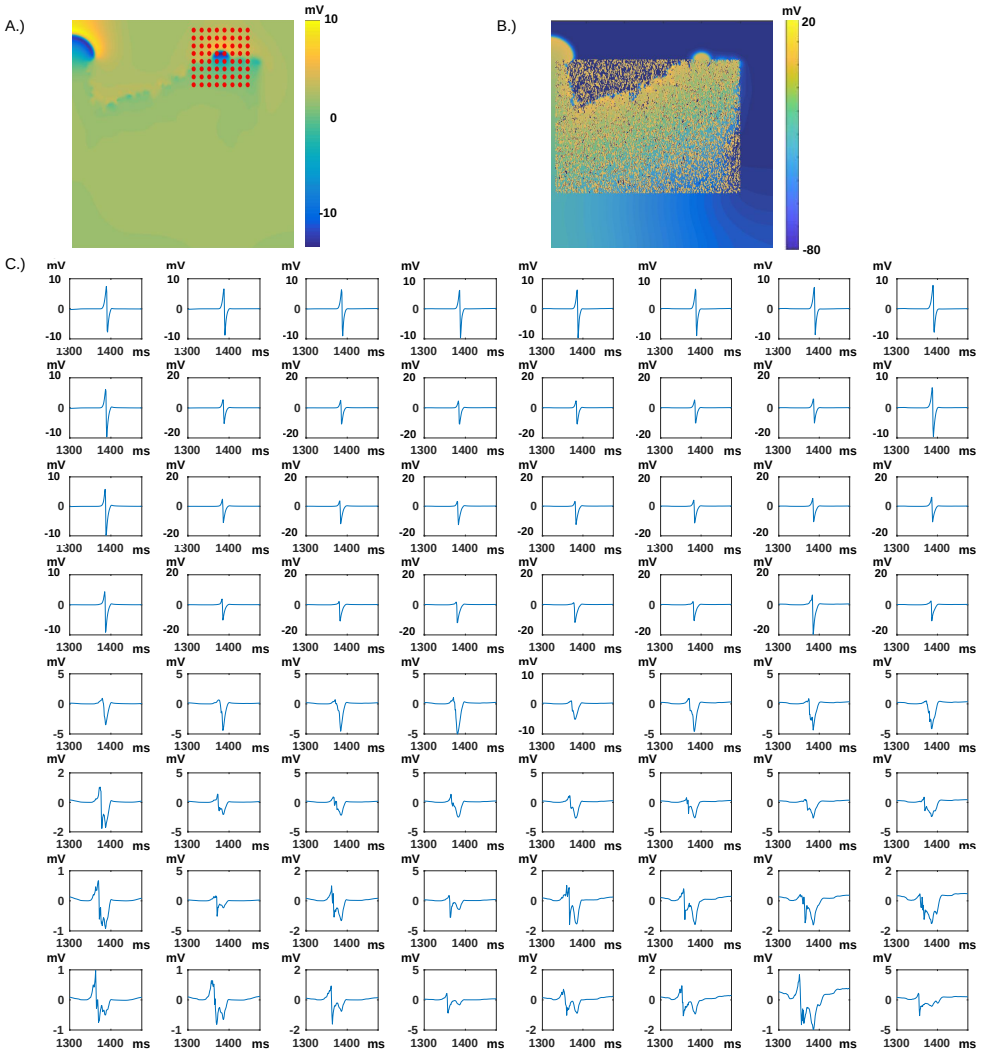

Figure 3.7: (A) Extracellular potential map and placed square catheter (8 x 8 electrodes (red dots)) at the upper fibrosis border zone at the focal exit location. (B) Transmembrane voltage map showing focal exit. (C) Resulting unipolar recordings of one cycle from the square catheter (8 x 8) placed in the upper part.

Measurements of LAT maps and cycle lengths dependent on different time periods and resolutions are depicted in Figure 3.8. These results show that rotational activities and focal exits were difficult to detect with low map resolution.

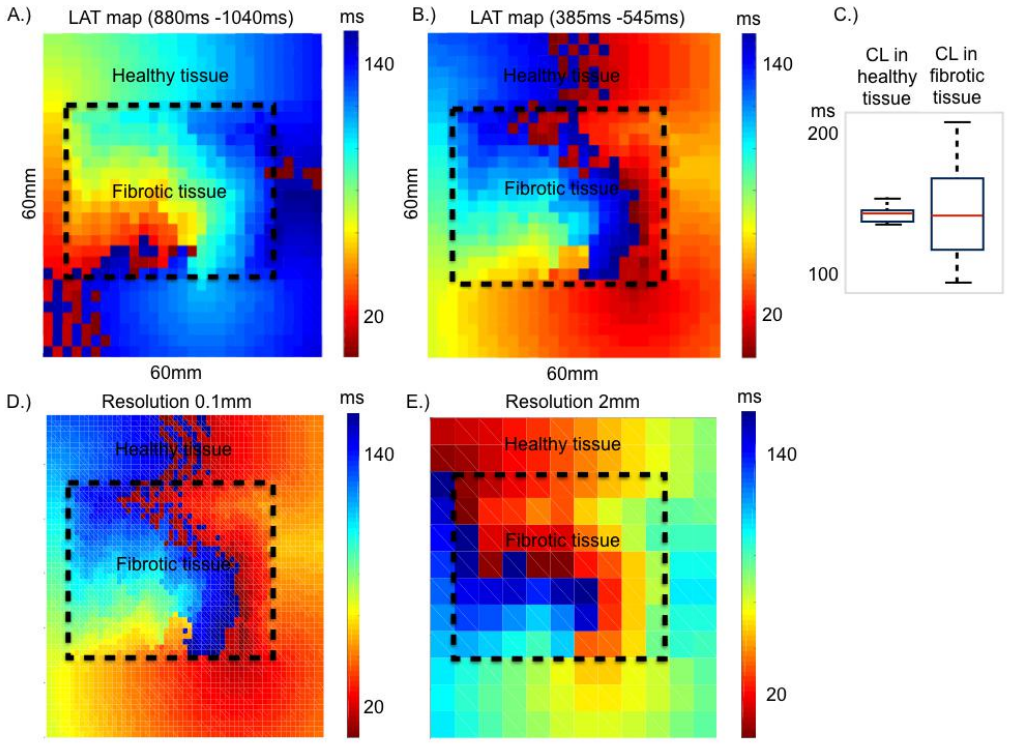

Figure 3.8: LAT maps of rotational and focal activities dependent on different times. (A) LAT map (880-1040 ms). (B) LAT map (385-545 ms). (C) Statistical analysis of cycle length measured in healthy and fibrotic tissue (median of 140 ms). (D) LAT map with a resolution of 0.1 mm, and (E) LAT map with a resolution of 2 mm.

3.3.6 Effects of fibrosis in sphere models mimicking the left atrium

Sphere models of the left atrium (40 mm diameter) with implanted 3D fibrosis regions were modeled. Additional pulmonary veins were integrated into sphere models. Fibrotic tissue regions of different sizes (from 5mm x 5mm to 50mm x 50mm) and degrees of fibrosis (from 0% to 50%) were implanted in order to investigate the effects of fibrosis.

3.3.7 Effects of fibrosis in sphere models with size of 10 mm x 10 mm and degree of fibrosis at 30%

The rotational activity was anchored over multiple cycles (>20) in the case of an integrated fibrotic region with 30% fibrosis (cf. Figure 3.9).

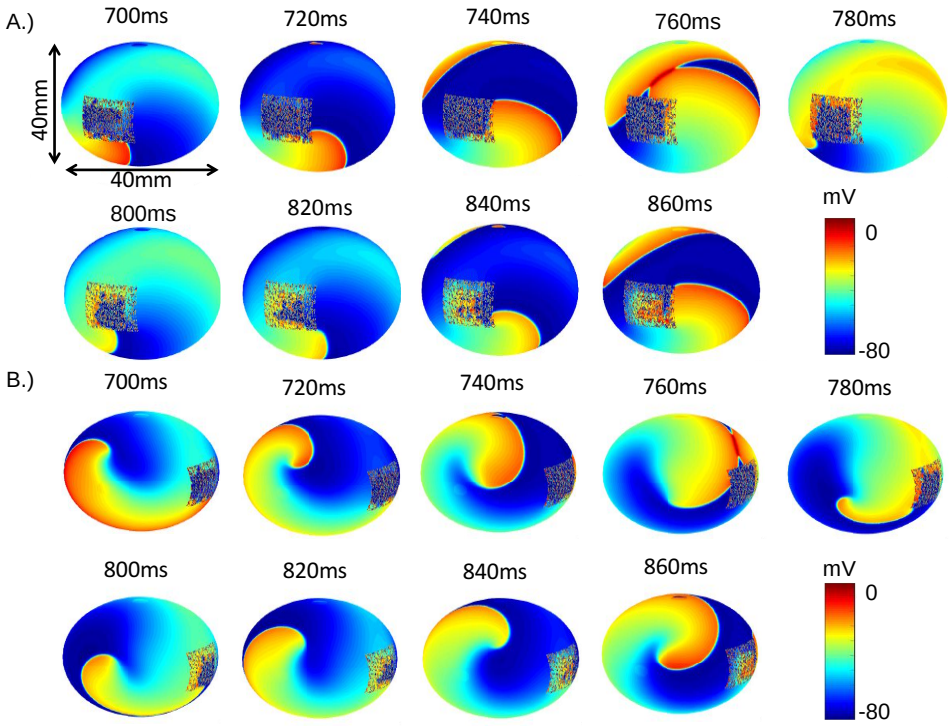

Figure 3.9: (A) Anchored rotational activity at fibrotic tissue with size of 10mm x 10mm. Rotational activity was stable over multiple cycles (>20). Near the center of the fibrotic tissue, continuous activated cells were detected. The rotational activity centers were located within the fibrosis area. (B) The transmembrane voltage maps show the second meandering rotating excitation wavefront end and its center within healthy tissue from another viewpoint. The times between 700 ms and 860 ms are presented.

Peak-to-peak amplitude maps of the simulation described in Figure 3.9 with a distance of 2 mm are presented in Figure 3.10 (A) with the threshold of 3 mV and in Figure 3.10 (B), of 4 mV. The low-voltage area (right side) resulted because of the fibrosis area, but on the left side, a functional low-voltage area resulted because of functional low-voltage effects of the meandering rotational activity (cf. Figure 3.9). At 4 mm distance to tissue, the peak-to-peak amplitude displayed the fibrosis region in smaller amplitudes. Functional low-voltage areas were more prominent, and the fibrosis region was displayed in less detail at 4mm distance to the tissue.

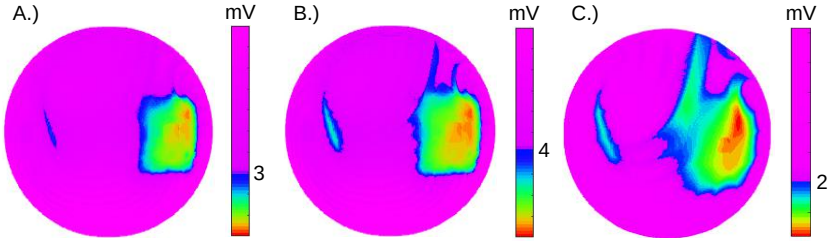

Figure 3.10: (A) Peak-to-peak map of persistent AF at a distance of 2 mm to tissue. The fibrotic tissue had a size of 10 mm x 10 mm, and the degree of fibrosis was 30 percent. The amplitude threshold used was 3 mV and (B) 4mV. (C) Peak-to-peak map of persistent AF at a distance of 4 mm to tissue. The amplitude threshold was 2 mV.

3.3.8 Effects of fibrosis in sphere model with the degree of fibrosis at 10 percent

Large fibrosis areas with less degree of fibrosis at 10 percent were investigated to analyze the effects of fibrosis (cf. Figure 3.11). Wavefronts had more reduced conduction velocities in fibrotic tissue than in healthy tissue. But no anchoring was observed during rotational activity induced by a second excitation from the left (horizontal) side.

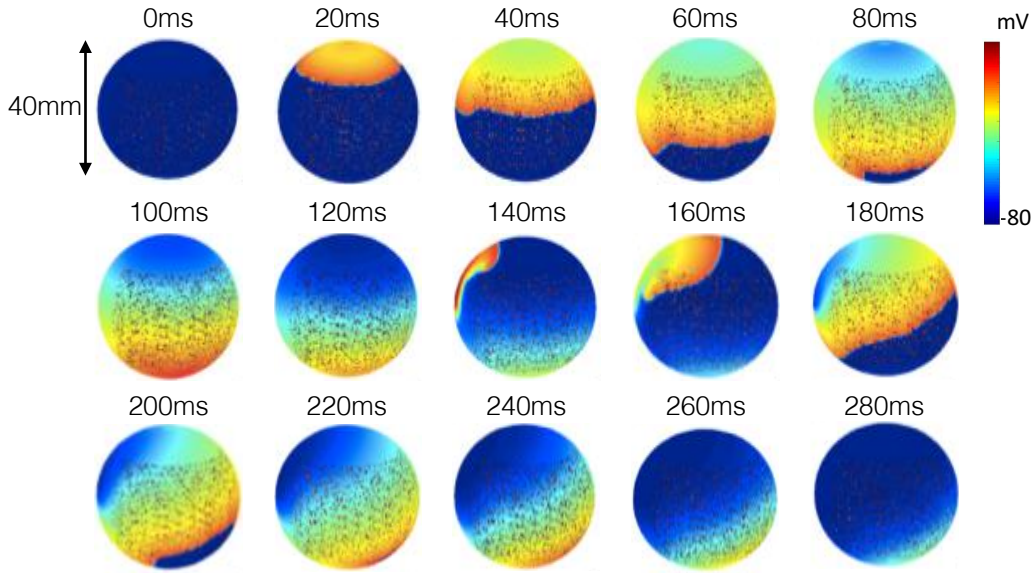

Figure 3.11: Transmembrane voltage of rotational activity in a fibrosis region with degree of fibrosis at 10 percent. The rotational activations terminated by themselves. No anchoring was observed.

3.3.9 Effects of fibrosis in a sphere model with degree of fibrosis at 20 percent

Rotational activities were induced by a planar wave from the upper region of the sphere and by a second stimulation of an area around the upper fibrosis region (cf. time point 140 ms (red area) in Figure 3.12). With the degree of fibrosis at 20 percent, a figure-eight pattern was induced and was anchored over multiple cycles (>20) between the fibrosis regions and the healthy tissue.

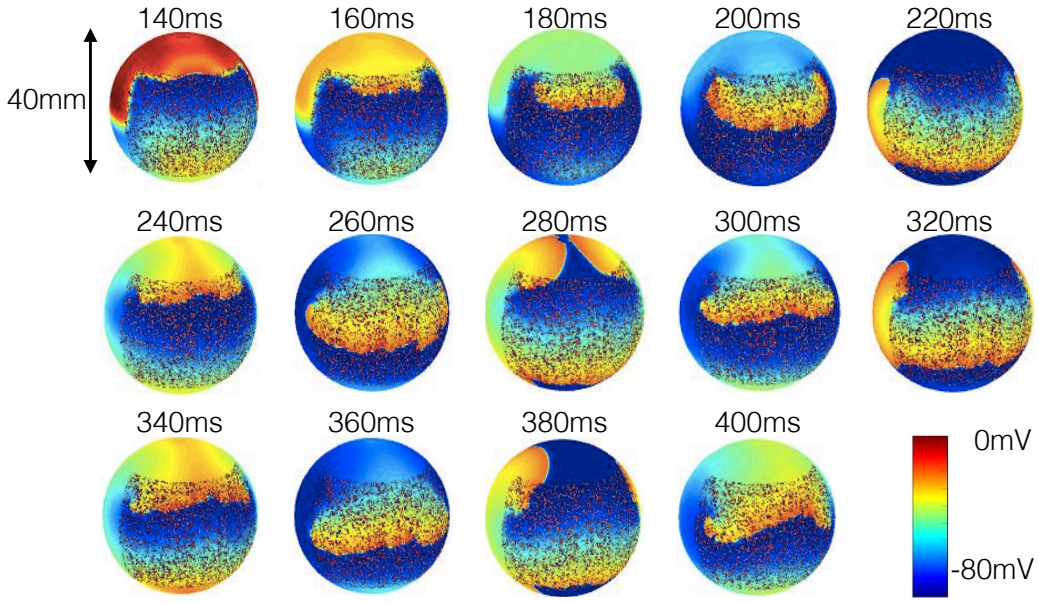

Figure 3.12: Transmembrane voltages of figure-eight pattern at the high-resolution fibroses area with degree of fibrosis at 20 percent. The figure-eight excitation pattern was induced by two stimulations. The first stimulation was induced from the upper part and the second was induced around the fibrosis region in the upper half of the sphere model.

3.3.10 Effects of fibrosis in a sphere model with degree of fibrosis at 30 percent

With the same stimulation protocol as described in Figure 3.12, fibrosis area with degree of fibrosis at 30 percent was proarrhythmogenic and resulted in persistent AF with multiple interacting rotational and focal sources (cf. Figure 3.13 (A)).

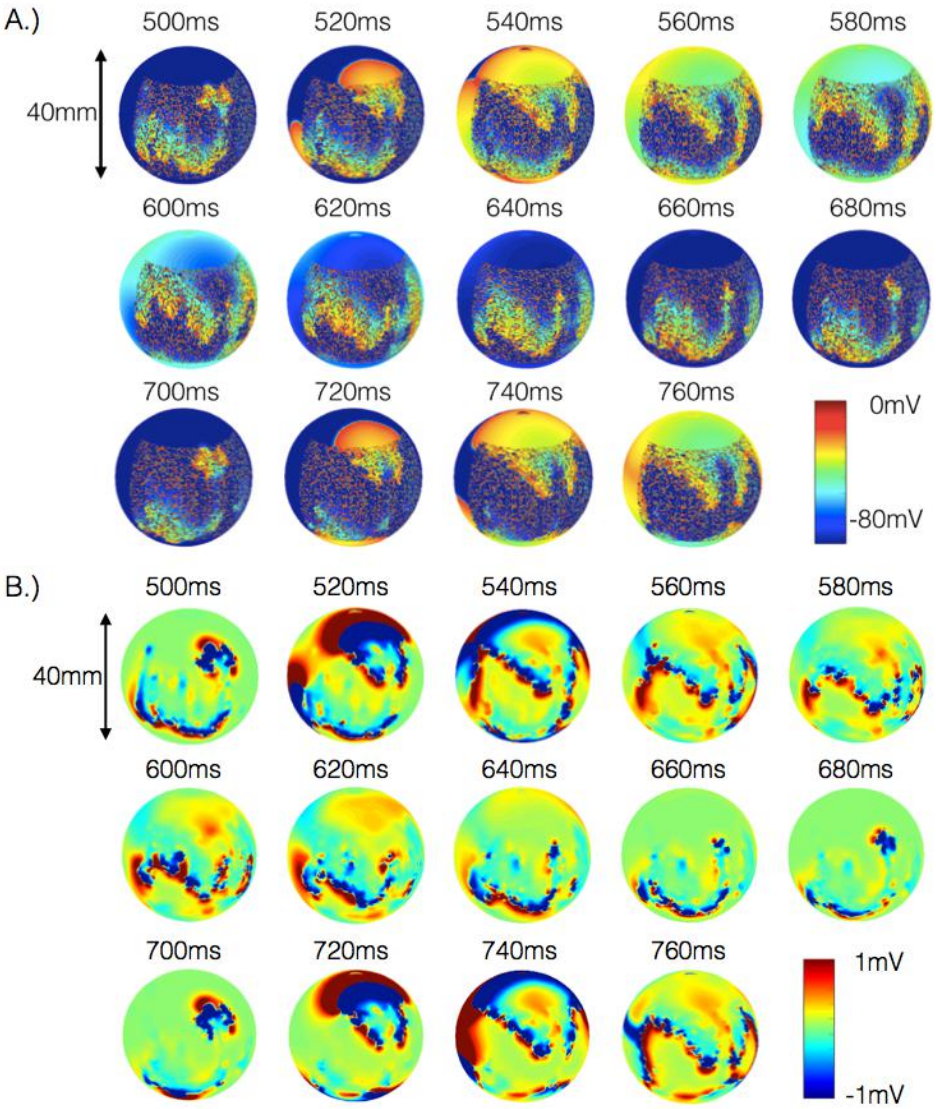

Figure 3.13: Transmembrane voltage of rotational and focal waves at high-resolution, three-dimensional fibrosis. Rotational activity and figure-eight excitation patterns were observed near the fibrotic border zone. Atrial fibrillation was persistent over multiple cycles.

Extracellular potential maps (cf. Figure 3.13 (B)) show the difficulties of detecting rotational activity. Multiple wavelets above the fibrotic tissue were observed. Focal

exit waves at fibrosis border zones and excitations in healthy tissue had significantly larger amplitudes, and signals above fibrotic tissue were low voltage, complex and fractionated signals (cf. Figure 3.13 (B), cf. Figure 3.14 (A)). The resulting LAT map and peak-to-peak maps with additional signal morphologies at the focal center, rotor center, fibrotic, and healthy tissue are shown in Figure 3.14 (A). The corresponding LAT map, substrate map, and signals at the same locations like in (A) during sinus rhythm are shown in Figure 3.14 (B).

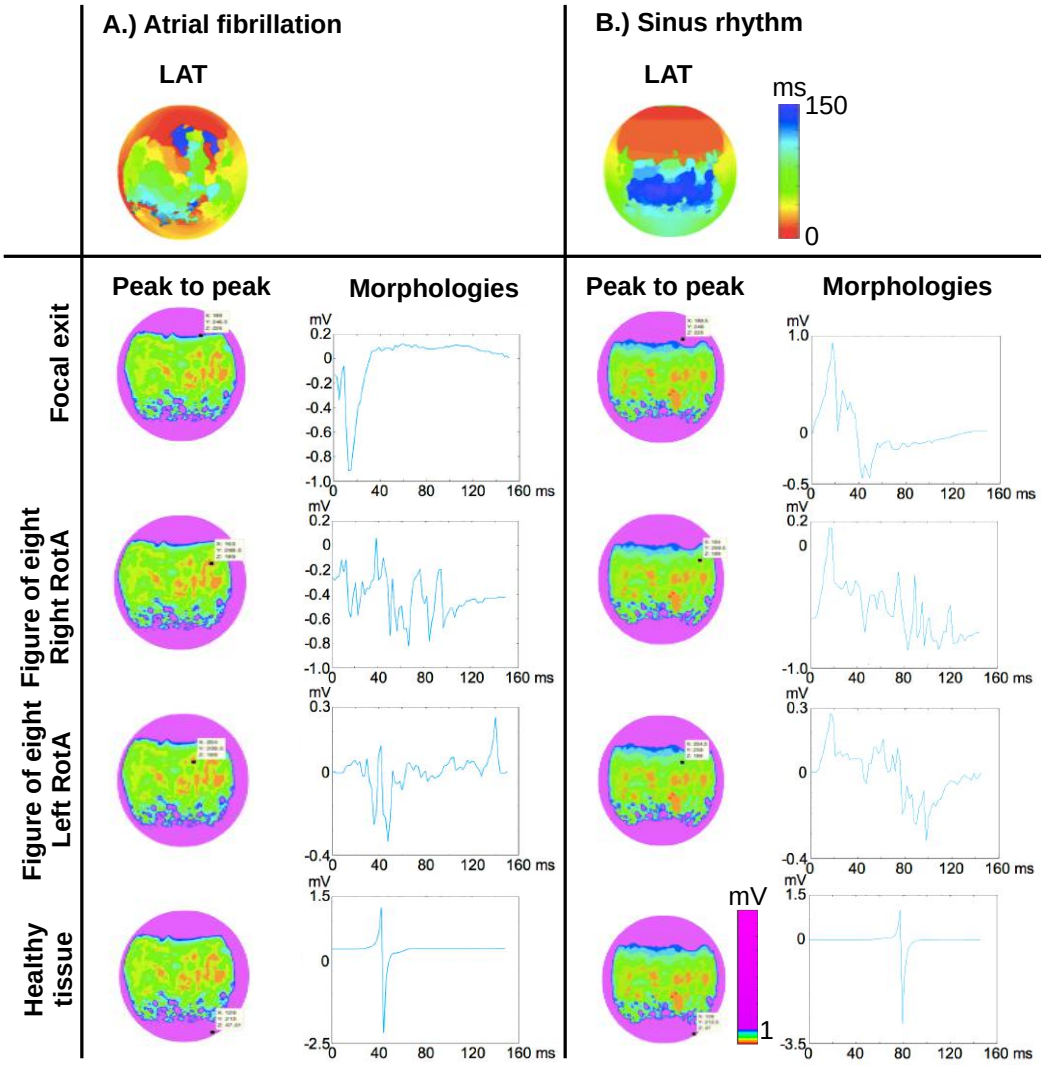

Figure 3.14: (A) Persistent AF at 3D Fibrosis with a degree of fibrosis at 30 degrees. Local activation time map. (B) LAT map in sinus rhythm in a distance of 2 mm to tissue. (A) Unipolar signal morphology at focal center, at right rotor tip, at left rotor tip, above the fibrosis, at the fibrosis border zone, and in healthy tissue. Locations of signal measurements are displayed on the voltage map on the left side. (B) Corresponding signal recordings during sinus rhythm. Locations of signal measurements are displayed on the voltage map on the left side (same locations in (A) and (B)).

Substrate mapping, i.e. during a sinus rhythm using peak-to-peak maps (cf. Figure 3.15 (A)), were strongly dependent on the threshold of low-voltage regions (cf. Figure 3.15 (B) and (C)). With a reduced threshold, not all fibrotic regions could be detected. Also, the distance to the tissue had a significant impact (cf. Figure 3.15) (D). At a 4-mm distance, less details were detected in the LAT map (cf. Figure 3.15) (D) as well as in peak-to-peak map (cf. Figure 3.15(E)) .

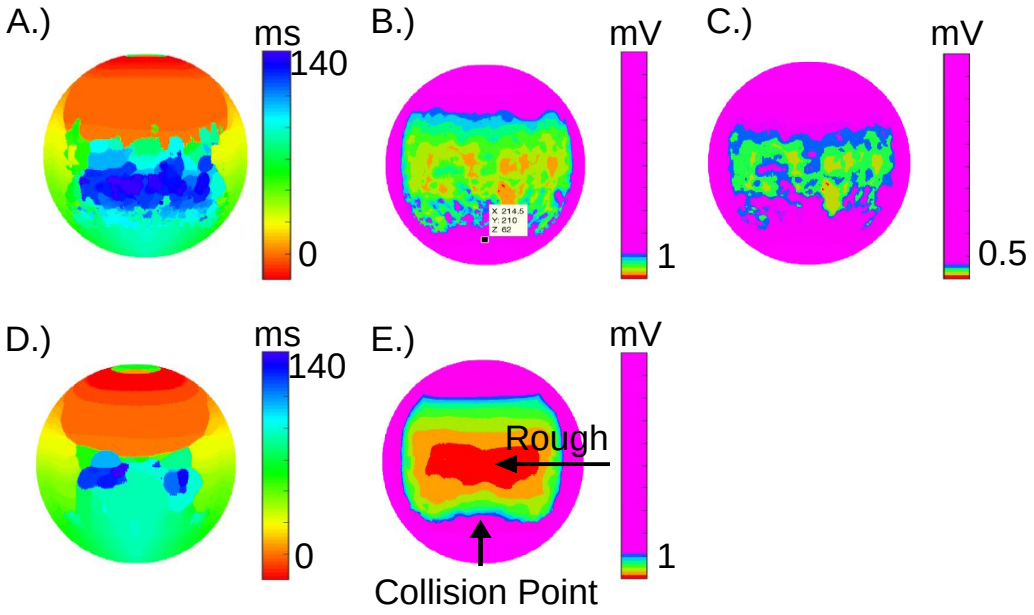

Figure 3.15: Substrate mapping during sinus rhythm. (A) A Sinus rhythm at a 3D fibrosis with a degree of fibrosis at 30%. Local activation time map at 2 mm distance. (B) Peak-to-peak map in distance of 2 mm to tissue. (C) Peak-to-peak map with another scale. (D) Local activation time map at 4 mm distance. (E) Peak-to-peak map at 4 mm distance.

3.3.11 Correlations between behavior of observed rotational and focal sources and size and degree of fibrosis

In table 3.1, the effects of fibrosis were correlated with size and degree of fibrosis. If there is less degree of fibrosis $\leqslant$ 10%, no persistent AF was observed, but a reduced conduction velocity. Focal exits were only observed in large (45mm x 35mm x 2mm) and dense fibrotic tissue ($\geq$30%). Rotational activities meandered and also focal exit locations changed from cycle to cycle at the fibrotic regions with a 20% degree of fibrosis. With an increasing degree of fibrosis $\geq$30%, rotational and focal activities became more stable over time. With a degree of fibrosis > 50%, no electrical excitation (block) was observed throughout the fibrosis region, and rotational activities took place only around the block area but not partially between healthy and partially

Table 3.1: Correlations between size and degree of fibrosis correlated with observed rotational and focal activity.

	Small Size of Fibrosis Area 10mm x 10mm x 2mm	***Large Size of Fibrosis Area 45mmx35mmx2mm***
Degree of Fibrosis 0%	No Anchoring, collapse of rotational source (<1 AF cycle).	No Anchoring, collapse of rotational source (<1 AF cycle).
10% (≙Reduced CV)	No Anchoring, collapse of rotational source (<1 AF cycle).	No Anchoring, collapse of rotational source (<1 AF cycle).
20% (≙Slow Conduction)	Important meandering of the rotational source at low voltage area (>20 AF cycles).	Important meandering of the rotational source at low voltage border zone (>20 AF cycles).
30% (≙Slow Conduction)	Anchoring of the meandering rotational source within low voltage area. No focal discharges (>20 AF cycles).	Anchoring of the meandering rotational source at low voltage border zone over the entire simulation interval (>20 AF cycles). Dynamic focal discharges.
40% (≙Slow Conduction)	Anchoring of the rotational source within and around the small low voltage area; over the entire simulation interval (>20 AF cycles). No focal discharges.	Anchoring of the rotational source at a stable location at low voltage border zone; over the entire simulation interval (>20 AF cycles). Stable focal discharges.
>50% (Fibrosis≙Block)	No electrical conduction into the heterogeneous area (electrical silence). Rotations occur around the non-conducting area; over the entire simulation interval (>20 AF cycles). No focal discharges.	No electrical conduction into the heterogeneous area (electrical silence). Rotations occur around the non-conducting area; over the entire simulation interval (>20 AF cycles). No focal discharges.

within the fibrotic tissue. No focal exits were observed at fibrotic tissue with degree of fibrosis > 50%.

3.3.12 Comparison between simulations of focal and rotational sources at 3D fibrosis and high-resolution clinical data

Simulated wave maps, cycle lengths, and signal morphologies of rotational and focal activities of 3D fibrosis (cf. Figure 3.16) were compared with clinical high-density observations (cf. Figure3.17) in the literature [133]. The black circle in Figure 3.16 B) symbolizes a diameter of 26 mm similar to the black circles in Figure 3.17 A.) and B.). The measured cycle lengths (cf. Figure (3.16 C.)) in simulation data were similar to the clinical measurements of the cycle lengths in Figure 3.17 B.). Morphologies at the

focal exits resulted in double potentials and fractionated signals (cf. Figure 3.16 D.) and Figure 3.18) similar to the clinical observations in Figure 3.17 B.).

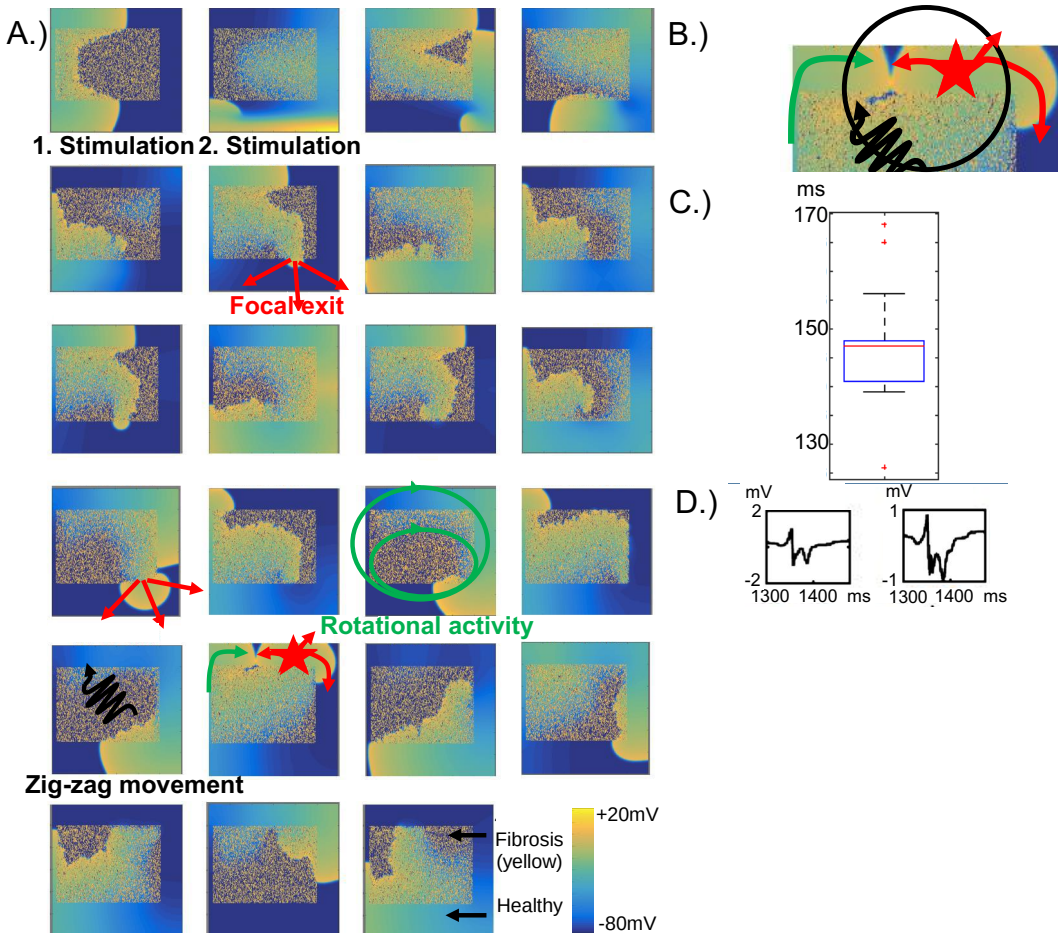

Figure 3.16: Rotational and focal waves at fibrotic tissue in a 3D patch. (A) Transmembrane voltage maps of moving rotational and focal sources in a fibrotic region with a degree of fibrosis at 30%. (B) Analysis of simulation wave maps. The circles symbolize a diameter of 26 mm. (C) Boxplot of detected cycle lengths in simulation data. (D) Morphologies at the focal exits resulted in double potentials. Figure parts are adapted from Rottmann et al. 2016 [131] © IEEE [2016] with permission.

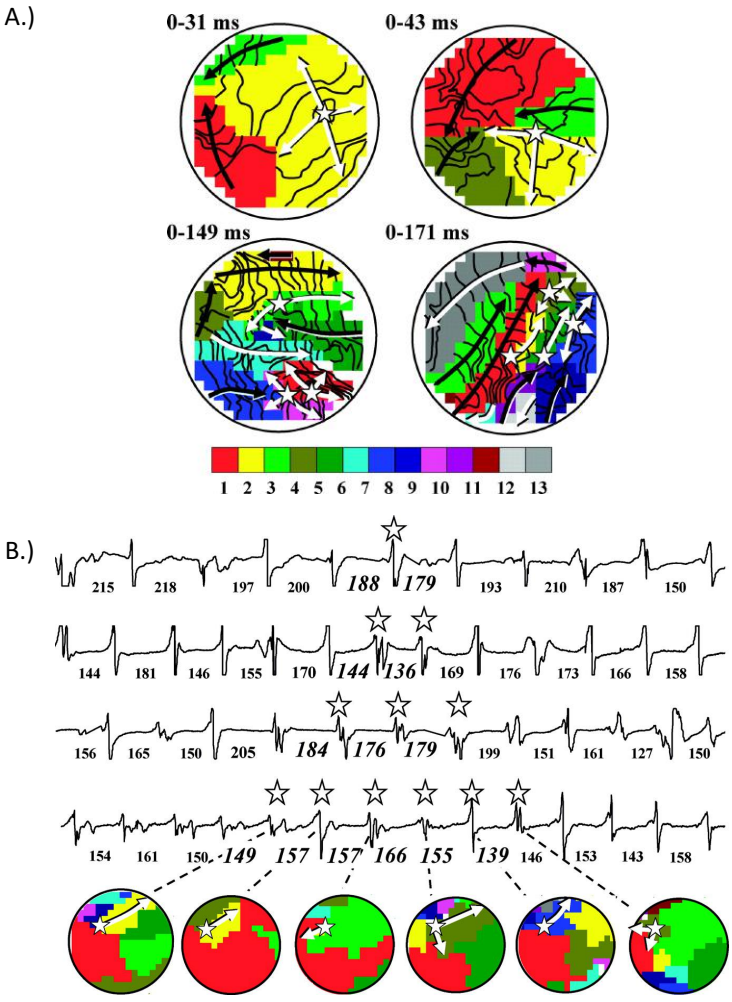

Figure 3.17: (A) Analysis of wave maps: clinical wave maps from high-density mapping at 2 mm inter-electrode distance. The black circle symbolize a diameter of 26 mm. (B) Morphologies at the focal exits (marked with stars) were also analyzed and resulted in double potentials and fractionated signals. The figure is from [133] with permission.

Figure 3.18 shows signal morphologies measured with a virtual square catheter covering the rotational activity center and focal source center. Unipolar signal recordings above fibrotic tissue were nearly 10 x smaller than those for healthy tissue. At the rotational activity center, continuous fractionated signals were measured. At focal exit points, strong negative amplitudes were observed. Because of near-field effects, these negative amplitudes overlapped small signals above fibrotic tissue near the exit point (cf. the black dashed line in Figure 3.18).

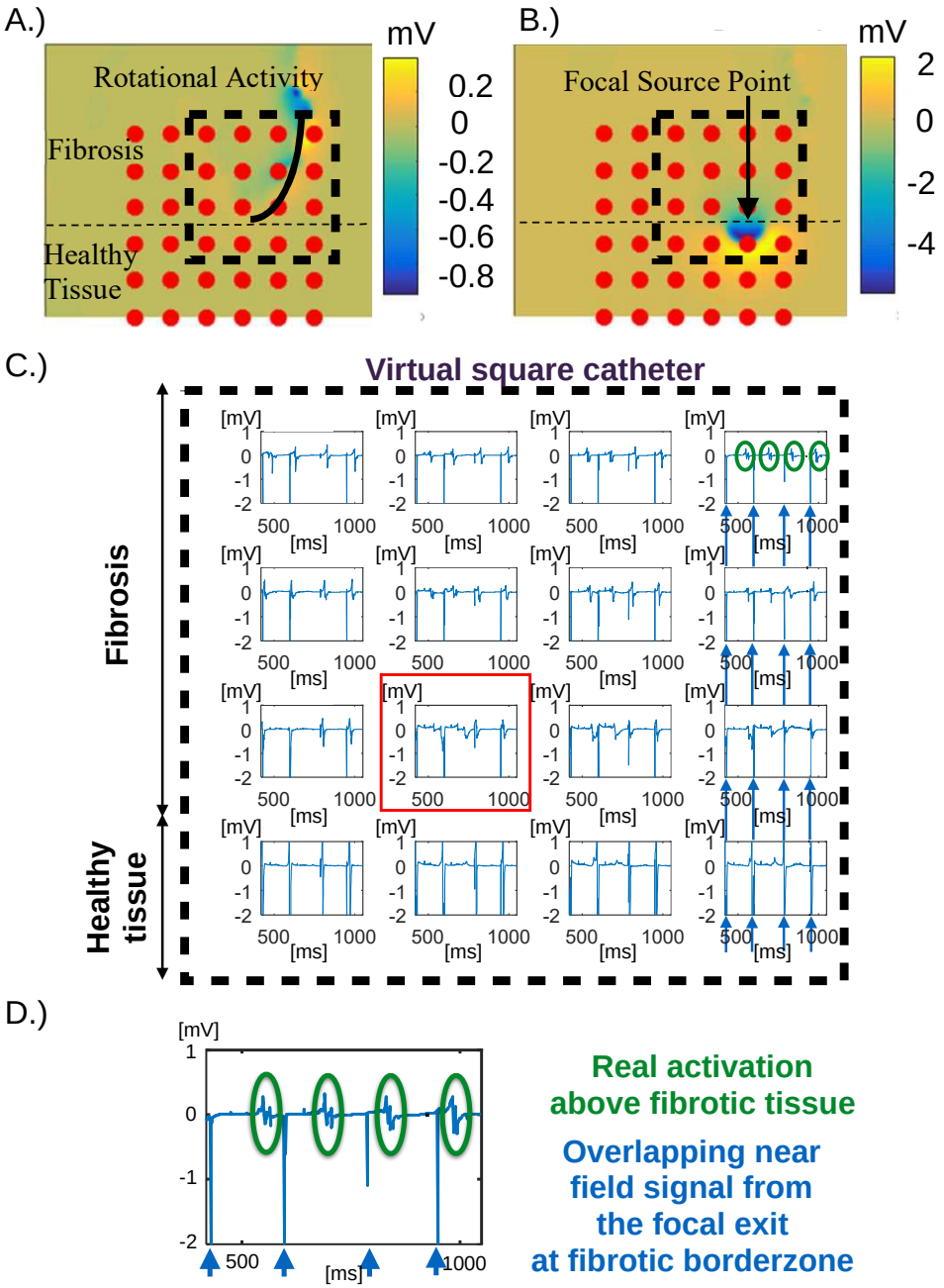

Figure 3.18: A.) Voltage map with a rotational wavefront in a 3D fibrosis region. Value range between 0.2mV and -0.8mV shows nearly 10 x smaller amplitudes above the fibrotic tissue than those from the focal exit and the propagation in healthy tissue in figure part B.). B.) Focal exit point at a border between fibrosis and healthy tissue. Red dots in (A) and (B) mark the electrode positions of measured signals with a square catheter of 2-mm interelectrode distance. C.) Signal analysis of rotational and focal sources in the 3D patch with a degree of fibrosis at 40% measured. Signals were analyzed within the region marked with dashed black box, compare A.), B.). The upper three rows were measured above fibrotic tissue. The lower row was measured in healthy tissue. Real activation (small amplitudes) at the fibrotic tissue is marked in green. Exemplary overlapping near-field signals from the 10 x times larger amplitudes from the focal exit point at the fibrotic border zone. D.) Zoomed exemplary overlapping near-field signals. The figure is adapted from [131] © IEEE [2016] with permission.

Figure 3.19 depicts intracardiac signal recordings at focal exit locations at different distances to the border zone and to the tissue. At a distance of 3mm to the tissue (in z-direction), the overlapping effects of the exit points could be detected within a distance of 8mm to the border zone.

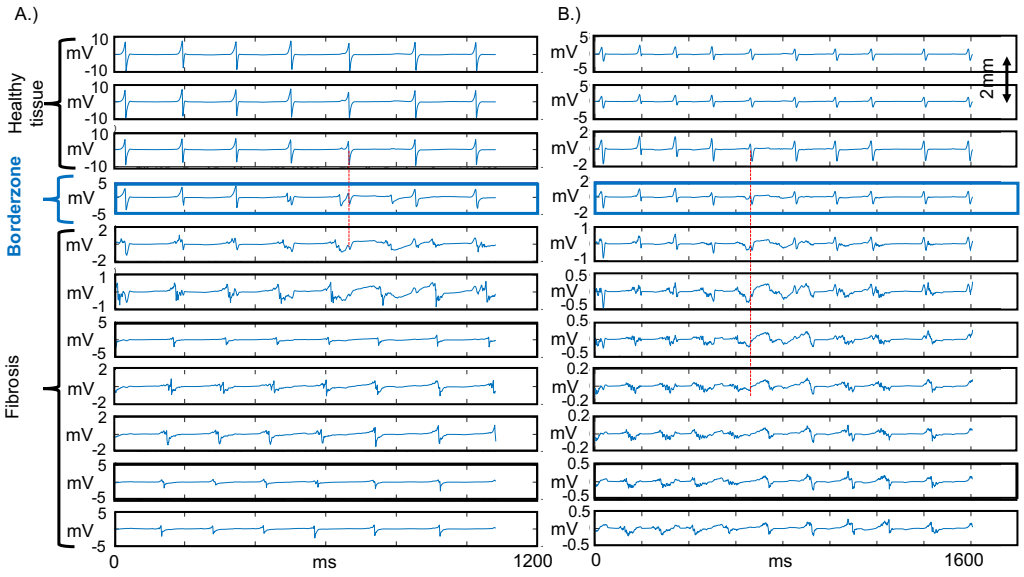

Figure 3.19: Unipolar signals measured in a line in 2mm distances vertical to the border zone at focal exit point covering the fibrosis region, border zone (blue) and healthy tissue (A) in 0 mm distance to the tissue and (B) in 3 mm distance to the tissue. The red line displays the overlapping of the negative S-wave of the exit point within the fibrosis area, which could be detected in 8mm distance to the border zone in (B). Signals were about 10 x smaller in 3 mm distance in (B) and overlapping near-field effects from focal exits deformed the small fibrosis signals stronger and resulted in more complex fractionated signals, compared to those in 0mm distance to the tissue (A).

3.3.13 Rotational activity centers and focal source center locations over time

The positions of rotational and focal source centers were localized in 20 simulated persistent AF cycles in Figure 3.20. It is shown that both rotational and focal centers were located near fibrosis border zones. The rotor centers and focal sources moved more with a lesser degree of fibrosis of 30%. With a degree of fibrosis at 40%, AF source centers were found to be more stable.

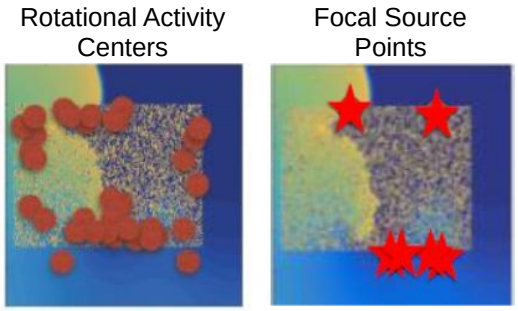

Figure 3.20: (Left) Rotational activity centers and (Right) focal source point locations were detected near fibrosis border zones over multiple cycles.

3.3.14 Breakthrough because of different fibrosis sizes between endocardium and epicardium

Transmural fibrosis regions with the same sizes of fibrosis between endocardium and epicardium is a simplification. In Figure 3.21 A.), the fibrosis area was smaller at the epicardium than at the endocardium. In Figure 3.21 A.) two exit points were first observed at the epicardium. Because of the larger fibrosis region, the rotating excitation within the fibrotic tissue needed more time in order to meet the border zone, and thus focal exits were observed at the endocardium some milliseconds later. From endo-epicardial measurements, excitations similar to endo-epicardial breakthroughs, described in the literature [103], were observed. An endo-epicardial breakthrough in a more realistic sphere model is depicted in Figure 3.21 (B).

3.3.15 High-density maps of the human endocardium

Measured high-density maps with interelectrode distances of 2 mm from human endocardium were analyzed in 14 cycles and are depicted in Figure 3.22 - 3.23. High-density data [111] was provided by Richard Houben (2BMedical, Maastricht, Netherlands).

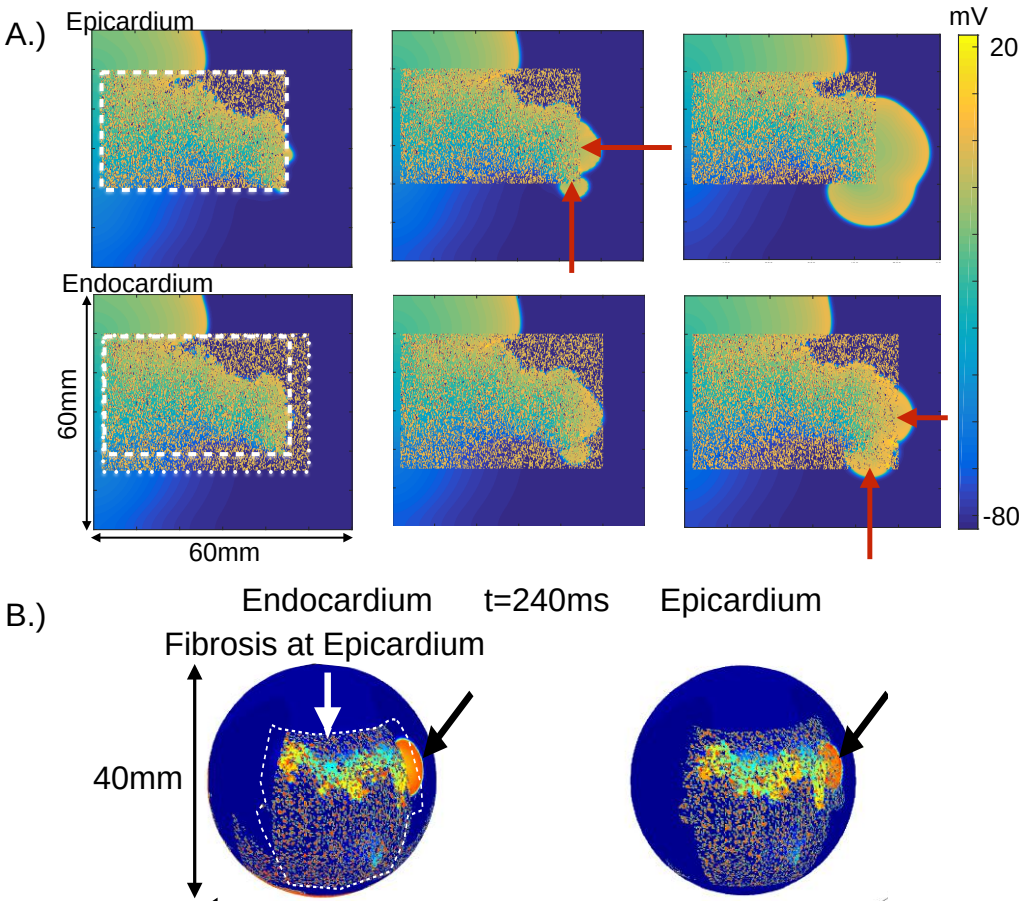

Figure 3.21: Transmembrane voltage maps. (A) 3D-patch: Breakthrough points (red arrow) from the epicardium to the endocardium because of different fibrosis sizes between endocardium and epicardium. The strong focal exit signals were first detected at the epicardium and then some milliseconds later at the endocardium, similar to clinical observations, described in the literature [103]. (B) Endo-epicardial breakthrough (black) due to different fibrosis sizes of endocardium and epicardium in an atrial sphere model. The fibrosis region in this sphere model was smaller at the endocardium compared to the epicardium. The large focal exit potentials (marked with the black arrow) were first detected at the endocardium and then some milliseconds later at the epicardium.

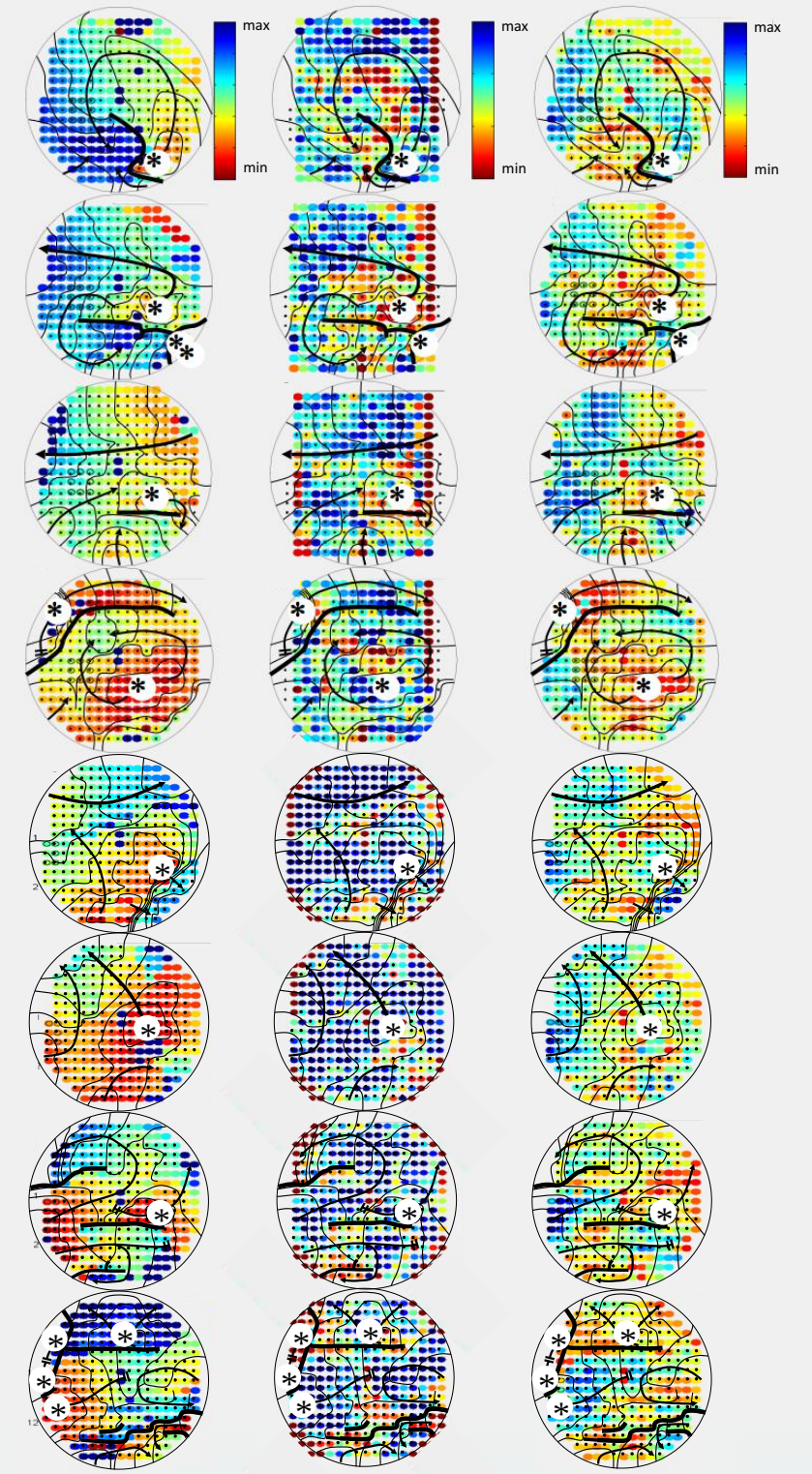

Figure 3.22: High-density maps of the human endocardium [111]. (Left) LAT maps. (Center) Conduction velocity maps. (Right) Peak-to-peak maps of cycles 1-8. Stars symbolize focal waves. The figure was generated in collaboration with Richard Houben (2BMedical, Maastricht, Netherlands).

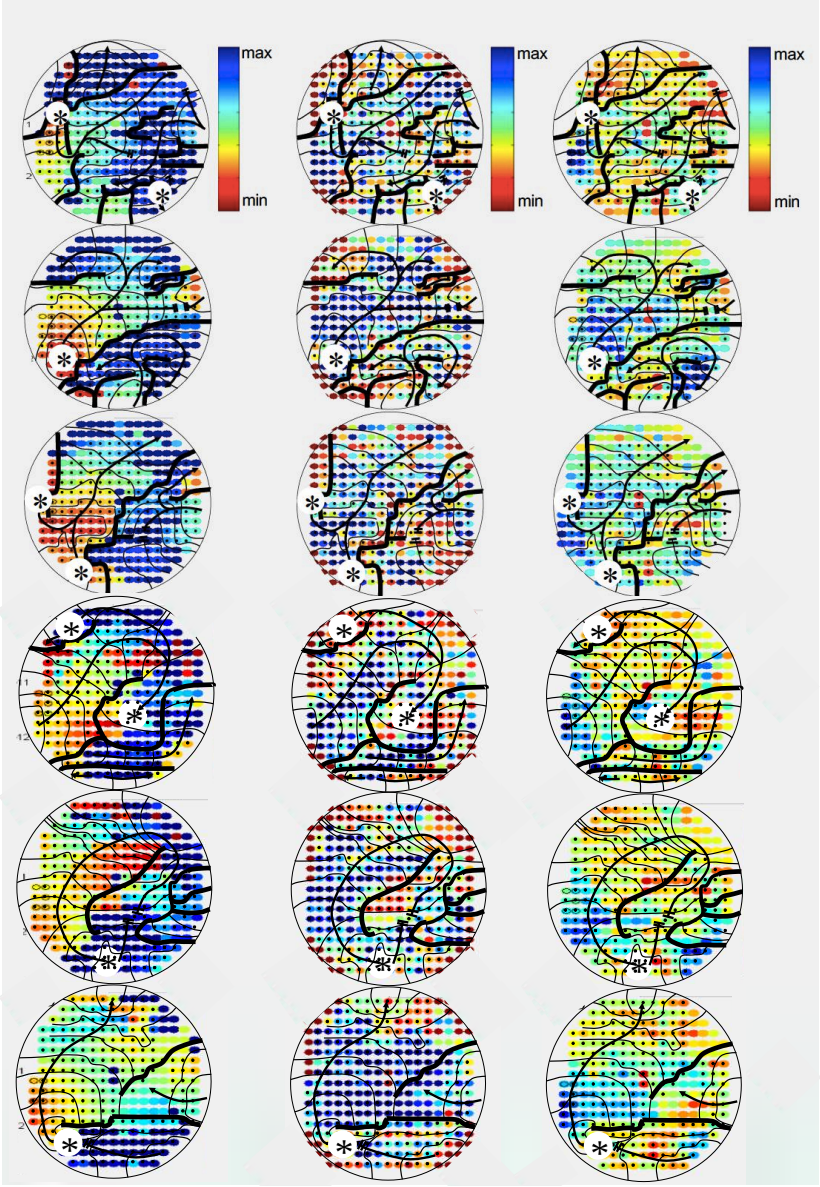

Figure 3.23: High-density maps of the human endocardium [111]. (Left) LAT maps. (Center) Conduction velocity maps. (Right) Peak-to-peak maps of Cycles 9-14. Stars symbolize focal waves. The figure was generated in collaboration with Richard Houben (2BMedical, Maastricht, Netherlands).

Focal sources of the cycles analyzed were located at the border zone of low-voltage areas. The numbers of observed focal sources per cycle are presented in the histogram (cf. Figure 3.24).

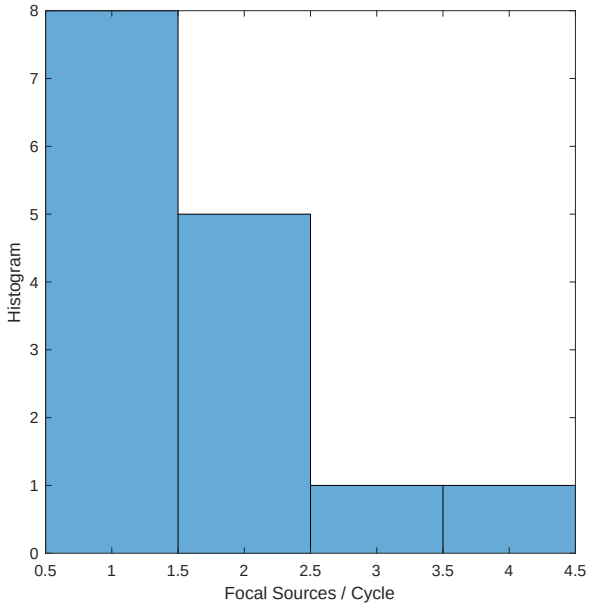

Figure 3.24: Number of observed focal sources per cycle in the histogram.

3.3.16 Large fibrosis regions

3.3.16.1 Multiple rotational and focal sources at 3D fibrosis in a 3D patch

Planar waves which moved through a large fibrosis region (800mm x 800mm) resulted in split wavefronts. Importantly, the conduction velocity was strongly dependent on the simulated degree of fibrosis between 10% and 40%. Only one wavefront was necessary for the induction and maintenance of persistent atrial fibrillation, if the degree of fibrosis was 40% using the cell model under AF condition. In the case of the degree of fibrosis at 40%, a planar wave at the dense fibrotic tissue resulted first in curved wavefronts, then in wave breaks, and finally in multiple interacting rotational, focal, and wavelet activities over multiple cycles. Notably, the focal exits, rotational activities, and wavelet rotations and collisions were repetitive over multiple cycles. If the focal exit locations changed, also the activation patterns within the fibrotic tissue varied strongly (cf. Figure 3.25).

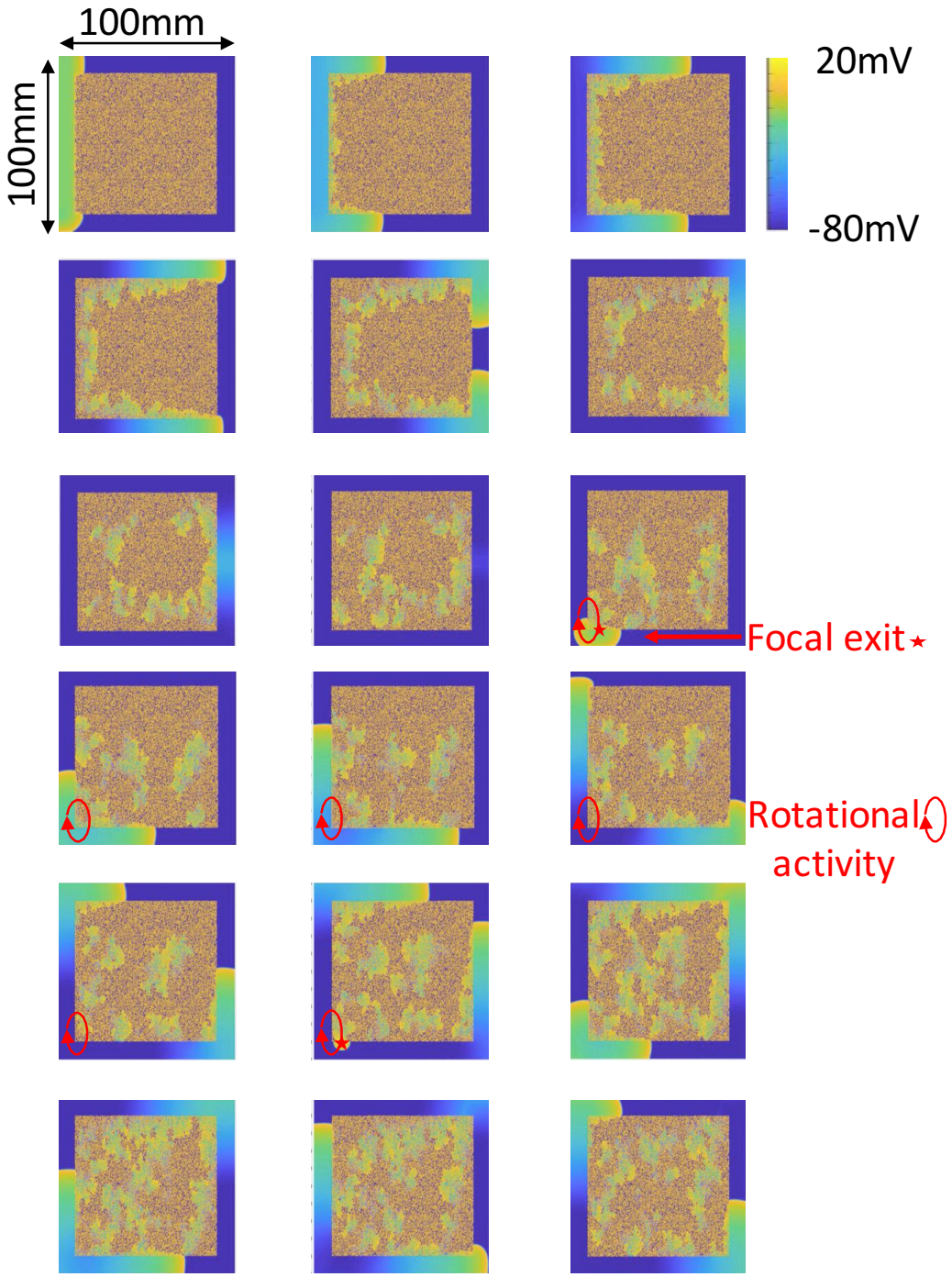

Figure 3.25: Multiple interacting rotational, focal, and wavelet activities within large fibrosis region with the size of 800 mm x 800 mm. Persistent AF was induced by one single planar wavefront. The time between two figures is 40ms.

3.3.17 Persistent atrial fibrillation with multiple rotational, focal, and wavelet activities within a realistic atrial model

A large 3D fibrosis region was implemented in a realistic atrial model with included fiber orientation, (cf. Figure 3.26 and Figure 3.27). The geometry and fiber orientation of the heart model was adapted from [134]. Persistent atrial fibrillation with multiple rotational, focal, and wavelet activities was induced by two stimulations from the upper and the left side. Focal exit locations were repetitive over multiple cycles. Also, the rotational activities, wavelets, and even collision points were repetitive and similar cycle by cycle, cf. Figure 3.26 and Figure 3.27. The focal exit points were located near the pulmonary veins, cf. Figure 3.26 and Figure 3.27. Trajectories of multiple rotational, focal, and wavelet activities (cf. Figure 3.27) in the realistic atrial model with included fiber orientation are displayed in the zoomed Figure 3.26.

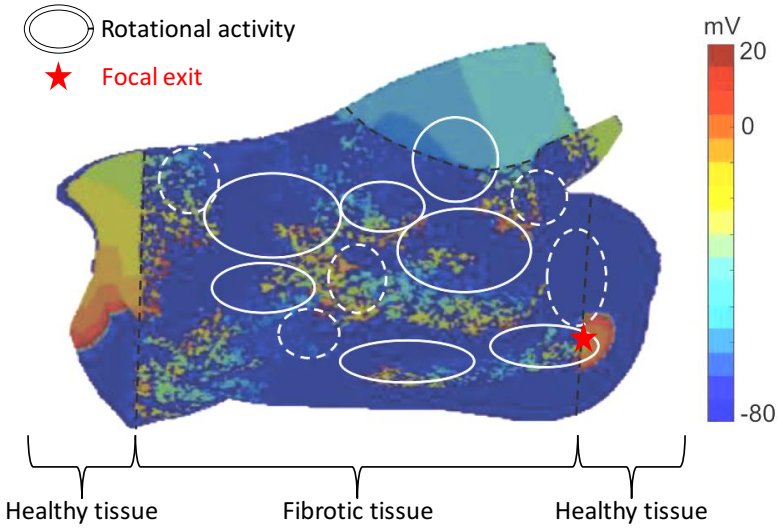

Figure 3.26: Persistent atrial fibrillation with multiple rotational, focal, and wavelet activities in a realistic atrial simulation model with an implemented 3D fibrosis region (black dashed lines). Focal exits were located at fibrosis border zones near the pulmonary veins. The trajectories of the rotational activities are displayed in white. The zoomed figure is from Figure 3.27.

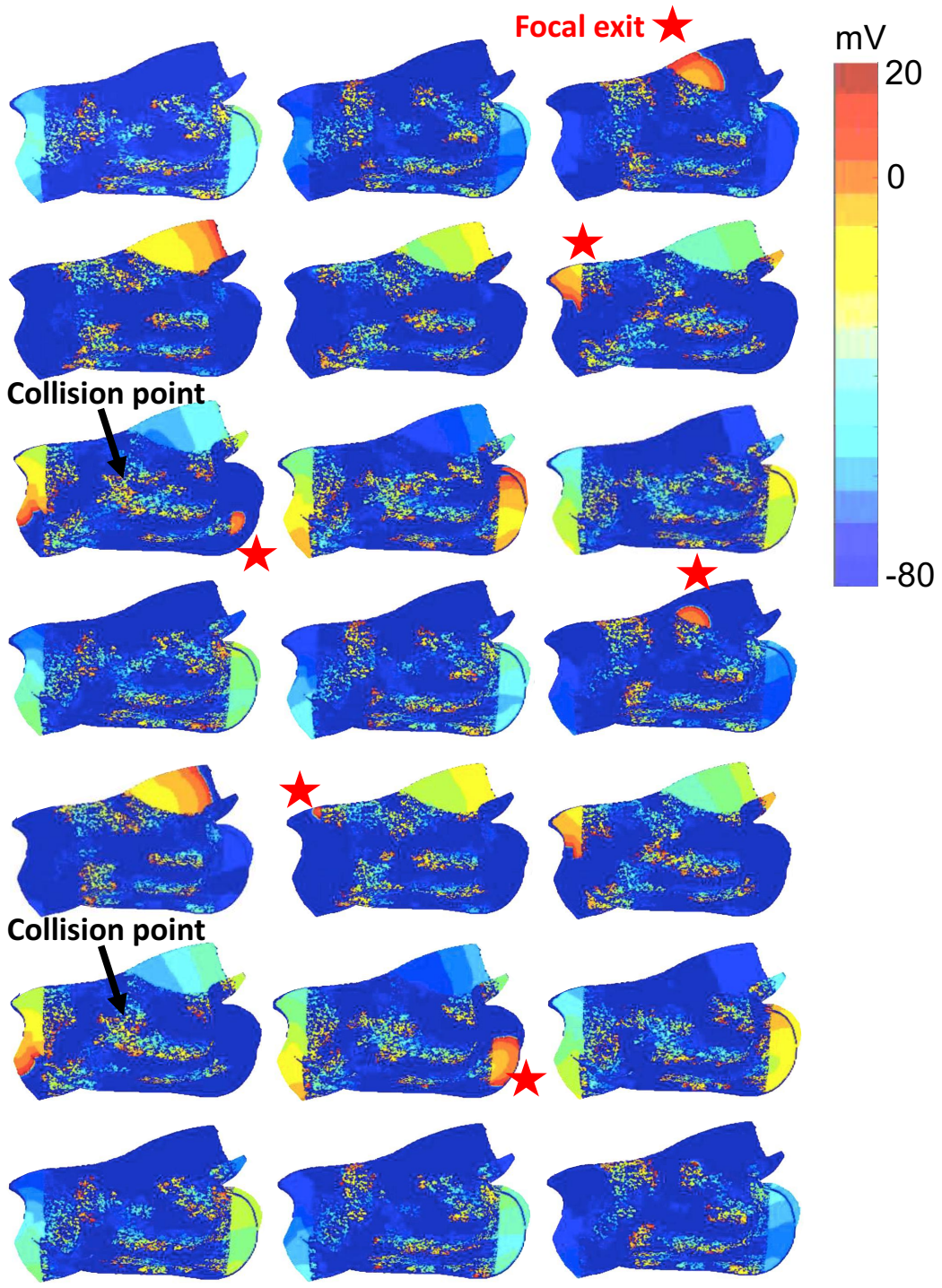

Figure 3.27: Multiple interacting rotational, focal, and wavelet activities in a realistic atrial simulation model with implemented 3D fibrosis region. Rotational and focal activities, wavelets, and even collision points were repetitive and similar cycle by cycle. Focal exits were located at fibrosis border zones near the pulmonary veins. The fibrosis region and the trajectories of the multiple interacting rotational activities are given in the zoomed Figure 3.26.

3.3.18 Rotational and focal sources at multiple fibrosis regions

Rotational and focal sources in two dense fibrosis regions with the size of 20mm x 20mm resulted in complex excitation patterns and signals (cf. Figure 3.28). Multiple rotational activity centers, figure-eights, and multiple focal exit locations interacted cycle by cycle. But in spite of these complex patterns, fibrosis regions correlated with low-voltage regions over time.

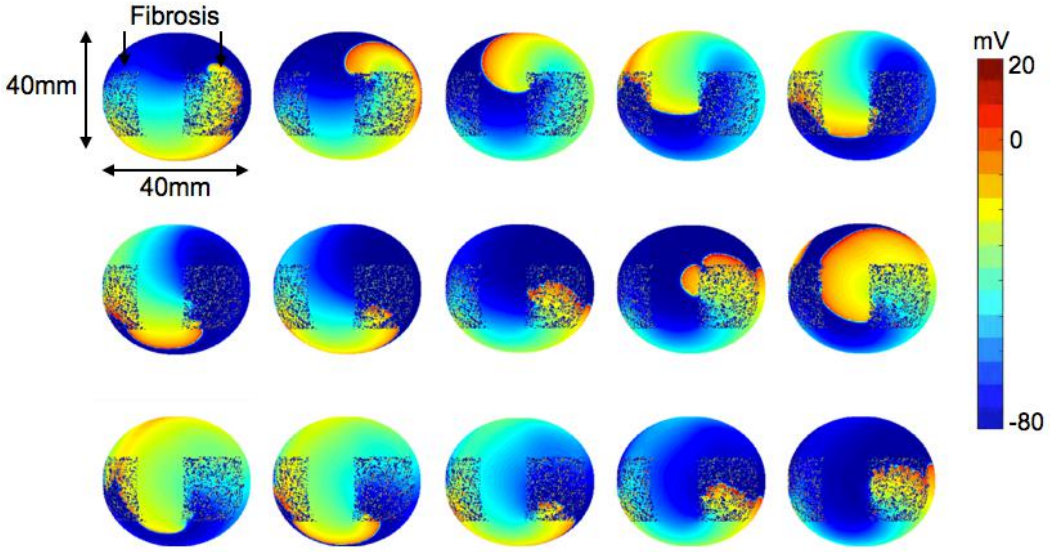

Figure 3.28: Multiple rotational and focal sources in two fibrosis regions resulted in complex excitation patterns. The time between two figures is 20ms.

3.4 Discussion

The studies described demonstrate that rotational, focal, and wavelet activities develop and maintain persistent AF in heterogeneous regions. The identification of these proarrhythmogenic regions and sources can be targeted by ablation guided by low-voltage and by mapping of rotational, focal, and wavelet activities. Furthermore, signal characteristics at different degrees of fibrosis were analyzed with activation time maps, peak-to-peak maps, and conduction velocity maps. These findings from simulation studies correlate with findings from clinical studies with multi-electrode catheters [135] and high-density endocardial mapping [133]. The computer simulation analyzed the impact of size and degree of fibrosis on the development and maintenance of rotational, focal and wavelet activities. Without implemented fibrosis regions

rotational activities AF did not anchore and did not maintain. However, induced rotational activities were rotated over multiple cycles around a small dense fibrosis region (10mm x 10mm x 2mm). In the case of larger fibrosis (voxel resolution 0.1mm x 0.1mm x 0.1mm) region (35mm x 45mm x 2mm) and the degree of fibrosis of 30% rotational activity meandered between healthy tissue and fibrosis, but the rotor centers stayed within the fibrosis area (< 5mm to the fibrosis borders). Furthermore, the developed model revealed focal exits from different exit point locations. At the degree of 40% the rotational activity at the fibrosis border zone was more stable and also the focal exit point locations were stable over multiple AF cycles. In the more realistic case of a 3D sphere model mimicking the left atrium, "figure-of-eight" patterns, consisting of two rotors developed and maintained over more than 20 cycles. The necessary condition for the induction and maintenance of AF was in the case of a small fibrosis region (10mm x 10mm) a crossfield stimulation or two planar waves stimulations with a degree shift of 90° and with a time delay. In order to simulate the additional induction of focal exits, a larger fibrosis region and the degree of fibrosis between 30%-40% was a necessary condition. Multiple rotating wavelets resulted in the case of the degree of fibrosis at 40%. The only necessary condition for the induction of AF was one single planar wavefront at a large fibrosis region of 800mm x 800mm using cell model under AF condition. The different hypotheses rotor hypothesis, focal wave hypothesis at pulmonary veins and multiple wavelet hypothesis could be integrated within one realistic atrial model with high voxel resolution (voxel resolution 0.1mm x 0.1mm x 0.1mm) of fibrotic tissue. This model integrated fiber orientation (atrial geometry and fiber orientation adapted from the model described in Krueger et al. (2013) [134]). Multiple rotational, focal and wavelet activities interacted at heterogeneous atrial regions. The complexity of AF increased with increasing degree and size of atrial heterogeneities, and with the number of fibrosis regions. These findings from the simulation studies were correlated with clinical high-density measurements of multiple focal waves and rotational activities. Both, the developed simulation models and clinical measurements were compared regarding the amplitude maps, wave maps, conduction velocity maps, statistical analyses of cycle lengths. Additional signal characteristics at the focal exits per cycle were analyzed. Furthermore, the near-field effects and the resulting signal morphologies of resulting double potentials were described. These findings could be used for the detection of proarrhythmogenic substrate as ablation target points.

3.5 Resulting Publications

The results of this chapter were published in :

M. Rottmann, J. Chen, H. Lehrmann, V. Markstein, U. Arslan, W. Kaltenbacher, L. Kienle, J. Zürn, R. Weber, J. Allgeier, B. Müller-Edenborn, C. Keyl, D. Trenk, F. Neumann, O.

Dössel, T. Arentz, A. Jadidi. Rotational and focal drivers develop at heterogeneous atrial sites displaying low voltage and slow conduction, Clin Res Cardiol (2017), 106 (Suppl 1), 2017.

M. Rottmann, U. Arslan, W. Kaltenbacher, V. Markstein, T. Arentz, O. Dössel, A. Jadidi. Impact of three dimensional atrial fibrosis on development and stability of rotational activity in atrial fibrillation. A 3D simulation and clinical high-density mapping study in persistent atrial fibrillation, Computing in Cardiology, 2016.

M. Rottmann, U. Aslan, V. Markstein, H. Lehrmann., J. Allgeier, R. Weber, W. Kaltenbacher, F. Rafdionza, T. Arentz, O. Dössel, A. Jadidi. Dynamics of rotational and focal drivers in persistent atrial fibrillation at cardiac fibrosis. A clinical mapping and simulation study, Journal of Clinical Experimental Cardiology, 2016.

CHAPTER 4

Signal Processing Methods for the Detection of Atrial Fibrillation Sources

"Mathematical analysis is as extensive as nature itself; it defines all perceptible relations, measures times, spaces, forces, temperatures; this difficult science is formed slowly, but it preserves every principle which it has once acquired; it grows and strengthens itself incessantly in the midst of the many variations and errors of the human mind. It's chief attribute is clearness; it has no marks to express confused notations. It brings together phenomena the most diverse, and discovers the hidden analogies which unite them."

— Jean Baptiste Joseph Fourier

4.1 Introduction

Despite extensive research, AF sources often remain undetected during the electrophysiological study. One limitation is the current catheter design in clinical usage. Other limitations are the current signal processing methods which are mainly the local activation time (LAT) map, peak-to-peak voltage map, and complex fractionated atrial electrograms (CFAE) map. There are no automatically methods for detecting rotational and focal sources integrated in commonly used navigation systems. In order to find the sources responsible for the induction and maintenance of atrial fibrillation, it is essential to develop new signal processing methods. In this chapter, developed and analyzed signal processing methods for detecting rotational and focal sources are presented.

4.1.1 Methods for AF source detections based on local activation times

In the literature, the cosine fit method [113] describes the determination of the conduction velocity and direction of propagation of planar waves detected with circular catheters. This chapter investigates new activation patterns and the parameter cycle length coverage (CLC), not only of the Lasso catheters but also for AFocusII, PentaRay, and new designs like the square catheter.

4.1.2 Methods for AF source detections based on voltage and morphology

In the literature, i.e. methods based on approximate entropy [136] were described in order to detect AF sources. This section presents the methods to detect AF sources developed from simplified tissue patches, atrial sphere models, and realistic atrial geometry models. Furthermore, new methods were presented for analyzing stable and unstable rotations in atrial models and new findings of typical signal characteristics near stable and unstable rotor centers.

4.1.3 Methods for AF source detections based on phase singularities

Notably, Gray [137] developed phase mapping methods for cardiac excitations already in the year 1998. Phase singularity filaments within the heart tissue were published in literature. In numerous studies, 3D filaments were demonstrated in tissue slabs, especially in ventricular walls. Epicardial and transition to surface phase maps were given from Rodrigo et al. (2014) [138] in a sphere model. This chapter presents phase singularity filaments in blood using a realistic atrial model. Based on the hypothesis that reentries can drive atrial fibrillation, methods were developed for determining rotor centers in the tissue (transmembrane voltages) but also in the blood (extracellular potentials).

4.1.4 Methods for AF source detections based on the dominant frequency

Previous studies have analyzed rotors in the frequency domain (Berenfeld et al. (2000) [139]) with dominant frequency maps (Mansour et al. (2001) [140]) of optical signals. This chapter presents algorithms that use the dominant frequency for automatic rotor detection methods.

4.2 Developed Methods

4.2.1 Developed local activation time-based methods

4.2.1.1 Calculation of the local activation time in unipolar and bipolar recordings

Local activation times from unipolar recordings were usually calculated using the steepest negative slope (Spach et al. (1979) [141]). In complex signal morphologies, the LAT cannot be clearly determined because of multiple negative slops during a certain time period. In 1993, the NLEO operator for measurement of the energy of signals was introduced by Kaiser. In the literature the LAT was also determined by the maximum of the low-pass filtered NLEO [142] signal. LATs were defined as maximum of the low pass filtered NLEO signal with the maximal energy E_n and the sequences x in the Equation 4.1 [142]. The parameter LAT was calculated with the steepest negative slope and with the NLEO. The Figure 4.1 presents those two described possibilities of determining the LAT (cf. Figure 4.1). The low-pass filtered non-linear energy operator had the advantage that especially in complex signal morphologies, the LAT could be determined more robustly [113]. Figure 4.1 (A) presents the workflow of the LAT calculation. Examples of LATs calculated based on a unipolar signal are presented in Figure 4.1 (B). For transmembrane voltage potentials, the parameter of the steepest positive slope of the transmembrane voltage was used to calculate the LAT.

$$E_n = x_n^2 - x_{n+1} \cdot x_{n-1} \tag{4.1}$$

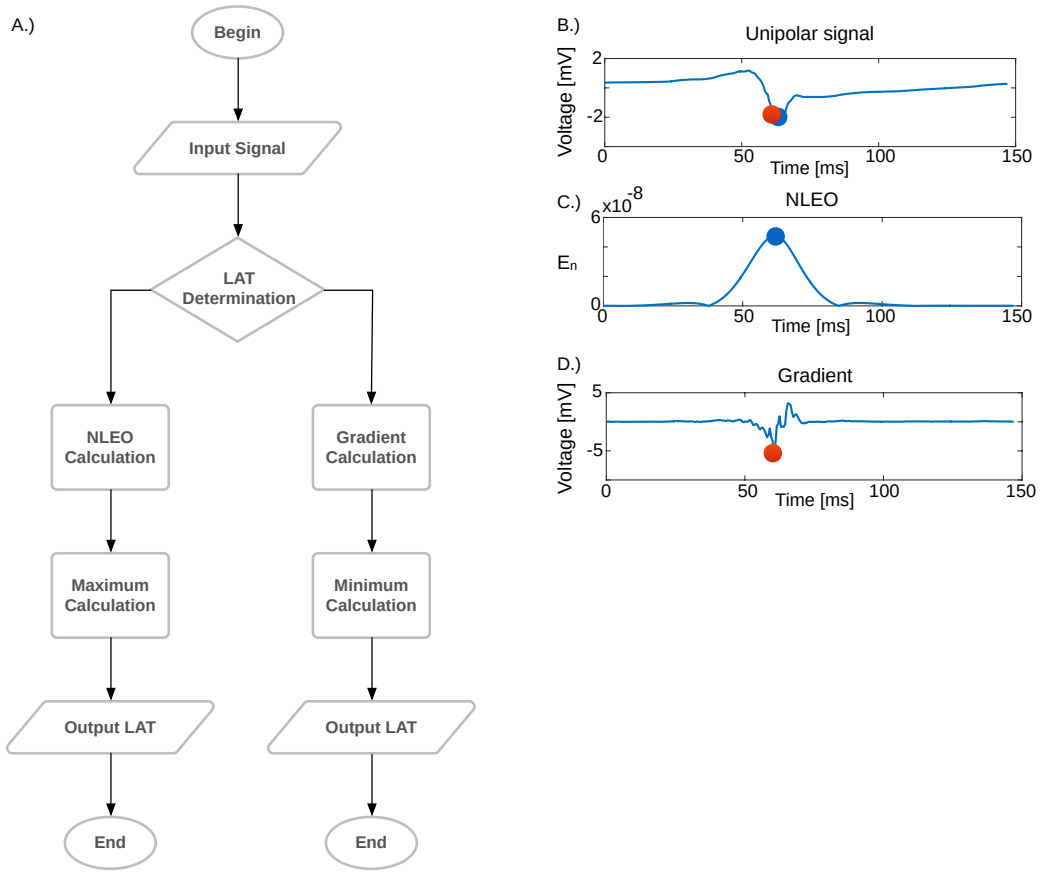

Figure 4.1: (A) Workflow for determining the LAT with the parameter steepest negative slope and with the parameter NLEO. (B) Example of a unipolar signal with LAT determined from the (C) NLEO (marked in blue) and (D) the steepest negative slope (marked in red). The Figure is adapted from [S5] [117] [118].

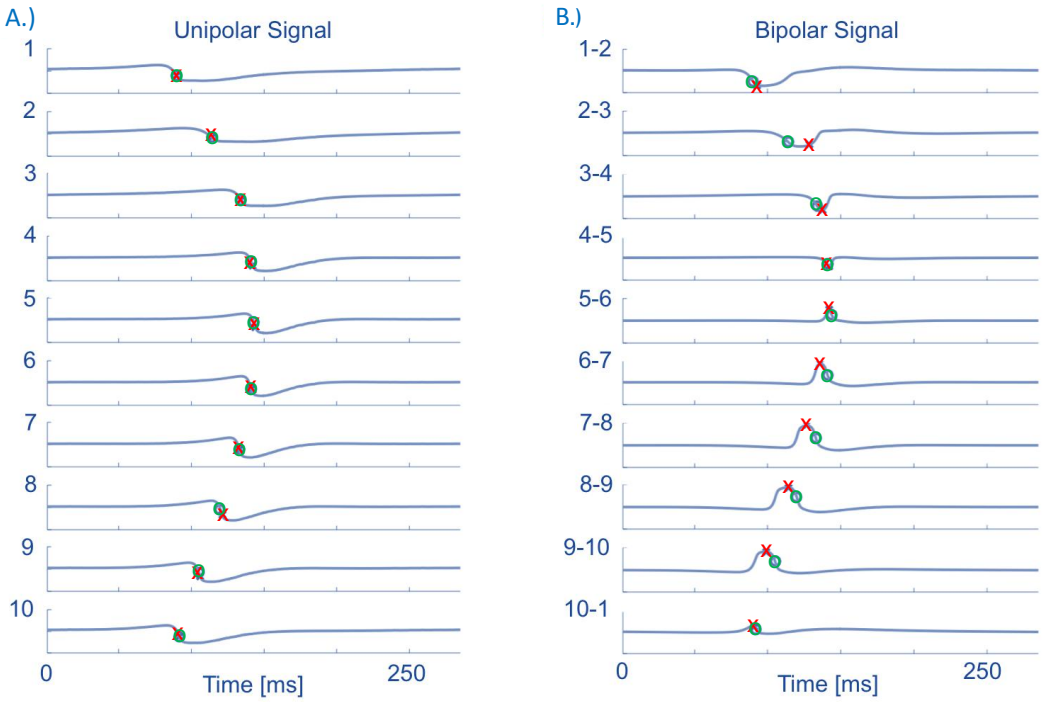

Figure 4.2: Unipolar and bipolar example recordings of stable rotational activity in a 3D patch. Calculations of the LAT parameter with the steepest negative slope (green) and the NLEO (red) in (A) unipolar and (B) bipolar recordings. The figure is adapted from [S5] [117] [117].

4.2.1.2 Cycle length coverage

The cycle length coverage (CLC) was defined as the difference between the first and the last activation time within one cycle length divided by the cycle length [135].

$$CLC = \frac{LAT_{First} - LAT_{Last}}{CL} \tag{4.2}$$

A Lasso catheter centered at the rotor tip measured high CLC of nearly 90%, and faraway Lasso catheter measured significant reduced CLC (cf. Figure 4.3).

4.2.1.3 Calculation of conduction velocity

The conduction velocity and direction of propagation could be calculated by the cosine fit method [113] in the case of planar waves measured with a circular catheter (cf. Figure 4.4 (A)). The cosine pattern was fitted between the bipolar local activation

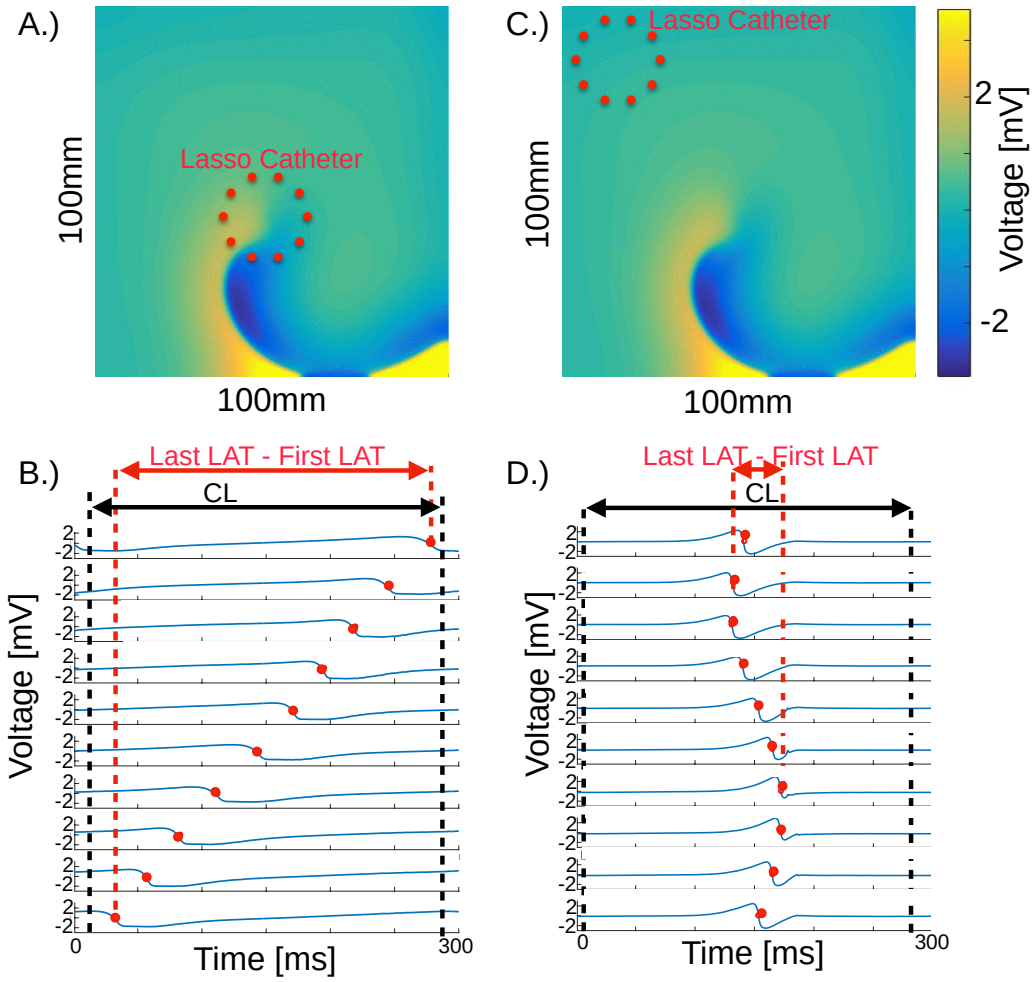

Figure 4.3: Voltage map and Lasso catheter centered at the rotational core (A). (B) LAT line pattern of Lasso in (A). Calculations of CLC = 90%. (C) Voltage map and Lasso catheter positioned at a distance to the rotational core. (D) LAT line pattern of Lasso in (C). The figure is adapted from Rottmann et al. (2014) [107], Rottmann et al. (2015) [115], [117] [118], [S5].

times detected. From the amplitude *A* and phase of the fitted cosine pattern (cf. Figure 4.4 (B)), the conduction velocity could be calculated [113].

An example of the conduction velocity calculations of a non-regular arrangement is shown in Figure 4.5 (A). The conditions necessary for calculating a conduction velocity vector are three electrodes which detect three LATs. Figure 4.5 (B) presents the equations for calculating the conduction velocity from the activation times detected in the case of a regular grid catheter. The gradient functions are described in the formulas in Equations 4.3 and 4.4.

Regular electrode arrangements:

$$grad_x = \frac{LAT_{i+1,j} - LAT_{i-1,j}}{2d}. \tag{4.3}$$

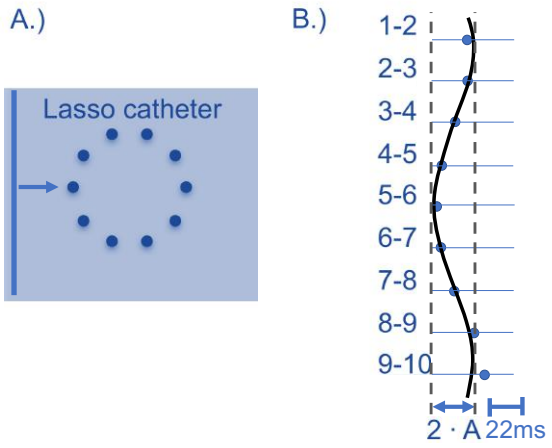

Figure 4.4: Determining the conduction velocity by the cosine fit method. (A) Planar wave measured with the Lasso catheter, (B) cosine patterns fitted between the bipolar activation times. The figure part A is adapted from [S5] [117] [118]. The figure part B is adapted from [113].

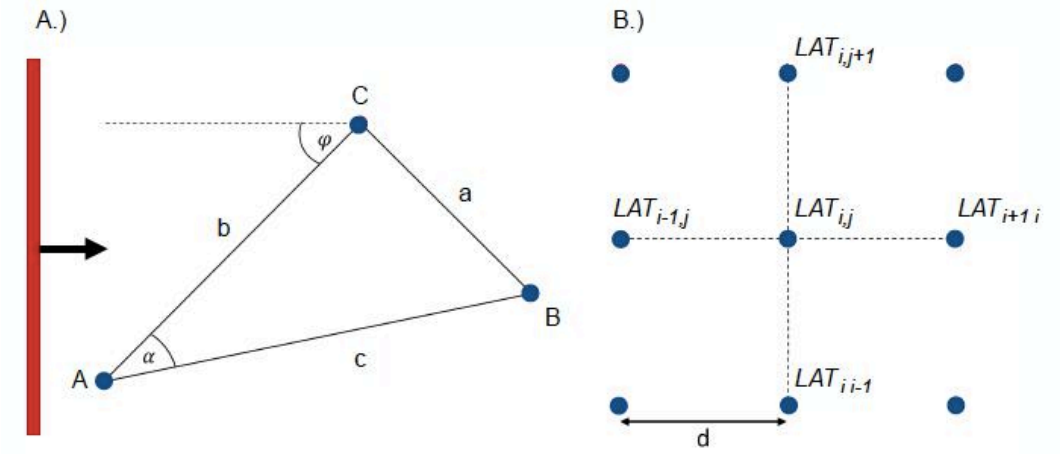

Figure 4.5: A) The triangulation method is illustrated by a planar wave measured by three electrodes for calculating the conduction velocity vectors. (B) A square catheter with regular electrode grid measures the activation times. The interelectrode distance is defined with the parameter *d*. The figure is adapted from [S8] [143].

$$grad_y = \frac{LAT_{i,j+1} - LAT_{i-1,j-1}}{2d}. \tag{4.4}$$

The resulting conduction velocity is defined in Equation 4.5:

$$CV = \frac{1}{\sqrt{grad_x^2 + grad_y^2}}. \tag{4.5}$$

Non-regular electrode arrangements:

The equations 4.6 to 4.8 describe the calculation of the conduction velocity dependent

on the activation time. The distances between two electrodes a, b, c are described in Figure 4.5 (A). The corresponding measured times at these distances are t_a, t_b and t_c.

$$\alpha = arccos\left(\frac{|b|^2 + |c|^2 - |a|^2}{2|b|^2|c|^2}\right) \tag{4.6}$$

$$\phi = arctan\left(\frac{t_c|b| - t_b|c|cos(\alpha)}{t_b|c|sin(\alpha)}\right) \tag{4.7}$$

$$CV = \left(\frac{|c|cos(\phi)}{t_c}\right) \tag{4.8}$$

4.2.1.4 Vector field processing

Vector field formulas for calculating the divergence and the rotation of the conduction velocities are defined with Equations 4.9 to 4.10.

$$div(CV) = \frac{\Delta CV_x}{\Delta x} + \frac{\Delta CV_y}{\Delta y} \tag{4.9}$$

$$rot(CV) = \frac{\Delta CV_y}{\Delta x} - \frac{\Delta CV_x}{\Delta y} \tag{4.10}$$

4.2.1.5 Intersection point method for determining the AF source locations

The intersections of the prolonged CV vectors were used for determining the focal source point (cf. Figure 4.6) (A). Rotor tip positions were determined by the intersection points of the CV vector verticals (cf. Figure 4.6) (B).

4.2.2 Amplitude and morphology-based methods

4.2.2.1 Peak-to-peak amplitude and RS difference

The peak-to-peak amplitude was calculated by adding the positive peak R to the absolute of the negative peak S. For analyzing the signal morphologies, the RS-ratio parameter [111] [112] was used (cf. Equation 4.11).

$$RS - ratio = \frac{|R| - |S|}{|R| + |S|}. \tag{4.11}$$

Statistical analyses for the RS-ratio of different AF complexities (Type I, Type II, Type III) are shown in Figure 4.7.

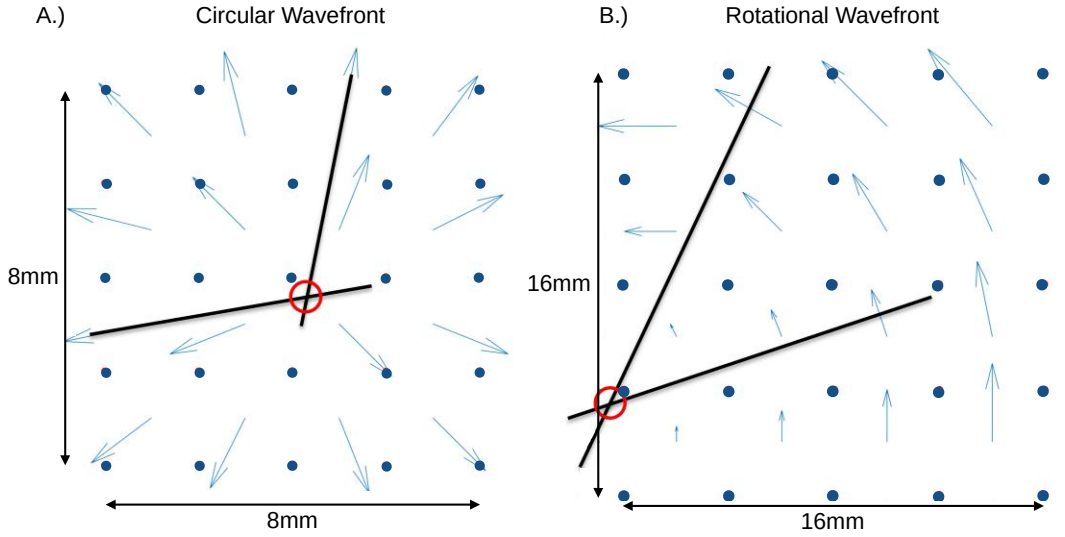

Figure 4.6: (A) Detection of the focal source location by intersections (marked in red) of prolonged CV vectors (marked in blue). (B) Detection of the rotor tip position by intersections of prolonged CV vector verticals. The electrode positions are marked with blue dots. The figure is adapted from [S8] [143].

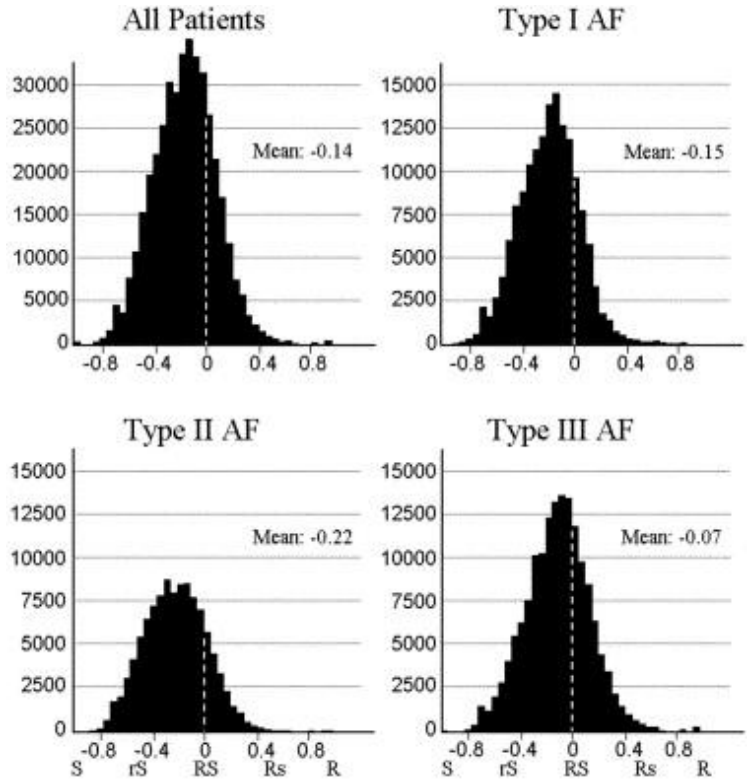

Figure 4.7: Statistical analysis of the RS-ratio parameter (Type I, Type II, Type III) calculated from clinical recordings. The figure is from [111] with permission.

4.2.2.2 Approximate entropy

The approximate entropy was introduced by Pincus [144] in the year 1991 for the determining the regularity of statistical data. The approximate entropy value increases with increasing irregularity of the signal. Standard parameters (ApEn(2, 0.1,500)) were used in the literature [136] [107] [115] for the detecting rotor centers. The following calculation steps 1 to 6 (adapted from [144][145]) describe, how to calculate the approximate entropy.

step1:
The signal X=[x(1),x(2),...x(N)] is embedded in an m-dimensional subspace,

$X_m(i) = [x(i), x(i+1), ..., x(i+m-1)]$,

$1 <= i <= N-m+1$,

m is 2 in this study.

step2:
The scaling range r is calculated with

r= g x SD,

the coefficient of tolerance was 0.1,

SD is the standard deviation of the time series X.

step3:
The maximal absolute difference $d[X(i), X(j)]$ between $X(i)$ and $X(j)$ in corresponding element is calculated with

$$d[X(i), X(j)] = \max_{k=0,...,m-1}(|x(i+k) - x(j+k)|)$$

.

step4:
The values of $d[x(i),x(j)]$ <r were recorded as C_i and $C_i^m(r)$ = $\frac{C_i}{N-m+1}$.

step5:
Define: $\Phi^m(r)$ = $\frac{1}{N-m+1}\sum_{i=1}^{N-m+1} ln\, C_i^m(r)$.

step6:
The embedded dimension increases to $m+1$ and $\Phi^{m+1}(r)$ is calculated.

The approximate entropy is calculated with the equation

$$ApEn(m,r) = \lim_{n\to\infty}[\Phi^m(r) - \Phi^{m+1}(r)].$$

4.2.2.3 Near-field effects

During persistent AF, different multiple rotational, focal, and wavelet activities interact and result in multiple overlapping near-fields. Especially in low voltage areas, those near-field effects strongly impact the resulting signal recordings measured by electrodes. At focal exits and functional and non-functional blocks, near-field effects were measured (cf. Figure 4.8 (B)). Furthermore, the electrical fields above the fibrotic region were overlapped by large near-fields from healthy tissue. Figure 4.8 (A) shows an example of overlapping electrical fields that was shielded by a plate.

4.2.3 Hilbert phase-based methods

4.2.3.1 Hilbert phase

The Hilbert phase $\varphi(t)$ is used to determine phase singularities and rotor center trajectories during fibrillation. The Hilbert phase was calculated using the Equations 4.12 to

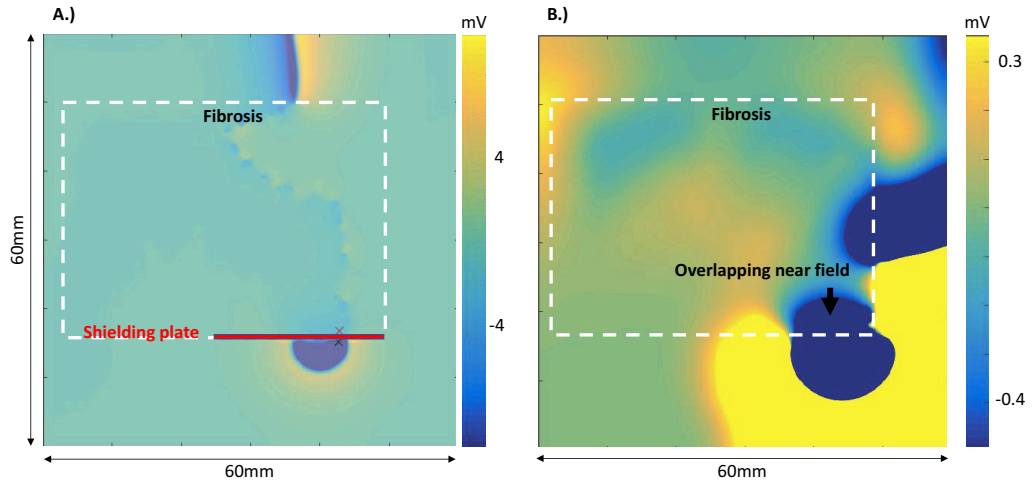

Figure 4.8: Near-field analysis. (A) Near-field analysis with shielding, in which the amplitude ranges between 1 mV and -1 mV. (B) Near-field analysis without shielding, in which the amplitude ranges between 0.3 mV and -0.4 mV. Without shielding, electrical fields from the healthy tissue region overlap the small electrical fields above the fibrotic region.

4.13 with the analytic signal z(t) [146] [147]. Phase singularity points are surrounded by phase progresses between $-\Phi$ and Φ [148].

$$z(t) = \tilde{y}(t) + jH\{\tilde{y}(t)\} \tag{4.12}$$

$$\varphi(t) = arctan\left(\frac{imag\{z(t)\}}{real\{z(t)\}}\right) \tag{4.13}$$

4.3 Results

4.3.1 Results of developed LAT-based methods

4.3.1.1 Activation patterns measured at the rotational activity

The activation time patterns of different catheter designs, Lasso, AFocusII, PentaRay, and square catheters, are analyzed in Figure 4.9 during stable rotational activity.

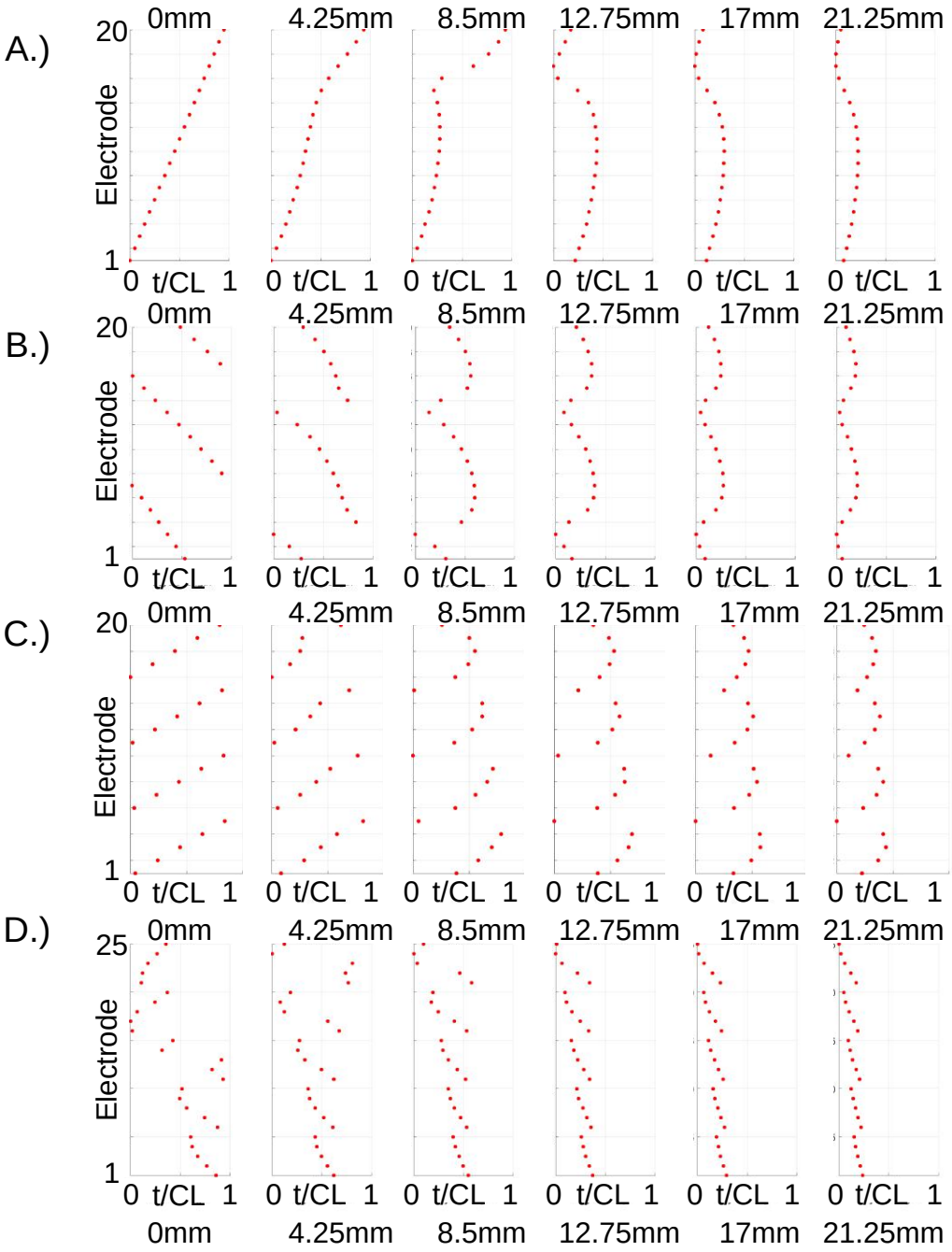

Figure 4.9: LAT patterns of (A) Lasso catheter (20 electrodes and diameter of 20mm), (B) AFocusII (20 electrodes and diameter of 20mm), (C) PentaRay (25 electrodes and diameter of 35mm), and (D) square catheter (5x5 electrodes and 4mm interelectrode distances) at different distances to the rotational activity center, which were 0 mm, 4.25 mm, 8.5 mm, 12.75 mm, 17 mm, and 21.25 mm. The figure is adapted from [S8] [143].

These patterns show the reduction of the CLC with increasing distance to the center of the rotational activity as depicted in Figure 4.10. The cycle length coverage of the different catheter designs depends on their various distances to the rotational core as presented in Figure 4.10.

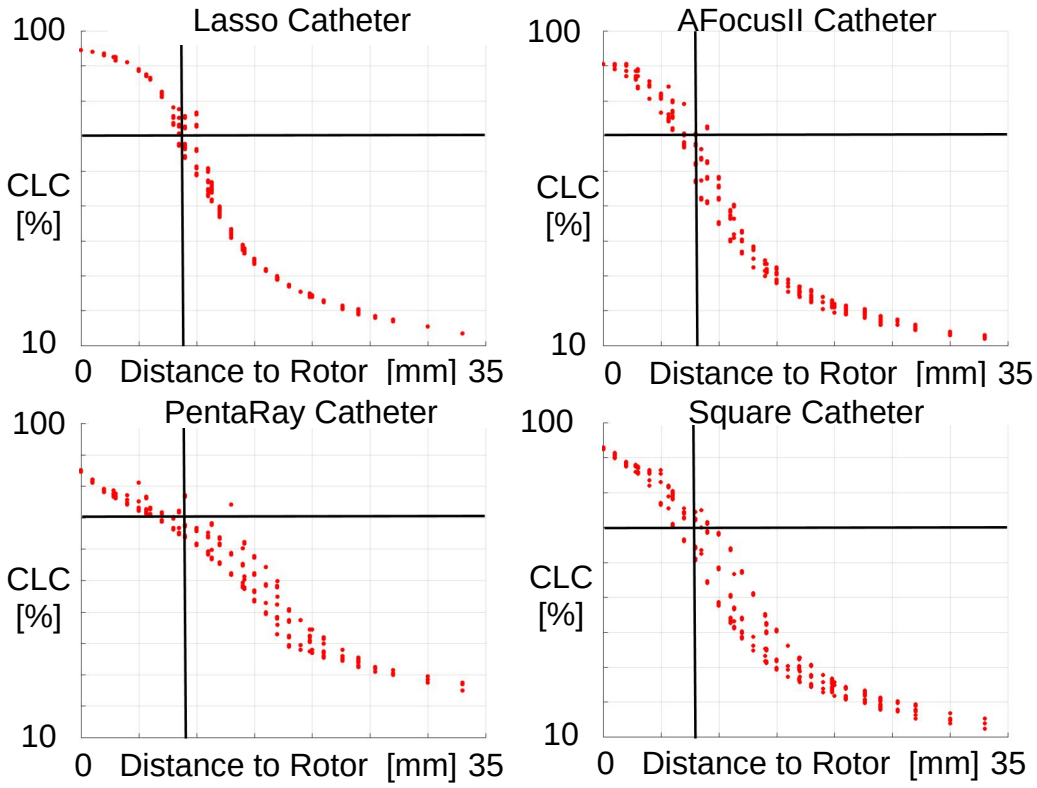

Figure 4.10: Cycle length coverage dependent on different distances between the catheter center and the rotor tip position. Measurements with (A) the Lasso catheter (20 electrodes and diameter of 20mm). (B) AFocusII catheter (20 electrodes and diameter of 20mm). (C) PentaRay catheter (25 electrodes and diameter of 35mm) and (D) Square catheter (5x5 electrodes and 4mm interelectrode distances). The figure is adapted from [S8] [143].

4.3.1.2 Activation patterns at the focal sources

Figure 4.11 presents the activation patterns of different catheter designs measured at the ideal focal activity. Notably, centered at the focal source, the same activation times were measured with the Lasso catheter (cf. Figure 4.11 A (Left)).

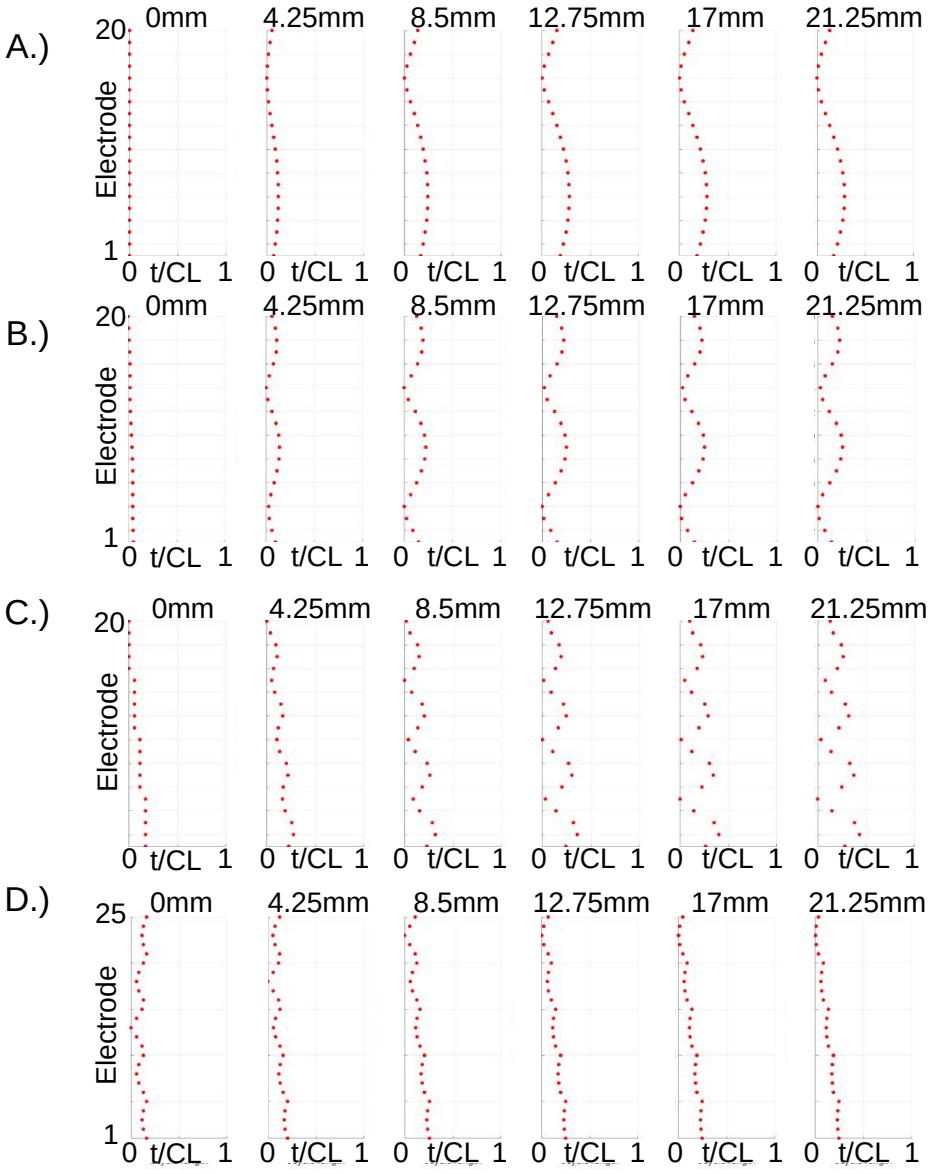

Figure 4.11: LAT patterns at the focal activities of (A) Lasso catheter, (B) AFocusII, (C) PentaRay, and (D) square catheter at different distances to rotational activity center, which were 0 mm, 4.25 mm, 8.5 mm, 12.75 mm, 17 mm, and 21.25 mm. The figure is adapted from [S8] [143].

4.3.1.3 Activation patterns at the collisions

Figure 4.12 presents the activation patterns of different catheter designs measured at the collision of two ideal planar waves.

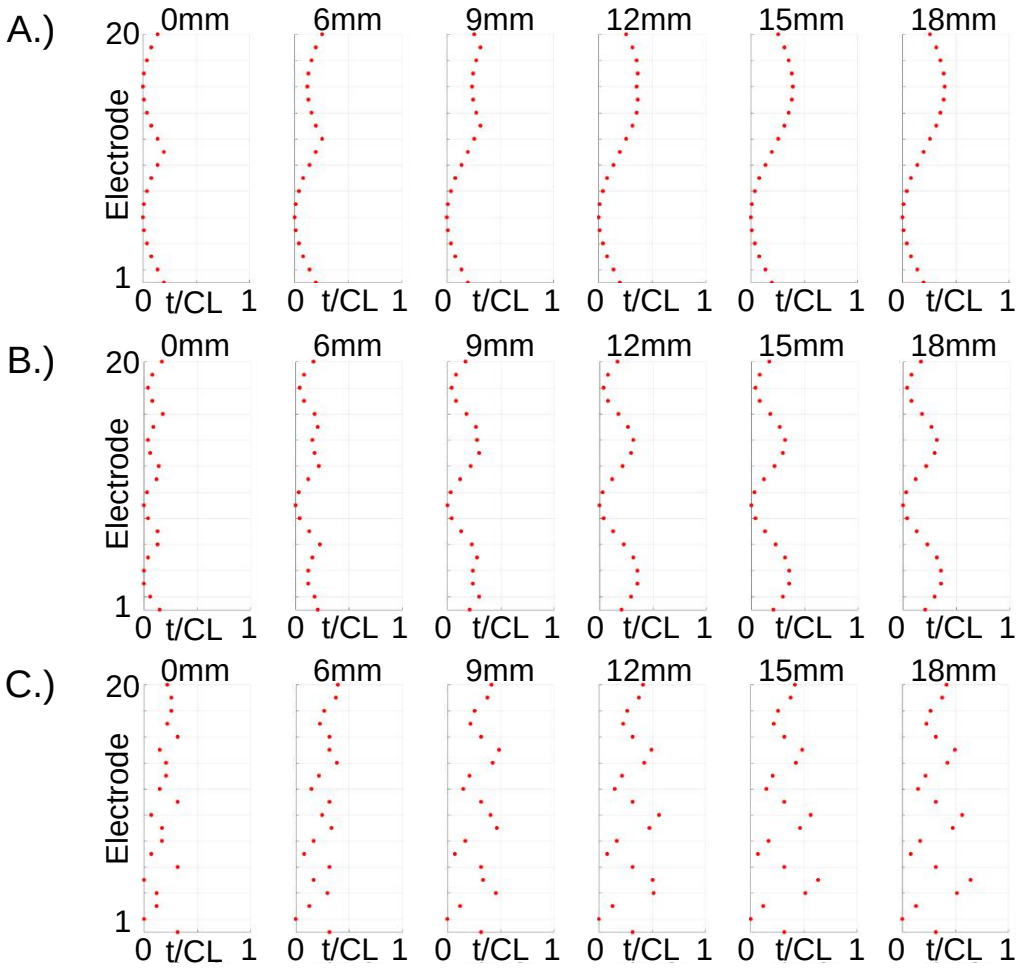

Figure 4.12: LAT patterns at the collision of two planar waves measured with (A) Lasso catheter, (B) AFocusII, (C) PentaRay, and (D) square catheter at different distances to the rotational activity center, which were 0 mm, 4.25 mm, 8.5 mm, 12.75 mm, 17 mm, and 21.25 mm. The figure is adapted from [S8] [143].

4.3.1.4 Characteristic LAT patterns of mapping catheters in different distances between catheter center and rotational core

Characteristic LAT patterns of the commonly used circular catheter are presented in Figure 4.13 for different distances between the catheter center and the rotor center position. If the catheter was centered at the rotational core, the LAT pattern became a line pattern (cf. Figure 4.13 (B)).

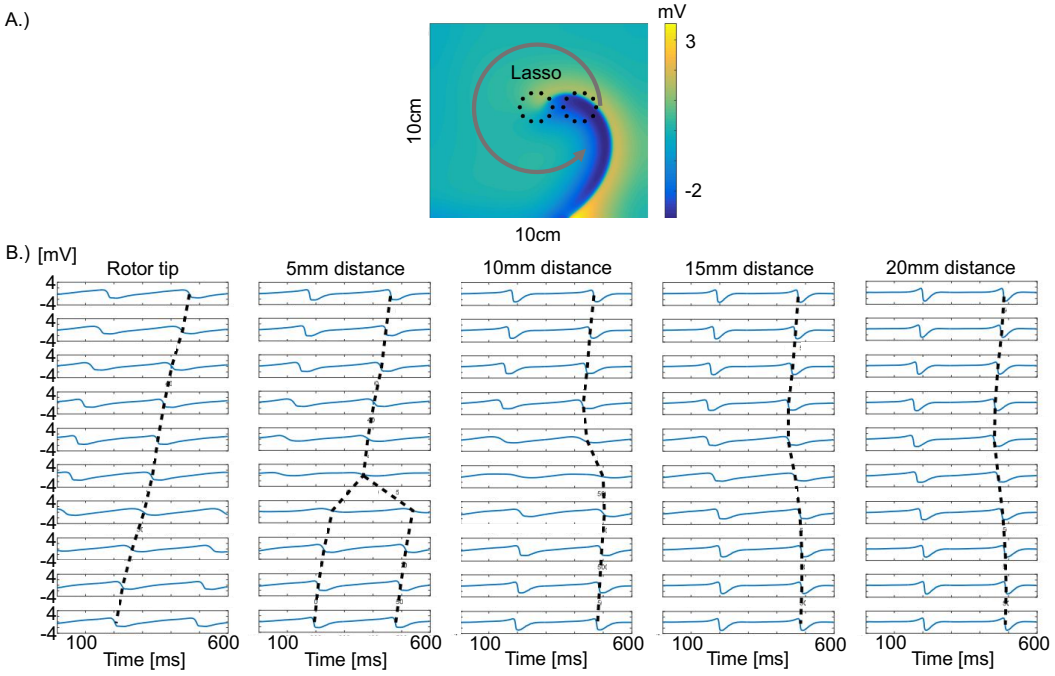

Figure 4.13: Lasso catheter centered at the rotational core and at 20 mm distance. (A) Voltage map with Lasso catheters centered at and at 20 mm distance to rotational core. (B) LAT patterns of the Lasso catheter in 0 mm, 5 mm, 10 mm, 15 mm, and 20 mm distance to rotational core. The figure is adapted from Rottmann et al. (2014) [107], Rottmann et al. (2015) [115] © IEEE [2015] with permission.

4.3.1.5 Rotational activity in realistic 3D atria

AF was induced in the atrial geometry model [134] in Figure 4.14 by ectopic foci. The AF simulation model resulted in stable and unstable rotational activities in the left and in the right atrium with colliding wavefronts (cf. Figure 4.14). In the left atrium, an unstable rotor was detected and at the right atrium, a stable rotor. The trajectories of the stable and unstable rotor centers were calculated with phase singularities. Phase maps over a time period of 200 ms are presented in Figure 4.14.

4.3.1.6 Signal characteristics at rotational activities in the realistic 3D atria

The stable rotational activity had a cycle length of 145 ms in a region of 3 mm x 1.5 mm at the right atrium close to the tricuspid valve. The trajectory of the unstable rotor in the left atrium covered an area of 10 mm x 4 mm. The unstable rotational activity had a cycle length of 190 ms.

4.3.1.7 Excitation patterns of circular catheters

The measurements of the Lasso catheter centered on the stable rotational activities resulted in nearly straight line patterns Figure 4.15 (A) between the activation times of each electrode with cycle length coverage > 70%. LAT patterns of the stable and unstable rotational activities in the realistic atrial model are shown in the following Figure 4.15.

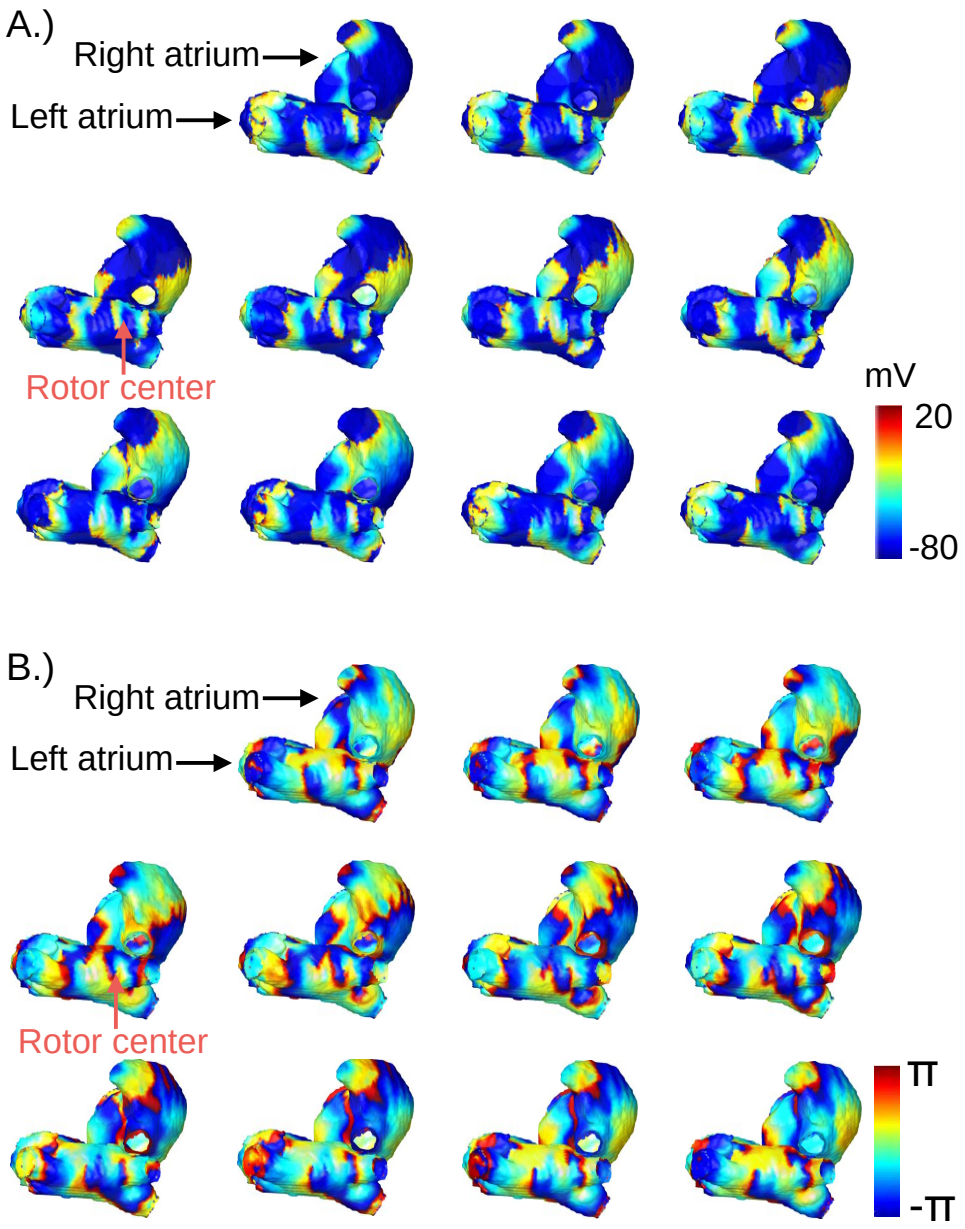

Figure 4.14: (A) Transmembrane voltage maps of rotational activities in a personalized model with included fiber orientation over a period of 200 ms. (B) Hilbert phase maps of rotational activities in a personalized model with included fiber orientation in a time period of 200 ms, compare transmembrane voltage maps (reference) in figure part A.). Rotor center at phase singularity point is marked in red. The figure is adapted from [S1], [149], [115], [150].

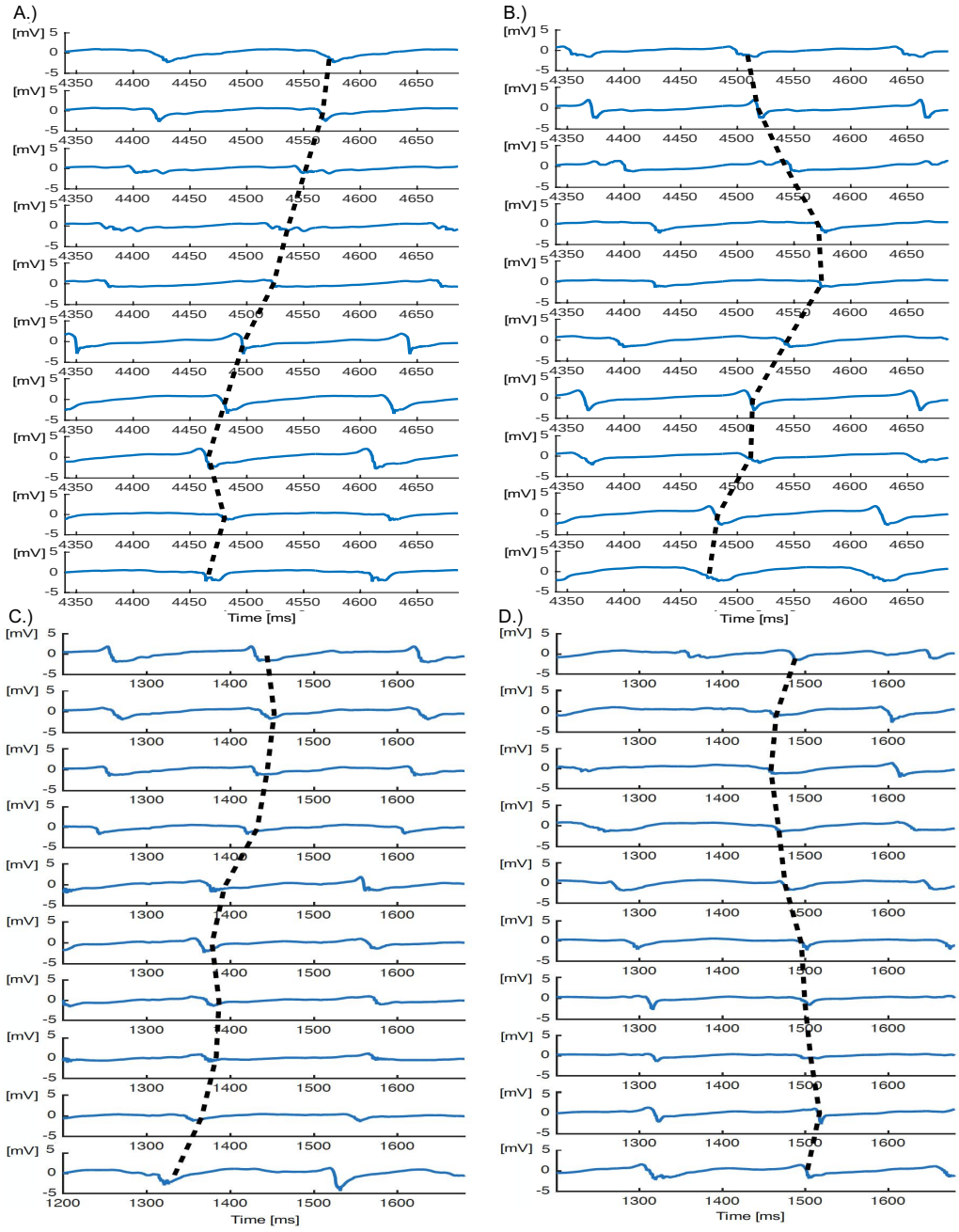

Figure 4.15: LAT pattern of the Lasso catheter (A) centered at stable rotational activity and (B) distant to the rotational activity in the realistic atrial geometry model. LAT pattern of the Lasso catheter (C) centered at unstable rotational activity and (D) distant to the rotational activity. The figure is adapted from [115] © IEEE [2015] with permission.

4.3.2 Development of an automatic cycle length coverage detection

4.3.2.1 Automatic cycle length calculation

For automatically calculating the CL, the following workflow was investigated. First, the frequency spectrum of the limited time signal was measured with the FFT and then upsampled to the next power of 2 (cf. Figure 4.16). Further, a modified spectrum was created by adding the next five harmonics to each frequency. The dominant frequency was found at the maximum of the spectrum. This workflow was repeated for each electrode.

The parameter CL was automatically calculated from the automatically dominant frequency calculation, of which the workflow is shown in Figure 4.17. First, the signal was limited to the inverse of the calculated dominant frequency, and the parameter LAT was found with the steepest negative slope in this time window. The next time window was set starting with the LAT_1 determined for the time window of the inverse of the dominant frequency, multiplied by the factor of 1.3. Then the next LAT_2 was determined in this time window. The resultant CL was defined as LAT_2 minus LAT_1.

4.3.2.2 Automatic cycle length coverage calculation

The automatic CL calculations were strongly dependent on the time window chosen. Therefore, the LAT patterns were sorted into the correct time window in the following workflow diagram (cf. Figure 4.18 A.)). An example of the algorithm results is shown in Figure 4.18 (B, D0-D9).

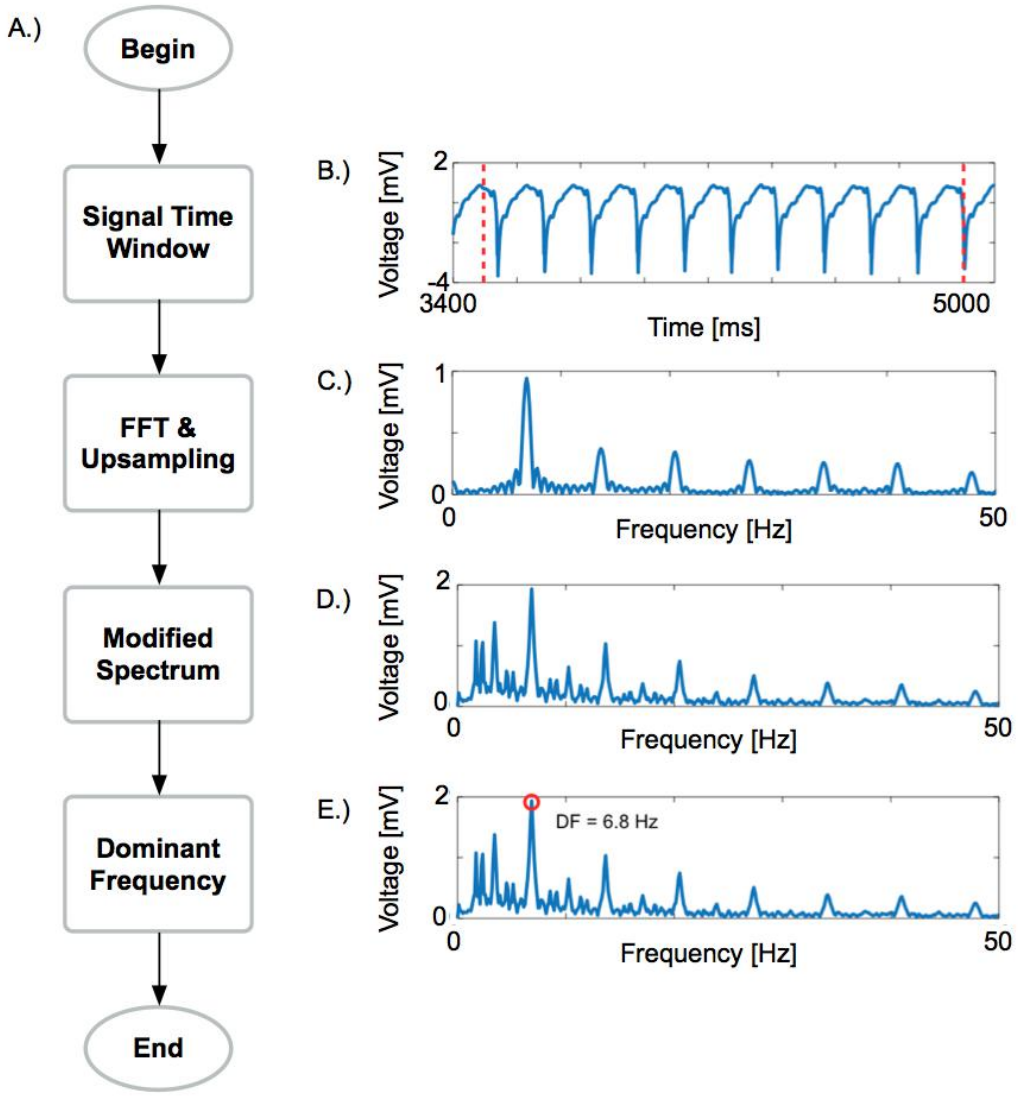

Figure 4.16: (A) Workflow of the dominant frequency calculation. (B) Signal time window. (C) Spectrum calculated with FFT and upsampling. (D) Modified spectrum. (E) Determined dominant frequency (marked). The figure is adapted from [S5], [117], [118].

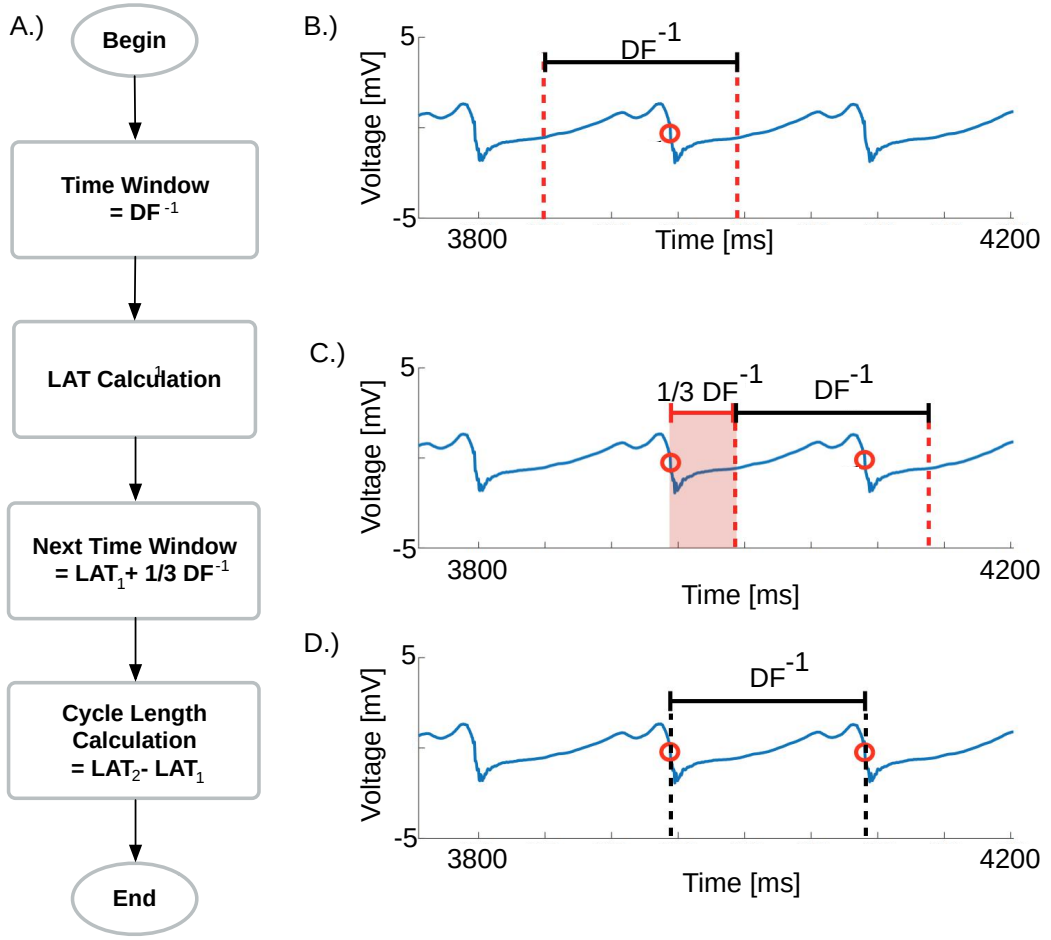

Figure 4.17: A.) Workflow of automatically CL calculations. (B.) Time windows, parameter LAT_1 (marked) in the example signal. (C.) Next time window with the start at the time point of the determined LAT plus $\frac{1}{3}$ of the inverse of the dominant frequency. Calculated LAT_2 within the new time window. (D.) Determined cycle length based on calculated LATs. The figure is adapted from [S5], [117], [118].

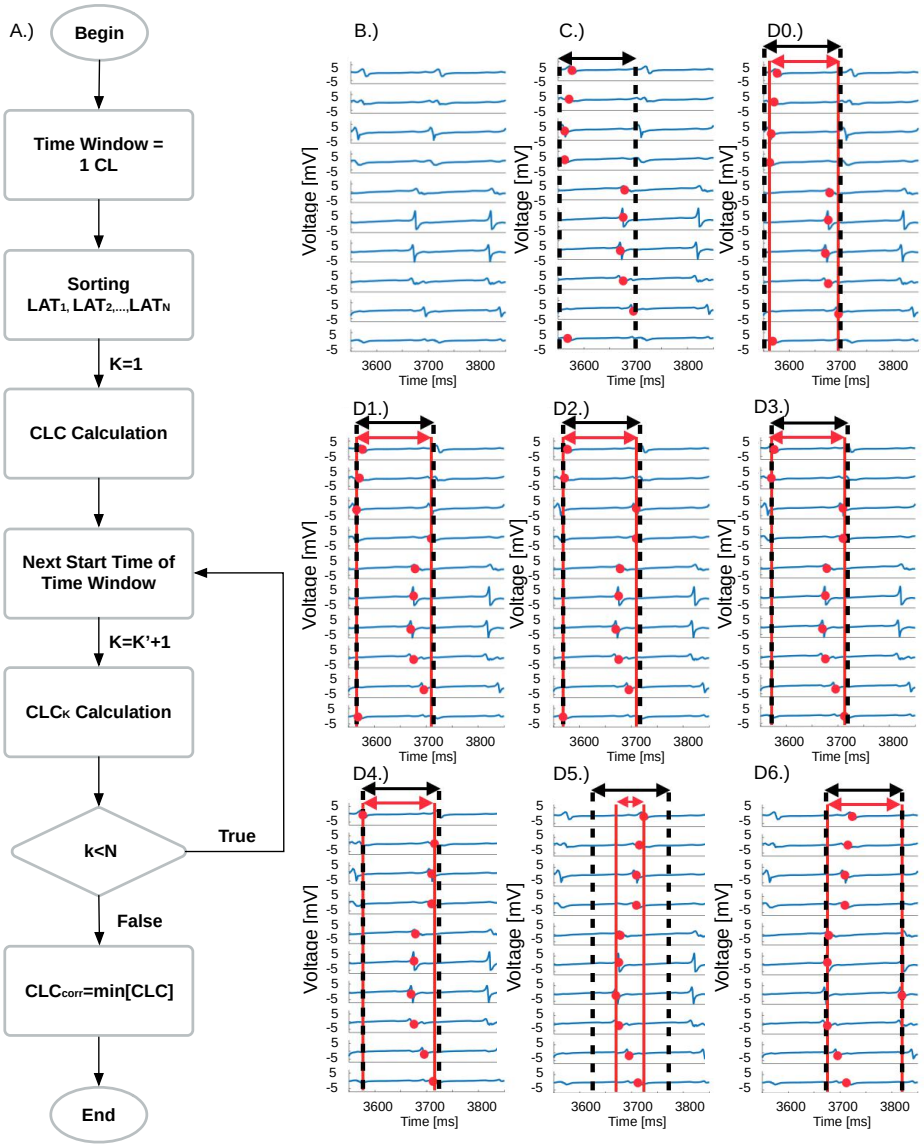

Figure 4.18: A.) Workflow of calculating the correct CLC by sorting and choosing the correct time window. Algorithm results of the automatic calculation of the correct CL with the Lasso catheter. (B) Example of unipolar signal recordings. (C) Initial time window. (D0) to (D9): Calculations of the CL within time for all 10 possible time windows between the first and last activation. D5 represents the correct CLC with minimal time between the first and last activation within time window. The figure is adapted from [S5], [117], [118].

4.3.2.3 Calculation of cycle length fluctuation

The cycle length fluctuation (CLF) parameter was used to determine the stability of the excitation pattern measured. Stable rotational activities resulted in small values in measurements with CLF. Larger CLF values were measured in moving unstable rotational activities. The workflow of the calculation steps for the parameter CLF is depicted in Figure 4.19. First LAT was detected within the calculated time window determined by the calculated CL (cf. Figure 4.19(B)).

The next time window started at the time point of the determined first LAT plus $\frac{1}{3}$ of the the inverse of the dominant frequency (cf. Figure 4.19(C)). The cycle length was calculated as time difference between the second and first LAT (cf. Figure 4.19(D)). In the last step, the differences of the cycle lengths were calculated (cf. Figure 4.19(E)).

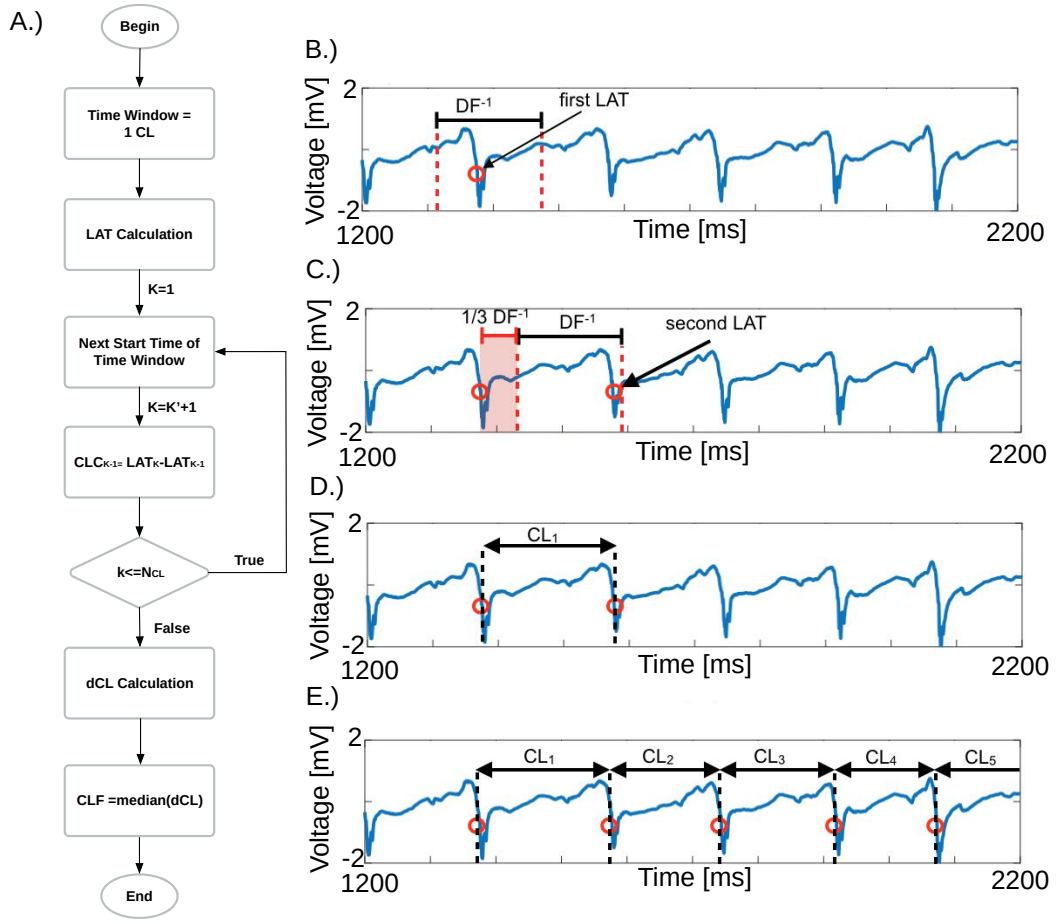

Figure 4.19: (A) Workflow of calculations of cycle length fluctuation. (B) Example signals of calculation steps, CL time window based on inverse of the dominant frequency and determined first LAT within the time window. (C.) Calculating next time window and second LAT with the start at the time point of the determined LAT plus $\frac{1}{3}$ of the inverse of the dominant frequency. D.) Determining the CL from the two detected LATs. (E.) Cycle length differences over time. The figure is adapted from [S5], [117], [118].

4.3.2.4 Calculation of the dominant frequency parameter

In this simulation study, the dominant frequency parameter was used for calculating the parameters CL and CLC. The Figure 4.20 (A) shows an example of unipolar signal recordings measured with the virtual Lasso catheter (10 electrodes in equal spacing, diameter of 20 mm) sampled with 2000 Hz. The FFT spectra calculated with upsampling resulted in the dominant frequency of 6.8 Hz (electrode 2-4). The inverse of the dominant frequency was 147 ms (cf. Figure 4.20).

The Figure 4.20 shows the resultant spectra without Figure 4.20 (B) and with upsampling Figure 4.20 (C). The resulting DFs were 6.8 Hz and the inverse was 147 ms. Adding the next five harmonics to the frequencies the spectra in Figure 4.20 (D,E) resulted in additional upsampling and showed an optimized spectrum.

The resulting spectra with upsampling and additional added harmonics are presented in Figure 4.20 (F,G).

4.3.2.5 Cycle length coverages of catheter designs dependent on distances between catheter center and rotational core.

At the idealized rotational activity in a 3D patch, the parameter CLC was measured with different catheters and at different distances to the core of the rotational activity (cf. Figure 4.21).

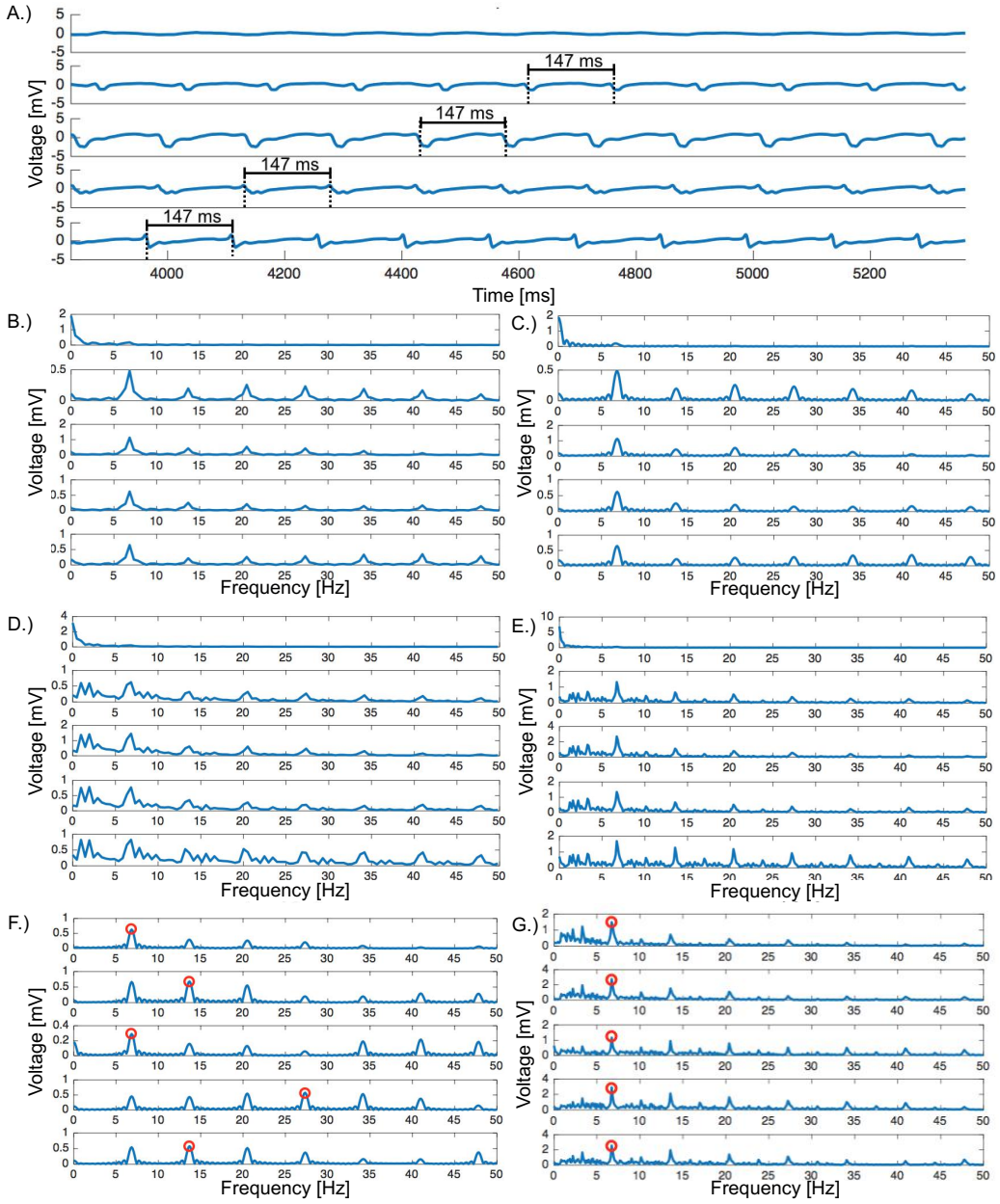

Figure 4.20: A.) Unipolar signal recordings of the Lasso catheter (10 electrodes in equal spacing, diameter of 20 mm) measured with the sampling rate of 2000 Hz. Calculated frequency spectra. (B) Spectrum for the signal recordings in Figure 4.20 without upsampling (3000 values). (C) Spectrum calculated from signal recordings with upsampling (16384 values). (D) Spectrum calculated by adding the next five harmonics to every frequency. (E) Spectrum calculated from the sum of frequencies and next five harmonics with upsampling. (F) Spectra of the bipolar signal recordings (figure part (A)) with upsampling. The dominant frequency values calculated are marked. (G) Upsampling and additional added harmonics resulted in correct dominant frequency values (marked). The figure is adapted from [S5], [117], [118].

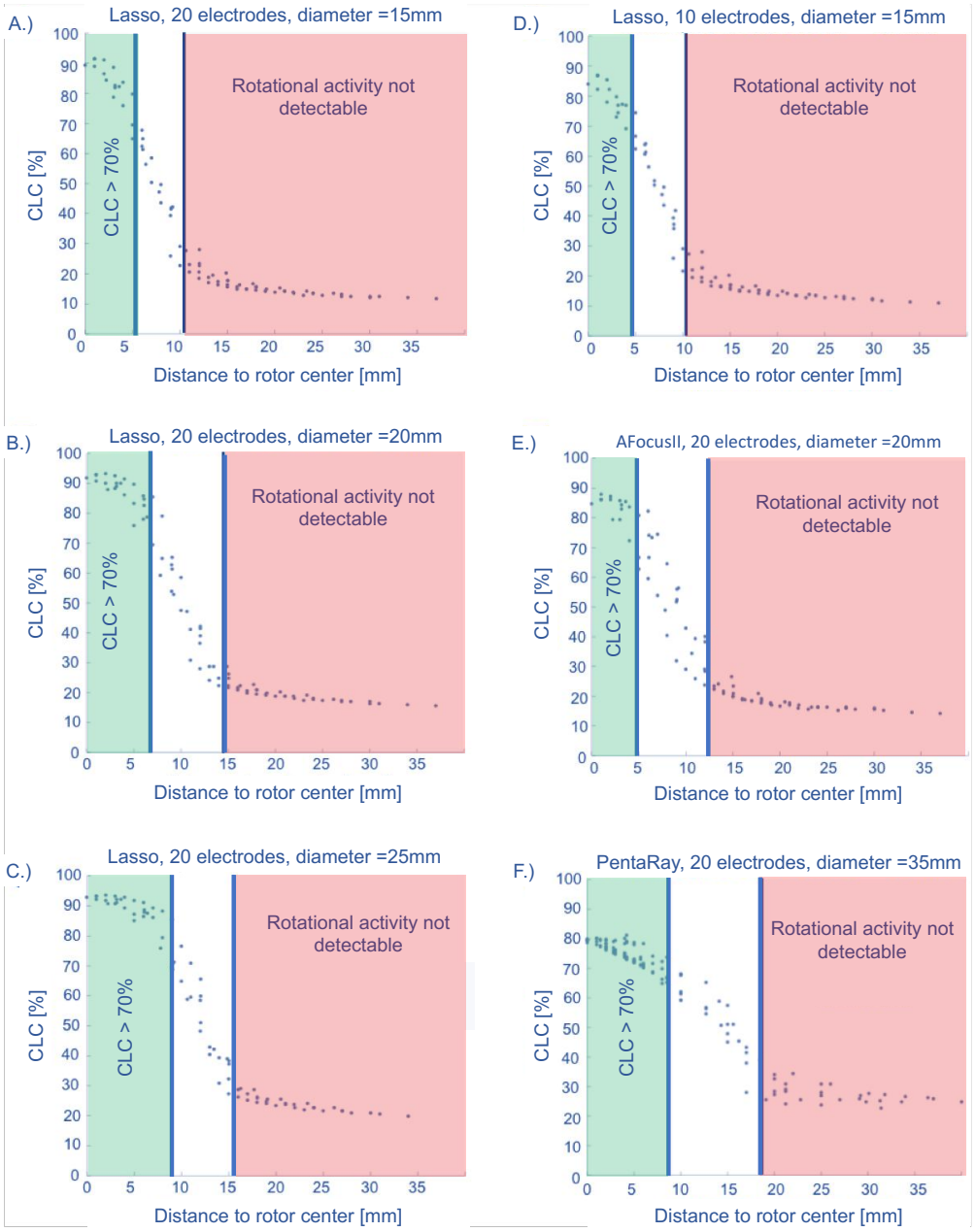

Figure 4.21: Cycle length coverages of catheter designs measured dependent on distances between catheter center and rotational core at stable rotational activity in a 3D patch. Rotational activity can be detected at distances of CLC > 70% (marked in green with border at lowest CLC=70%) in the case of the PentaRay catheter (> 60%). Distances with no further significant variances of the parameter CLC were marked in red. CLC calculations of (A) a Lasso catheter (20 electrodes, diameter 15 mm), (B) a Lasso catheter (20 electrodes, diameter 20 mm), (C) a Lasso catheter (20 electrodes, diameter 25 mm), (D) a Lasso catheter (10 electrodes, diameter 15 mm), (E) an AFocusII catheter (20 electrodes, diameter 20 mm), (F) a Lasso catheter (20 electrodes, diameter 35mm). The figure is adapted from [S5], [117], [118].

In the more realistic case of the 3D atrial geometry model with stable and unstable rotational activities, more irregularities were measured at the parameter CLC dependent on distance to the rotational core (cf. Figure 4.22). In the more realistic geometry models of rotational activities, higher values for parameter CLC were calculated also at a larger distance to the core of the rotational activity. The larger CLC values measured even at distant places to the rotational core were caused by wave collisions and other disturbing effects.

Signal recordings measured with the Lasso catheter (10 electrodes) at a larger distance to the rotational core (12mm) is shown in Figure 4.22 C.). This example illustrates that necessary conditions for the detection of rotational activities are, on the one hand, the parameter CLC > 70% and, on the other hand, the typical activation line pattern.

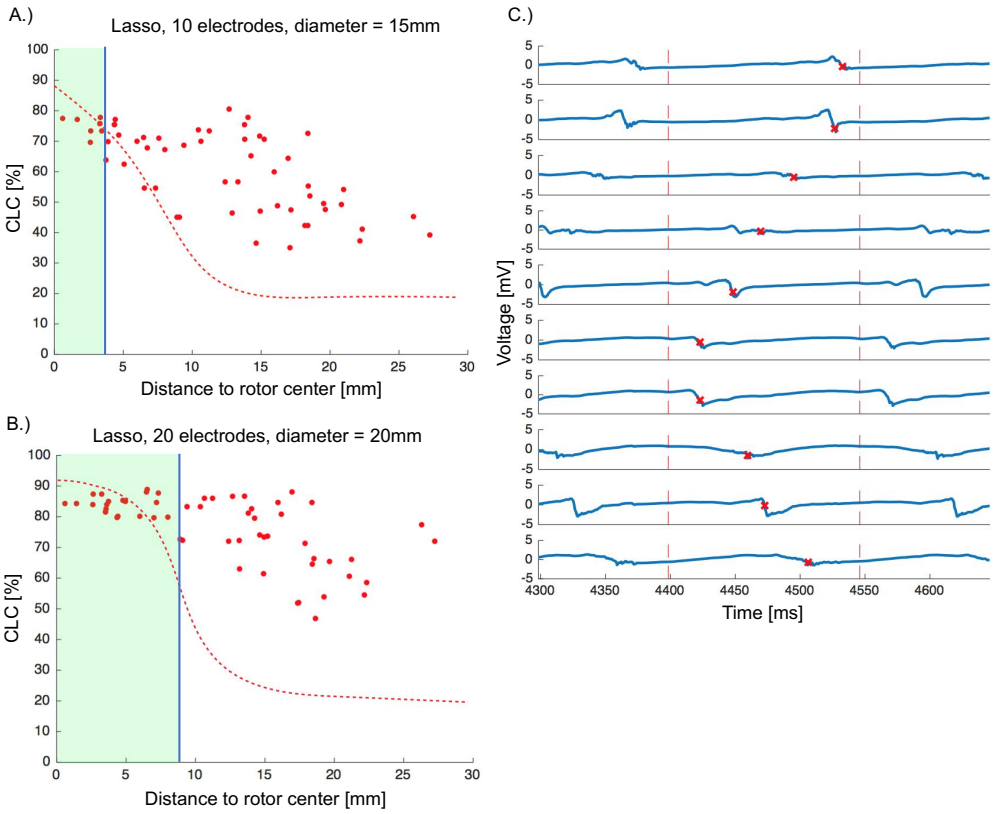

Figure 4.22: CLC measured at rotational activity in realistic 3D atrial model (dots) in comparison to reference results from an ideal rotor in a 3D patch (dashed line). CLC was measured with (A) a Lasso catheter (diameter 15 mm, 10 electrodes) and (B) a Lasso catheter (diameter 20 mm, 20 electrodes). (C) Measured unipolar recordings from a Lasso catheter (10 electrodes) that was placed at a distance of 12 mm to the rotational core. The calculated CLC was 75%. The figure is adapted from [S5], [117], [118].

4.3.2.6 Statistical analysis of cycle lengths calculated in the 3D atrial model

Statistical CL analyses were conducted of regions with stable (cf. Figure 4.23(A)) and unstable rotational activities (cf. Figure 4.23(B)). Additionally, other regions were analyzed for reference (cf. Figure 4.23(C)).

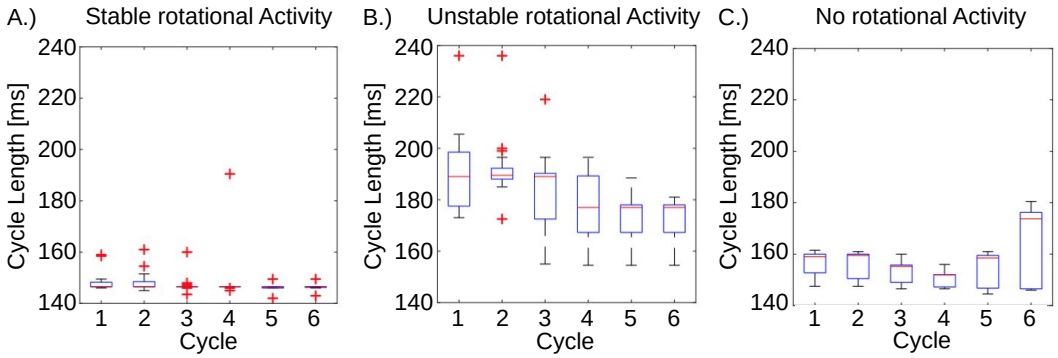

Figure 4.23: Statistical analysis of CL measured with the Lasso catheter (diameter of 20 mm, 20 electrodes), measured for a time duration of 6 cycles. (A) CL analysis of the centered Lasso catheter at stable rotational activity and (B) at the unstable rotational activity. (C) CL analysis of the Lasso catheter placed on other regions. The figure is adapted from [S5], [117], [118].

The statistical analyses of the CLs showed significant differences between stable and unstable rotational activities. Stable rotational activities resulted in small variances of CLs. In contrast, CLs at unstable rotational activities resulted in large CL variances.

The parameter CL detected with the Lasso catheter (20 electrodes, diameter 20 mm) for each electrode was calculated during a time period of 10 cycles with stable (cf. Figure 4.24 (A)) and unstable rotational activities (cf. Figure 4.24 (B)) in the 3D atrial model). For reference, also CLs of other regions with nearly planar waves were analyzed (cf. Figure 4.24 (C), (D)).

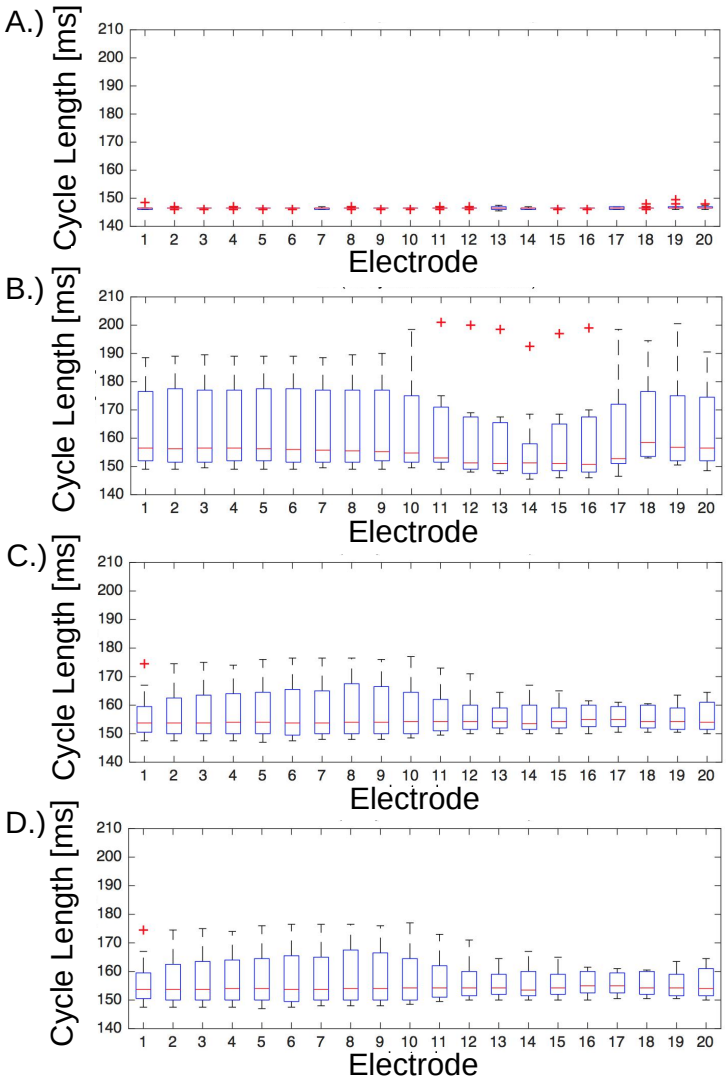

Figure 4.24: CLF calculated for the Lasso catheter (20 electrodes, diameter of 20 mm) at (A) stable rotational activity (mean CLF = 0.3ms) and at (B) unstable rotational activity (mean CLF = 4ms) in the 3D atrial model. Statistical CL analyses of planar waves measured with Lasso catheter (20 electrodes, diameter of 20 mm) at (C) the dorsal wall in the left atrium and at (D) the dorsal wall in the right atrium. The figure is adapted from [S5], [118].

A.)

SNR	CLC [%]	CLF [ms]
no noise	84.8	3.9
15dB	81.1 $\pm$2.6	4.0 $\pm$0.6
10dB	79.4 $\pm$2.9	4.7 $\pm$1.2
6dB	76.8 $\pm$4.1	7.2 $\pm$3.5
3dB	72.8 $\pm$8.5	16.5 $\pm$9.8

B.)

SNR	CLC [%]	CLF [ms]
no noise	37.5	3.4
15dB	37.5 $\pm$0.2	3.5 $\pm$0.3
10dB	37.5 $\pm$0.4	3.7 $\pm$0.6
6dB	37.5 $\pm$0.5	4.3 $\pm$1.0
3dB	37.5 $\pm$2.2	4.7 $\pm$1.2

Table 4.1: (A) Center of unstable rotational activity. Sensitivity analysis of the noise level (no noise, SNR = 15dB, SNR = 10dB, SNR = 6dB and SNR = 3dB) impact on the CLC determination with the low-pass filtered NLEO parameter. 200 LATs were taken in account. (B) Dorsal wall of the left atrium, far away from the rotor centers. CLC and CLF (mean value and standard deviation) dependent on added noise levels in the 3D atrial model. LATs were calculated with the low-pass filtered NLEO from unipolar recordings. The table is adapted from [S5], [118].

4.3.2.7 Sensitivity analysis of the CLC determination

The impact of added noise levels for CL calculations based on 200 measured LATs calculated with the NLEO parameter were analyzed (cf. Table 4.1). Table 4.1 (A) shows the resultant values of the CLC and CLF parameters dependent on added noise levels in the case of the unstable rotational activity in the realistic 3D atrial geometry model. The detected CLC was 84.8% and CLF was 3.9ms without added noise, and 72.8$\pm$8.5% and 16.5$\pm$9.8ms with added noise level (SNR of 3dB). In the case of measurements far away from the stable and unstable rotational activity at the dorsal wall (B), the detected CLC was 37.5% and CLF was 3.4ms without added noise, and 37.5$\pm$2.2% and the CLF was 4.7$\pm$1.2ms with added noise level (SNR of 3dB).

The impact of the filter setting and deviations from the LAT calculation were analyzed and shown in Figure 4.25.

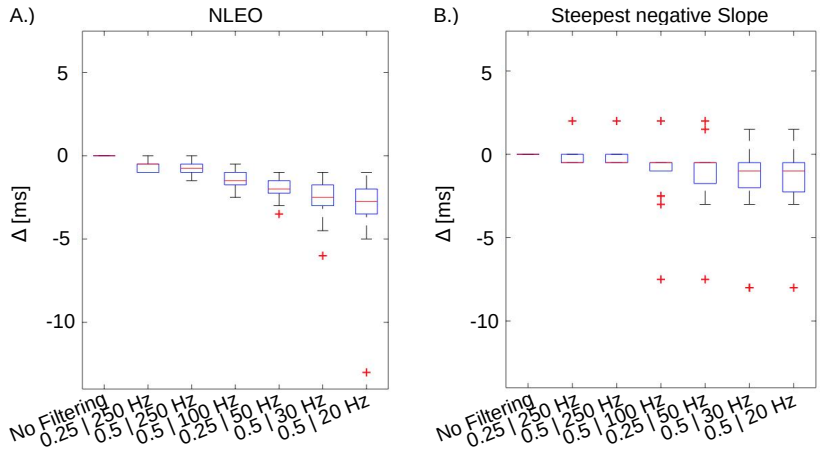

Figure 4.25: Impact of filters on the detection of LATs. Time deviations were calculated at different filter settings from LATs determined with (A) the NLEO parameter and (B) the steepest negative slope. The figure is adapted from [S5] [118].

4.3.3 Methods developed based on conduction velocity

The conduction velocity was calculated with a virtual square catheter measured at rotational and focal sources is shown in Figure 4.26. The conduction velocity was calculated by using the described method for CV calculations based on regular electrode grids, compare equation 4.5.

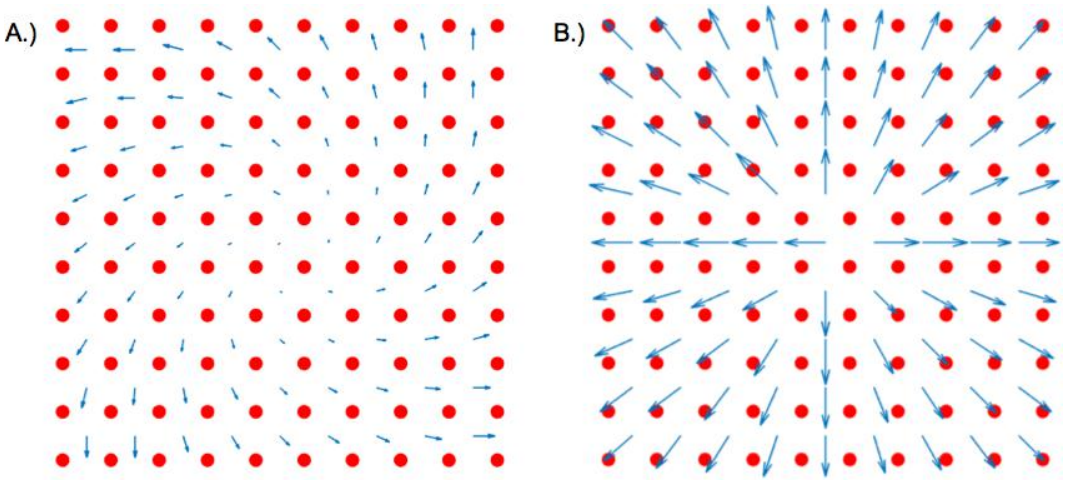

Figure 4.26: Conduction velocity vectors measured with virtual square catheter at (A) the rotational activity and (B) the focal source. The electrode localizations are marked in red. The conduction velocity vectors are marked in blue. The figure is adapted from [S8], [143].

4.3.4 Methods for the detection of AF excitation patterns based on curl and divergence

The curl and divergence methods were calculated with the square catheter in order to detect specific AF sources and AF excitation patterns, (cf. Figure 4.27). The excitation patterns rotor, focus, colliding wavefronts, and block were analyzed in the case of the centered catheter on the specific excitation pattern.

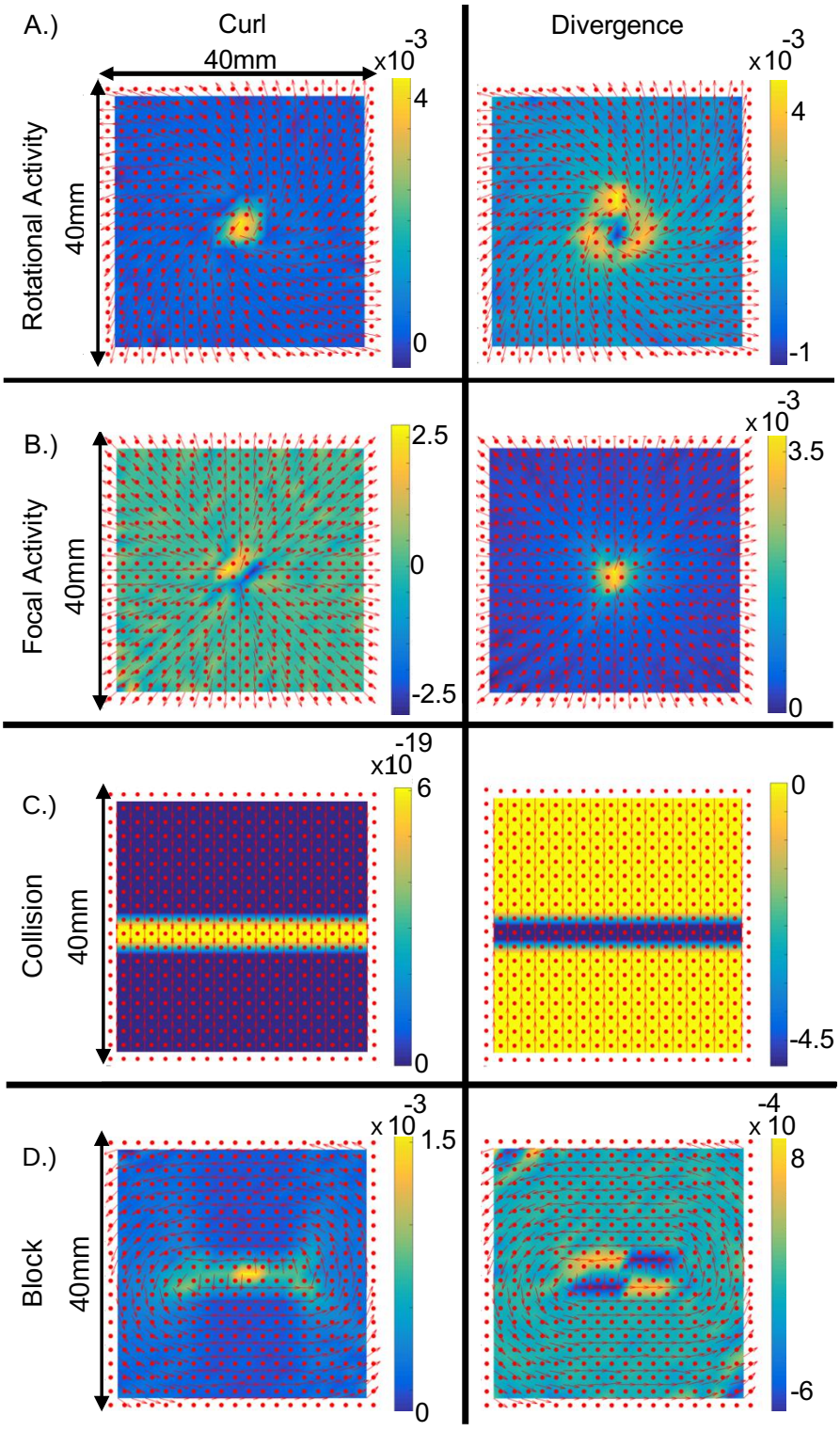

Figure 4.27: Overview of curl and divergence maps for the excitations (A) rotor, (B) focus, (D) colliding wavefronts, and (D) block. Red dots symbolize electrode positions. Calculated conduction velocity vectors are marked in red. The figure is adapted from [S8], [143].

4.3.5 Sensitivity analysis of curl and divergence

In order to analyze the robustness of the methods, curl and divergence were used for the detection of AF sources and patterns sensitivity analyses. The sensitivity analysis of curl and divergence of the rotor and focal activity are presented in Figure 4.28 and Figure 4.29.

The sensitivity analysis of curl and divergence in the scenario excitation around a line of block is presented in Figure 4.30.

The sensitivity analysis of curl and divergence in the scenario collision is presented in Figure 4.31.

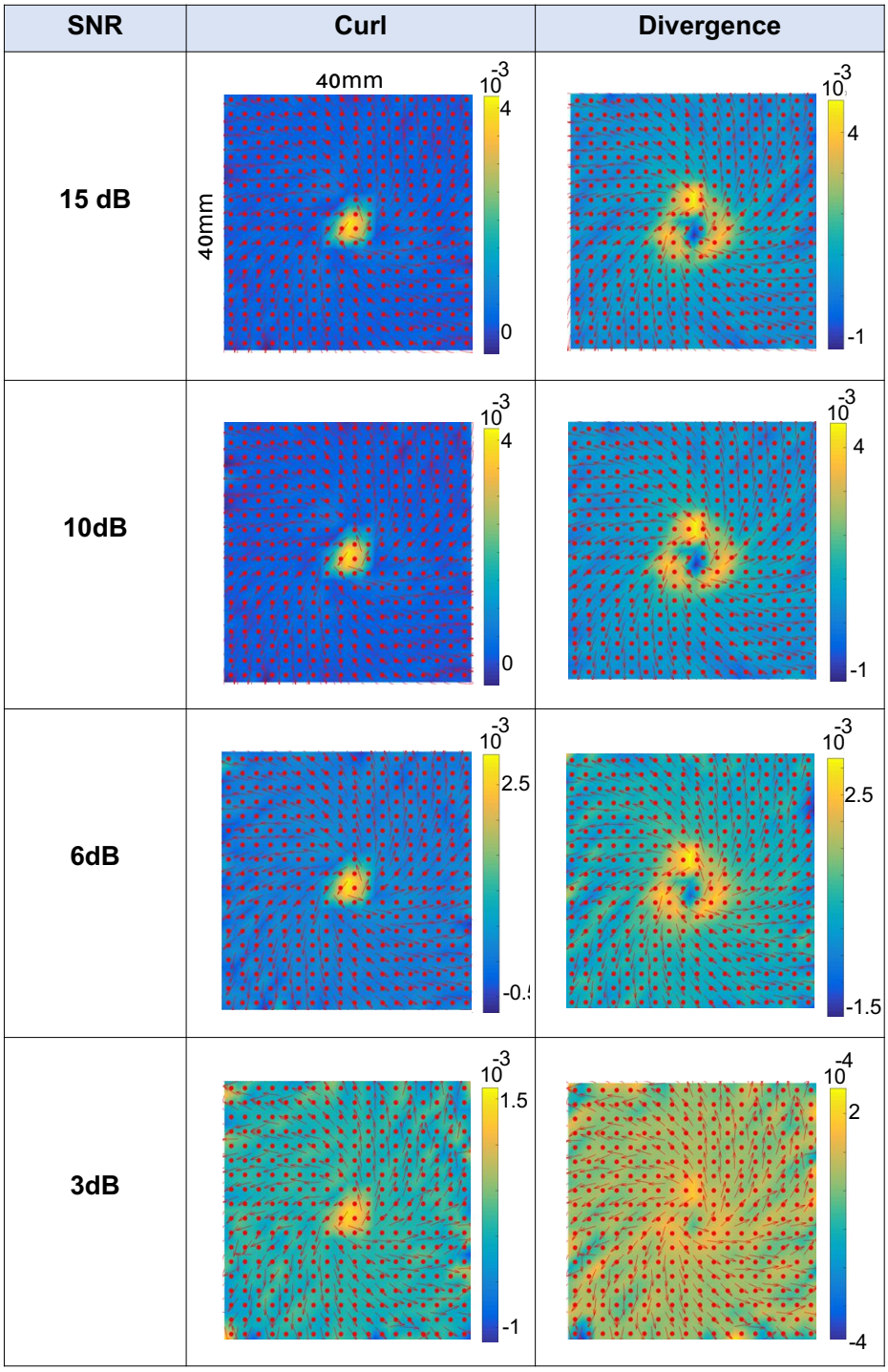

Figure 4.28: Curl and divergence maps for the excitation rotational activity at noise levels 15 dB, 10 dB, 6 dB, and 3 dB measured with a virtual square catheter. Red dots symbolize electrode positions. Calculated conduction velocity vectors are marked in red. The figure is adapted from [S8], [143].

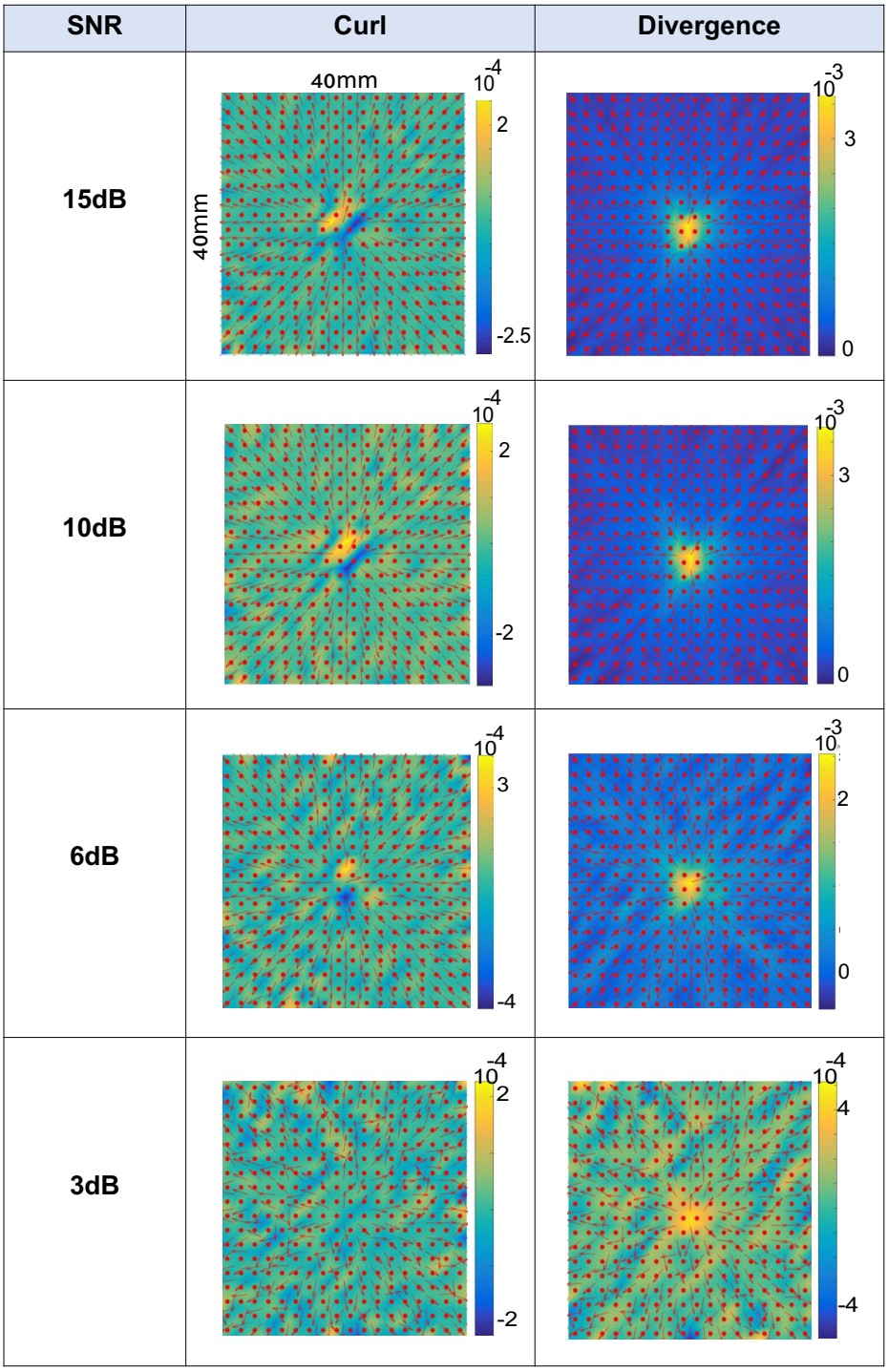

Figure 4.29: Curl and divergence maps for the excitation focal activity at noise levels 15 dB, 10 dB, 6 dB, and 3 dB measured with a virtual square catheter. Red dots symbolize electrode positions. Calculated conduction velocity vectors are marked in red. The figure is adapted from [S8], [143].

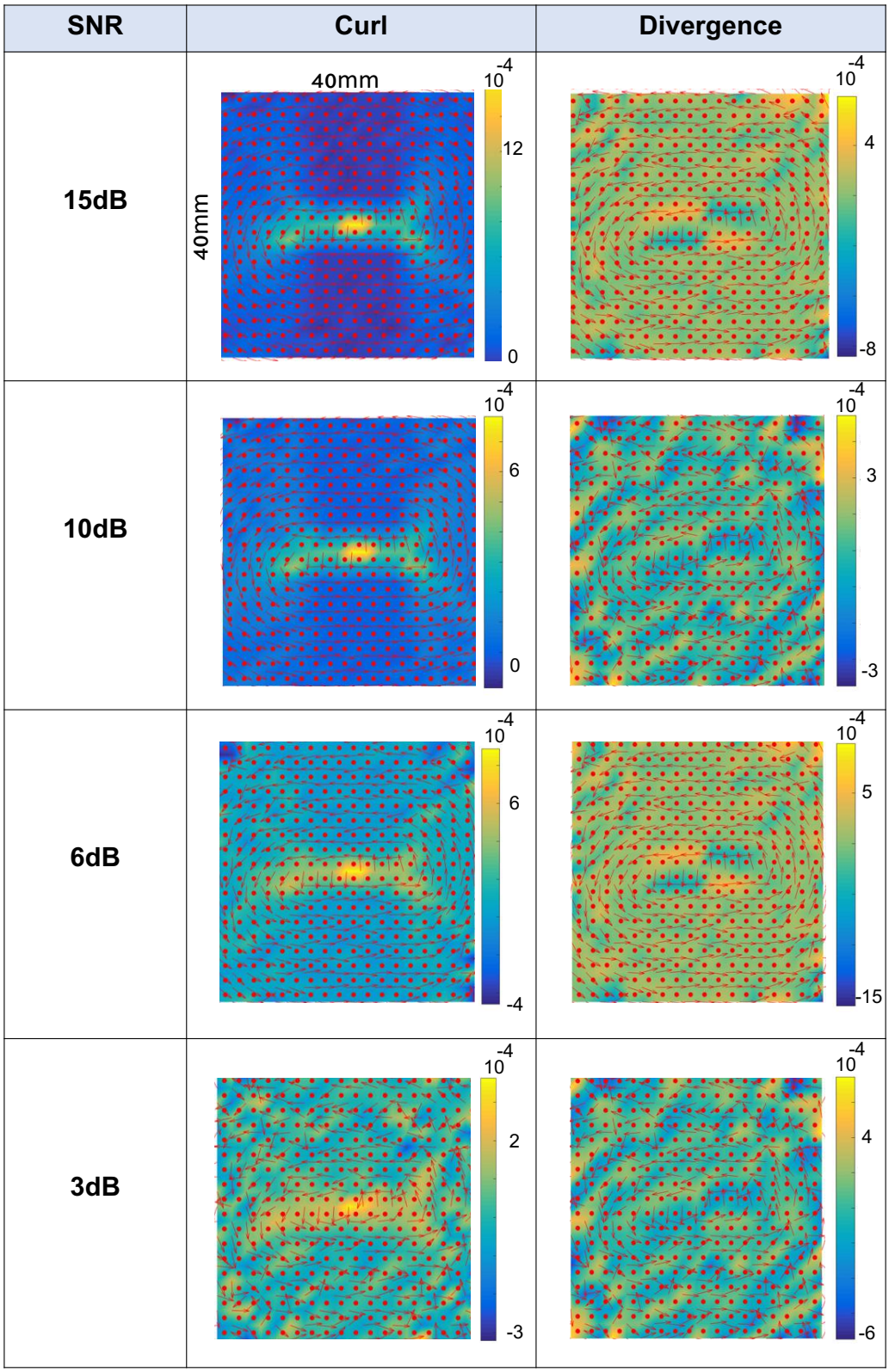

Figure 4.30: Curl and divergence maps for the scenario line of block block at noise levels (A) 15 dB (B) 10 dB, (C) 6 dB, (D) 3 dB measured with a virtual square catheter. Red dots symbolize electrode positions. Calculated conduction velocity vectors are marked in red. The figure is adapted from[S8], [143].

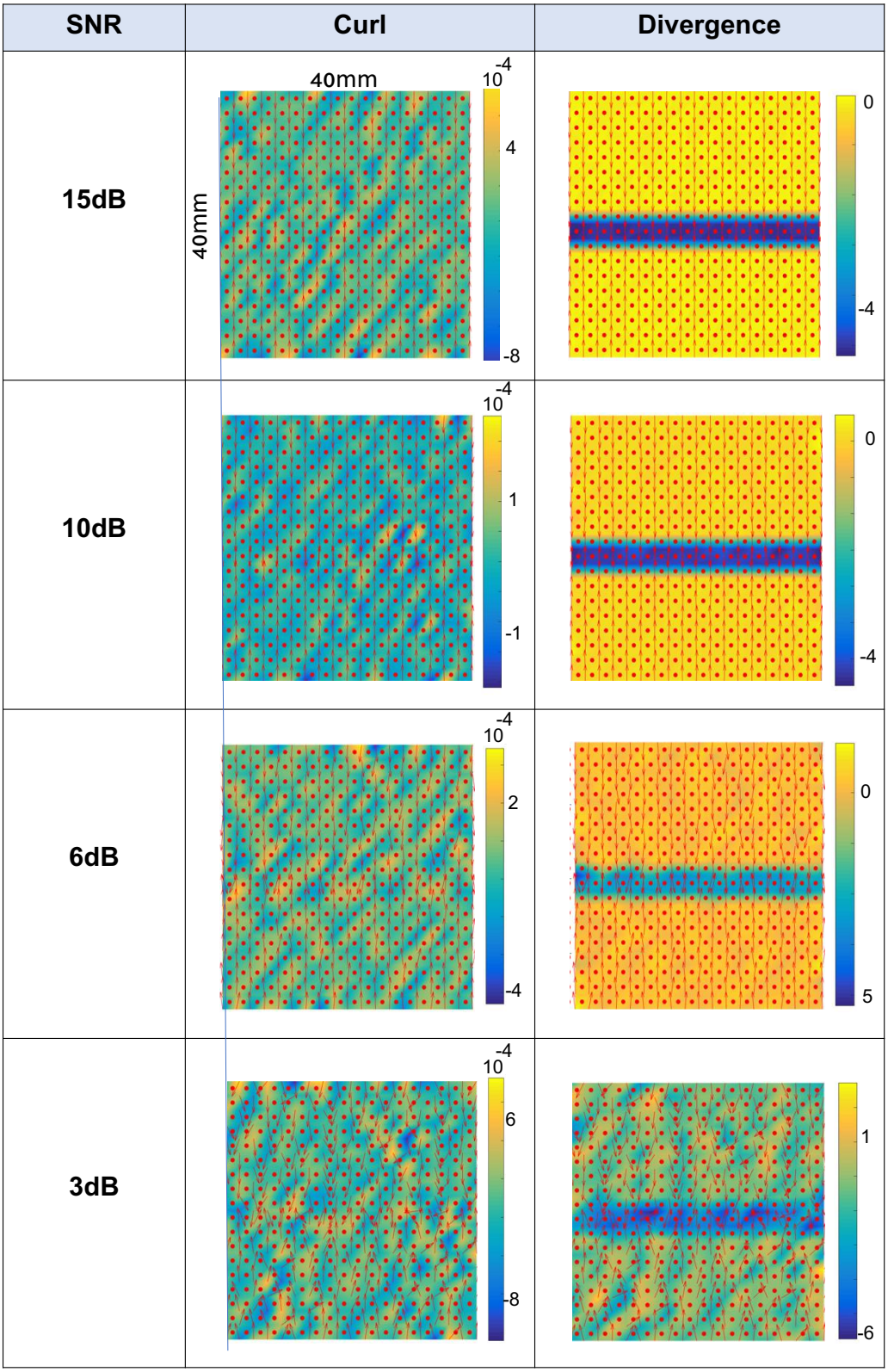

Figure 4.31: Curl and divergence maps for the excitations collision at noise levels (A) 15 dB (B) 10 dB, (C) 6 dB, (D) 3 dB measured with a virtual square catheter. Red dots symbolize electrode positions. Calculated conduction velocity vectors are marked in red. The figure is adapted from [S8], [143].

4.3.6 Developed amplitude and morphology based methods

4.3.6.1 Influence of the transmural angle and curved wavefronts on signal morphology

The transmural angle of the wavefront impacts the resulting signal morphology significantly. In Figure 4.32, the transmural angle in a 3D patch model was induced by different stimulations in the tissue depth layers and variated over time (cf. Figure 4.32). Because of the reaction-diffusion behavior, strong transmural angles were balanced after a certain time. Strong transmural angle α (cf. Figure 4.32A.)) resulted in a strong predominance of S-wave (negative peak in signal) signals [111] (cf. Figure 4.32(B)). No transmural angle α (cf. Figure 4.32) (E) resulted in similar R- (positive peak in signal) and S-wave signal (cf. Figure 4.32(F)).

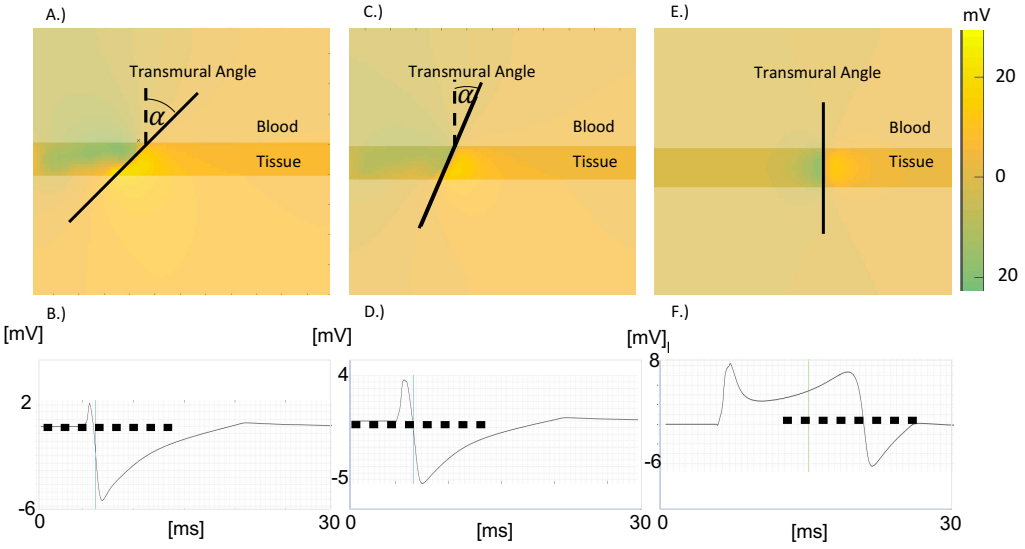

Figure 4.32: Change in the transmural angle over time. (A) Strong transmural angle α with (B) strong a predominance of an S-wave signal. (C) Reduced transmural angle α with (D) a reduced S-wave predominance morphology. (E) No transmural angle α with (F) a unipolar recording of nearly similar R- and S-waves. The figure is adapted from [S7], [119].

A predominance of S-wave signals [111] was also detected at curved wavefronts of rotational activities. The R-wave was missing in unipolar recordings at curved wavefronts (cf. Figure 4.33). Transmembrane and extracellular potentials are represented in Figure 4.33. The time point of the upstroke in the transmembrane voltage signal was equal to the time point of the steepest negative slope in the extracellular potential signal. Furthermore, the beginning time of the upstroke in the transmembrane voltage signal was equal to the time of the maximum in the extracellular potential signal. The time of the maximum in the transmembrane voltage signal was similar to the minimum

in the extracellular potential signal, and the plateau phase was equal to the time point of the 0V in the extracellular potential.

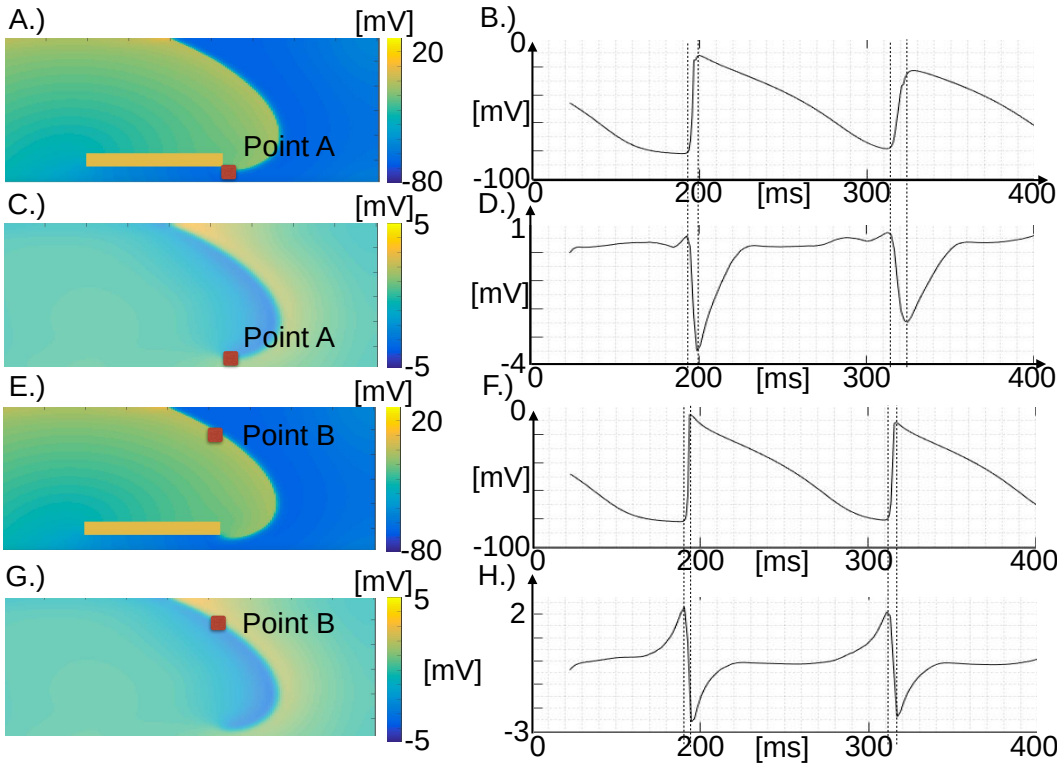

Figure 4.33: Transmembrane voltage maps of rotational activity around a block line (A) with measurement point A (at line of block), (E) (distant to line of block). Extracellular potential maps of rotational activity around a block line (C) with measurement point A (at line of block), (G) (distant to line of block). Demonstration of the missing R-wave due to curved wavefronts in a 3D patch model of stable rotational activity around a block. (B) Transmembrane voltage signals measured at point A near the block line. (D) Resultant extracellular potential signals at point A, where the S-wave amplitude is marked in red. (E,G) Transmembrane voltage at the outer region of rotational activity at point B. (H) Resultant extracellular potentials at point B show a similar S-wave as in B, but with a significantly larger R-wave. The steepest negative slope of extracellular potential correlates with the upstroke of the transmembrane voltage. The maximum of the extracellular potential correlates with the beginning of the upstroke of the transmembrane voltage. The minimum of the extracellular potential correlates with the maximum transmembrane voltage, and the 0-signal of extracellular potential correlates with the plateau phase of the transmembrane voltage. The figure parts A,C,E,G are adapted from [S6], [114], [114].

The rotational activity in a 3D model around a non-conductive area is shown in Figure 4.34 (A) and (B). The impact of the transmural angle during atrial fibrillation of the extracellular potential and transmembrane voltage in a cross-section of the realistic atrial model during AF is depicted in Figure 4.34 (C) and (D).

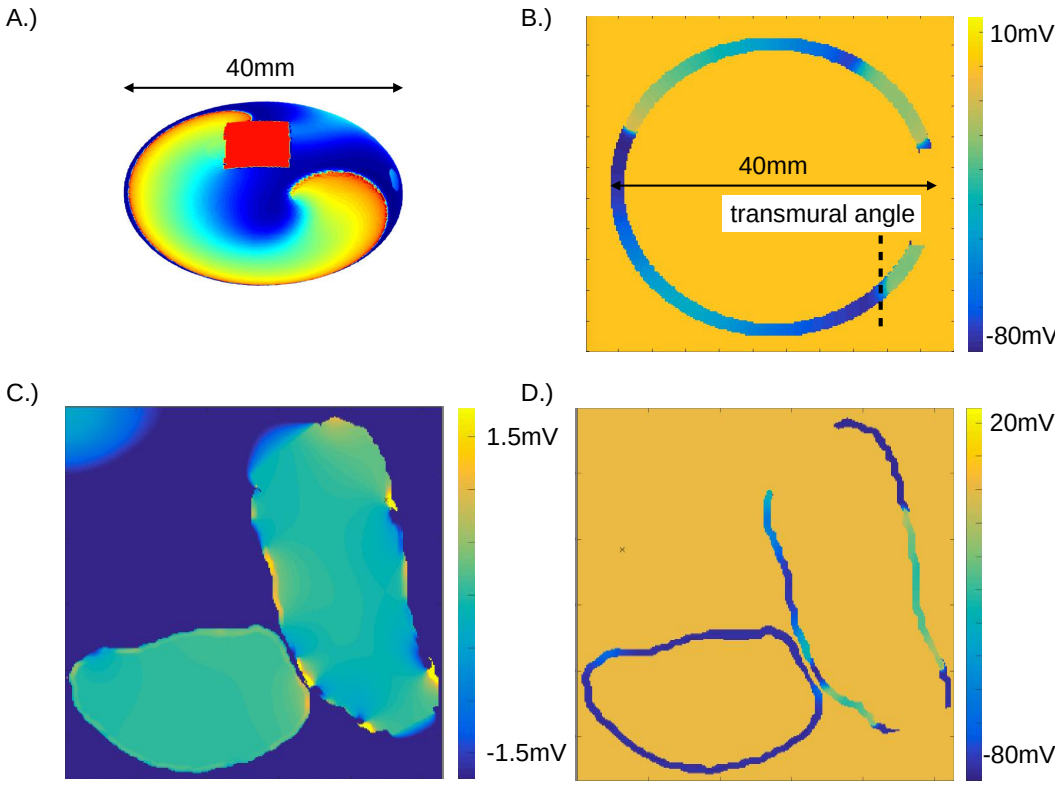

Figure 4.34: Rotational activity in a 3D sphere model around a non-conductive block resulted in two rotational activity centers. (A) Transmembrane voltage map. The figure part (A) is adapted from [S6] [114]. (B) Cross-section of the transmembrane voltage map with different transmural angles because of curved wavefronts. Cross-section of the realistic atrial model during AF with different transmural angles at (C) the extracellular potential map and at (D) the transmembrane voltage map. The atrial model was adapted from a model described in [134].

The statistical analysis of the RS-ratio measured at the realistic heart model is presented in Figure 4.35. The simulation results are strongly similar to those measured with high-density electrode systems [111].

4.3.6.2 Signal recordings of a 5 x 5 virtual square catheter centered on the unstable rotational activity center

Signal characteristics near the stable and unstable rotational activity were analyzed with a new square catheter (5 x 5) with an interelectrode distance of 2 mm. Near the center (2 mm from rotor core) of the rotational activity, smaller amplitudes and

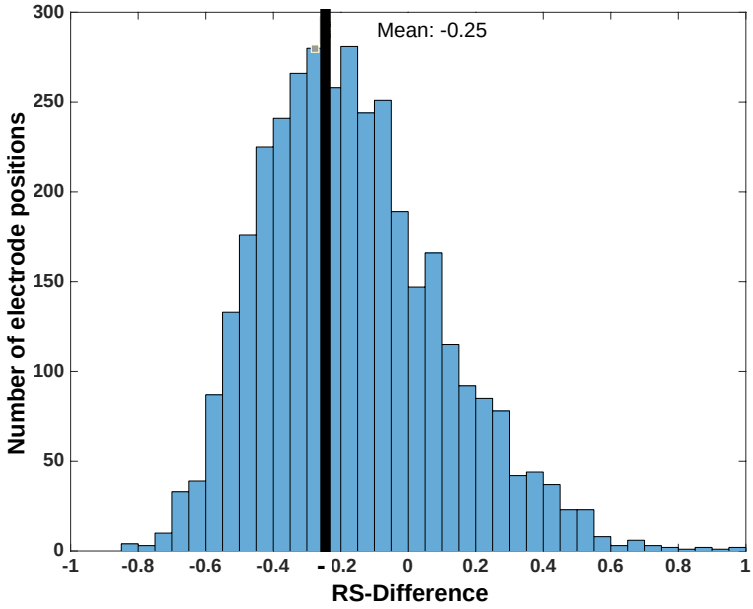

Figure 4.35: RS-ratios measured during AF in the realistic AF simulation model. The Figure is adapted from [S7], [119].

fractionated signals were measured. This was the reason why local activation times could not clearly be detected. In the case of measurements at the stable rotational activities, the detected cycle lengths were nearly the same cycle by cycle, whereas the cycle lengths in the case of the unstable rotational activity differed cycle by cycle because of the movement of this activity (cf. Figure4.36).

The resulting characteristic maps of the phase, entropy, RS-ratio, and peak-to-peak are presented in Figure 4.36. Rotor centers can be detected in these simulation data by phase maps using the phase singularity point. Also, the maximum of the approximate entropy could be used to detect rotors. Because of the curved wavefronts, predominantly S-wave signals [111] were measured near the rotor center but directly at the center, the signal had small amplitudes with less S-wave predominance. This is the reason why the maximum of these signals could also be used to detect rotors.

The Figure 4.36 shows the signal recordings of the virtual square catheter centered on the unstable rotational activity center. Smaller amplitudes with lower peak-to-peak values were detected at the center electrode.

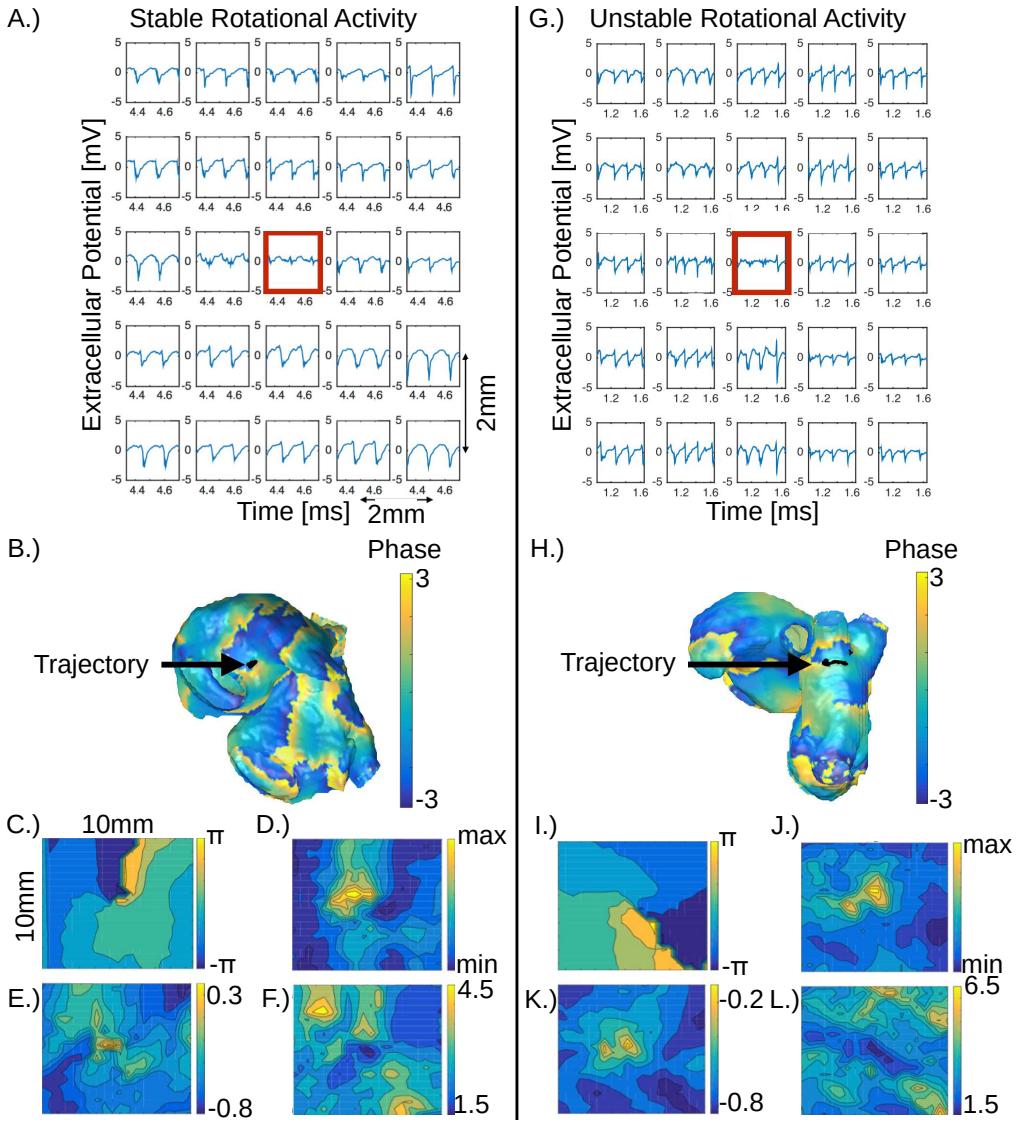

Figure 4.36: Lasso catheter centered on stable rotational activity in the right atrium. (A) Characteristic unipolar signal morphologies measured with 5 x 5 virtual square catheter with 2 mm interelectrode distances centered at stable rotational activity center. The center electrode covers the rotor tip. (B) Trajectory of the stable rotor tip positions. (C-F) Characteristic maps measured from unipolar recordings at stable rotational activity. (C) Phase map. (D) Entropy map. (E) RS-ratio map. (F) Peak to peak map displaying low voltage < 1.5 mV. (G) Signal recordings of a 5 x 5 virtual square catheter centered on the unstable rotational activity center show low voltage at the rotor tip (center electrode).(H) The trajectory (black) of the unstable rotor tip positions. The area covered by the square catheter (5 x 5) was 10 mm x 10 mm. (I-L) Characteristic maps of the unstable rotational activity in an region of 10 mm x 10 mm. (I) Phase map. (J) Approximate entropy map. (K) RS-ratio map. (L) Peak-to-peak map. The figure is adapted from Rottmann et al. 2015 [115] © IEEE [2015] with permission.

4.3.7 Phase-based methods developed

Phase singularities (PS) were calculated in order to determine the rotor trajectories in 3D patches, curved surfaces, and myocardial and blood layers.

4.3.7.1 Determining phase singularity on curved surfaces

The Figure 4.37 shows the results of the binning algorithm for detecting phase singularities by using 5-phase value ranges on an endocardial surface in a realistic atrial model. The phase singularity is marked in red in Figure 4.37. The phase singularity point is surrounded by points displaying phase values between $-\Pi$ and Π [148], cf. Figure 4.37 A-E.

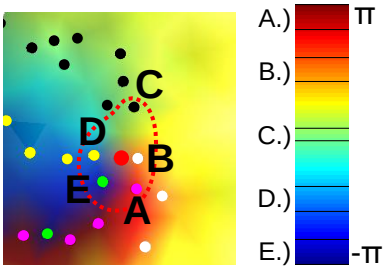

Figure 4.37: Rotor tip detection on a three-dimensional endocardial surface. Contour lines are shown as colored dots. The corresponding values (A-E) are defined between Π and $-\Pi$. The figure is adapted from [150], [S1], [149].

4.3.7.2 Phase singularity filaments

Phase singularity points based on extracellular potentials within the blood layers in a realistic atrial model with included fiber orientation were connected to phase singularity filaments. The following figure presents the filaments within blood within a time period of 90 ms (cf. Figure 4.38). The phase singularity filaments were curved within the blood and the curvature of phase singularity filaments changed over time.

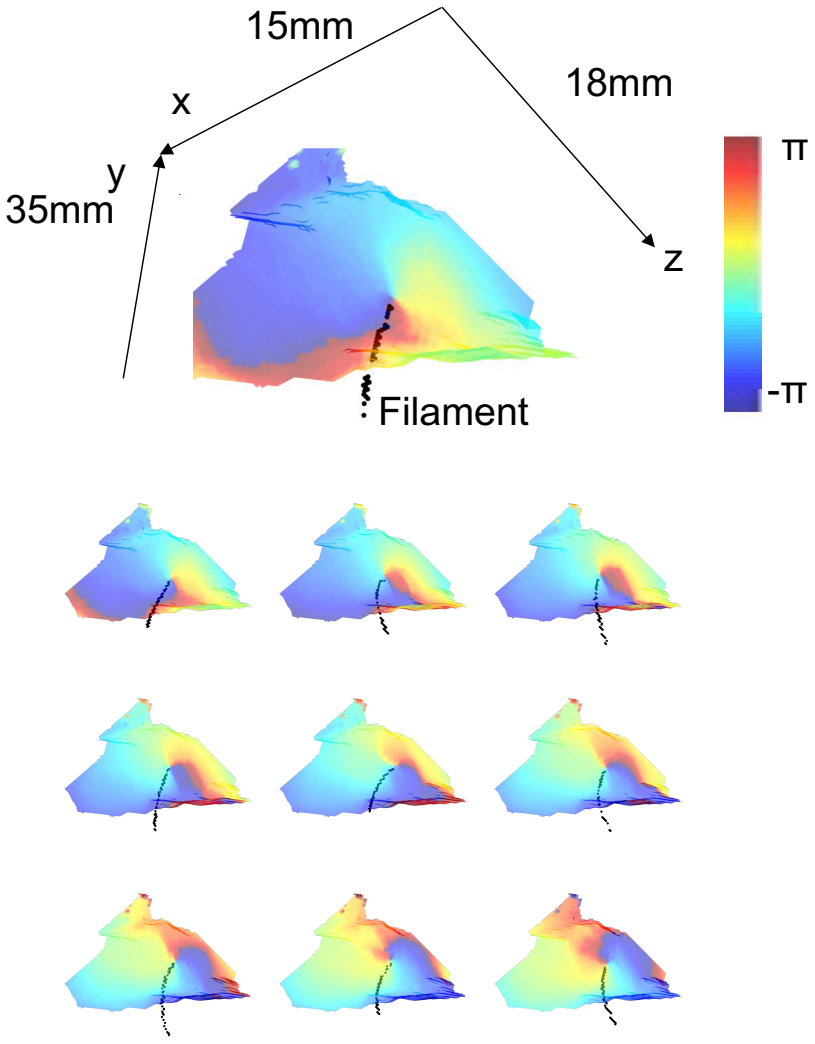

Figure 4.38: Filaments of PSs (black) of stable rotational activity in the right atrium in the period between 4.50 s and 4.59 s. The time between two figures is 10ms. The figure is adapted from [S1], [149], [150].

4.4 Discussion

For detecting and terminating of rotational activities and focal sources during AF, it is important to determine AF activities in a robust manner. But the signal characteristics of stable and unstable AF sources are not well understood. This chapter presents new knowledge about the signal characteristics of stable and unstable rotational and focal activities in 3D patches and realistic atrial models.

4.4.1 Local activation time-based methods

Local activation time-based methods like detecting line patterns of activations using the cycle length > 70% of AF cycle length could be used to detect rotational activities with e.g. Lasso catheters only within a distance of 7 mm. The method CLC > 70% of AF cycle length was also used in clinical data. Furthermore, differences between signal characteristics of stable and unstable rotors were represented. The detected cycle length variances were larger in the region 10 mm x 10 mm around the rotor core in the case of the unstable rotor.

4.4.2 Amplitude-based methods

Amplitude-based methods like finding low-voltage regions, regions with high ApEn values, and high RS-ratio values could be used only within an area of 2 mm toward the rotor center. Regions of minimal amplitudes and maximal approximate entropy values were correlated with rotor centers in homogeneous atrial tissue patches and atrial models. But there was no fibrotic region implanted in these models thus these observations were functional. Models with implanted fibrotic tissue also showed a decrease of amplitudes near the rotor center thus being substrate based. These regions had amplitudes of half the amplitude of the recordings above the fibrotic regions. Also, clinical studies confirmed the low-voltage, fractionated area at centers of rotational activities [151]. Unstable rotational activities resulted in more variances between the cycle lengths and amplitudes cycle by cycle. The approximate entropy could be used for rotor detection if the rotational activity was within a healthy substrate. At proarrhythmogenic substrates of fibrotic regions with degree of fibrosis of 40%, the recordings became more fractionated with increasing distance to tissue because of near-field effects at focal exit points. Curved wavefronts at the rotational activities resulted in predominating S-wave signals, if the rotational activity was within healthy tissue. Statistical histograms of the RS-ratio of the 3D atrial model signals were close to statistical RS histograms in clinical data [111]. Within the fibrotic tissue, strong

S-waves were detected at focal exit points and overlapping low-voltage signals above the fibrotic region.

4.4.3 Conduction velocity-based methods

Conduction velocity based-methods could detect AF sources such as the intersection point method for determining the rotor and focal source centers. Further, the curl and divergence methods could detect AF excitation patterns rotor, focus, block, and colliding wavefronts.

4.4.4 Phase-based methods

In order to analyze also the influence of the distance to tissue, phase singularities were detected in different blood layers toward the endocardium. Phase singularity filament curvatures within the blood differed and reoccurred in time periods which were similar to the cycle lengths. These results show the importance of contact mapping in order to detect accurately phase singularity points originating from heart tissue. However, phase singularities could not clearly be detected at fractionated recordings above fibrotic tissue.

4.4.5 Outlook

Commonly used navigation systems do not have the feature for displaying rotor centers, focal sources and their trajectories integrated. These results show that different features could be combined to detect AF sources in a robust manner and to separate stable and unstable AF activities.

4.5 Resulting Publications

Results of this chapter were published in :

M. Rottmann, T. Oesterlein, C. Reich, A. Luik, C. Schmitt, O. Dössel. Characteristic Features of Electrograms of Depolarization Waves During Atrial Fibrillation. In 38th Annual International Conference of the IEEE Engineering in Medicine and Biology Society, 2016.

M. Rottmann, L. A. Unger, W. Kaltenbacher, Seemann G., A. Loewe, M. W. Krueger, A. S. Jadidi, T. Arentz, and O. Dössel. Methods for analyzing signal characteristics of stable

and unstable rotors in a realistic heart model. In Computing in Cardiology, Vol. 42, pp. 485-488, 2015.

M. Rottmann, M. W. Keller, T. Oesterlein, G. Seemann and O. Dössel, Comparison of different methods and catheter designs to estimate the rotor tip position. A simulation study, Computing in Cardiology, pp. 133-136. 2014.

W. Kaltenbacher, M. Rottmann, O. Dössel. An algorithm to automatically determine the cycle length coverage to identify rotational activity during atrial fibrillation. A simulation study. Current Directions in Biomedical Engineering, 2(1), pp. 167-170, 2016.

C. Reich, T. Oesterlein, M. Rottmann, G. Seemann, O. Dössel. Classification of cardiac excitation patterns during atrial fibrillation. In Current Directions in Biomedical Engineering, Vol. 2(1), pp. 161-166, 2016.

L. A. Unger, M. Rottmann, G. Seemann, and O. Dössel. Detecting phase singularities and rotor center trajectories based on the Hilbert transform of intraatrial electrograms in an atrial voxel model. In Current Directions in Biomedical Engineering, Vol. 1(1), pp. 38-41, 2015.

CHAPTER 5

Impact of Catheter Design on the Detection of Atrial Fibrillation Sources

"When you can measure what you are speaking about, and express it in numbers, you know something about it."

— William Thomson, 1. Baron Kelvin

5.1 Introduction

Atrial fibrillation may be driven by non-pulmonary rotational sources and vein focals. This chapter assesses the capability and limitations of detecting AF sources with catheters in current clinical use such as Lasso, AFocusII and PentaRay and novel catheter geometries. The parameter cycle length coverage (CLC) has been published in clinical and simulation settings [135] [115].

The measurement system for intracardiac signals at the myocardium during the catheter ablation procedure is the catheter. For clinical use, multielectrode catheters with 10-25 electrodes are the most common. There are also basket catheters with 64 electrodes. However, the impact of catheter design, electrode size and form, and the impact of the deformation dependent on the force on intracardiac recordings are not clear. This simulation work also presents unipolar and bipolar recordings from different commonly used multielectrode catheter designs and future catheter designs.

Furthermore, to optimize the signal quality, commonly used and new electrode concepts were investigated. With these signal recordings, quantitative parameters and signal processing methods for the detection of AF sources can be analyzed. In clinical measurements, there is also a deformation of splines. In this Chapter, the main topics of simulation studies were investigated as follows.

A) Modeling of different commonly used and new catheters with different geometries.

B) Modeling and analyzing the impact of different electrode sizes on unipolar recordings.
C) Modeling of the deformation of the PentaRay catheter. The developed mechanical deformation model was evaluated with optical measurements and integrated into the electrophysiological simulation environment.

5.2 Methods

5.2.1 Modeling of mechanical rigid catheter designs

Different catheters were modeled in order to analyze unipolar and bipolar recordings from the simulation data. The Figure 5.1 presents the catheter designs in clinical use and their parameters, diameter, and the number of electrodes. The commonly used catheters Lasso, AFocusII, PentaRay and square catheter were modeled with point-like electrodes. These point-like measurements were placed directly at the endocardium or in different distances to the tissue. These models were also used in more complex 3D atrial models in order to analyze the resulting signal recordings. Furthermore, and experimental square catheters were investigated as well as new mapping designs with flat micro-electrodes.

	Lasso	Focus II	PentaRay	Square
Diameter [mm]	10-20	20	35	6 / 8
Electrodes	10-20	20	20-25	16 / 25
Geometries	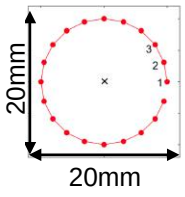	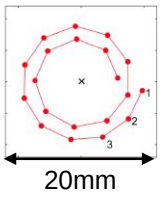	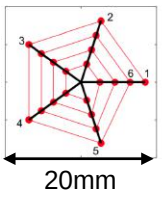	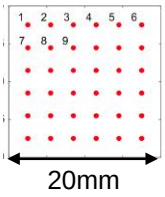

Figure 5.1: Catheter designs Lasso (diameter 10-20 mm, number of electrodes 10-20), AFocusII (diameter 20 mm, number of electrodes 20), PentaRay (diameter 35 mm, number of electrodes 20), and square (various diameters and numbers of electrodes). The figure is adapted from [S9] [152].

5.2.2 Methods for the modeling and implementing of mechanical deformations of the PentaRay catheter in the 3D sphere model

For modeling the deformation behavior, a mechanical deformation model was developed. The stress tensor σ was described by a linear relationship of the strain tensor with the elasticity tensor, which was described by a tensor equation of the fourth-order. This chapter includes the following formulas and explanations, which were adapted from literature [153], [154], [155]. This chapter was also part of [152] [S9].

5.2.2.1 Generalized Hooke's law

Hooke's law 'Ut tensio sic vis' or 'The power (sic) of any springy body is in the same proportion with the extension' was developed by the British natural philosopher and inventor Hooke (1635-1702) in the year 1678 [156] [157].

In literature, Hooke's law is defined with the applied force F (not the power that was suggested by Hooke), the deformation u, and the spring constant k as [156] [157] :

$$F = ku \tag{5.1}$$

The French mathematician and physicist Augustin-Louis Cauchy (1789 -1857) generalized Hooke's law for 3D deformations with 6 components of stress which are linearly related to 6 components of strain, compare formula 5.2 and 5.3.

$$\tilde{\sigma} = \tilde{\tilde{C}}\tilde{\varepsilon} \tag{5.2}$$

The matrix form with the general stress tensor σ, the stiffness matrix C and the strain tensor ε can be written as:

$$\begin{bmatrix} \sigma_{xx} \\ \sigma_{yy} \\ \sigma_{zz} \\ \sigma_{yz} \\ \sigma_{zx} \\ \sigma_{xy} \end{bmatrix} = \begin{bmatrix} C_{11} & C_{12} & C_{13} & C_{14} & C_{15} & C_{16} \\ C_{21} & C_{22} & C_{23} & C_{24} & C_{25} & C_{26} \\ C_{31} & C_{32} & C_{33} & C_{34} & C_{35} & C_{36} \\ C_{41} & C_{42} & C_{43} & C_{44} & C_{45} & C_{46} \\ C_{51} & C_{52} & C_{53} & C_{54} & C_{55} & C_{56} \\ C_{61} & C_{62} & C_{63} & C_{64} & C_{65} & C_{66} \end{bmatrix} \begin{bmatrix} \varepsilon_{xx} \\ \varepsilon_{yy} \\ \varepsilon_{zz} \\ \varepsilon_{yz} \\ \varepsilon_{zx} \\ \varepsilon_{xy} \end{bmatrix} \tag{5.3}$$

The general stress tensor (Cauchy stress tensor) can be written as:

$$\tilde{\sigma} = \begin{pmatrix} \sigma_{xx} & \tau_{xy} & \tau_{xz} \\ \tau_{yx} & \sigma_{yy} & \tau_{yz} \\ \tau_{zx} & \tau_{zy} & \sigma_{zz} \end{pmatrix} \tag{5.4}$$

The strain tensor can be written as:

$$\tilde{\varepsilon} = \begin{pmatrix} \varepsilon_{xx} & \varepsilon_{xy} & \varepsilon_{xz} \\ \varepsilon_{yx} & \varepsilon_{yy} & \varepsilon_{yz} \\ \varepsilon_{zx} & \varepsilon_{zy} & \varepsilon_{zz} \end{pmatrix} \tag{5.5}$$

For the isotropic case the stress tensor is defined as

$$\tilde{\sigma} = \lambda sp(\tilde{\varepsilon})\tilde{I_3} + 2\mu\tilde{\varepsilon} \tag{5.6}$$

dependent on the two Lamé constants named after the French mathematician and physicist Gabriel Lamé (1795-1870), λ and μ (cf. the following equations) [158] with the modulus of elasticity E (Young modulus) and the Poisson's ratio ν, named after the French mathematician, engineer, and physicist Siméon Denis Poisson (1781-1840).

$$\lambda = \frac{\nu E}{(1+\nu)(1-2\nu)} \tag{5.7}$$

$$\mu = \frac{E}{2(1+\nu)} \tag{5.8}$$

The Young modulus E, discovered (in 1807) from the British physicist, physician doctor and Egyptologist Thomas Young (1773-1829), is a measure of the elasticity if materials describe the linear relationship between the change in stress and the change in strain with the constant Young modulus E [159]. The relationship between stress and strain can be written with the Young modulus as [159]:

$$E = \frac{\Delta\sigma}{\Delta\varepsilon} \tag{5.9}$$

5.2.2.2 Contact algorithms

The contact problem can be described by a tension spring (cf. Figure 5.2), when it moves toward a wall.

If the gap is larger or equal to 0 (g $\geq$ 0), the following equations are applied.

$$F = ku \tag{5.10}$$

$$F_{max} = k\Delta x \tag{5.11}$$

If the force *F* is larger than F_{max}, the contact force at the wall F_c is:

$$F_c = k\Delta x - F \tag{5.12}$$

The energy is defined as (in the case of an open contact):

$$W = \frac{1}{2}ku^2 - uF \tag{5.13}$$

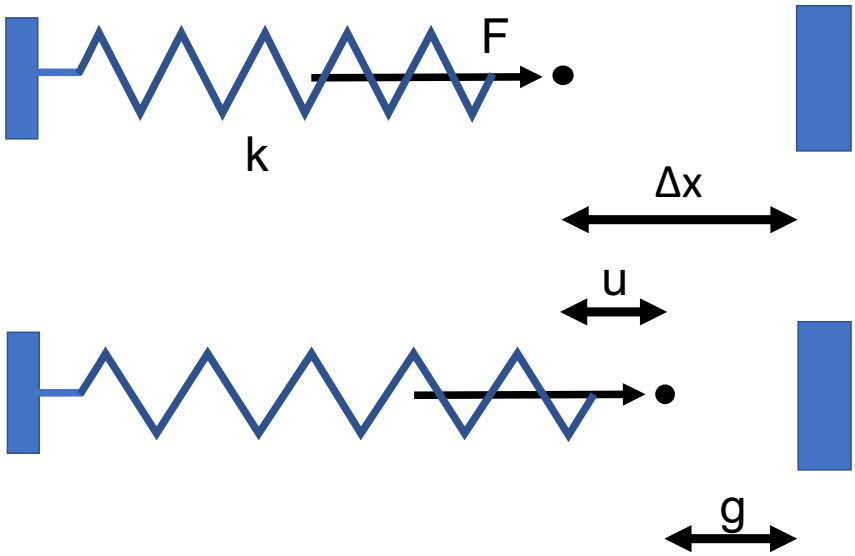

Figure 5.2: Contact problem described with a tension spring which moves in towards a wall. *u* is the shift of the tension spring from its idle state; Δx is the distance to the wall, and the gap g = Δx-u. The figure is adapted from [155].

5.2.2.3 Penalty method

The penalty method is a method for solving optimization problems. As long as the contact is open, the potential energy is defined as :

$$W = \frac{1}{2}ku^2 - uF \rightarrow Min \tag{5.14}$$

If there is contact the described system of the potential energy is no longer in balance and an additional penalty term must be added to solve the contact problem. In the case of contact, the potential energy can be written with the penalty-parameter ε as:

$$W = \frac{1}{2}ku^2 - uF + \frac{1}{2}\varepsilon g(u)^2 \rightarrow Min \tag{5.15}$$

The aim is to find the minimum of the potential energy.

$$\frac{\partial W}{\partial u} = \frac{\partial}{\partial u}\left[\frac{1}{2}ku^2 - uF + \frac{1}{2}\varepsilon g(u)^2\right] = 0 \tag{5.16}$$

$$ku - F - \varepsilon(\Delta x - u) = 0 \tag{5.17}$$

$$ku - F - \varepsilon\Delta x + \varepsilon u = 0 \tag{5.18}$$

$$(k+\varepsilon)u = -F + \varepsilon\Delta x \tag{5.19}$$

$$u = \frac{F + \varepsilon \Delta x}{k + \varepsilon} \tag{5.20}$$

In the case of a penetration is g < 0, and

$$F > k\Delta x \tag{5.21}$$

The influence of the penalty-parameter ε is described in following formulas with n > 1:

$$F = nk\Delta x \tag{5.22}$$

$$u = \frac{nk\Delta x + \varepsilon \Delta x}{k + \varepsilon} = \frac{nk + \varepsilon}{k + \varepsilon}\Delta x \tag{5.23}$$

For ε»k:

$$u \to \Delta x \tag{5.24}$$

The contact condition is fulfilled for penalty parameter ε tending to infinity, which is limited due to numerical reasons. This is the reason for the remaining penetration.

$$g = \left(1 - \frac{nk + \varepsilon}{k + \varepsilon}\right) \Delta x \tag{5.25}$$

A disadvantage of the penalty method is that in the case of a large penalty parameter value ε, the contact simulation is more realistic but the effort for convergence is also large.

5.2.2.4 Lagrange multiplier method

In the Lagrange multiplier method, the term λ g(u) is added to the potential energy instead of the penalty term and the modified energy can be written with the unknown Lagrange multiplier λ as:

$$W = \frac{1}{2}ku^2 - uF + \lambda g(u) \to Min, \tag{5.26}$$

The potential energy is minimal if :

$$\frac{\partial W}{\partial u} = ku - F + \lambda = 0 \text{ (equilibrium)}, \tag{5.27}$$

$$\frac{\partial W}{\partial \lambda} = g(u) = 0 \tag{5.28}$$

$$ku - F - \lambda = 0 \tag{5.29}$$

$$\Delta x - u = 0 \tag{5.30}$$

This result in:

$$u = \Delta x \tag{5.31}$$

This means that the Lagrange multiplier method is equal to the contact force F_c:

$$\lambda = k\Delta x - F \tag{5.32}$$

5.2.2.5 Augmented Lagrange method

In this work, the augmented Lagrange method was used for the solving the contact problem. The augmented Lagrange method is a combination between the penalty and the Lagrange multiplier method (cf. following equation), eliminates disadvantages of the penalty and Lagrange methods [160], uses an iterative procedure and a predetermined tolerance for contact constraints [161].

$$W^{AL} = \frac{1}{2}\varepsilon g(u)^2 + \lambda g(u) \tag{5.33}$$

5.2.2.6 Mechanical simulation using the finite element method

For implementing a realistic deformation model of the PentarRay catheter in the electrophysiological simulation environment, the necessary steps are shown in a workflow diagram as follows. The used contact algorithm was the augmented Lagrangian method with pinball-radius of 0.5mm [162]. The used finite element program was Abaqus (Simulia, Providence, RI).

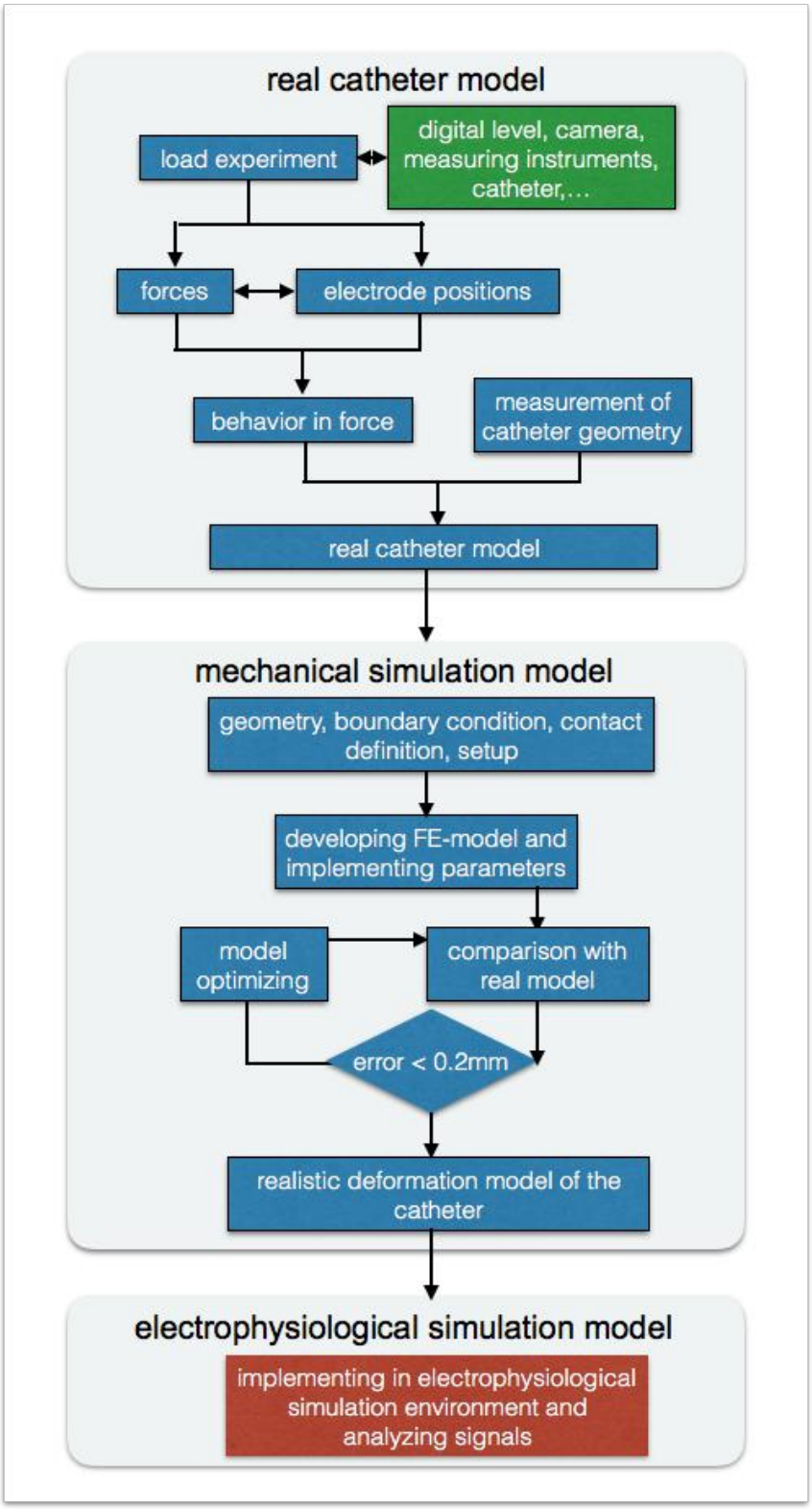

Figure 5.3: Workflow for optical and mechanical measurement of a real catheter, developing the mechanical deformation model and implementing the electrode positions in the electrophysiological model for reading out intracardiac recordings. The figure is adapted from [S9] [152].

The mechanical deformation of the PentaRay catheter was simulated by using the static-mechanical analysis [162]. It was supposed that the splines consisted of metal wires surrounded by an elastomer. The isotropic elastic behavior was used while considering the friction contact of the PentaRay catheter modeled with homogeneous equivalent material with the Poisson's ratio of 0.325. In the literature, the typical value of the Poisson's ratio for metal is 0.3 [163] and for elastomers 0.35 [164]. The coefficient of friction was 0.2 (typical value of the coefficient of friction between plastic and steel [165]).

5.3 Results

5.3.1 Development of a mechanical deformation model of the PentaRay catheter in a 3D Sphere Model

5.3.1.1 Mechanical and optical measurement

To measure the deformations of the PentaRay splines, an experimental setup of photometric and mechanical measurements was developed.

The Figure 5.7 shows the experimental setup of photometric and mechanical measurements of the catheter spline deformations.

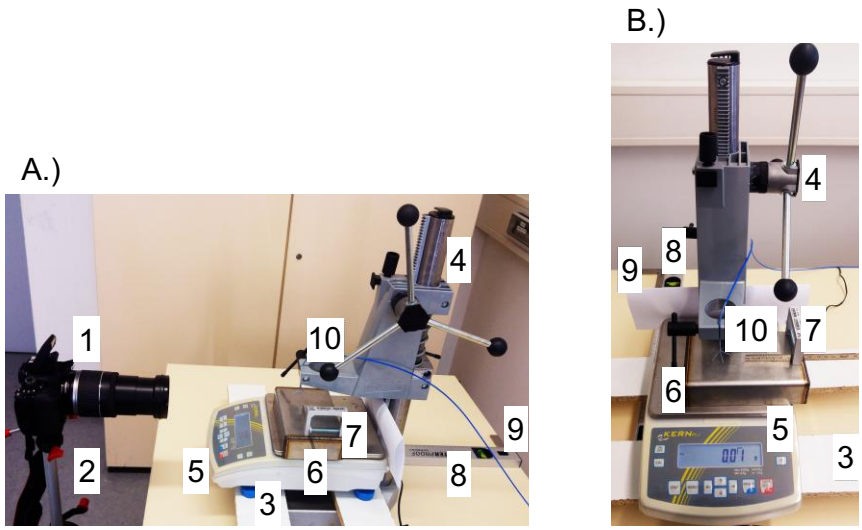

Figure 5.4: Experimental setup: (1) camera; (2) camera tripod; (3) wood washer; (4) sliding drill stand; (5) digital scale; (6) stainless steel apparatus; (7) reference scale and clamp; (8) aluminum level; (9) flat angle; (10) PentaRay catheter. The figure is adapted from [S9], [152].

load step	load from	load to	load step
1-9	0.02g	4g	0.5g
9-11	4g	6g	1g
11-15	6g	14g	2g
15-19	14g	30g	4g
19-24	30g	70g	8g

Table 5.1: Table of adapted step widths with increasing loads. The table is adapted from [S9], [152].

To analyze the deformations of the catheter splines, the following load steps were investigated. The load step widths were adapted with increasing loads (cf. Figure 5.1).

The corresponding diagram is plotted in Figure 5.5. First electrode positions of

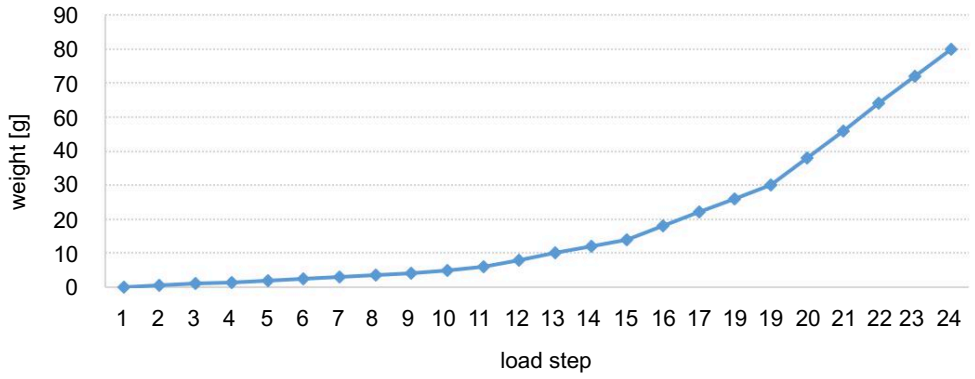

Figure 5.5: Load experiment. Adapted step width with increasing loads. The figure is adapted from [S9], [152].

the PentaRay catheter were analyzed by optical measurement function of a camera dependent on different loads (0.02 g to 70 g) which were measured using a digital level. At the load of 30 g, all electrodes were in contact with the planar plate (see Figure 5.6 (F)). In the case where all electrodes had contact, the positions were used for the further signal analysis in a sphere model (cf. Figure 5.14). The splines of the PentaRay catheter were deformed, depending on the force on the catheter. The catheter was photometrically measured with the camera in each load step from load 0.02 g to 70 g. Altogether, 72 electrode positions from 3 splines were measured. The 72 electrode positions were measured photometrically. The *y*-axis was set to the center of the catheter, and the *x*-axis was set to the line of the surface (cf. Figure 5.6(A)).

The *x* and *y* electrode coordinates measured are shown in Figure 5.7 (A-D). The heights of the splines, dependent on the forces, are presented in Figure 5.7(E).

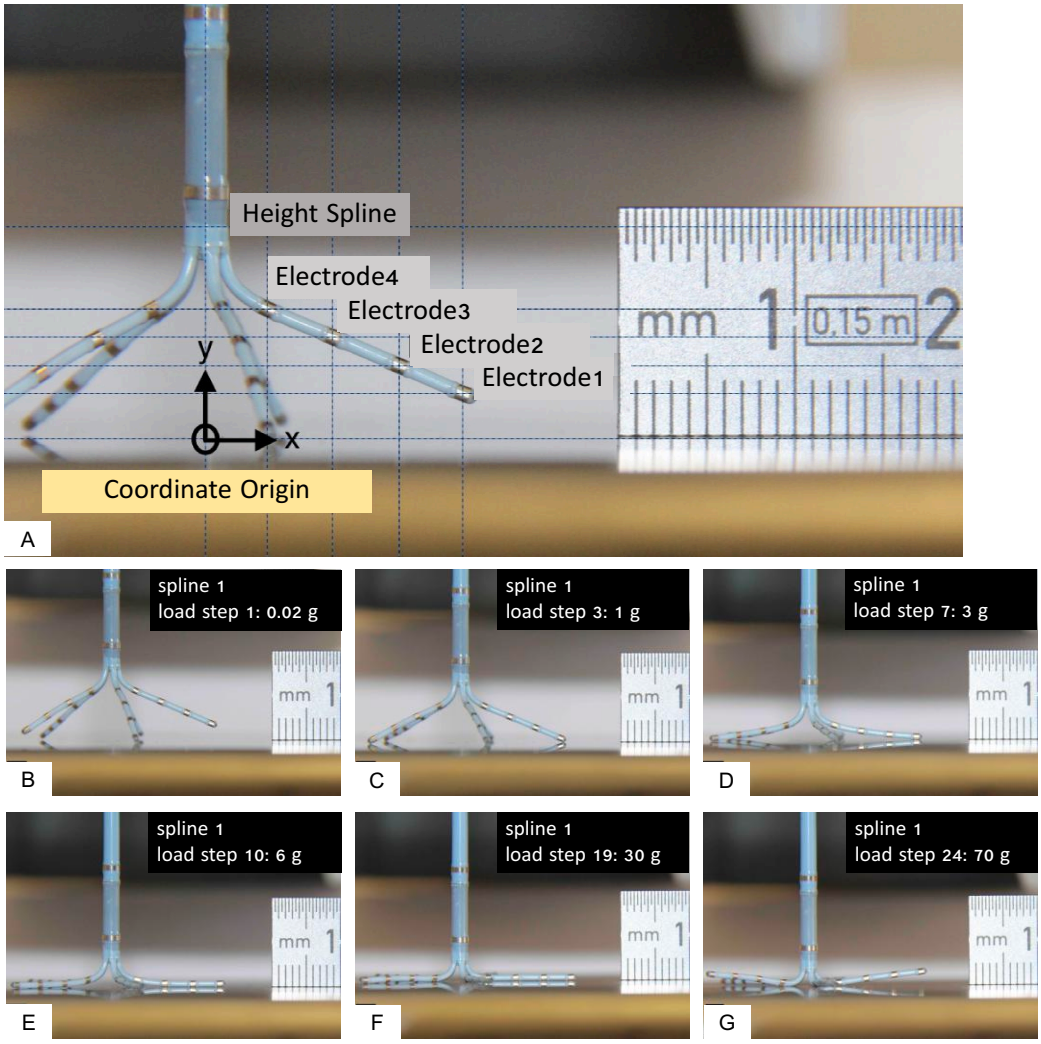

Figure 5.6: (A) Example of optical measurement of electrode position (x,y) and height of splines defined as node point of the five splines. (B-G) Optical measurements of the electrode positions of a PentaRay catheter on a planar plate, dependent on mechanical force. The figure is adapted from [S9], [152].

5.3.2 Experimental mechanical deformation

Unipolar and bipolar recordings in simulation studies resulted from point-like electrodes of one single voxel in literature. In this chapter, realistic signals were recorded from realistic electrode sizes, measured by real catheters used in clinical electrophysiological studies. Signal morphologies from intracardiac recordings were strongly dependent on the distance to the tissue. For analyzing realistic simulation scenarios for the catheter measurements, a mechanically deformed model of the PentaRay catheter was developed with its splines deformed depending on the acting force. This model was evaluated with optical and mechanical measurements and achieved a quality criterion in electrode position errors of < 0.2 mm. The mechanical model of the

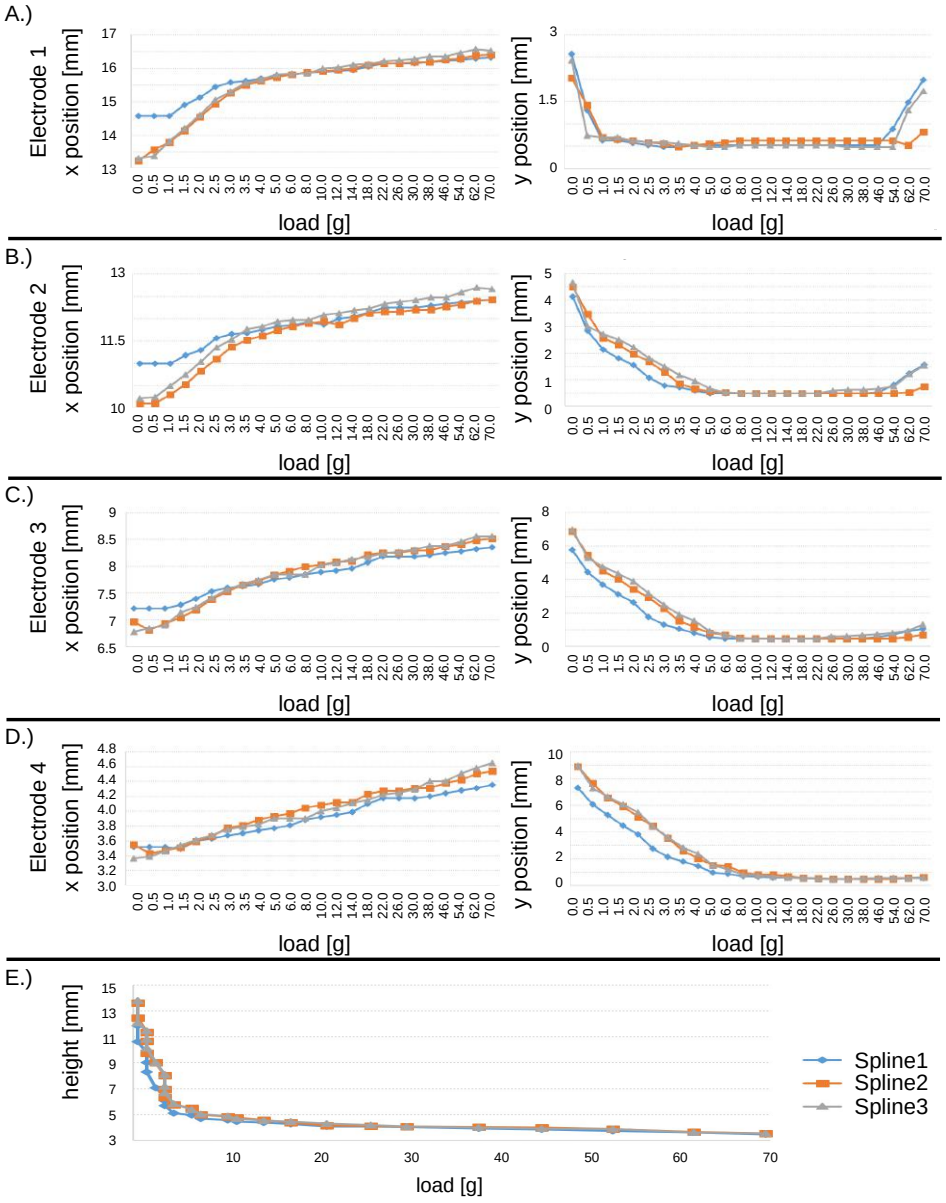

Figure 5.7: (A-D) *x* and *y* coordinates of electrode 1 to 4 of 3 measured splines dependent on load. (E) Heights of the splines (node point of splines, cf. Figure 5.6) dependent on load. The figure is adapted from [S9], [152].

PentaRay catheter that resulted from the optical and mechanical measurements is shown in Figure 5.8 (A). Figure 5.8 (B,D) shows the contact definition for the metal electrodes of the PentaRay catheter making contact with the planar plate. The forces acting on top of the bundle are shown. The area of the bundle is cylindric and has a frictionless bearing. There is one degree of freedom in the axial direction. The plate is

fixed on the lower surface (cf. Figure 5.8) (C). The penetration was maximally 0.026 mm in the first load step.

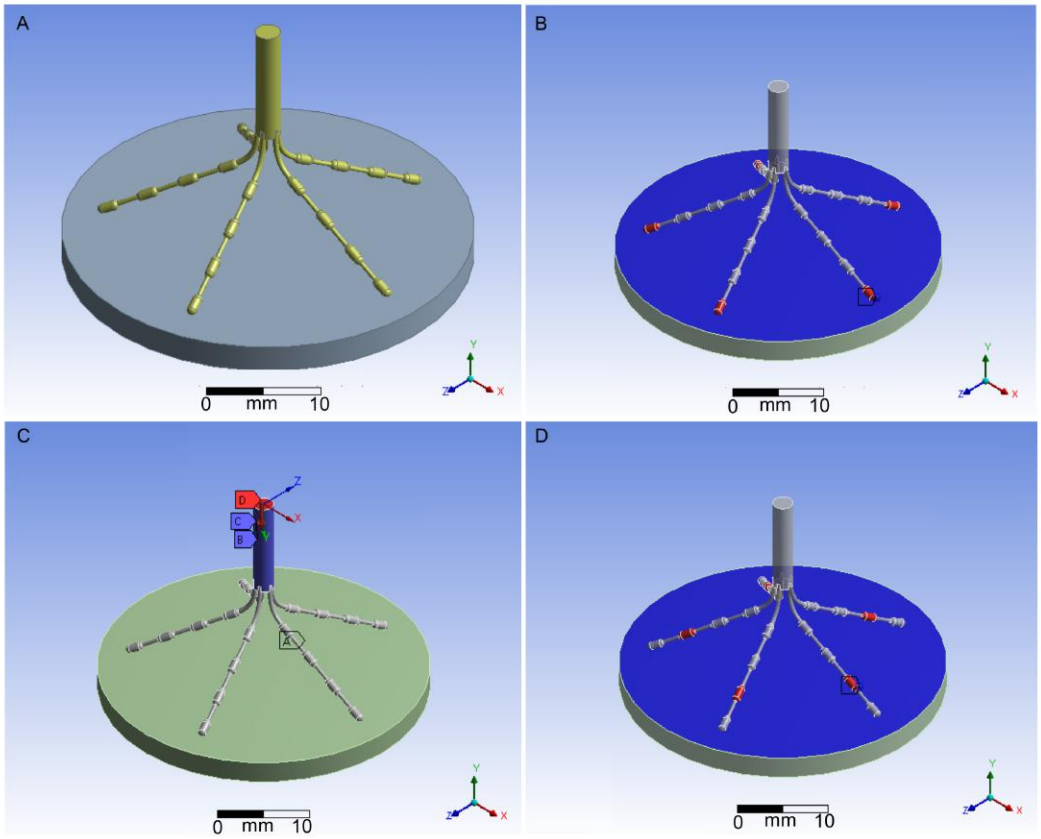

Figure 5.8: (A) Computer-aided design model of the PentaRay catheter and the planar plate. (B) Contact definition. Electrodes (marked in red) making contact with the target element planar plate (marked in blue) in the initial time state. (C) Label A: Fixed bearing on bottom side of the plate. Label B: Friction-free cylindric bearings. Label C: Contact surface. Label D: Force. (D) Second-row spline electrodes at distance to the tissue in the initial time state are marked in red. The figure is adapted from [S9], [152].

5.3.3 Determining the parameter

The parameter modulus of elasticity (E-value) was determined by a parameter study of comparing of electrode coordinates in the experiment to those involving mechanical simulation. The quality criterion was an absolute variance error of < 0.2 mm. The parameter study started with the E-value of 500 MPa that resulted from the experiment. In the parameter study, the E-values varied from 500 MPa to 700 MPa. The minimum of the parameter maximum absolute deviation of electrode position between simulation and experimental data was at the E-value of 621.5 MPa (cf. Figure 5.9 (A)). The mean absolute deviation was 0.1 mm (cf. Figure 5.9 (B)), and the maximum relative deviation was 0.21 mm (cf. Figure 5.9 (C)).

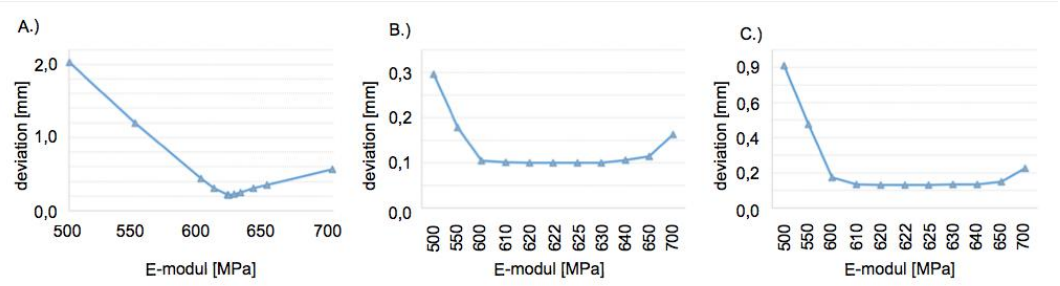

Figure 5.9: (A) Maximum absolute deviation of electrode position between simulation and experimental data was < 0.2mm. The absolute deviation is the root of the square error. The smallest value of the parameter maximum absolute deviation was at the E-module at 621.5 MPa. (B) Mean absolute deviation. (C) Maximum relative deviation. The figure is adapted from [S9] [152].

The deviations of the individual electrodes in the load steps are depicted in Figure 5.10).

5.3.4 Coefficient of friction

The synthetic material of the catheter was not known. In the literature, the coefficient of friction between steel and synthetic material is between 0.1 and 0.3. In this simulation study, the coefficient of friction was set to $\mu = 0.2$.

5.3.5 Mechanical finite element model in the real environment

Values of the Poisson's ratio of human tissue in the literature were between 0.49 and 0.5. In this work, the Poisson's ratio was set to 0.495. The coefficient of friction was set to 0.017 [166]. The tissue thickness was set to 2 mm, similar to typical human atrial

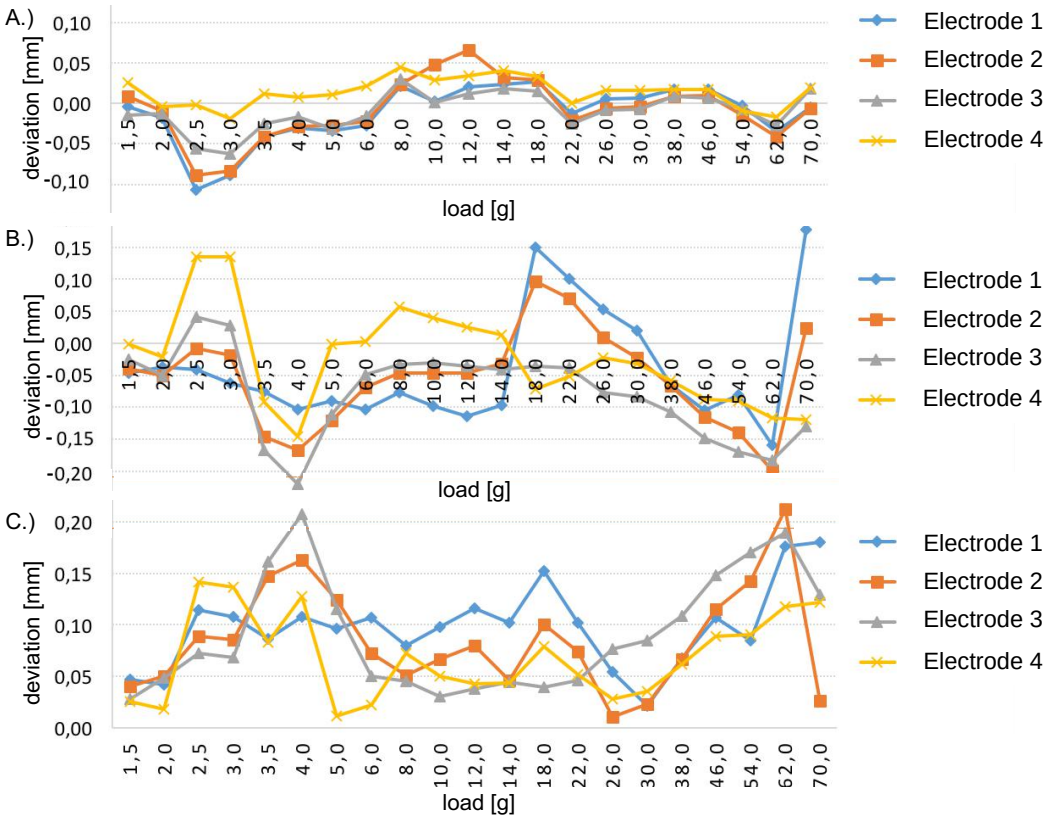

Figure 5.10: Deviation of (A) x electrode coordinates, (B) y electrode coordinates and (C) z electrode coordinates in the first spline dependent on the force at the E-module of 621.5 MPa. The figure is adapted from [S9], [152].

tissue thickness. For simplification, the tissue patch was fixed on the lower surface. The tolerance for perturbation was set to 0.02 mm. The simulation results are shown in Figure 5.11 (A-C).

5.3.6 PentaRay catheter in a sphere model mimicking the left atrium

The left atrium was a simplified model of a sphere model with a diameter of 40 mm and tissue thickness of 2 mm. For simplification, the outer surface of the sphere was fixed (cf. Figure 5.11 (D-F)).

The coefficient of friction was set to 0.017. In this scenario, every cylindrical area of the catheter and each electrode was defined as the contact area. The penetration tolerance was set to 0.02 mm. In Figure 5.12, the sectional images of the deformations of the PentaRay catheter splines are depicted for forces of 1g, 5g, and 62g.

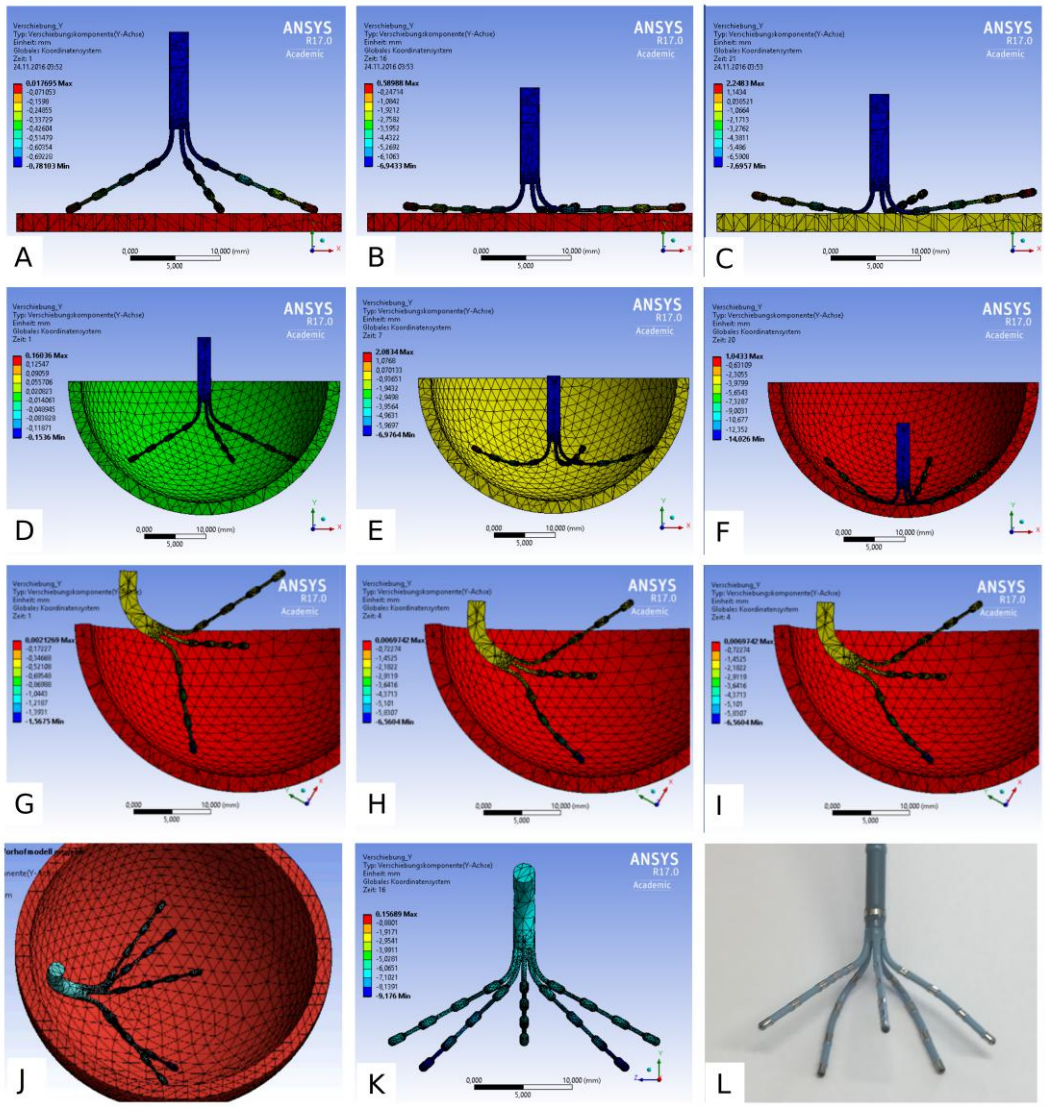

Figure 5.11: Sectional images of PentaRay catheter on a patch with tissue properties (A) 1.5g, (B) 30g, (C) 70g. Sectional images on the symmetrical plane of the model. The force in (D) is 1g, (E) 5g, and (F) 62g. Sectional images of a strongly deformed PentaRay catheter in (G) its initial state with a force of 1.5 g. (H) Deformation of the PentaRay catheter at an acting force of 3 g. (I-J) Broom-shaped splines at an acting force of 10 g with most electrodes having no tissue contact. (K) Deformed splines (top view). (L) Optical measurement of the deformed splines. The figure is adapted from [S9] [152].

In clinical cases, the PentaRay splines can be strongly deformed, similar to the broom-shaped deformation of the splines in the following figure. In these cases, most electrodes do not have contact with the tissue (cf. Figure 5.11(G-I)).

The figure shows the broom shaped splines from another viewpoint of the PentaRay catheter (cf. Figure 5.11(J)). The deformed splines are depicted in Figure 5.11 (K-L).

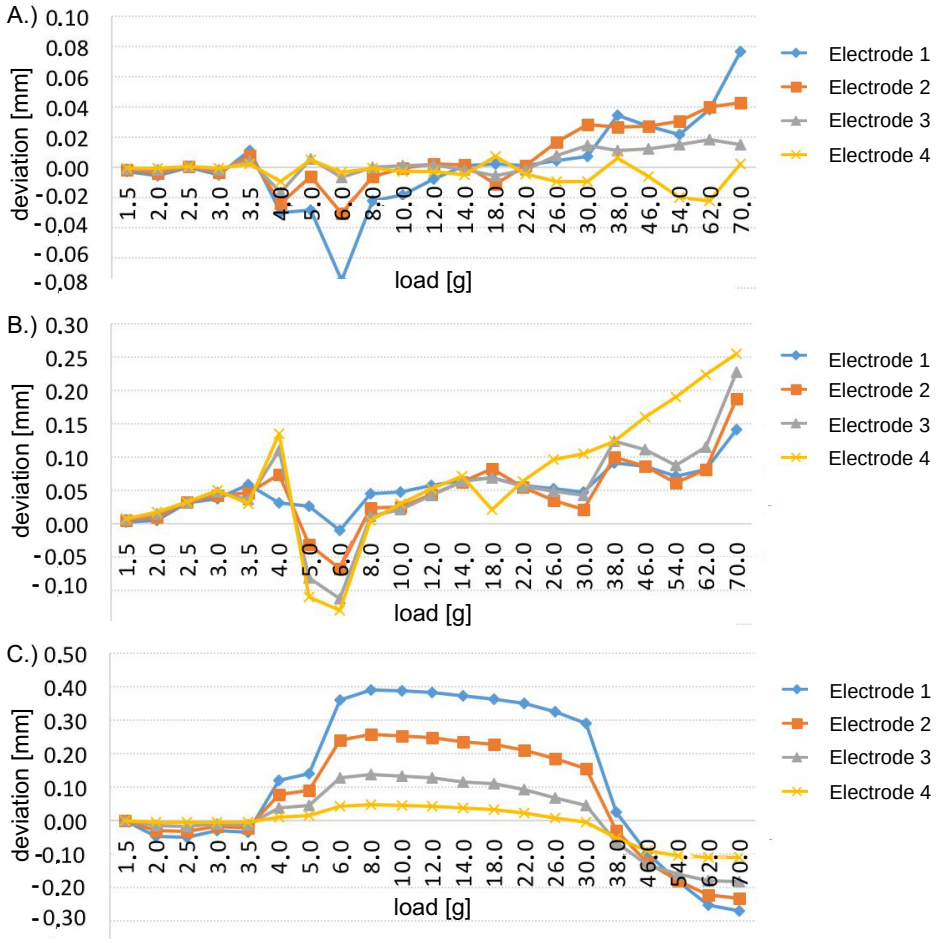

Figure 5.12: Deviation of the (A) *x*, (B) *y*, and (C) *z*-coordinates of the electrodes in the first spline of sphere model with tissue properties versus fixed sphere model. The figure is adapted from [S9], [152].

5.3.7 Detection of rotational sources in atrial fibrillation with the parameter cycle length coverage > 70% of AF cycle length

A circular catheter with ten electrodes centered on a rotational activity measured cycle length coverage values of 90%. The activation patterns of unipolar and bipolar recordings showed consecutive line patterns at the ideal rotational activity in a 3D patch over multiple cycles. With increasing distance between the center of the Lasso catheter and the core of the stable rotational activity, the activation patterns were transformed from line pattern with CLC of 91% to cosine pattern with CLC of 12% at a distance of 20mm. In this section, it was analyzed at which distance from the center of the rotational activity the line pattern and the parameter CLC > 70% can be detected if various clinical mapping catheters were compared. The rotational activity

is detectable with a 20-mm diameter Lasso catheter within a distance of 7 mm to the center of the rotational activity. At this distance, the CLC > 70% is observable. Distances beyond 7 mm from the core of the rotational activity display CLC < 50%, similar to planar wavefronts. The Figure 5.13 presents the activation patterns of the catheter designs Lasso, AFocusII, and PentaRay, and the corresponding quantitative parameter CLC for the detection of rotational activity. Only within the distance of 0 to 7 mm could a stable rotational activity be identified with the parameter CLC > 70% by using the circumferential mapping catheters of 15 - 25 mm in diameter. In contrast to the PentaRay catheter (35 mm diameter), rotational sources were detected up to a distance of 12 mm from the core of the rotational activity. Beyond a distance of 12 mm from the core, no further rotational activity was detectable. The Figure 5.13 (A) displays the activation time patterns of the catheters with the Lasso, AFocusII, and PentaRay catheters. Within a distance of 7 mm to the rotor core, the Rotor activity could be detected with the Lasso, AFocusII, and the PentaRay catheters (cf. Figure 5.13 (B)). Because of the larger diameter of the PentaRay catheter, the ideal rotor could be detected even when the catheter center was placed at a distance of 14 mm to the rotor core (cf. Figure 5.13 (B)). In the realistic atrial geometry model with included fiber orientation, the CLC was measured when the Lasso catheter was placed at different distances to the center of the rotational activity (cf. Figure 5.13 (C-D) (red dots)). The results were similar to those in the ideal tissue patch (cf. Figure 5.13 (C-D) (black line)). However, because of disturbing effects like wave collisions and more irregularities, the detected CLCs variated more and this resulted in larger values of CLC with increasing distance to the core. These findings show the difficulty of rotor detections when the catheter is not placed centered at the core of the rotational activity.

5.3.8 Impact of mechanical deformation of the PentaRay catheter on the signal measurement quality at 3D fibrosis tissue

Sinus rhythm excitations resulted in curved wavefronts around the large fibrosis region and in collisions in the lower part of the fibrotic border zone. The resulting peak-to-peak map correlates with the fibrotic region. However, in the lower part, the border zone could not be detected clearly. The Figure 5.14 shows the deformed PentaRay catheter splines at 3D fibrosis during sinus rhythm, when all electrodes have contact to the tissue.

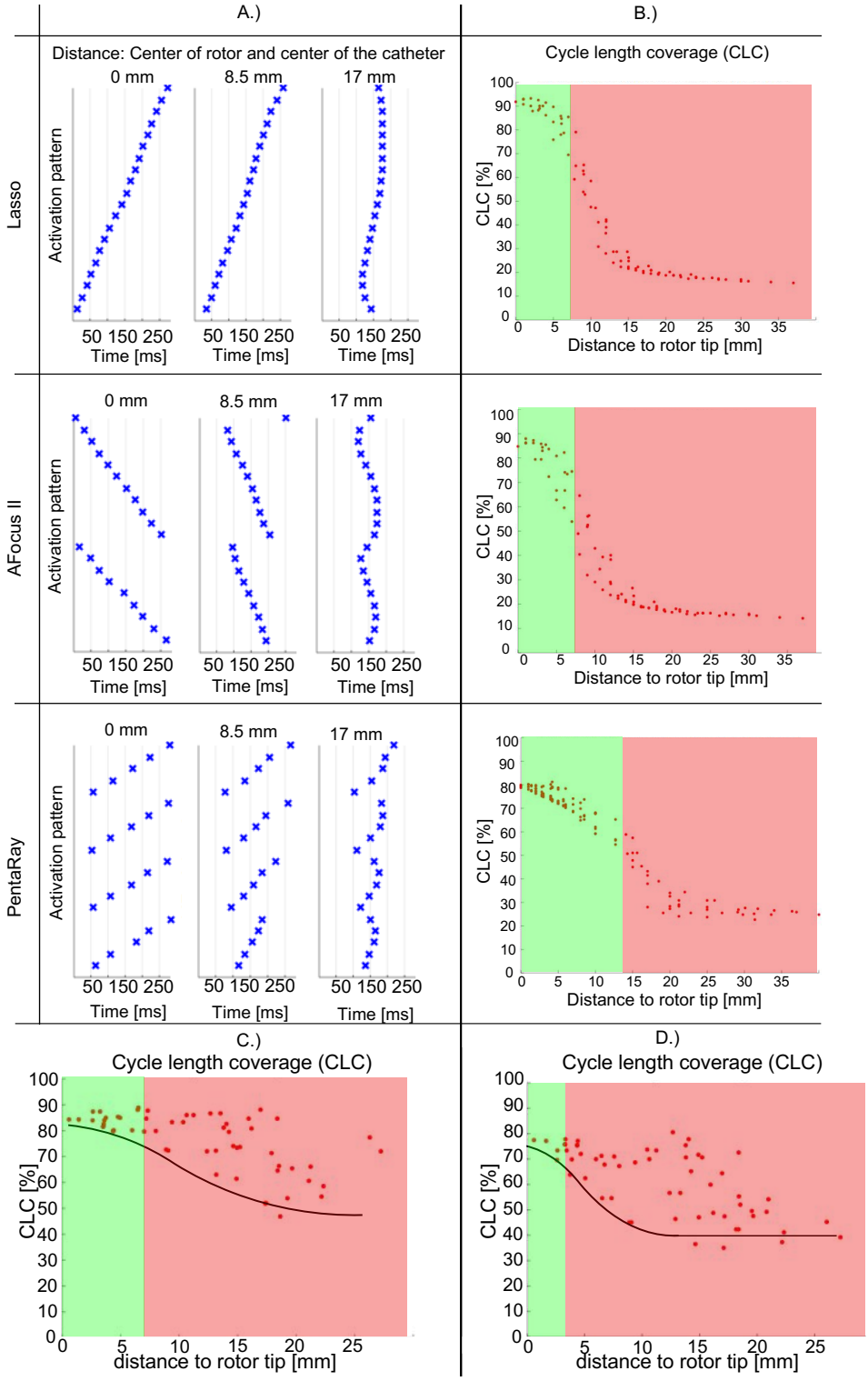

Figure 5.13: (A) The activation time patterns of Lasso, AFocusII, and PentaRay catheters at distances 0 mm, 8.5 mm and 17 mm to the rotor core. (B) Resulting CLC diagrams dependent on the distance to the core of the rotational activity within a 3D atrial patch model. The green area displays the region where the AF sources could be detected (with the parameter CLC>70%, for the PentaRay CLC>60%). CLC measurements (C) with the Lasso catheter (20 electrodes, diameter of 25mm), (D) with the Lasso (10 electrodes, diameter of 15 mm). (Red dots: measurements in the realistic atrial model), (black line: ideal rotor in the patch). (Green: region of possible rotor detection with the parameter CLC>70%). The figure is adapted from [S5], [117][118].

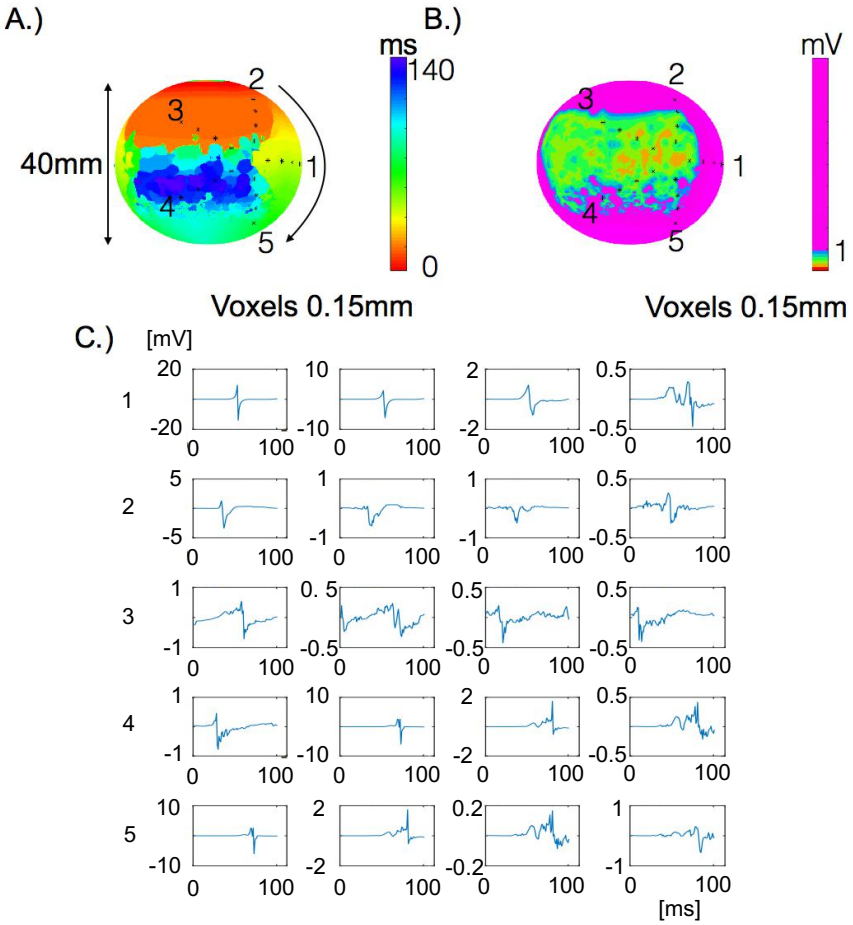

Figure 5.14: Deformed PentaRay catheter at 3D Fibrosis during Sinus rhythm. (A) LAT map with electrode positions displayed. (B) Peak-to-peak map with deformed electrode positions displayed. (C) Resulting unipolar recordings measured with deformed electrode positions.

5.3.9 Catheter designs and their ability to detect rotational sources within a 3D-AF model incorporating heterogeneities

The ability to detect rotational sources was investigated using a circumferential catheter (diameter 12 mm) and a novel square-like catheter with 64 electrodes. The catheter with an interelectrode distance of 3 mm was placed in the spherical 3D-AF model (0.15 mm x 0.15 mm x 0.15 mm) with the degree of heterogeneity (fibrosis) of 40%. The Figure 5.15 shows the transmembrane potential map with a double-loop rotational activity at the fibrotic region and a focal exit at the top fibrotic border. The two parts of the figure-eight reentry are marked in Figure 5.15. Notably, the figure-

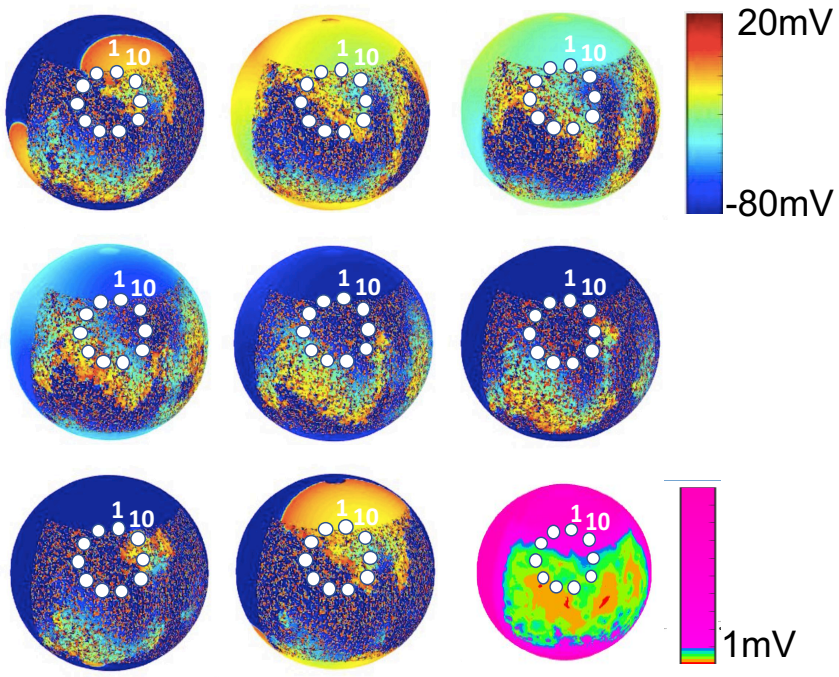

Figure 5.15: Transmembrane voltage maps of multiple rotational and focal activities in the 3D sphere model using an integrated Lasso catheter (white dots). Additional corresponding peak-to-peak map with Lasso electrode positions displayed. Before the focal wave (focal exit at the fibrotic border) development there is a thin channel showing small amplitudes because of little-activated cells.

eight pattern moved cycle by cycle. The observed rotational patterns were stable over multiple cycles. After six consecutive AF cycles, the figure-eight pattern could not be detected further because of wave collisions.

When using the 20 mm circumferential catheter, the rotational activity was not identifiable (cf. Figure 5.16(A)) although the catheter was placed close to the rotational

sources. At the position B, the rotational activity could be identified (cf. Figure 5.16(B)) using the parameter CLC > 70%.

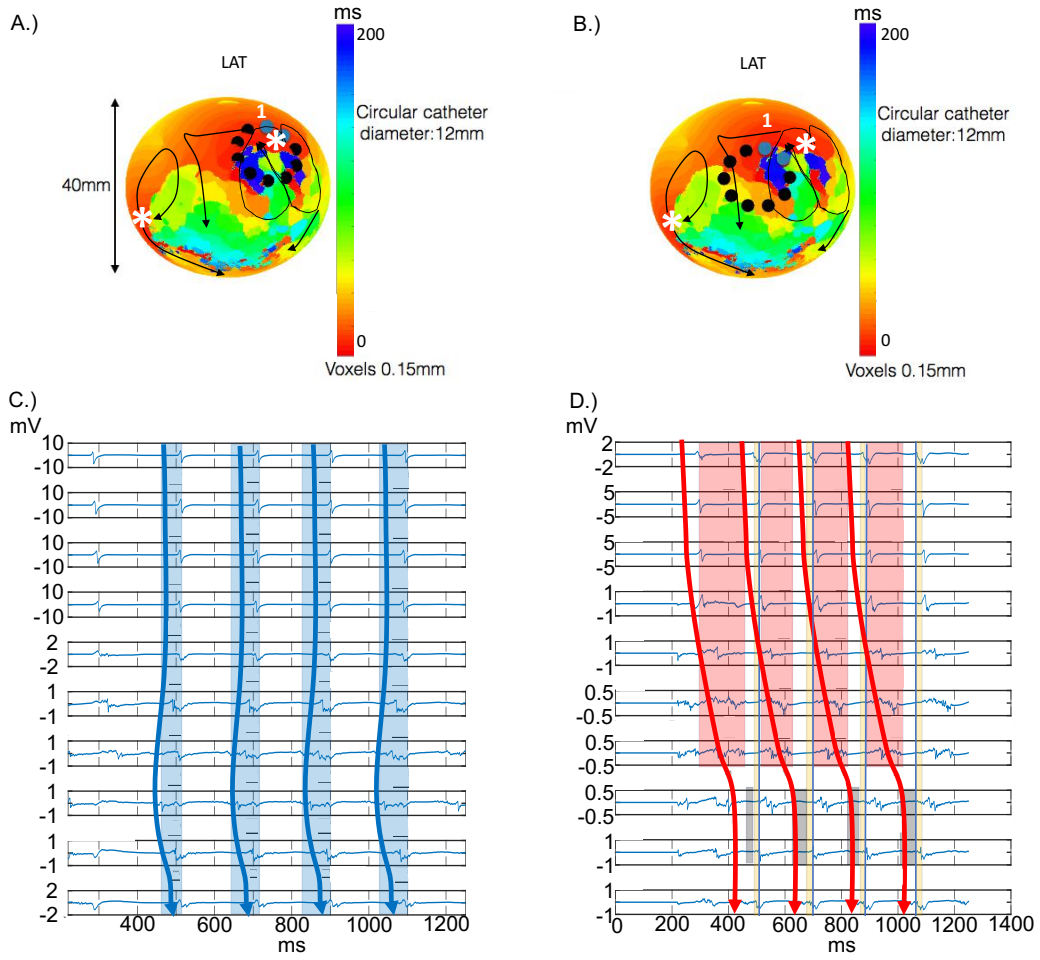

Figure 5.16: (A) LAT map of multiple rotational and focal sources at a 3D fibrosis region with placed Lasso catheter. Black lines symbolize the direction of propagation of the different excitation waves. The white stars symbolize the focal exit locations. (C) Resulting signal recordings of the placed Lasso catheter. Although the Lasso catheter was placed directly at the figure-eight pattern, no line pattern and CLC > 70% was detected. If the catheter was placed in a distance to the left site (B), the gradient pattern could be detected in the unipolar recordings (D).

In this sphere model during persistent AF with multiple rotational and focal sources, the resulting peak-to-peak map differed in comparison to the peak-to-peak map (cf. Figure 5.17A.)) during the sinus rhythm. The Figure 5.17 B.) presents measurements with the Lasso catheter above the fibrotic region, centered at the rotational activity. In this case, all electrodes have contact. These unipolar recordings resulted in a typical line pattern with CLC > 70%. But the LATs could not be clearly detected above the fibrotic region.

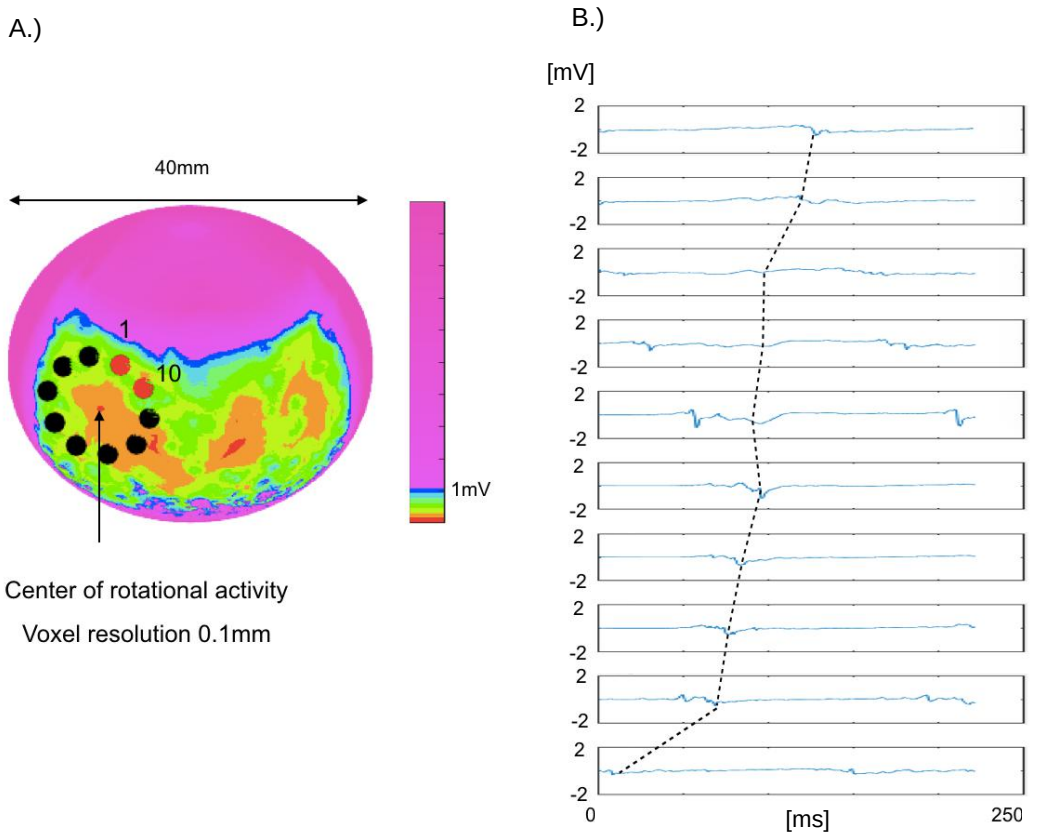

Figure 5.17: Rotational activity of AF at 3D fibrosis measured with Lasso catheter with the parameter CLC > 70%. A.) Lasso catheter centered at rotational activity. Peak-to-peak map showing low voltage area < 1mV. B.) Unipolar recordings. Upper signal was measured with electrode 1. Lower signal was measured with electrode 10.

5.3.10 New DecaRay catheter design

New catheter designs were analyzed with mechanical deformation models. In the Figure 5.18, a DecaRay catheter with 10 splines having 40 electrodes is shown with parameters similar to the deformation models of the PentaRay catheter, but with doubled splines. The catheter was deformed with a friction coefficient of 0.2. The Figure 5.18 (C) shows the factor of the force needed to deform the splines of the DecaRay versus that of the PentaRay catheter.

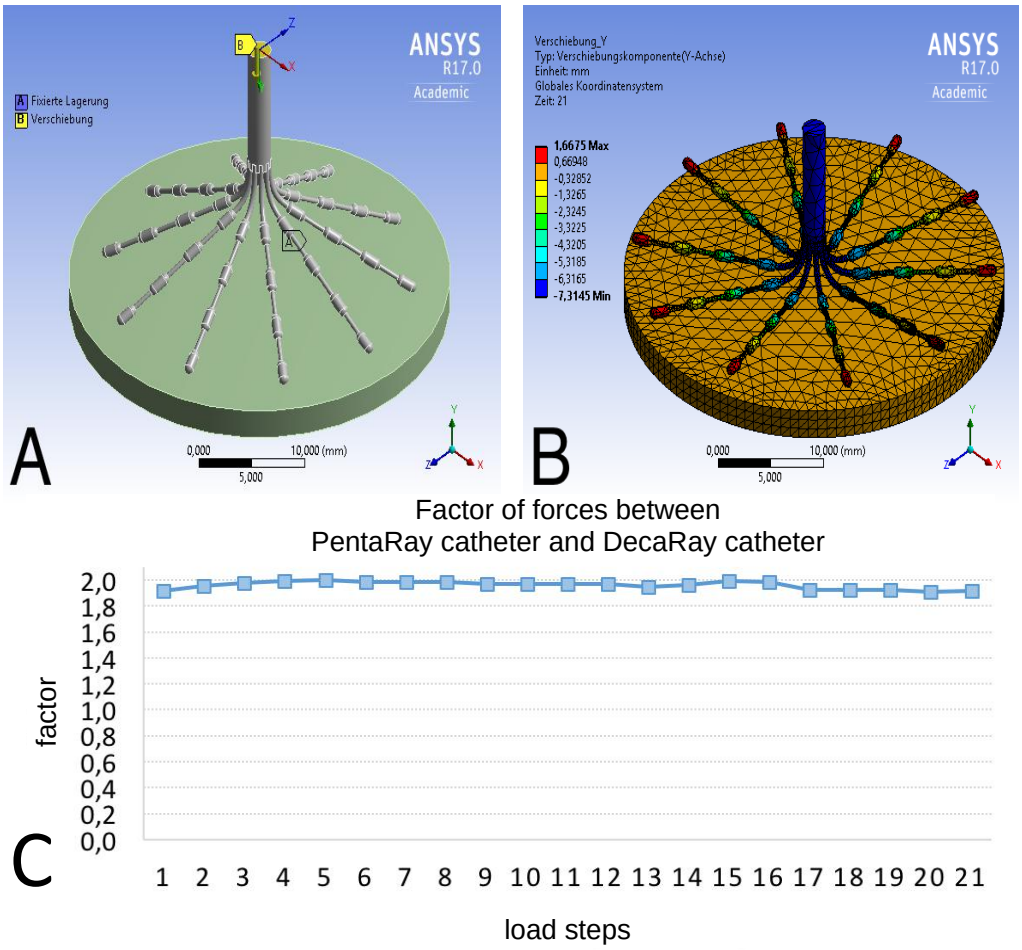

Figure 5.18: A.) Geometry of the mechanical deformation model of a new DecaRay catheter with 10 splines having 40 electrodes. (B) Deformed DecaRay catheter with 10 splines having 40 electrodes. (C) Force factor between forces for DecaRay catheter and PentraRay catheter. This factor is nearly 2 in all load steps. The figure is adapted from [S9], [152].

5.3.11 Detecting multiple rotational and focal activities using a noval curved square catheter

The transmembrane voltage values and extracellular potentials of a figure-eight pattern are shown in Figure 5.19 A-B.). 64 unipolar signals were recorded using a noval curved square catheter (8 x 8).

The resulting extracellular potential maps of the left figure-eight pattern and the square catheter are shown in the Figure 5.20 (B).

From multiple rotational activities within the fibrotic region, only some could be detected by the Lasso catheter. In contrast to the circumferential catheter, a high-density mapping catheter with large mapping field (curved grid catheter with 64 electrodes, measuring 24 mm x 24 mm) could cover and detect multiple interacting

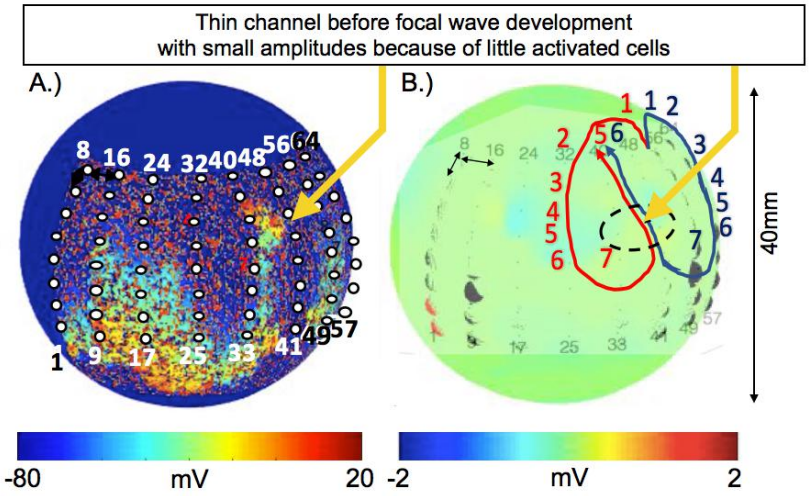

Figure 5.19: A.) Transmembrane voltage map showing the thin channel before focal wave development. B.) In the extracellular potential map, the excitation is displayed in a figure-eight pattern indicated by red and blue arrows. The curved square catheter (8 x 8) had the interelelectrode of 3mm.

rotational and focal activities with one single measurement placement (cf. Figure 5.20 and Figure 5.21).

5.3.12 Clinical validation of simulated signal morphologies at rotational activities

The novel catheter geometry in form of a curved grid covered the fibrotic region, displaying low voltage and slow conduction. The resulting unipolar recordings of both rotational activities (left and right parts of the figure-eight pattern) are presented in Figure 5.21(B) and (D). These morphologies were close to the clinical measurements in Figure 5.21(A) and (C).

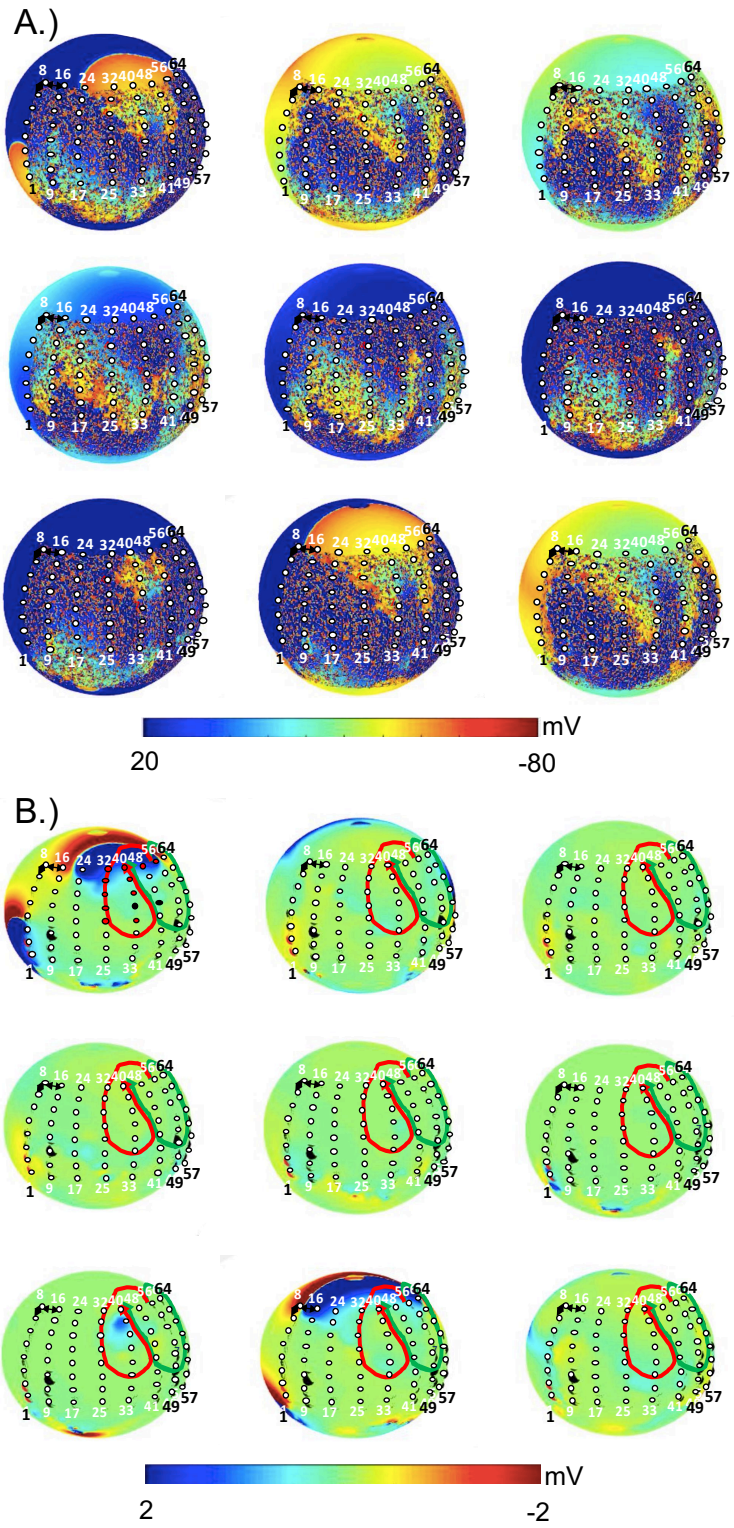

Figure 5.20: (A) Transmembrane voltage maps of rotational and focal activities within the 3D sphere model. (B) Corresponding extracellular potential map. The red line symbolizes the left, and the green line symbolizes the right rotational activity of the figure-eight excitation pattern. The curved square catheter with 64 electrodes (8 x 8) is placed on the transmembrane voltage maps and on corresponding extracellular potential maps. The time between two figures is 20ms.

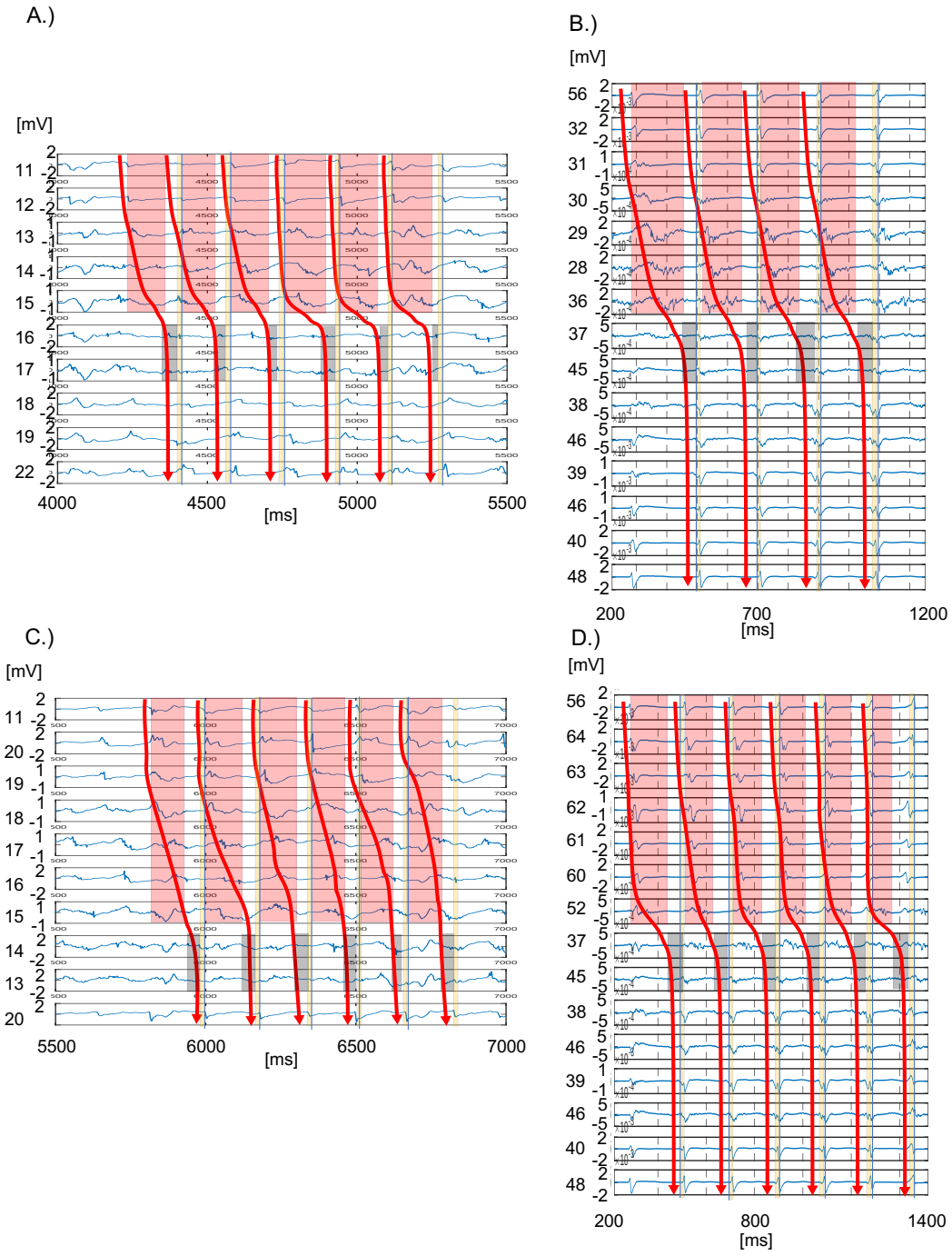

Figure 5.21: (A) Clinical measurement of a rotational activity with the AFocusII catheter (inner loop). (B) Corresponding simulation result with similar signal morphologies of the left part of the figure-eight pattern. (C) Clinical measurement with the AFocusII catheter of a rotational activity in the other direction (compare the order of the electrode numbers). (D) Corresponding signal morphologies of the right rotational activity of the figure-eight pattern. Red symbolizes the activation gradient pattern. Clinical data was delivered from Dr. Jadidi, University Heart Center Freiburg Bad Krozingen, Germany. Gray symbolizes the time of the thin channel before the development of the focal exit, compare Figure 5.15. Yellow symbolizes the time of the development of the focal exit.

5.3.13 New electrode concepts

There is a need for new catheter designs. This chapter presents new electrode designs and new electrode concepts. Commonly used Lasso electrodes consist of one cylindric metal electrode. The Figure 5.22 shows a new electrode concept of mini metal electrodes with the volume of a Lasso electrode. This electrode arrangement made possible optimized measurements of the direction of propagation, conduction velocity of the measured excitation, and the distance to the tissue (cf. Figure 5.22). In the case of a planar wave (direction of propagation in y-direction), the unipolar signal recordings 2 and 3 were equal. In the case of an ectopic focus, the activation time of the unipolar signal three was measured earlier than the activation time from the unipolar signal 2.

5.4 Discussion

There are no automatic methods implemented in the clinical navigation systems Carto, NavX, or Rhythmia for detecting rotational and focal sources. This chapter presents the impact of commonly used and new catheter geometries on the ability to detect AF sources. These findings show that commonly used catheters can detect rotational activity only when the catheter is placed within the distance of 5 to 7 mm to the rotor center with the parameter CLC > 70%. Also, realistic fibrosis simulations of the high resolution were used for the analyses of the different catheter designs. In this chapter, new catheter designs like the square catheter and curved grid catheter in the 3D sphere model were analyzed regarding the capability to detect AF sources. With the 8 x 8 curved grid catheter (an interelectrode distance of 3mm), multiple rotational and focal sources could be detected by placing single measurement. These results of rotational and focal sources at low-voltage regions are close to the clinical measurements. In order to obtain further realistic simulation results, the deformations of the splines of the PentaRay catheter were modeled on a mechanical deformation model. The results of the deformations were evaluated and were found to be close to the experimental measurements. Errors between the model deformations and the experimental deformations were smaller than 0.2 mm. This deformation model was used to read out unipolar and bipolar signals in the sphere model with multiple rotational and focal sources at 3D fibrosis with high resolution. Future catheters with a higher density of electrodes might allow a more robust detection of multiple interacting rotational and focal sources. These findings present an impact analysis of catheter geometries, deformations of splines, electrode sizes and forms, and present possibilities and limitations for the detection of AF sources. Also, optimization potentials of new catheters were presented in this chapter. With these findings and the optimization potentials

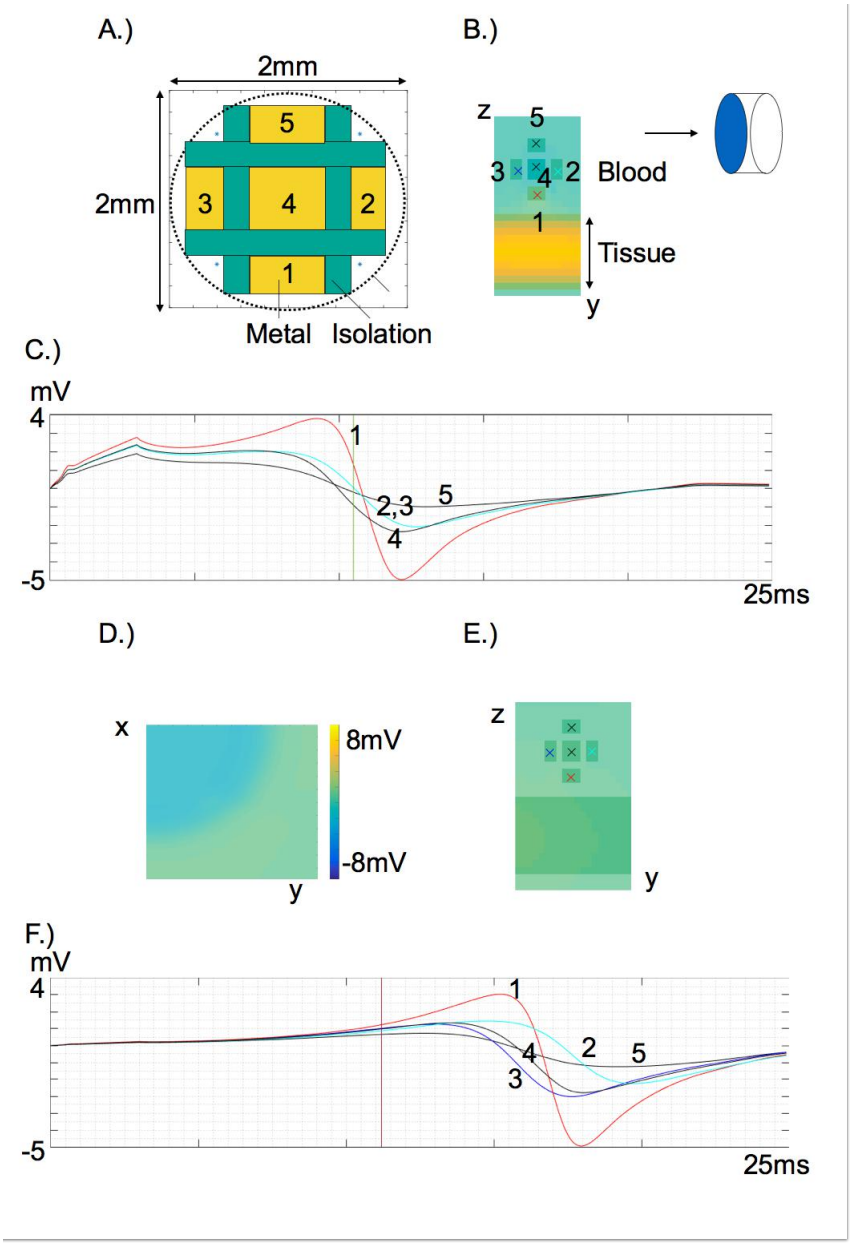

Figure 5.22: (A)-(C): Optimized measurement using a new electrode concept in the case of a planar wave. (A) Electrode arrangement with metal electrodes (1-4). (B) (zy-view) of the extracellular potentials including the tissue, blood an electrode positions. (C) Unipolar electrograms 2 and 3 resulted in the same activation time because the planar wave (direction of propagation in y-direction) was parallel to the electrodes 3 and 2. The unipolar signal 1 is larger than 5, 3, and 2. (D)-(F):Optimized measurement using a new electrode concept in the case of an ectopic focus. Extracellular potential map (xy-view) of the focal wave excitation. The ectopic focus is located top left. (F) (zy-view) of the extracellular potentials including the tissue, blood an electrode positions. Signal 1 resulted in the largest amplitude, which is the reason why electrode 1 is the closest electrode to the tissue.

described, future catheter designs and electrode concepts could be developed for more accurately and robustly detecting AF sources.

5.5 Resulting Publications

Results of this chapter were published in :

M. Rottmann, W. Kaltenbacher, G. Seemann, V. Markstein, H. Lehrmann, J. Allgeier, R. Weber, O. Dössel, T. Arentz, A. S. Jadidi. Impact of Catheter Design for Identification of Rotational Activity in Atrial Fibrillation. Deutsche Gesellschaft für Kardiologie- Herz- und Kreislaufforschung Clin Res Cardiol, Springer Berlin Heidelberg, 106 (Suppl 1), 2017.

W. Kaltenbacher, M. Rottmann, O. Dössel. (2016). An algorithm to automatically determine the cycle length coverage to identify rotational activity during atrial fibrillation - a simulation study. Current Directions in Biomedical Engineering, 2(1), pp. 167-170, 2016.

C. Reich, T. Oesterlein, M. Rottmann, G. Seemann, O. Dössel. Classification of cardiac excitation patterns during atrial fibrillation. In Current Directions in Biomedical Engineering, Vol. 2(1) , pp. 161-166, 2016.

M. Rottmann, M. W. Keller, T. Oesterlein, G. Seemann and O. Dössel, Comparison of different methods and catheter designs to estimate the rotor tip position - A simulation study, Computing in Cardiology, pp. 133-136, Cambridge, 2014.

CHAPTER 6

Evaluation of Ablation Strategies with Simulation Models

"Essentially, all models are wrong, but some are useful."

— George Edward Pelham Box

6.1 Introduction

Until today, the mechanisms of AF and the effects of different ablation strategies on the termination of AF are still not clear. PVI became the standard procedure. But also CFAE ablation, rotor guided, and low voltage guided ablation strategies were used ablation strategies. In the literature, there are simulation studies of different ablation strategies [167] within the simulated healthy tissue. This work presents the effects of different ablation strategies on AF models incorporating high-resolution, three-dimensional fibrosis.

6.2 Methods

6.2.1 Modeling of different ablation strategies

Different ablation strategies were investigated in simulation models of persistent AF with multiple rotational, focal, and wavelet activities. Ablation dots and lines were integrated into atrial tissue models incorporating high-resolution, three-dimensional fibrosis. Ablation lines were modeled as non-conductive regions. The ablation strategies investigated in 3D patches, sphere models, and atrial geometry models were:
- box isolation of a low-voltage area [168],
- ablations at the low-voltage area [135],
- pulmonary vein isolation.

6.3 Results

6.3.1 Different investigated ablation strategies at proarrhythmogenic fibrosis regions

6.3.1.1 Ablation lines to fibrotic regions

AF was induced by two stimulations from the left and lower side. An integrated ablation line to the fibrotic region did not result in AF termination (cf. Figure 6.1). The rotational activity around the fibrotic region did not terminate although the ablation line was integrated. The wavefront was not stopped at the ablation line and could avoid the non-conducting ablation line. The Figure 6.1 presents the induction and maintenance of persistent AF even if an ablation line was integrated into the fibrotic region.

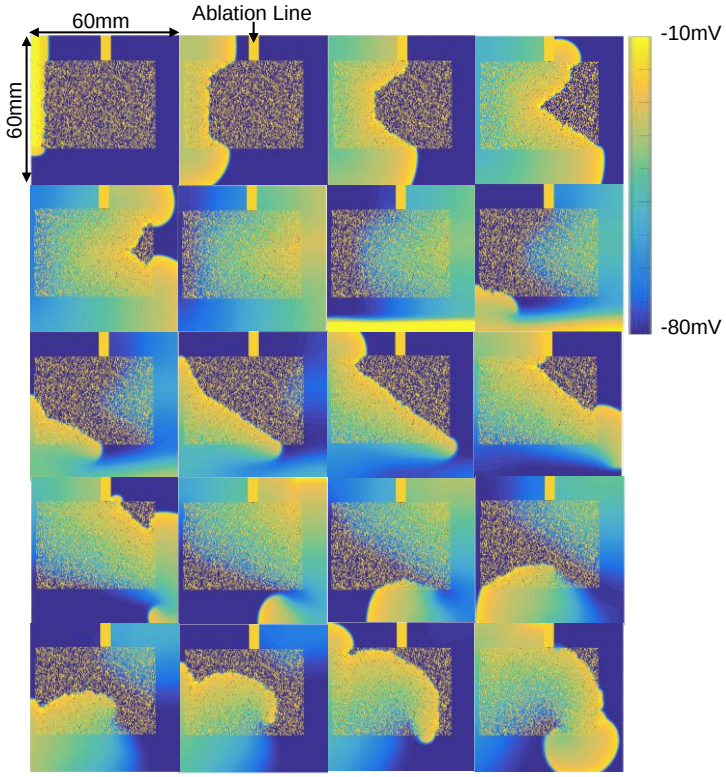

Figure 6.1: Inducing and maintaining persistent AF in 10 ms steps. AF was induced by two stimulations from the lower and the left side. First, the rotational activity meandered within the healthy tissue and then anchored between the fibrosis region and healthy tissue. Further, another rotational activity anchored around the fibrosis region and collided with another excitation wavefront around the fibrosis region.

6.3.1.2 Isolation lines around fibrosis regions and additional lines to the isolated region

In order to isolate proarrhythmogenic substrates, ablation lines around the fibrosis region were integrated into the simulation model which is depicted in Figure 6.2. The rotational activity induced could not be anchored within the fibrosis region nor between fibrosis and healthy tissue. Because of the additional vertical ablation line to the isolated region, also the rotational activity around the isolation box could not be anchored and terminated. The Figure 6.2 shows the results of the ablation line to the fibrosis region and additional box isolation of fibrotic regions. In the case of ablation lines to fibrotic regions, AF was not terminated, but in the case of box isolation, AF was terminated.

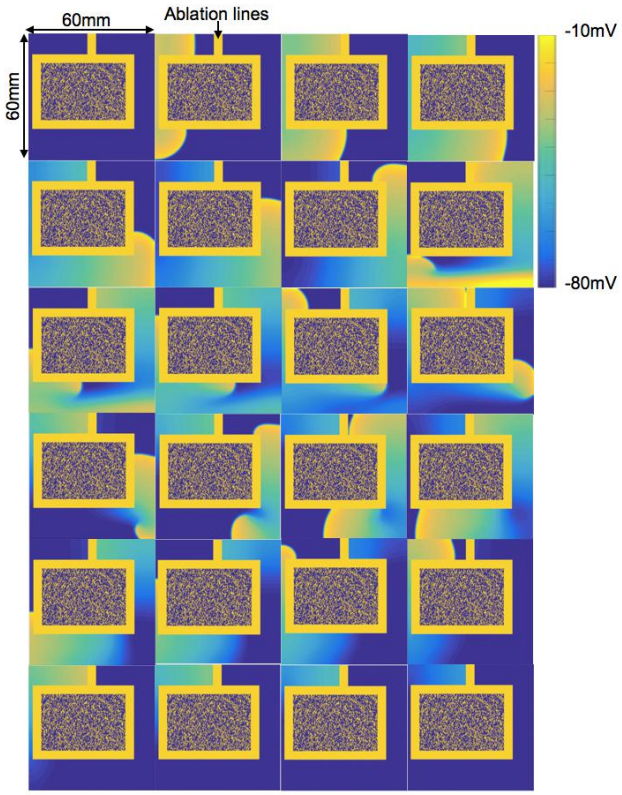

Figure 6.2: Box isolation of fibrotic regions. The time steps of the following pictures are in 200 ms. AF was induced by two stimulations from the lower and the left side. Because of the isolation of the fibrotic area, the rotational activity could not be anchored within the fibrosis region. The additional vertical ablation line in the upper region stopped the rotational activity around the isolation box. AF was terminated in the last figure parts.

6.3.1.3 Pulmonary vein isolation in a sphere model mimicking the left atrium

Fibrosis was implemented in the sphere model between the four pulmonary veins. The degree of fibrosis in the fibrotic region was 20%. Persistent AF was induced by 2 stimulations (cf. Figure 6.3) and resulted in figure-of-eight patterns over multiple AF cycles. Pulmonary vein isolation did not stop AF in this model (cf. Figure 6.3).

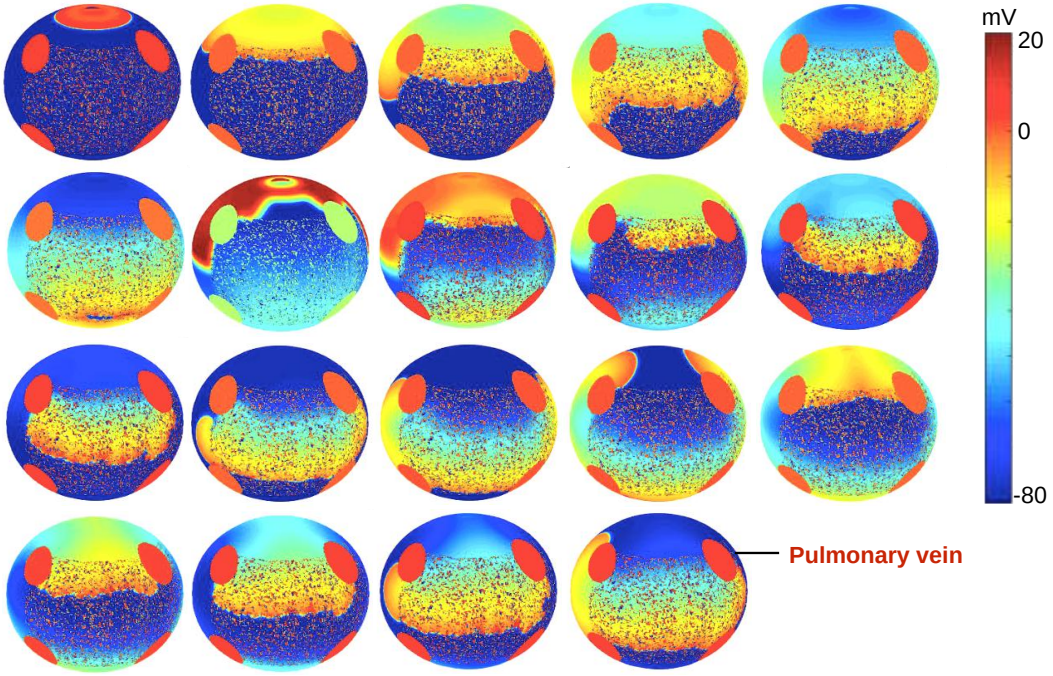

Figure 6.3: Pulmonary vein isolation (red symbolizes the isolated veins). AF was induced by two stimulations. The resultant focal sources were located at the border zone near the pulmonary veins. The time steps of following pictures are in 20 ms.

In the case of the same fibrosis size and the same stimulation protocol but the integrated degree of fibrosis of 30% in the fibrotic area, the focal sources were also observed near the left pulmonary veins (cf. Figure 6.4). Also in this simulation pulmonary vein isolation did not stop AF (cf. Figure 6.4).

6.3.1.4 Pulmonary vein isolations in persistent atrial fibrillation with multiple rotational, focal, and wavelet activities within a realistic atrial model

Pulmonary vein isolation resulted in reduced rotational sources (cf. Figure 6.5). In the isolated pulmonary vein region, rotational and focal activities existed further (on the right side of the PVI (white line) in Figure 6.5), but these AF sources could not

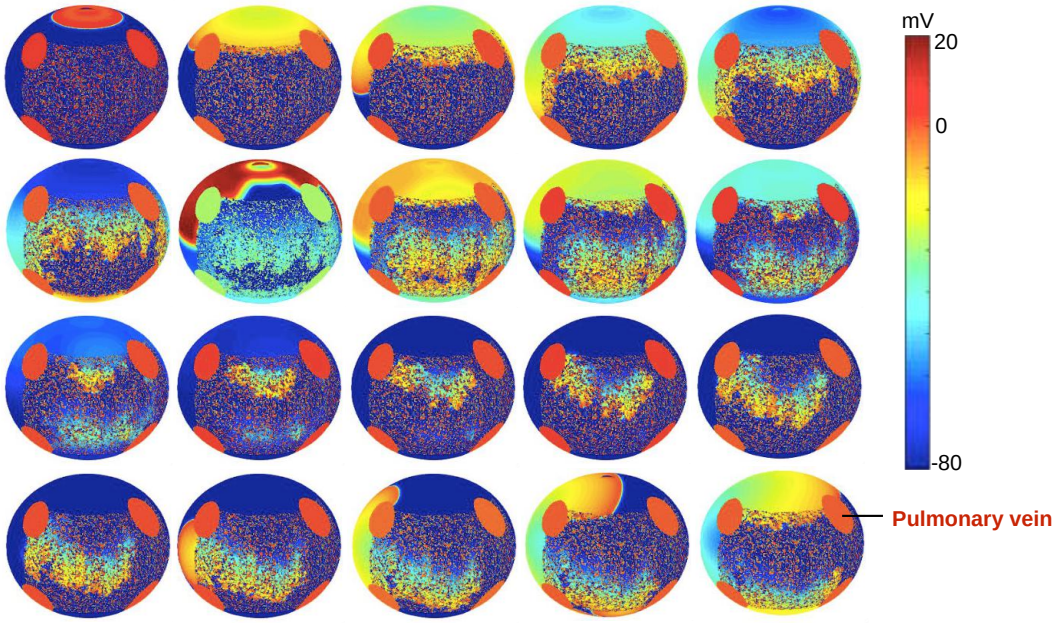

Figure 6.4: Multiple rotational and focal sources within fibrosis region with the degree of fibrosis at 30%. The red circles symbolize the isolated veins. AF was induced by two stimulations. The resulting focal sources were located at the border zone near the pulmonary veins. The time steps of following pictures are in 20 ms.

interact and influence the atrium (on the left side of the PVI in Figure 6.5) because of the isolation.

Pulmonary vein isolation was implemented in the same atrial model with the same fibrosis region and the same stimulations as described in Figure 3.27.

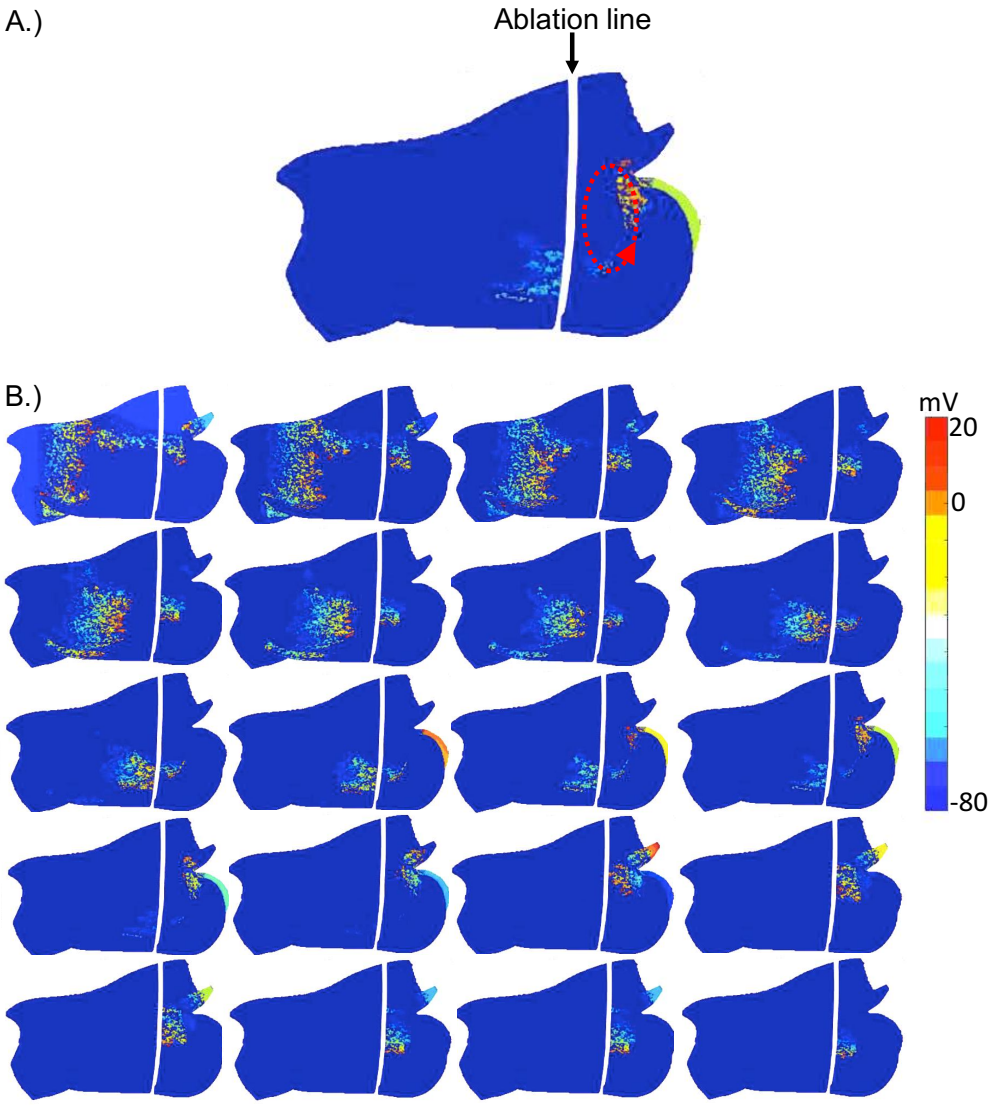

Figure 6.5: Impact of pulmonary vein isolation on termination of AF sources in a realistic atrial simulation model with implemented 3D fibrosis region. The stimulation protocol and the fibrosis region is similar to the model described in Figure 3.27, but in this model (A) an ablation line (white line) is integrated. (B) Rotational (red in A) and focal activities existed further after the isolation (on the right side of the PVI (white line), but these AF sources could not interact furthermore with the tissue on the left side of the PVI.

6.4 Discussion

Simulation models offer the possibility to evaluate different catheter designs, methods for detection of rotational and focal sources, but also different ablation strategies can be evaluated. Single ablations in the fibrosis area displaying low voltage did not stop AF. However, the AF was terminated by the box isolation of the fibrosis region displaying a low voltage area and the additional ablation line from the isolated box to the edge of the simulation model. Pulmonary vein isolation did not stop the AF sources in all AF simulations. A large isolation region, which covered two veins and dense fibrosis tissue with focal exits locations reduced the proarrhythmogenic substrate and stopped AF behind the isolation line, in contrast to the simulations with small isolation regions around the pulmonary veins. Also clinical results of AF-free survival after selective voltage-guided ablation versus pulmonary vein isolation, depicted in Figure 6.6, show that PVI and additional selective voltage-guided ablation resulted in a higher AF-free survival rate than PVI only [135].

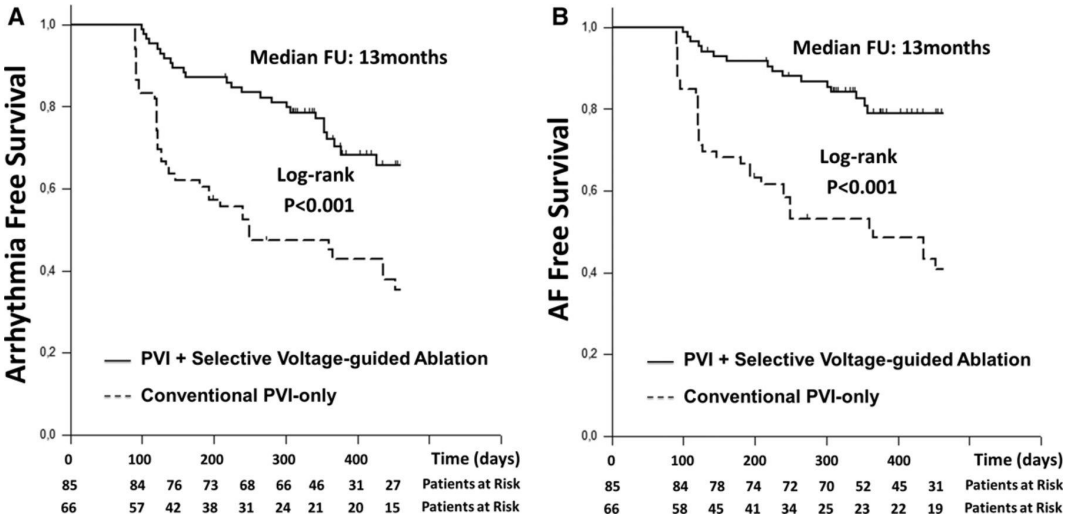

Figure 6.6: Kaplan Meier curves show freedom from (A) any atrial arrhythmia (B) and freedom from atrial fibrillation in patients undergoing PVI and selective substrate-based ablation vs. pulmonary vein isolation (PVI)-only approach. The figure is from [135] with permission.

CHAPTER 7

Experimental Evaluation of Fibrosis Simulation

"An experiment is a question which science poses to Nature and a measurement is the recording of Nature's answer. "

— Max Planck

7.1 Introduction

Cardiac arrhythmias are risk factors for sudden death. Fibrotic regions are correlated with cardiac arrhythmias. Despite extensive research, the effects of fibrosis on intracardiac recordings are still not clear. In the literature, simulations of excitations around fibrosis are mostly based on randomly distributed mathematical models or on extractions from real heart tissue from delayed enhancement MRI data. However, the disadvantage of delayed enhancement is the reduced resolution of 667 x 667 x 1500 μm^3 [169], [129]. The randomly distributed fibrosis models described in the literature were implemented into the whole tissue between the endocardium and epicardium. Also described in the literature are simulations based on 3D reconstructions of ventricular tissue sections, but without including fibrotic regions [170]. This simulation study in this work is based on a real fibrosis region of the high-resolution histological tissue sections of a mouse model. 3D fibrosis regions were reconstructed in high resolution from histological tissue sections and implemented in simulation models for analyzing signal characteristics of excitations around a fibrosis region.

7.2 Methods

7.2.1 Overview

The Figure 7.1 shows the workflow from histological tissue sections, segmentation of fibrosis regions, 3D reconstruction of fibrosis, and signal recording analysis from numerous field simulations.

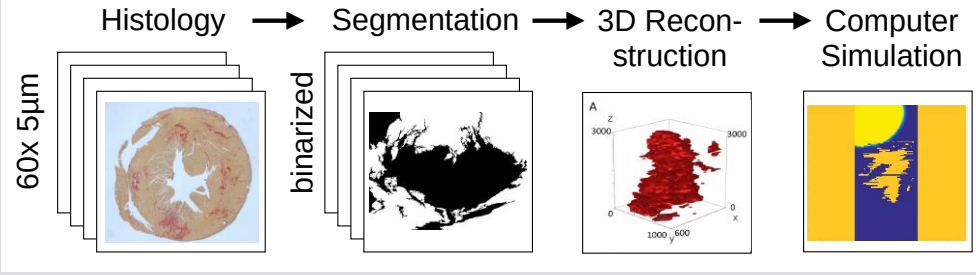

Figure 7.1: Workflow from histological tissue sections, segmentations of fibrosis regions, 3D reconstruction of fibrosis, and signal analysis from computer simulations. The figure is adapted from Rottmann et al. (2016) [171].

7.2.2 Histological tissue section

The histological tissue sections from the mouse heart were generated and delivered by Prof. Dr. med. Karin Klingel (Department of Molecular Pathology, University Hospital Tübingen, Germany).

In order to analyze the effects of fibrosis reconstructed from histological tissue sections on extracellular potentials, a Coxsackievirus B3 infection of ABY/SnJ [172] was used to induce fibrosis in mouse heart models. Fibrosis became obvious in mouse hearts models four weeks after inducing the Coxsackievirus B3 infection of ABY/SnJ. When fibrosis became obvious, the mouse hearts were fixed in 4% paraformaldehyde and were then embedded in paraffin. The mouse heart was cut in 60 x $5\mu m$-thick tissue sections of the left and the right ventricle.

7.2.3 Reconstruction of fibrosis areas from histological mouse sections

Forty images from a Zeiss Axioskop microscope (Carl Zeiss Microscopy GmbH, Jena, Germany) were used for reconstruction. Each histological image had the size of $750\mu m$ x $1000\mu m$. The fibrosis regions were reconstructed from histological tissue sections where each image represented a segment of the fibrosis. The Figure 7.2 shows an example of a $5\mu m$-thick tissue section with the fibrotic tissue stained in Sirius red.

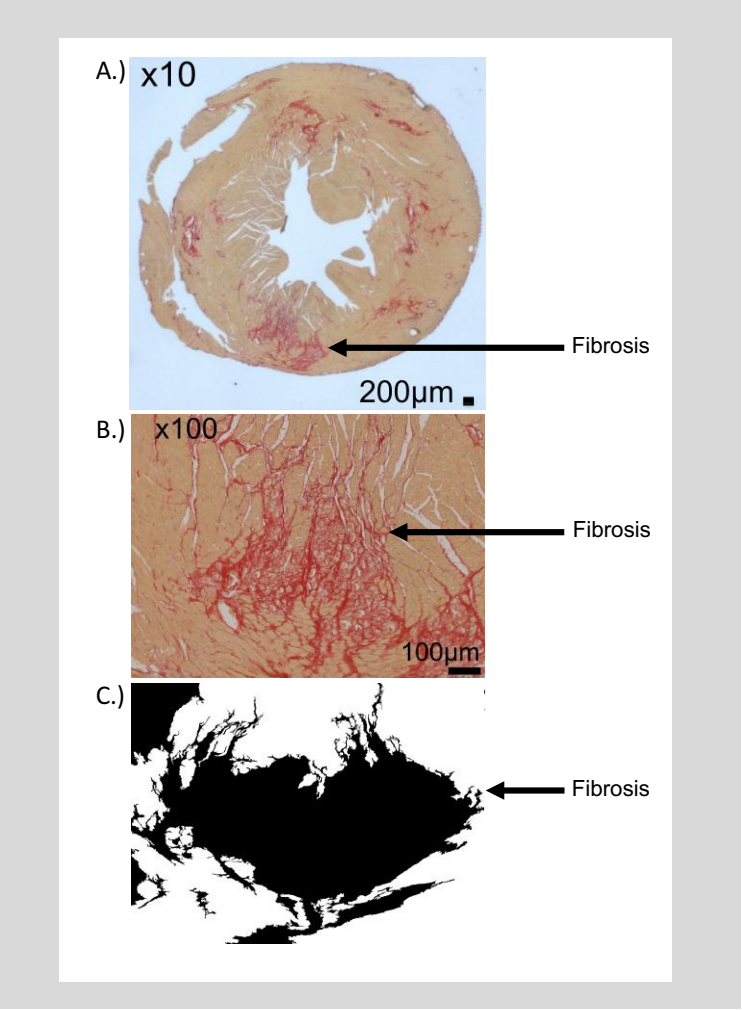

Figure 7.2: (A) Cross-section of the ventricles show fibrosis regions stained with the color Sirius red. (B) Zoomed focal fibrosis region in high resolution in a part of the cross-section of the mouse ventricles. (C) Segmented fibrosis region (black) surrounded by healthy tissue (white). The figure is adapted from Rottmann et al. (2016) [171].

The Figure 7.2 (B) shows a zoomed part of the cross-section of the mouse ventricles with focal fibrosis.

In a previous study [173] color thresholds were applied for the detection and quantification of collagen in Sirius red stained histological tissue sections. In this study, collagen areas were segmented (cf. Figure 7.2 (C) with color-based segmentation using a color thresholder program (image processing and computer vision toolbox) in MATLAB. The specific color threshold for collagen areas was detected in each histological image because of different densities of the Sirius red staining.

Images were rescaled to a voxel length of $12.5\mu m$. A scaling factor 20 was used to magnify the mouse scale to human scale. The thickness of the ventricular wall in mouse heart is 0.75 mm, in human heart 1.5 cm [174].The resultant segmented fibrosis regions were then stacked on top of each other.

In the next step, the segmented and registered 3D fibrosis region was rescaled by a scaling factor of 20 for human size. The resultant 3D fibrosis region was implemented into healthy tissue in a 3D patch of size 200 x 200 x 200 voxels with a voxel length of 0.25 mm. The fibrosis regions were programmed as non-conductive elements.

7.2.4 Calculation of intracardiac electrograms

As a ventricular cell model, the cell model ten Tusscher was used [80]. The monodomain equations were solved using the parallel solver acCELLerate [110]. Extracellular potentials were calculated from transmembrane currents using the sampling rate of 1kHz.

7.3 Results

7.3.1 Stimulations from different directions

The tissue was stimulated from different directions for analyzing the effects of fibrosis on the extracellular potential. The impact of the fibrosis region on a planar wave is shown in Figure 7.3. Using planar stimulation from the upper part of the tissue, the excitation wavefront was split, which resulted in various transmural angles and conduction velocities over time.

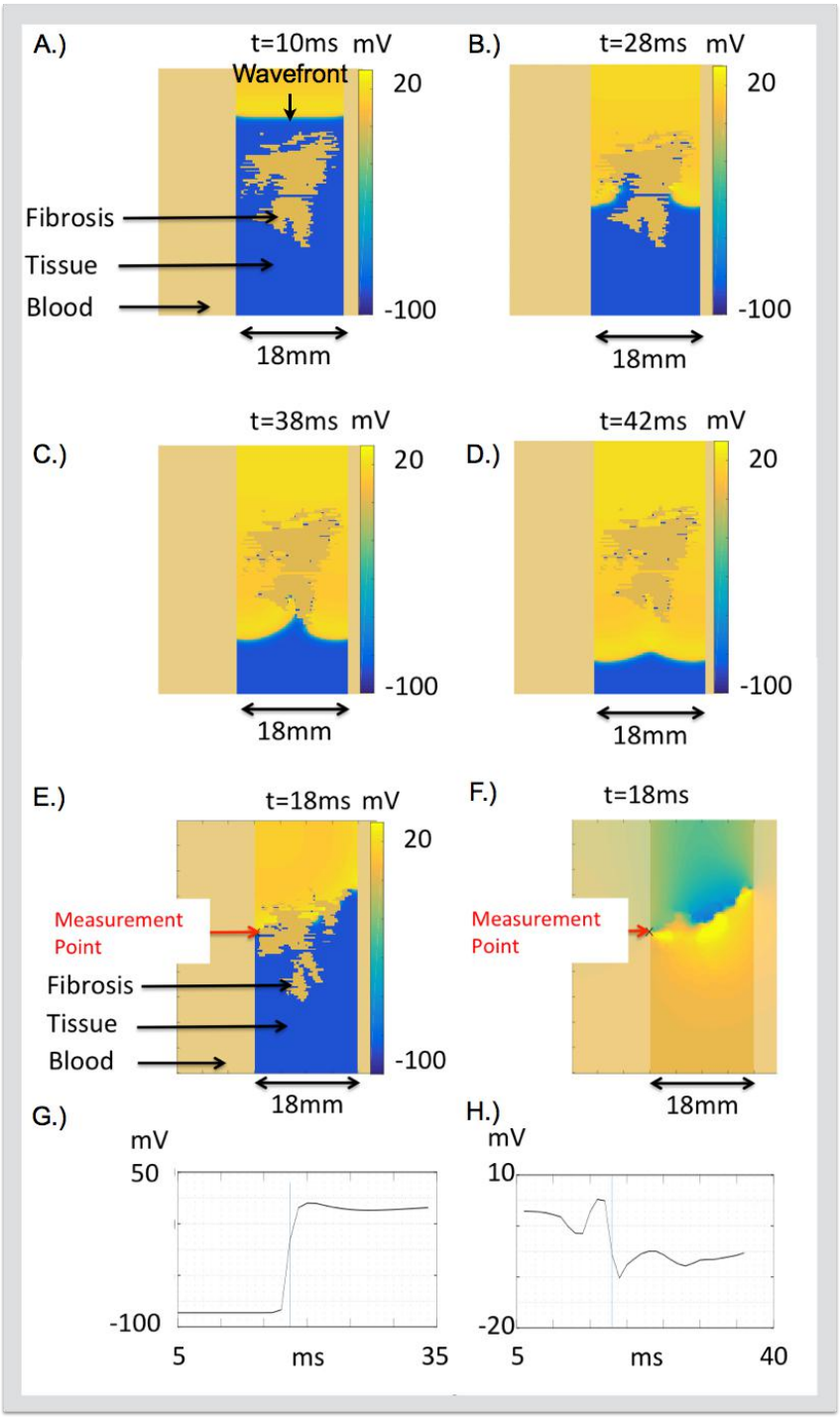

Figure 7.3: Excitation wavefront analysis at a cross-section in a simulation model of a reconstructed 3D fibrosis region. Transmembrane voltage was mapped at the times (A) 10 ms, (B) 28 ms, (C) 38 ms and (D) 42 ms. Signal analysis at the cross-section in a simulation model of reconstructed 3D fibrosis region of stimulation in the left upper corner (10 x 10 x 10 voxels). (E) Transmembrane voltage map and (G) measured transmembrane voltage. (F) Extracellular potential map and (H) measured unipolar signal morphology. The figure is adapted from Rottmann et al. (2016) [171].

By stimulations of 10 x 10 x 10 voxels in the left upper corner, the following wavefronts were observed. The Figure 7.3 (E-H) shows the excitation wavefront of a stimulation in the upper left corner.

7.3.2 Signal analysis

Unipolar signals at the endocardium were dependent on the specific fibrosis region. Resulting morphologies (cf. Figure 7.3(G)) were also strongly dependent on the direction of the wavefront and its transmural angle.

7.3.3 Rotational activity around reconstructed 3D fibrosis

Rotational activity was induced by a cross-field stimulation. The rotational activity anchored at the ventricular fibrosis region. The fibrosis region is based on real fibrosis data, extracted from histological tissue sections. The resulting cycle length was nearly 350 ms because of the large size of the fibrosis region.

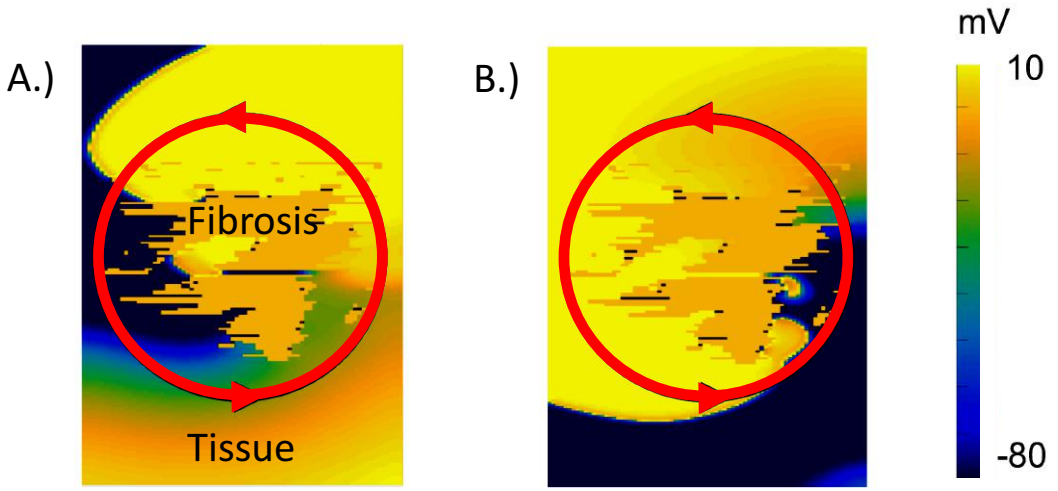

Figure 7.4: (A) and (B) Rotational activity around a real fibrosis region reconstructed from histological data. The figure is adapted from Rottmann et al. (2016) [171].

7.4 Discussion

This simulation study of excitations around fibrosis regions is, for the first time, based on real fibrotic tissue that is based on histological tissue sections. The resulting unipolar signal morphologies were strongly dependent on the influence of the transmural

angle parameter and the localization of the stimulation. In this proof of concept, the resulting morphologies of unipolar recordings were, on the one hand, deformed, and on the other hand, these signals were low voltage signals. In future, clinical navigation systems mapping of fibrotic tissue could be implemented by stimulations from different directions and signal recordings done by high-resolution mapping catheters. This study showed that fibrosis was proarrhythmogenic at larger fibrosis regions. With stimulations from different directions, fibrosis regions could be detected more robustly by comparing these recordings, characteristics and their correlations.

7.5 Resulting Publications

The results of this chapter were published in :

M. Rottmann, J. Zuern, U. Arslan, K. Klingel, O. Dössel, Effects of fibrosis on the extracellular potential based on 3D reconstructions from histological sections of heart tissue, Current Directions in Biomedical Engineering, vol. 2, no. 1, pp. 675-678, 2016.

M. Rottmann, J. Zuern, U. Arslan, K. Klingel, O. Dössel, Correlations between fibrosis and intracardiac recordings based on 3D reconstructions in the murine model of viral myocarditis. 83. Jahrestagung der deutschen Gesellschaft für Kardiologie – Herz- und Kreislaufforschung, Mannheim, Clinical Research in Cardiology, vol. 106, no. 1, pp. 11, Apr. 2017.

CHAPTER 8

Conclusion

8.1 Understanding Atrial Fibrillation Mechanisms

This thesis presented important studies for the understanding of AF mechanisms. In the last 60 years, different hypotheses have been published regarding the AF mechanisms multiple wavelet, focal wave, and rotor. This study is the first to present one model containing all the different multiple wavelet, focal wave, and rotor excitations, including 3D heterogeneous regions and important correlations between these excitations and substrate characteristics.

8.1.1 Developed atrial fibrillation computer models in atrial tissue incorporating 3D fibrotic tissue

The AF mechanisms were explained by 3D-computer simulation data of atrial fibrillation in human tissue models, incorporating variable sizes and degrees of fibrosis with high voxel resolution (0.1mm x 0.1mm x 0.1mm). The development, and the stability of focal and reentrant sources during persistent AF, depended on the sizes and the amount of atrial heterogeneity. On the one hand, rotational activity anchored in a small region of a heterogeneous area (10mm x 10mm x 2mm). Rotational sources meandered in larger areas of the heterogeneous myocardium (35mm x 45mm x 2mm). Furthermore, the developed models incorporating fibrotic patterns revealed focal exits from the fibrosis border zone. Both rotational and focal sources were located in regions displaying low voltage and slow conduction in clinical and simulation data. In simulation data, rotational and focal sources were located in fibrotic tissue with a degree of fibrosis between 30% and 40%. More complex AF simulations in the spherical 3D model showed the development and maintenance of reentries in figure-eight patterns with multiple and varying focal exit locations near the borders of heterogeneous areas. The simulation study showed that the pro-arrhythmogenic substrate consisted

of fibrotic regions with a degree of fibrosis between 20% and 50%. At higher degrees of fibrosis above 50%, the fibrosis area became a conduction block. Wavefronts in large (80mm x 80mm x 2mm) and dense (40%) fibrosis areas resulted first in curved wavefronts, then in wave breaks and then at the border zone in reentries with trajectories that were partly in fibrotic tissue and partly in healthy tissue. These reentries resulted in focal excitations at the fibrosis border zone in the high-resolution simulation model with voxel resolution (0.1mm x 0.1mm x 0.1mm). Correlations between reentries (reentrant hypothesis), and between focal waves (focal wave hypothesis), were explained by the developed model incorporating 3D fibrotic tissue (cf. Figure 8.1).

8.1.2 Correlations between focal waves, reentries and fibrosis during atrial fibrillation

In this thesis, computer simulation models and clinical mapping showed that AF sources, and rotational, and focal sources developed and maintained in heterogeneous areas. The main part of the rotational activity trajectories was within the fibrotic tissue and was difficult to detect from extracellular potentials, because of low voltage and fractionated signals. Rotational activity trajectories could also cover the border zone between fibrotic and more healthier tissue, and resulted in focal excitations at the focal exit points from the fibrotic tissue to the more healthier tissue. These focal exit signals had ten times larger amplitudes than those in the fibrotic tissue, and their strong negative S-waves overlapped the surrounding small fibrotic tissue signals such that the complete reentrant cycles were difficult to detect from extracellular potentials. The existence of focal waves at the fibrosis border zones and reentries was dependent on the size and degree of fibrosis. Rotational activity around a fibrosis region was observed if the degree of fibrosis was $\geq$ 20% and the fibrosis region was $\geq$ 10mm x 10mm. Rotational activity rotated at the fibrosis border zone partially within the fibrotic and partially within the more healthier tissue, if the fibrosis region was large (45mm x 35mm x 2mm) and the degree of fibrosis was $\geq$ 20%. Focal exits were observed in large (45mm x 35mm x 2mm) and dense ($\geq$ 30%) fibrotic regions at the fibrosis border zones. If the size of the large fibrosis region was different between the endocardium and epicardium, focal exits at endocardium and epicardium had a time delay, similar to clinical observations of endo-epicardial breakthroughs. The dynamics of rotational activity centers and focal exit locations were dependent on the degree of fibrosis. At a degree of fibrosis of 30%, rotational activities meandered between fibrosis and healthy tissue and also focal exit locations changed their locations cycle by cycle. At a degree of fibrosis of 40%, rotational activities and focal exit locations were stable over multiple cycles.

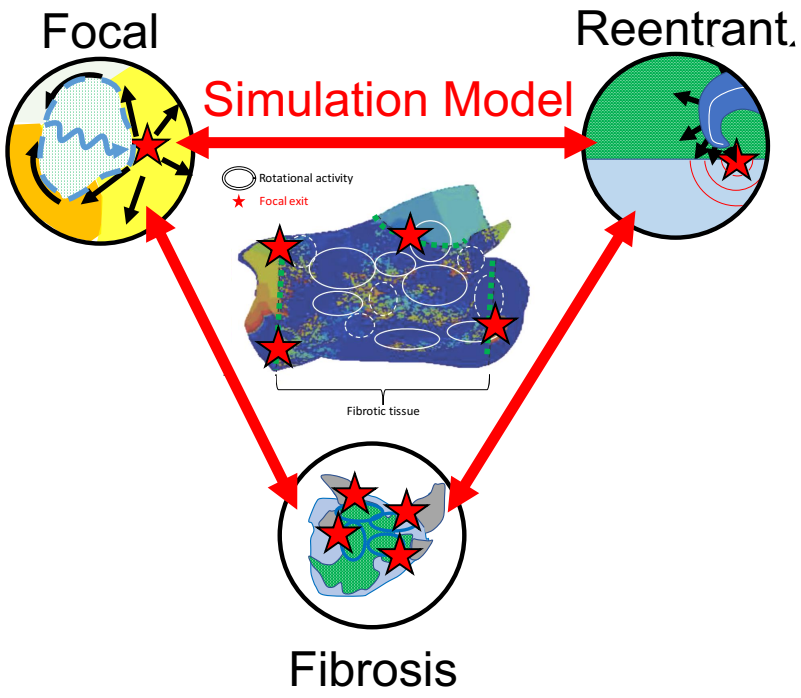

Figure 8.1: Correlations of AF between the focal source hypothesis, reentrant hypothesis, and fibrosis hypothesis. Figure parts within circles are adapted from de Groot et al. [132], Schotten et al. [38] and Marrouche et al. [175] .

8.1.3 Main conclusion

Persistent AF consists of multiple interacting rotational and focal sources, which developed and anchored in large proarrhythmogenic regions displaying low voltage and slow conduction.

8.2 Methods for Detection of Proarrhythmogenic Sources in Atrial Fibrillation

This thesis evaluated methods for AF detection using simulation models and clinical data. Furthermore, the thesis provided new methods of detecting AF sources. Local activation-based methods, such as the repetitive activation patterns showing CLC > 70%, AF cycle length, and activation line patterns were robust for the detection of reentries even in fibrotic regions and at the border zone between fibrosis and healthy tissue. Phase singularities based on the Hilbert phase could be used at rotors in healthy tissue models. In addition, the method approximate entropy method, the method peak-to-peak amplitude method, and the method RS-ratio method were suitable

for detecting AF sources in healthy tissue models. The findings from the simulation studies were evaluated and compared with clinical data. Strongly proarrhythmogenic substrates were large fibrosis regions with a degree of fibrosis between 30% and 40%. With increased fibrosis regions, the number of rotational, focal, and wavelet activities grew. The degree of fibrosis could be detected with the peak-to-peak amplitude < 1 mV in the case of contact, while the size of the fibrosis region could be detected from the resulting peak-to-peak amplitude during sinus rhythm and during atrial fibrillation.

8.2.1 Main conclusion

A combination of different methods should be used to robustly detect AF sources. For instance, low-voltage regions could detect proarrhythmogenic substrates, while the main focus for detecting AF sources should be the large low voltage areas with amplitudes <0.1 mV. On the other hand, conduction velocity vector maps could detect the AF sources rotational activity and focal source waves; the main focus should be on regions with conduction velocities below 300 mm/s.

8.3 Impact of Catheter Designs on Atrial Fibrillation Source Detection

This thesis evaluated different catheter models in clinical use, such as Lasso, PentaRay, and AFocusII, regarding their ability to detect AF sources. Furthermore, new catheter designs were developed for optimized AF detection. With the commonly used catheter designs, the detection of AF sources was only possible within 7 mm to the rotor center. The study also analyzed the impact of electrode sizes and forms on the resulting signals and the influence of the distance to the tissue. Furthermore, a realistic deformation model of a mechanical deformation model of a catheter was developed. Then, using the developed models, realistic signal recordings were collected from virtual catheters. Signal characteristics like the signal morphology, amplitude, and calculated conduction velocity were highly similar to those from clinical observations.

8.3.1 Main conclusion

Commonly used catheter designs were limited in detecting AF sources. If the rotational activity was within healthy tissue, it could only be detected within a distance of 7 mm to the core. Within fibrotic tissue, multiple interacting rotational and focal sources and colliding wavelets impeded the detection of AF sources. Furthermore, in within a certain distance to the tissue, no clear detection of AF sources was pos-

sible because of near-field effects. However, multiple rotational, focal, and wavelet activities could be detected with new catheter designs like curved square catheter designs with interelectrode distances < 3 mm. The developed deformation model was accurate with errors < 0.2 mm.

8.4 Ablation Strategies

This thesis evaluated different ablation strategies were evaluated with realistic AF simulation models. Single ablation dots at rotor centers and focal sources did not terminate AF in a robust manner. In contrast, ablation lines that isolated the fibrosis areas (box isolation) did terminate AF. Finally, pulmonary vein isolation could reduce or terminate AF sources.

8.4.1 Main conclusion

Pulmonary vein isolation and additional isolating proarrhythmogenic substrate could terminate AF and stop the induction and maintenance of AF.

References

[1] D. Bredikis, A Wilber, *Cryoablation of cardiac arrhythmias*. Elsevier Health Sciences, 2011.

[2] A. Go, E. Hylek, K. Phillips, Y. Chang, L. Henault, J. Selby, and D. Singer, "Prevalence of diagnosed atrial fibrillation in adults: National implications for rhythm management and stroke prevention: the anticoagulation and risk factors in atrial fibrillation (atria) study." *JAMA*, vol. 285, no. 18, pp. 2370 – 2375, 2001.

[3] P. A. Wolf, R. D. Abbott, and W. B. Kannel, "Atrial fibrillation as an independent risk factor for stroke: the framingham study." *Stroke*, vol. 22, no. 8, pp. 983 – 988, 1991.

[4] F. R. Lake, K. J. Cullen, N. H. Klerk, M. G. McCall, and D. L. Rosman, "Atrial fibrillation and mortality in an elderly population," *Australian and New Zealand Journal of Medicine*, vol. 19, no. 4, pp. 321–326, 1989.

[5] S. J. Phillips, J. P. Whisnant, W. M. O'Fallon, and R. L. Frye, "Prevalence of cardiovascular disease and diabetes mellitus in residents of rochester, minnesota," *Mayo Clinic Proceedings*, vol. 65, no. 3, pp. 344 – 359, 1990.

[6] C. D. Furberg, B. M. Psaty, T. A. Manolio, J. M. Gardin, V. E. Smith, and P. M. Rautaharju, "Prevalence of atrial fibrillation in elderly subjects (the cardiovascular health study)," *The American Journal of Cardiology*, vol. 74, no. 3, pp. 236 – 241, 1994.

[7] K. Hirao, *Catheter ablation: A current approach on cardiac arrhythmias*. Springer Singapore, 2018.

[8] N. Talley and S. O Connor, *Examination medicine: A guide to physician training*. Elsevier Health Sciences, 2014.

[9] A. Verma, C. Jiang, T. Betts, J. Chen, I. Deisenhofer, R. Mantovan, L. Macle, C. Morillo, W. Haverkamp, R. Weerasooriya, J. Albenque, S. Nardi, E. Menardi, P. Novak, et al., "Approaches to catheter ablation for persistent atrial fibrillation," *New England Journal of Medicine*, vol. 372, no. 19, pp. 1812–1822, 2015.

[10] V. Fuster, L. Rydén, D. Cannom, H. Crijns, A. Curtis, K. Ellenbogen, J. Halperin, J. Le Heuzey, G. N. Kay, J. Lowe, S. Olsson, E. Prystowsky, J. Tamargo, S. Wann, et al., "ACC/AHA/ESC 2006 guidelines for the management of patients with atrial fibrillation," *Circulation*, vol. 114, no. 7, pp. e257 – e354, 2006.

[11] L. Magner, *A history of medicine*. Taylor & Francis, 1992.

[12] M. May, *Galen on the usefulness of the parts of the body.*, Cornell publications in the history of science. Cornell University Press, 1968.

[13] C. Duffin, R. Moody, and C. Gardner-Thorpe, *A history of geology and medicine.*, Geological Society London: Geological Society special publication. Geological Society, 2013.

[14] *https://commons.wikimedia.org/wiki/file:leonardo_da_vinci,_heart_and_its_blood_vessels.jpg, accessed: 2017-09-11*.

[15] R. Begg, D. Lai, and M. Palaniswami, *Computational intelligence in biomedical engineering*. CRC Press, 2007.

[16] S. Mills, *Histology for pathologists*. Wolters Kluwer Health, 2012.

[17] *https://upload.wikimedia.org/wikipedia/commons/thumb/e/e0/heart_diagram-en.svg/2000px-heart_diagram-en.svg.png, accessed: 2017-09-11*.

[18] G. Jenkins and G. Tortora, *Anatomy and physiology: From science to life*. Wiley, 2012.

[19] E. Applegate, *The anatomy and physiology learning system*. W.B. Saunders, 2000.

[20] *https://upload.wikimedia.org/wikipedia/commons/6/67/heart_diagram_blood_flow_en.svg, accessed: 2017-09-11*.

[21] D. Rosenbaum, *Quantitative cardiac electrophysiology*. CRC Press, 2002.

[22] A. O. Grant, "Cardiac ion channels," *Circulation: Arrhythmia and Electrophysiology*, vol. 2, no. 2, pp. 185–194, 2009.

[23] S. Nattel and L. Carlsson, "Innovative approaches to anti-arrhythmic drug therapy." *Nat Rev Drug Discov*, vol. 5, pp. 1034 – 1049, 2006.

[24] C. J. Schwiening, "A brief historical perspective: Hodgkin and Huxley." *The Journal of Physiology*, vol. 590, no. 11, pp. 2571–2575, 2012.

[25] A. L. Hodgkin and A. F. Huxley, "A quantitative description of membrane current and its application to conduction and excitation in nerve," *The Journal of Physiology*, vol. 117, no. 4, pp. 500–544, 1952.

[26] M. Courtemanche, R. J. Ramirez, and S. Nattel, "Ionic mechanisms underlying human atrial action potential properties: insights from a mathematical model," *Am J Physiol*, vol. 275, no. 1 Pt 2, pp. 1522–1539, 1998.

[27] J. D. Enderle, S. M. Blanchard, and J. D. Bronzino, "Introduction to biomedical engineering (second edition)," *Academic Press*, 2005.

[28] J. Sénac, *Traité de la structure du coeur de son action et de ses maladies par m. sénac*. chez Jacques Vincent, 1749.

[29] J. Bouilland, *Traité clinique des maladies du coeur*. chez Jacques Vincent, 1835.

[30] H. Nothnagel, *Über rhythmische Herztätigkeit*. Deutsches Archiv für Klinische Medizin, 1876.

[31] H. Bouilland, *Analyse des Pulsus Irregularis Perpetuus*. Prager Med Wochenschr, 1903.

[32] W. Einthoven, *Le télécardiogramme*. Arch Int de Physiol, 1906.

[33] S. S. Barold, "Willem einthoven and the birth of clinical electrocardiography a hundred years ago," *Cardiac Electrophysiology Review*, vol. 7, no. 1, pp. 99 – 104, 2003.

[34] P. Kirchhof, A. Auricchio, J. Bax, H. Crijns, J. Camm, H.-C. Diener, A. Goette, G. Hindricks, S. Hohnloser, L. Kappenberger, K.-H. Kuck, G. Y. Lip, B. Olsson, T. Meinertz, et al., "Outcome parameters for trials in atrial fibrillation: executive summary," *European Heart Journal*, vol. 28, no. 22, pp. 2803 – 2817, 2007.

[35] M. D. Smit and I. C. Van Gelder, "New treatment options for atrial fibrillation: towards patient tailored therapy," *Heart*, vol. 97, no. 21, pp. 1796–1802, 2011.

[36] A. L. Waldo, "Mechanisms of atrial fibrillation," *Journal of Cardiovascular Electrophysiology*, vol. 14, no. s12, pp. S267–S274, 2003.

[37] A. L. Waldo, "Mechanisms of atrial flutter and atrial fibrillation: distinct entities or two sides of a coin," *Cardiovascular Research*, vol. 54, no. 2, pp. 217–229, 2002.

[38] U. Schotten, S. Verheule, P. Kirchhof, and A. Goette, "Pathophysiological mechanisms of atrial fibrillation: A translational appraisal," *Physiological Reviews*, vol. 91, no. 1, pp. 265–325, 2011.

[39] M. D. Wilson, "Fibrogenesis: Mechanisms, dynamics and clinical implications." *Iranian Journal of Pathology*, vol. 10, no. 2, pp. 83–88, 2015.

[40] S. de Jong, T. A. B. van Veen, H. V. M. van Rijen, and J. M. T. de Bakker, "Fibrosis and cardiac arrhythmias." *Journal of Cardiovascular Pharmacology*, vol. 57(6), pp. 630–638, 2011.

[41] K. H. Ten Tusscher and A. V. Panfilov, "Influence of diffuse fibrosis on wave propagation in human ventricular tissue," *EP Europace*, vol. 9, no. suppl 6, pp. 38 – 45, 2007.

[42] T. Kawara, R. Derksen, J. de Groot, R. Coronel, S. Tasseron, A. Linnenbank, R. Hauer, H. Kirkels, M. Janse, and J. de Bakker, "Activation delay after premature stimulation in chronically diseased human myocardium relates to the architecture of interstitial fibrosis," *Circulation*, vol. 104, no. 25, pp. 3069 – 3075, 2001.

[43] V. Jacquemet and C. S. Henriquez, "Genesis of complex fractionated atrial electrograms in zones of slow conduction: a computer model of microfibrosis," *Heart Rhythm*, vol. 6, no. 6, pp. 803–810, 2009.

[44] S. Rohr, "Arrhythmogenic implications of fibroblast-myocyte interactions," *Circulation: Arrhythmia and Electrophysiology*, vol. 5, no. 2, pp. 442–452, 2012.

[45] S. Watson and K. Gorski, *Invasive cardiology: A manual for cath lab personnel*, Learning Cardiology. Jones & Bartlett Learning, 2011.

[46] *https://upload.wikimedia.org/wikipedia/commons/2/2e/cardiac_surgery_operating_room.jpg, accessed: 2017-09-11*.

[47] G. Moe, W. Rheinboldt, and J. Abildskov, "A computer model of atrial fibrillation," *American Heart Journal*, vol. 67, no. 2, pp. 200 – 220, 1964.

[48] A. Pullan, L. Cheng, and M. Buist, *Mathematically modelling the electrical activity of the heart: From cell to body surface and back again*. World Scientific, 2005.

[49] D. Noble, "A modification of the hodgkin huxley equations applicable to purkinje fibre action and pacemaker potentials," *The Journal of Physiology*, vol. 160, no. 2, pp. 317–352, 1962.

[50] R. E. McAllister, D. Noble, and R. W. Tsien, "Reconstruction of the electrical activity of cardiac purkinje fibres." *The Journal of Physiology*, vol. 251, no. 1, pp. 1–59, 1975.

[51] G. W. Beeler and H. Reuter, "Reconstruction of the action potential of ventricular myocardial fibres," *The Journal of Physiology*, vol. 268, no. 1, pp. 177–210, 1977.

[52] K. Yanagihara, A. Noma, and H. Irisawa, "Reconstruction of sino-atrial node pacemaker potential based on the voltage clamp experiments." *The Japanese Journal of Physiology*, vol. 30, no. 6, pp. 841–857, 1980.

[53] D. G. Bristow and J. W. Clark, "A mathematical model of primary pacemaking cell in sa node of the heart," *American Journal of Physiology-Heart and Circulatory Physiology*, vol. 243, no. 2, pp. 207–218, 1982.

[54] D. G. Bristow and J. W. Clark, "A mathematical model of the vagally driven primary pacemaker," *American Journal of Physiology-Heart and Circulatory Physiology*, vol. 244, no. 1, pp. 150–161, 1983.

[55] D. Noble and S. J. Noble, "A model of sino-atrial node electrical activity based on a modification of the DiFrancesco-Noble (1984) equations," *Proceedings of the Royal Society of London. Series B, Biological Sciences*, vol. 222, no. 1228, pp. 295–304, 1984.

[56] D. DiFrancesco and D. Noble, "A model of cardiac electrical activity incorporating ionic pumps and concentration changes," *Philosophical Transactions of the Royal Society of London. Series B, Biological Sciences*, vol. 307, no. 1133, pp. 353–398, 1985.

[57] D. Hilgemann and D. Noble, "Excitation-contraction coupling and extracellular calcium transients in rabbit atrium: reconstruction of basic cellular mechanisms," *Proceedings of the Royal Society of London. Series B, Biological Sciences*, vol. 230, no. 1259, pp. 163–205, 1987.

[58] Y. E. Earm and D. Noble, "A model of the single atrial cell: Relation between calcium current and calcium release," *Proceedings of the Royal Society of London. Series B, Biological Sciences*, vol. 240, no. 1297, pp. 83–96, 1990.

[59] C. H. Luo and Y. Rudy, "A model of the ventricular cardiac action potential. depolarization, repolarization, and their interaction." *Circulation Research*, vol. 68, no. 6, pp. 1501–1526, 1991.

[60] C. H. Luo and Y. Rudy, "A dynamic model of the cardiac ventricular action potential. I. simulations of ionic currents and concentration changes." *Circulation Research*, vol. 74, no. 6, pp. 1071–1096, 1994.

[61] C. H. Luo and Y. Rudy, "A dynamic model of the cardiac ventricular action potential. II. afterdepolarizations, triggered activity, and potentiation." *Circulation Research*, vol. 74, no. 6, pp. 1097–1113, 1994.

[62] S. S. Demir, J. W. Clark, C. R. Murphey, and W. R. Giles, "A mathematical model of a rabbit sinoatrial node cell." *American Journal of Physiology-Cell Physiology*, vol. 266, no. 3, pp. 832–852, 1994.

[63] S. Dokos, B. Celler, and N. Lovell, "Vagal control of sinoatrial rhythm: a mathematical model," *Journal of Theoretical Biology*, vol. 182, no. 1, pp. 21 – 44, 1996.

[64] D. S. Lindblad, C. R. Murphey, J. W. Clark, and W. R. Giles, "A model of the action potential and underlying membrane currents in a rabbit atrial cell," *American Journal of Physiology-Heart and Circulatory Physiology*, vol. 271, no. 4, pp. 1666–1696, 1996.

[65] S. Demir, B. O'Rourke, G. Tomaselli, E. Marban, and R. Winslow, "Action potential variation in canine ventricle: A modeling study," *Computers in Cardiology*, vol. 23, pp. 221–224, 1996.

[66] M. Jafri, J. Rice, and R. Winslow, "Cardiac Ca^{2+} dynamics: the roles of ryanodine receptor adaptation and sarcoplasmic reticulum load." *Biophysical Journal*, vol. 74, no. 3, March 1998.

[67] D. Noble, A. Varghese, P. Kohl, and P. Noble, "Improved guinea-pig ventricular cell model incorporating a diadic space, I_{Kr} and I_{Ks}, and length- and tension-dependent processes." *The Canadian Journal of Cardiology*, vol. 14, no. 1, pp. 123–134, 1998.

[68] L. Priebe and D. J. Beuckelmann, "Simulation study of cellular electric properties in heart failure," *Circulation Research*, vol. 82, no. 11, pp. 1206–1223, 1998.

[69] S. Demir, J. Clark, and W. Giles, "Parasympathetic modulation of sinoatrial node pacemaker activity in rabbit heart: a unifying model," *The American Journal of Physiology*, vol. 276, no. 6 Pt 2, pp. 2221 – 2244, June 1999.

[70] R. L. Winslow, J. Rice, S. Jafri, E. Marbán, and B. O'Rourke, "Mechanisms of altered excitation-contraction coupling in canine tachycardia-induced heart failure, ii." *Circulation Research*, vol. 84, no. 5, pp. 571 – 586, 1999.

[71] R. J. Ramirez, S. Nattel, and M. Courtemanche, "Mathematical analysis of canine atrial action potentials: rate, regional factors, and electrical remodeling." *American Journal of Physiology-Heart and Circulatory Physiology*, vol. 279, no. 4, pp. 1767 – 1785, 2000.

[72] H. Zhang, A. V. Holden, I. Kodama, H. Honjo, M. Lei, T. Varghese, and M. R. Boyett, "Mathematical models of action potentials in the periphery and center of the rabbit sinoatrial node." *American Journal of Physiology-Heart and Circulatory Physiology*, vol. 279, no. 1, pp. H397 – H421, 2000.

[73] M. R. Boyett, H. Zhang, A. Garny, and A. V. Holden, "Control of the pacemaker activity of the sinoatrial node by intracellular Ca^{2+}. Experiments and modelling." *Philosophical Transactions of the Royal Society of London A: Mathematical, Physical and Engineering Sciences*, vol. 359, no. 1783, pp. 1091 – 1110, 2001.

[74] S. Pandit, R. Clark, W. Giles, and S. Demir, "A mathematical model of action potential heterogeneity in adult rat left ventricular myocytes." *Biophysical Journal*, vol. 81, no. 6, 2001.

[75] J. L. Puglisi and D. M. Bers, "Labheart: an interactive computer model of rabbit ventricular myocyte ion channels and Ca transport." *American Journal of Physiology-Cell Physiology*, vol. 281, no. 6, pp. 2049 – 2060, 2001.

[76] J. Kneller, R. J. Ramirez, D. Chartier, M. Courtemanche, and S. Nattel, "Time-dependent transients in an ionically based mathematical model of the canine atrial action potential." *American Journal of Physiology-Heart and Circulatory Physiology*, vol. 282, no. 4, pp. 1437 – 1451, 2002.

[77] Y. Kurata and T. S. I Hisatome, S Imanishi, "Dynamical description of sinoatrial node pacemaking: improved mathematical model for primary pacemaker cell." *American Journal of Physiology-Heart and Circulatory Physiology*, vol. 283, no. 5, pp. H2074 – H2101, 2002.

[78] O. Bernus, R. Wilders, C. W. Zemlin, H. Verschelde, and A. V. Panfilov, "A computationally efficient electrophysiological model of human ventricular cells." *American Journal of Physiology-Heart and Circulatory Physiology*, vol. 282, no. 6, pp. H2296–H2308, 2002.

[79] N. H. Lovell, S. L. Cloherty, B. G. Celler, and S. Dokos, "A gradient model of cardiac pacemaker myocytes." *Progress in Biophysics and Molecular Biology*, vol. 85, no. 2, pp. 301 – 323, 2004.

[80] K. H. W. J. ten Tusscher, D. Noble, P. J. Noble, and A. V. Panfilov, "A model for human ventricular tissue," *American Journal of Physiology - Heart and Circulatory Physiology*, vol. 286, no. 4, pp. 1573–1589, 2004.

[81] V. Iyer and R. Mazhari, R Winslow, "A computational model of the human left-ventricular epicardial myocyte." *Biophysical Journal*, vol. 87, no. 3, pp. 1507 – 1525, 2004.

[82] K. H. W. J. ten Tusscher and A. V. Panfilov, "Alternans and spiral breakup in a human ventricular tissue model." *American Journal of Physiology-Heart and Circulatory Physiology*, vol. 291, no. 3, pp. 1088–1100, 2006.

[83] N. Denis, G. Alan, and N. P. J., "How the Hodgkin Huxley equations inspired the Cardiac Physiome Project." *The Journal of Physiology*, vol. 590, no. 11, pp. 2613 – 2628.

[84] R. Miri, *Computer assisted optimization of cardiac resynchronization therapy*, Karlsruhe transactions on biomedical engineering. Univ.-Verlag, 2009.

[85] M. Wilhelms, H. Hettmann, M. Maleckar, J. Koivumaeki, O. Dössel, and G. Seemann, "Benchmarking electrophysiological models of human atrial myocytes," *Frontiers in Physiology*, vol. 3, p. 487, 2013.

[86] R. J. Ramirez, S. Nattel, and M. Courtemanche, "Mathematical analysis of canine atrial action potentials: rate, regional factors, and electrical remodeling." *American Journal of Physiology-Heart and Circulatory Physiology*, vol. 279, no. 4, pp. 1767–1785, 2000.

[87] S. Nattel and M. Harada, "Atrial remodeling and atrial fibrillation," *Journal of the American College of Cardiology*, vol. 63, no. 22, pp. 2335 – 2345, 2014.

[88] M. C. E. F. Wijffels, C. J. H. J. Kirchhof, R. Dorland, J. Power, and M. A. Allessie, "Electrical remodeling due to atrial fibrillation in chronically instrumented conscious goats," *Circulation*, vol. 96, no. 10, pp. 3710–3720, 1997.

[89] M. C. Wijffels, C. J. Kirchhof, R. Dorland, and M. A. Allessie, "Atrial fibrillation begets atrial fibrillation. a study in awake chronically instrumented goats," *Circulation*, vol. 92, no. 7, pp. 1954 – 1968, 1995.

[90] A. Nygren, C. Fiset, L. Firek, J. W. Clark, D. S. Lindblad, R. B. Clark, and W. R. Giles, "Mathematical model of an adult human atrial cell." *Circulation Research*, vol. 82, no. 1, pp. 63–81, 1998.

[91] M. M. Maleckar, J. L. Greenstein, W. R. Giles, and N. A. Trayanova, "Electrotonic coupling between human atrial myocytes and fibroblasts alters myocyte excitability and repolarization," *Biophysical Journal*, vol. 97, no. 8, pp. 2179 – 2190, 2009.

[92] J. Koivumaki, T. Korhonen, and P. Tavi, "Impact of sarcoplasmic reticulum calcium release on calcium dynamics and action potential morphology in human atrial myocytes: A computational study." *PLOS Computational Biology*, vol. 7, no. 1, pp. 1–14, 2011.

[93] E. Grandi, S. V. Pandit, N. Voigt, A. J. Workman, D. Dobrev, J. Jalife, and D. M. Bers, "Human atrial action potential and Ca^{2+} model novelty and significance." *Circulation Research*, vol. 109, no. 9, pp. 1055 – 1066, 2011.

[94] O. Schmitt, *Biological information processing using the concept of interpenetrating domains. in: Leibovic K.N. (eds) Information Processing in the Nervous System*. Springer Berlin Heidelberg, 1969.

[95] L. Tung, "A bi-domain model for describing ischemic myocardial d-c potentials," PhD thesis, MIT, Cambridge, MA, 1978.

[96] E. J. Vigmond, R. W. dos Santos, A. J. Prassl, M. Deo, and G. Plank, "Solvers for the cardiac bidomain equations," *Progress in Biophysics and Molecular Biology*, vol. 96, no. 1, pp. 3 – 18, 2008.

[97] J. Malmivuo and R. Plonsey, *Bioelectromagnetism: Principles and applications of bioelectric and biomagnetic fields*. Oxford University Press, 1995.

[98] W. T. Geselowitz, D. B. Miller, "A bidomain model for anisotropic cardiac muscle." *Annals of Biomedical Engineering*, vol. 11, no. 3, pp. 191–206, 1983.

[99] M. Keller, *Formation of intracardiac electrograms under physiological and pathological conditions*, Karlsruhe transactions on biomedical engineering. KIT Scientific Publishing, 2014.

[100] V. Jacquemet, L. Kappenberger, and C. S. Henriquez, "Modeling atrial arrhythmias: Impact on clinical diagnosis and therapies." *IEEE Reviews in Biomedical Engineering*, vol. 1, pp. 94–114, 2008.

[101] M. Josephson, *Clinical cardiac electrophysiology: Techniques and interpretations*. Wolters Kluwer Health/Lippincott Williams & Wilkins, 2008.

[102] J. Steinberg, P. Jaïs, and H. Calkins, *Practical guide to catheter ablation of atrial fibrillation*. Wiley, 2015.

[103] N. de Groot, L. van der Does, A. Yaksh, E. Lanters, C. Teuwen, P. Knops, P. van de Woestijne, J. Bekkers, C. Kik, A. Bogers, and M. Allessie, "Direct proof of endo-epicardial asynchrony of the atrial wall during atrial fibrillation in humans," *Circulation: Arrhythmia and Electrophysiology*, vol. 9, no. 5, 2016.

[104] R. Houben, N. de Groot, J. Smeets, A. Becker, F. Lindemans, and M. Allessie, "S-wave predominance of epicardial electrograms during atrial fibrillation in humans: Indirect evidence for a role of the thin subepicardial layer," *Heart Rhythm*, vol. 1, no. 6, pp. 639 – 647, 2004.

[105] P. C. Franzone, L. Guerri, M. Pennacchio, and B. Taccardi, "Anisotropic mechanisms for multiphasic unipolar electrograms: Simulation studies and experimental recordings," *Annals of Biomedical Engineering*, vol. 28, no. 11, pp. 1326–1342, 2000.

[106] C. Kohl, *Auswirkungen von Substratänderungen und komplexer Erregungsmuster auf intrakardiale Potentiale.*, Master thesis. Institute of Biomedical Engineering, Karlsruhe Institute of Technology, Karlsruhe, Germany, 2015.

[107] M. Rottmann, M. Keller, T. Oesterlein, G. Seemann, and O. Dössel, "Comparison of different methods and catheter designs to estimate the rotor tip position. A simulation study," *Computing in Cardiology*, 2014.

[108] C. Reich, T. Oesterlein, M. Rottmann, G. Seemann, and O. Dössel, "Classification of cardiac excitation patterns during atrial fibrillation," *In Current Directions in Biomedical Engineering*, vol. 2(1), 2016.

[109] O. Dössel, G. Lenis, A. Loewe, M. Rottmann, G. Seemann, and T. Oesterlein, "Model assisted biosignal analysis of atrial electrograms," *In Technisches Messen*, vol. 83(2), 2016.

[110] G. Seemann, F. B. Sachse, M. Karl, D. L. Weiss, V. Heuveline, and D. O, "Framework for modular, flexible and efficient solving the cardiac bidomain equation using PETSc," *Mathematics in Industry*, vol. 15, pp. 363–369, 2010.

[111] R. P. Houben, N. M. de Groot, J. L. Smeets, A. E. Becker, F. W. Lindemans, and M. A. Allessie, "S-wave predominance of epicardial electrograms during atrial fibrillation in humans: indirect evidence for a role of the thin subepicardial layer," *Heart Rhythm*, vol. 1, no. 6, pp. 639 – 647, 2004.

[112] R. P. Houben, N. M. de Groot, F. W. Lindemans, and M. A. Allessie, "Automatic mapping of human atrial fibrillation by template matching," *Heart Rhythm*, vol. 3, no. 10, pp. 1221 – 1228, 2006.

[113] F. M. Weber, A. Luik, C. Schilling, G. Seemann, M. W. Krueger, C. Lorenz, C. Schmitt, and O. Dossel, "Conduction velocity restitution of the human atrium. an efficient measurement protocol for clinical electrophysiological studies." *IEEE Transactions on Biomedical Engineering*, vol. 58, no. 9, pp. 2648–2655, 2011.

[114] U. Arslan, *Auswirkungen von Fibrose auf kreisende Erregungen und Erregungen unterschiedlicher Richtungen im Vorhof.*, Bachelor thesis. Institute of Biomedical Engineering, Karlsruhe Institute of Technology, Karlsruhe, Germany, 2016.

[115] M. Rottmann, L. Unger, W. Kaltenbacher, G. Seemann, A. Loewe, M. Krueger, A. Jadidi, T. Arentz, and O. Dössel, "Methods for analyzing signal characteristics of stable and unstable rotors in a realistic heart model," *In Computing in Cardiology*, vol. 42, 2015.

[116] C. Reich, *Classification of cardiac excitation patterns during atrial fibrillation using multichannel mapping data.*, Master thesis. Institute of Biomedical Engineering, Karlsruhe Institute of Technology, Karlsruhe, Germany, 2015.

[117] W. Kaltenbacher, M. Rottmann, and O. Dössel, "An algorithm to automatically determine the cycle length coverage to identify rotational activity during atrial fibrillation - a simulation study," *Current Directions in Biomedical Engineering*, vol. 2(1), pp. 167–170, 2016.

[118] W. Kaltenbacher, *Vergleich verschiedener Methoden zur Parameterbestimmung von Rotoren bei unterschiedlichen Kathetergeometrien.*, Bachelor thesis. Institute of Biomedical Engineering, Karlsruhe Institute of Technology, Karlsruhe, Germany, 2016.

[119] F. Rafdionza, *Analyse der RS-difference bei verschiedenen Erregungsausbreitungen im menschlichen Vorhof.*, Bachelor thesis. Institute of Biomedical Engineering, Karlsruhe Institute of Technology, Karlsruhe, Germany, 2016.

[120] M. Haïssaguerre, P. Jaïs, D. C. Shah, A. Takahashi, M. Hocini, G. Quiniou, S. Garrigue, A. Le Mouroux, P. Le Métayer, and J. Clémenty, "Spontaneous initiation of atrial fibrillation by ectopic beats originating in the pulmonary veins," *New England Journal of Medicine*, vol. 339, no. 10, pp. 659–666, 1998.

[121] A. Verma, C.-y. Jiang, T. R. Betts, J. Chen, I. Deisenhofer, R. Mantovan, L. Macle, C. A. Morillo, W. Haverkamp, R. Weerasooriya, et al., "Approaches to catheter ablation for persistent atrial fibrillation," *New England Journal of Medicine*, vol. 372, no. 19, pp. 1812–1822, 2015.

[122] D. Scherr, P. Khairy, S. Miyazaki, V. Aurillac-Lavignolle, P. Pascale, S. B. Wilton, K. Ramoul, Y. Komatsu, L. Roten, A. Jadidi, et al., "Five-year outcome of catheter ablation of persistent atrial fibrillation using termination of atrial fibrillation as a procedural endpoint," *Circulation: Arrhythmia and Electrophysiology*, vol. 8, pp. 18–24, 2015.

[123] A. S. Jadidi, H. Lehrmann, C. Keyl, J. Sorrel, V. Markstein, J. Minners, C.-I. Park, A. Denis, P. Jaïs, M. Hocini, C. Potocnik, J. Allgeier, W. Hochholzer, C. Herrera-Siklody, et al., "Ablation of persistent atrial fibrillation targeting low-voltage areas with selective activation characteristics," *Circulation: Arrhythmia and Electrophysiology*, vol. 9, no. 3, 2016.

[124] C. M. Costa, F. O. Campos, A. J. Prassl, R. W. dos Santos, D. Sánchez-Quintana, H. Ahammer, E. Hofer, and G. Plank, "An efficient finite element approach for modeling fibrotic clefts in the heart," *IEEE Trans. Biomed. Engineering*, vol. 61, no. 3, pp. 900–910, 2014.

[125] M. W. Keller, A. Luik, M. S. Abady, G. Seemann, C. Schmitt, and O. Dössel, "Influence of three-dimensional fibrotic patterns on simulated intracardiac electrogram morphology," *Computing in Cardiology 2013*, pp. 923–926, 2013.

[126] S. Alonso and M. Baer, "Reentry produced by small-scale heterogeneities in a discrete model of cardiac tissue." *Journal of Physics: Conference Series*, vol. 727, conference 1, 2016.

[127] I. V. Kazbanov, K. H. W. J. ten Tusscher, and A. V. Panfilov, "Effects of heterogeneous diffuse fibrosis on arrhythmia dynamics and mechanism." *Scientific Reports*, vol. 6, pp. 2045 – 2322, February 2016.

[128] E. Vigmond, A. Pashaei, S. Amraoui, H. Cochet, and M. Hassaguerre, "Percolation as a mechanism to explain atrial fractionated electrograms and reentry in a fibrosis model based on imaging data," *Heart Rhythm*, vol. 13, no. 7, pp. 1536–1543, 2016.

[129] M. Haïssaguerre, A. J. Shah, H. Cochet, M. Hocini, R. Dubois, I. Efimov, E. Vigmond, O. Bernus, and N. Trayanova, "Intermittent drivers anchoring to structural heterogeneities as a major pathophysiological mechanism of human persistent atrial fibrillation," *The Journal of Physiology*, vol. 594, no. 9, pp. 2387–2398, 2016.

[130] K. McDowell, F. Vadakkumpadan, R. Blake, J. Blauer, G. Plank, R. MacLeod, and N. Trayanova, "Mechanistic inquiry into the role of tissue remodeling in fibrotic lesions in human atrial fibrillation," *Biophysical Journal*, vol. 104, no. 12, pp. 2764–2773, 2013.

[131] M. Rottmann, U. Arslan, W. Kaltenbacher, V. Markstein, T. Arentz, O. Dössel, and A. Jadidi, "Impact of three dimensional atrial fibrosis on development and stability of rotational activity in atrial fibrillation. a 3D simulation and clinical high-density mapping study in persistent atrial fibrillation," *Computing in Cardiology*, 2016.

[132] N. de Groot, R. Houben, J. Smeets, E. Boersma, U. Schotten, M. Schalij, H. Crijns, and M. Allessie, "Electropathological substrate of longstanding persistent atrial fibrillation in patients with structural heart disease clinical perspective: Epicardial breakthrough," *Circulation*, vol. 122, no. 17, pp. 1674 – 1682, 2010.

[133] M. A. Allessie, N. M. de Groot, R. P. Houben, U. Schotten, E. Boersma, J. L. Smeets, and H. J. Crijns, "Electropathological substrate of long-standing persistent atrial fibrillation in patients with structural heart disease: longitudinal dissociation," *Circulation: Arrhythmia and Electrophysiology*, vol. 3, no. 6, pp. 606–615, 2010.

[134] M. W. Krüger, *Personalized multi-scale modeling of the atria : Heterogeneities, fiber architecture, hemodialysis and ablation therapy*, Karlsruhe transactions on biomedical engineering ; 19. Karlsruhe: KIT Scientific Publishing, 2013.

[135] A. S. Jadidi, H. Lehrmann, C. Keyl, J. Sorrel, V. Markstein, J. Minners, C.-I. Park, A. Denis, P. Jaïs, M. Hocini, et al., "Ablation of persistent atrial fibrillation targeting low-voltage areas with selective activation characteristics." *Circulation. Arrhythmia and electrophysiology*, vol. 9, no. 3, 2016.

[136] A. Orozco-Duque, J. P. Ugarte, C. Tobon, J. Saiz, and J. Bustamante, "Approximate entropy can localize rotors, but not ectopic foci during chronic atrial fibrillation: A simulation study," *Computing in Cardiology*, 2013.

[137] R. Gray, A. Pertsov, and J. Jalife, "Spatial and temporal organization during cardiac fibrillation," *Nature*, vol. 392, no. 6671, pp. 75 – 78, 1998.

[138] M. Rodrigo, M. Guillem, A. M. Climent, J. Pedron-Torrecilla, A. Liberos, J. Millet, F. Fernandez-Avilas, F. Atienza, and O. Berenfeld, "Body surface localization of left and right atrial high-frequency rotors in atrial fibrillation patients: a clinical-computational study," *Heart Rhythm*, vol. 11, no. 9, pp. 1584 – 1591, 2014.

[139] O. Berenfeld, R. Mandapati, S. Dixit, A. Skanes, J. Chen, M. Mansour, and J. Jalife, "Spatially distributed dominant excitation frequencies reveal hidden organization in atrial fibrillation in the langendorff-perfused sheep heart," *Journal of Cardiovascular Electrophysiology*, vol. 11, no. 8, pp. 869 – 879, 2000.

[140] M. Mansour, R. Mandapati, O. Berenfeld, J. Chen, F. H. Samie, and J. Jalife, "Left-to-right gradient of atrial frequencies during acute atrial fibrillation in the isolated sheep heart," *Circulation*, vol. 103, no. 21, pp. 2631 – 2636, 2001.

[141] M. S. Spach, W. T. Miller, E. Miller-Jones, R. B. Warren, and R. C. Barr, "Extracellular potentials related to intracellular action potentials during impulse conduction in anisotropic canine cardiac muscle." *Circulation Research*, vol. 45, no. 2, pp. 188 – 204, 1979.

[142] J. Kaiser, "Some useful properties of teagers energy operators," *Proceedings of the IEEE international conference on acoustics, speech, and signal processing*, vol. 3, pp. 149 – 152, 1993.

[143] L. Kienle, *Optimierung und Evaluierung verschiedener Methoden zur Parameterbestimmung von Rotoren bei unterschiedlichen Kathetergeometrien.*, Bachelor thesis. Institute of Biomedical Engineering, Karlsruhe Institute of Technology, Karlsruhe, Germany, 2016.

[144] S. Pincus, "Approximate entropy: a complexity measure for biological time series data," *Proceedings of the 1991 IEEE Seventeenth Annual Northeast Bioengineering Conference*, pp. 35 – 36, 1991.

[145] D. Liu, S. Xie, Y. Li, D. Zhao, and E. El-Alfy, *Neural information processing: 24th international conference, iconip 2017, Guangzhou, China*, Lecture Notes in Computer Science, no. 4. Springer International Publishing, 2017.

[146] I. Nagrath, S. Sharan, R. Ranjan, and S. Kumar, *Signals & Systems*. Tata McGraw-Hill, 2011.

[147] H. Kantz, J. Kurths, and G. Mayer-Kress, *Nonlinear analysis of physiological data*. Springer Berlin Heidelberg, 2012.

[148] K. Umapathy, K. Nair, S. Masse, S. Krishnan, J. Rogers, M. P. Nash, and K. Nanthakumar, "Phase mapping of cardiac fibrillation," *Circulation: Arrhythmia and Electrophysiology*, vol. 3, no. 1, pp. 105 – 114, 2010.

[149] L. Unger, *Signalmorphologie basierte Bestimmung von Arrythmien und Parameterabschätzungen von Erregungsausbreitungen im Vorhof.*, Bachelor thesis. Institute of Biomedical Engineering, Karlsruhe Institute of Technology, Karlsruhe, Germany, 2014.

[150] L. Unger, M. Rottmann, G. Seemann, and O. Dössel, "Detecting phase singularities and rotor center trajectories based on the hilbert transform of intraatrial electrograms in an atrial voxel model," *Current Directions in Biomedical Engineering*, vol. 1(1), 2015.

[151] M. El Haddad, R. Houben, R. Tavernier, and M. Duytschaever, "Stable reentrant circuit with spiral wave activation driving atrial tachycardia," *Heart Rhythm*, vol. 11, pp. 716 – 718, 2014.

[152] P. Ahmed, *Mechanische Modellierung von deformierten Multielektrodenkathetern.*, Bachelor thesis. Institute for Applied Materials, Institute of Biomedical Engineering, Karlsruhe Institute of Technology, Karlsruhe, Germany, 2016.

[153] D. Gross, W. Hauger, and P. Wriggers, *Technische Mechanik 4: Hydromechanik, Elemente der Höheren Mechanik, Numerische Methoden*, Springer-Lehrbuch. Springer Berlin Heidelberg, 2014.

[154] H. Brinson and L. Brinson, *Polymer engineering science and viscoelasticity: An introduction*. Springer, 2015.

[155] W. Rust, *Nichtlineare Finite-Elemente-Berechnungen: Kontakt, Geometrie, Material*. Vieweg+Teubner Verlag, 2011.

[156] R. Hooke, *Lectures de potentia restitutiva, or of spring explaining the power of springing bodies*. John Martyn, 1678.

[157] J. Heilbron, *The oxford companion to the history of modern science*. Oxford University Press, 2003.

[158] T. Atanackovic and A. Guran, *Theory of elasticity for scientists and engineers*, Theory of Elasticity for Scientists and Engineers. Birkhäuser Boston, 2000.

[159] S. Holgate, *Understanding solid state physics*. CRC Press, 2009.

[160] J. Simo and T. Laursen, "An augmented lagrangian treatment of contact problems involving friction," *Computers Structures*, vol. 42, no. 1, pp. 97 – 116, 1992.

[161] A. Khoei, *Extended finite element method: Theory and applications*, Wiley Series in Computational Mechanics. Wiley, 2015.

[162] H. Lee, *Finite element simulations with ANSYS workbench*. SDC Publications, 2017.

[163] W. Bolton, *Engineering science*. Taylor & Francis, 2007.

[164] J. Wiley Sons, *Properties and behavior of polymers*. Wiley, 2012.

[165] H. Wittel, D. Muhs, D. Jannasch, and J. Voßiek, *Maschinenelemente: Normung, Berechnung, Gestaltung*. Springer Fachmedien Wiesbaden, 2015.

[166] K. Takashima, R. Shimomura, T. Kitou, H. Terada, K. Yoshinaka, and K. Ikeuchi, "Contact and friction between catheter and blood vessel," *Tribology International*, vol. 40, no. 2, pp. 319 – 328, 2007.

[167] M. Rotter, L. Dang, V. Jacquement, N. Virag, L. Kappenberger, and M. Haïssaguerre, "Impact of varying ablation patterns in a simulation model of persistent atrial fibrillation," *Pacing and Clinical Electrophysiology*, vol. 30, no. 3, pp. 314–321, 2007.

[168] H. Kottkamp, J. Berg, R. Bender, A. Rieger, and D. Schreiber, "Box isolation of fibrotic areas (bifa): A patient-tailored substrate modification approach for ablation of atrial fibrillation," *Journal of Cardiovascular Electrophysiology*, vol. 27, no. 1, pp. 22 – 30, 2015.

[169] K. McDowell, S. Zahid, F. Vadakkumpadan, J. Blauer, R. MacLeod, and N. Trayanova, "Virtual electrophysiological study of atrial fibrillation in fibrotic remodeling," *JPLoS One*, vol. e0117110, no. 3, pp. 324 – 328, 2015.

[170] G. Plank, R. A. Burton, P. Hales, M. Bishop, T. Mansoori, M. O. Bernabeu, A. Garny, A. J. Prassl, C. Bollensdorff, F. Mason, F. Mahmood, B. Rodriguez, V. Grau, J. E. Schneider, et al., "Generation of histo-anatomically representative models of the individual heart: tools and application," *Philosophical Transactions of the Royal Society of London A: Mathematical, Physical and Engineering Sciences*, vol. 367, no. 1896, pp. 2257–2292, 2009.

[171] M. Rottmann, J. Zuern, U. Arslan, K. Klingel, and O. Dössel, "Effects of fibrosis on the extracellular potential based on 3D reconstructions from histological sections of heart tissue," *Current Directions in Biomedical Engineering*, vol. 2, no. 1, pp. 675 – 678, 2016.

[172] G. Szalay, M. Sauter, M. Haberland, U. Zuegel, A. Steinmeyer, R. Kandolf, and K. Klingel, "Osteopontin. A fibrosis-related marker molecule in cardiac remodeling of enterovirus myocarditis in the susceptible host," *Circulation Research*, vol. 104, no. 7, pp. 851 – 859, 2009.

[173] C. Segnani, C. Ippolito, L. Antonioli, C. Pellegrini, C. Blandizzi, A. Dolfi, and N. Bernardini, "Histochemical detection of collagen fibers by sirius red/fast green is more sensitive than van gieson or sirius red alone in normal and inflamed rat colon," *PLOS ONE*, vol. 10, no. 12, pp. 1 – 10, 2015.

[174] G. Khanna, *Concise pathology for exam preparation - E-Book*. Elsevier Health Sciences, 2016.

[175] N. Marrouche, D. Wilber, and G. Hindricks, "Association of atrial tissue fibrosis identified by delayed enhancement MRI and atrial fibrillation catheter ablation: The DECAAF study," *JAMA*, vol. 311, no. 5, pp. 498 – 506, 2014.

List of Publications and Supervised Theses

Journal Articles

M. Rottmann, J. Zürn, U. Arslan, K. Klingel, O. Dössel. (2016). Effects of fibrosis on the extracellular potential based on 3D reconstructions from histological sections of heart tissue. Current Directions in Biomedical Engineering, 2(1), pp. 675-678, 2016.

O. Dössel, G. Lenis, A. Loewe, M. Rottmann, G. Seemann, T. Oesterlein, Model Assisted Biosignal Analysis of Atrial Electrograms. In Technisches Messen, Vol. 83(2), pp. 102-111, 2016.

Refereed Conference Articles

M. Rottmann, U. Arslan, W. Kaltenbacher, V. Markstein, T. Arentz, O. Dössel, A. Jadidi. Impact of Three Dimensional Atrial Fibrosis on Development and Stability of Rotational Activity in Atrial Fibrillation. A 3D Simulation and Clinical High-density Mapping Study in Persistent Atrial Fibrillation, Computing in Cardiology, 2016.

M. Rottmann, L. A. Unger, W. Kaltenbacher, Seemann G., A. Loewe, M. W. Krueger, A. S. Jadidi, T. Arentz, and O. Dössel. Methods for analyzing signal characteristics of stable and unstable rotors in a realistic heart model. In Computing in Cardiology, Vol. 42, pp. 485-488, 2015.

M. Rottmann, M. W. Keller, T. Oesterlein, G. Seemann and O. Doessel, Comparison of different methods and catheter designs to estimate the rotor tip position. A simulation study, Computing in Cardiology, Cambridge, pp. 133-136, 2014.

W. Kaltenbacher, M. Rottmann, O. Dössel. (2016). An algorithm to automatically determine the cycle length coverage to identify rotational activity during atrial fib-

rillation. A simulation study. Current Directions in Biomedical Engineering, 2(1), pp. 167-170, 2016.

C. Reich, T. Oesterlein, M. Rottmann, G. Seemann, O. Dössel. Classification of cardiac excitation patterns during atrial fibrillation. In Current Directions in Biomedical Engineering, Vol. 2(1) , pp. 161-166, 2016.

L. A. Unger, M. Rottmann, G. Seemann, and O. Dössel. Detecting phase singularities and rotor center trajectories based on the Hilbert transform of intraatrial electrograms in an atrial voxel model. In Current Directions in Biomedical Engineering, Vol. 1(1), pp. 38-41, 2015.

M. Rottmann, T. Oesterlein, and O. Dössel. Local activation time-based estimation of the direction of propagation of plane waves and the corresponding conduction velocity in simulated electrograms. In Biomedizinische Technik / Biomedical Engineering, Vol. 59(s1), pp. 152-155, 2014.

Refereed Conference Abstracts

M. Rottmann, J. Chen, H. Lehrmann, V. Markstein, U. Arslan, W. Kaltenbacher, L. Kienle, J. Zürn, R. Weber, J. Allgeier, B. Müller-Edenborn, C. Keyl, D. Trenk, F. Neumann, O. Dössel, T. Arentz, A. Jadidi. Rotational and Focal Drivers Develop at Heterogeneous Atrial Sites Displaying Low Voltage and Slow Conduction. Kardiologie - Herz- und Kreislaufforschung, Mannheim, Clinical Research in Cardiology, vol. 106, no. 1, pp. 11, Apr 2017.

M. Rottmann, J. Zürn, U. Arslan, K. Klingel, O. Dössel. (2017). Correlations between fibrosis and intracardiac recordings based on 3D reconstructions in the murine model of viral myocarditis. 83. Jahrestagung der deutschen Gesellschaft für Kardiologie. Herz- und Kreislaufforschung, Mannheim, Clinical Research in Cardiology, vol. 106, no. 1, pp. 11, Apr 2017.

M. Rottmann, W. Kaltenbacher, G. Seemann, V. Markstein, H. Lehrmann, J. Allgeier, R. Weber, O. Dössel, T. Arentz, A. S. Jadidi. Impact of Catheter Design for Identification of Rotational Activity in Atrial Fibrillation. Deutsche Gesellschaft für Kardiologie- Herz- und Kreislaufforschung Clin Res Cardiol (2016) 105(Suppl 2): 1, 2016.

M. Rottmann, U. Aslan, V. Markstein, H. Lehrmann., J. Allgeier, R. Weber, W. Kaltenbacher, F. Rafdionza, T. Arentz, O. Dössel, A. Jadidi. Dynamics of rotational and focal drivers in

persistent atrial fibrillation at cardiac fibrosis- A clinical mapping and simulation study, Journal of Clinical Experimental Cardiology, 2016.

M. Rottmann, T. Oesterlein, C. Reich, A. Luik, C. Schmitt, O. Dössel. Characteristic Features of Electrograms of Depolarization Waves During Atrial Fibrillation. In 38th Annual International Conference of the IEEE Engineering in Medicine and Biology Society, 2016.

O. Dössel, A. Luik, T. Oesterlein, M. Rottmann, B. Verma, C. Schmitt. Computer modeling of the atria and clinical electrograms. In 37th Annual International Conference of the IEEE Engineering in Medicine and Biology Society, 2015.

M. Rottmann, G. Seemann, and O. Dössel. Analysis of characteristic signal morphologies of double potentials near block lines in an atrial simulation model. In Biomedical Technology/ Biomedical Engineering, 2015.

Invited Talks

M. Rottmann, J. Chen, H. Lehrmann, V. Markstein, U. Arslan, W. Kaltenbacher, L. Kienle, J. Zürn, R. Weber, J. Allgeier, B. Müller- Edenborn, C. Keyl, D. Trenk, F. Neumann, O. Dössel, T. Arentz, A. Jadidi. The Relationship Between Atrial Fibrosis as Drivers of Atrial Fibrillation: Data from Computer Modeling, Signal Summit, Boston, 2017.

M. Rottmann, U. Aslan, V. Markstein, H. Lehrmann., J. Allgeier, R. Weber, W. Kaltenbacher, F. Rafdionza, T. Arentz, O. Dössel, A. Jadidi. Dynamics of rotational and focal drivers in persistent atrial fibrillation at cardiac fibrosis- A clinical mapping and simulation study, Journal of Clinical Experimental Cardiology, 2016.

Patents

1 american patent application. 3 invention disclosures. (Not for disclosure).

Supervised Student Theses

S9 Pala Ahmed, *Mechanische Modellierung von deformierten Multielektrodenkathetern*, Bachelor Thesis, Institute for Applied Materials, Karlsruhe Institute of Technology (KIT), 2016

S8 Linus Kienle, *Optimierung und Evaluierung verschiedener Methoden zur Parameterbestimmung von Rotoren bei unterschiedlichen Kathetergeometrien*, Bachelor Thesis, Institute of Biomedical Engineering, Karlsruhe Institute of Technology (KIT), 2016

S7 Farhan Rafdionza, *Analyse der RS-Difference bei verschiedenen Erregungsausbreitungen im menschlichen Vorhof*, Bachelor Thesis, Institute of Biomedical Engineering, Karlsruhe Institute of Technology (KIT), 2016

S6 Ufuk Arslan, *Auswirkungen von Fibrose auf kreisende Erregungen und Erregungen unterschiedlicher Richtungen im Vorhof*, Bachelor Thesis, Institute of Biomedical Engineering, Karlsruhe Institute of Technology (KIT), 2016

S5 Wenzel Kaltenbacher, *Vergleich verschiedener Methoden zur Parameterbestimmung von Rotoren bei unterschiedlichen Kathetergeometrien*, Bachelor Thesis, Institute of Biomedical Engineering, Karlsruhe Institute of Technology (KIT), 2016

S4 Christian Reich, *Classification of Cardiac Excitation Patterns during Atrial Fibrillation using Multichannel Mapping Data*, Master Thesis, Institute of Biomedical Engineering, Karlsruhe Institute of Technology (KIT), 2015

S3 Constantin Kohl, *Auswirkungen von Substratänderungen und komplexer Erregungsmuster auf intrakardiale Potentiale*, Master Thesis, Institute of Biomedical Engineering, Karlsruhe Institute of Technology (KIT), 2015

S2 Max Barchet, *Methoden zur Parameterbestimmung unterschiedlicher Arrythmien im Vorhof*, Bachelor Thesis, Institute of Biomedical Engineering, Karlsruhe Institute of Technology (KIT), 2015

S1 Laura Unger, *Signalmorphologie basierte Bestimmung von Arrythmien und Parameterabschätzungen von Erregungsausbreitungen im Vorhof*, Bachelor Thesis, Institute of Biomedical Engineering, Karlsruhe Institute of Technology (KIT), 2014

Award

Semi-Finalist Young Investigator Award, Computing in Cardiology (CinC), 2016, Vancouver, Markus Rottmann: "Impact of Three Dimensional Atrial Fibrosis on Development and Stability of Rotational Activity in Atrial Fibrillation. A 3D Simulation and Clinical High-density Mapping Study in Persistent Atrial Fibrillation".